105-14-11

COMPLETED
254

Y3.N88:25/4573

NUREG/CR-4573
BMI-2135

ORIGINAL

Elastic-Plastic Finite Element Analysis of Crack Growth in Large Compact Tension and Circumferentially Through-Wall-Cracked Pipe Specimen

Results of the First Battelle/NRC Analysis Round Robin

Prepared by J. Ahmad, M. Nakagaki, V. Papaspyropoulos, G. Wilkowski

Battelle's Columbus Division

Prepared for
U.S. Nuclear Regulatory Commission

NOTICE

This report was prepared as an account of work sponsored by an agency of the United States Government. Neither the United States Government nor any agency thereof, or any of their employees, makes any warranty, expressed or implied, or assumes any legal liability of responsibility for any third party's use, or the results of such use, of any information, apparatus, product or process disclosed in this report, or represents that its use by such third party would not infringe privately owned rights.

NOTICE

Availability of Reference Materials Cited in NRC Publications

Most documents cited in NRC publications will be available from one of the following sources:

1. The NRC Public Document Room, 1717 H Street, N.W.
   Washington, DC 20555
2. The Superintendent of Documents, U.S. Government Printing Office, Post Office Box 37082, Washington, DC 20013-7082
3. The National Technical Information Service, Springfield, VA 22161

Although the listing that follows represents the majority of documents cited in NRC publications it is not intended to be exhaustive.

Referenced documents available for inspection and copying for a fee from the NRC Public Document Room include NRC correspondence and internal NRC memoranda; NRC Office of Inspection and Enforcement bulletins, circulars, information notices, inspection and investigation notices; Licensee Event Reports; vendor reports and correspondence; Commission papers; and applicant and licensee documents and correspondence.

The following documents in the NUREG series are available for purchase from the GPO Sales Program: formal NRC staff and contractor reports, NRC-sponsored conference proceedings, and NRC booklets and brochures. Also available are Regulatory Guides, NRC regulations in the *Code of Federal Regulations*, and *Nuclear Regulatory Commission Issuances*.

Documents available from the National Technical Information Service include NUREG series reports and technical reports prepared by other federal agencies and reports prepared by the Atomic Energy Commission, forerunner agency to the Nuclear Regulatory Commission.

Documents available from public and special technical libraries include all open literature items, such as books, journal and periodical articles, and transactions. *Federal Register* notices, federal and state legislation, and congressional reports can usually be obtained from these libraries.

Documents such as theses, dissertations, foreign reports and translations, and non NRC conference proceedings are available for purchase from the organization sponsoring the publication cited.

Single copies of NRC draft reports are available free, to the extent of supply, upon written request to the Division of Technical Information and Document Control, U.S. Nuclear Regulatory Commission, Washington, DC 20555.

Copies of industry codes and standards used in a substantive manner in the NRC regulatory process are maintained at the NRC Library, 7920 Norfolk Avenue, Bethesda, Maryland, and are available there for reference use by the public. Codes and standards are usually copyrighted and may be purchased from the originating organization or, if they are American National Standards, from the American National Standards Institute, 1430 Broadway, New York, NY 10018.

NUREG/CR-4573
BMI-2135
RF, R5

Elastic-Plastic Finite Element Analysis of Crack Growth in Large Compact Tension and Circumferentially Through-Wall-Cracked Pipe Specimen

Results of the First Battelle/NRC Analysis Round Robin

Manuscript Completed: September 1986
Date Published: October 1986

Prepared by
J. Ahmad, M. Nakagaki, V. Papaspyropoulos, G. Wilkowski

Battelle's Columbus Division
505 King Avenue
Columbus OH 43201

Prepared for
Division of Engineering Safety
Office of Nuclear Regulatory Research
U.S. Nuclear Regulatory Commission
Washington, DC 20555
NRC FIN B8134

BLANK PAGE

II

ABSTRACT

As part of the Degraded Piping Program - Phase II, Battelle organized an international round robin involving elastic-plastic fracture mechanics analyses by the finite element method. Two crack-growth analysis problems were addressed: a large planform compact (tension) specimen of Type 304 stainless steel at 550 F (288 C), and a circumferentially through-wall-cracked pipe of Type 304 stainless steel, subjected to four-point bending at room temperature. The experimental data necessary for the analyses of both problems were supplied by Battelle. Participation in the round robin was sought from organizations in the U.S. and abroad.

For each of the two problems, five organizations (including Battelle) provided solutions. The results were first presented at the 1985 ASME Pressure Vessel and Piping Conference held in New Orleans in June 1985. Subsequently, the round-robin participants provided Battelle with written contributions describing the specific numerical modeling techniques used and the results. This report contains the compilation of these contributions and a comparison of the round-robin results.

BLANK PAGE

CONTENTS

Page

1. INTRODUCTION 1-1

1.1 Description of Problems 1-1
1.2 Presentation of Results 1-2
1.3 References for Section 1 1-3

2. FEM SOLUTIONS OF THE CT SPECIMEN PROBLEM (PROBLEM A) 2-1-5

2.1 Solution by Participant Number 1 2-2-6
2.2 Solution by Participant Number 2 2-6-10
2.3 Solution by Participant Number 3 2-7-11
2.4 Solution by Participant Number 4 2-9-13
2.5 Solution by Participant Number 5 2-13-17
2.6 References for Section 2 2-15-19

3. FEM SOLUTIONS OF THE PIPE PROBLEM (PROBLEM B) 3-1-65

3.1 Solution by Participant Number 1 3-2-66

3.2 Solution by Participant Number 2 3-4-68
3.3 Solution by Participant Number 3 3-6-70
3.4 Solution by Participant Number 4 3-7-71
3.5 Solution by Participant Number 5 3-11-75

4. J-ESTIMATION SCHEME RESULTS 4-1-125

4.1 Analysis of Problem A by a J-Estimation Scheme 4-1
4.2 Analysis of Problem B by a J-Estimation Scheme 4-2-126
4.3 References for Section 4 4-3-127

5. DISCUSSION OF RESULTS AND CONCLUSION 5-1-130

APPENDIX A. FINITE ELEMENT MODEL ROUND ROBIN PROBLEM STATEMENT A-1-144

LIST OF TABLES

Page

Table 1.1 List of participants and affiliations 1-4

Table 2.1.1 Summary of computed 10T C(T) results (Participant Number 1) 2-4

Table 2.3.1 Crack lengths used in the calculations (Participant Number 3) 2-7

Table 2.3.2 Summary of results (Participant Number 3) 2-9

Table 2.4.1 FE-Models (Participant Number 4) 2-10

Table 2.4.2 Crack initiation results (Participant Number 4) 2-12

Table 2.4.3 Calculated maximum load compared with experimental data (Participant Number 4) 2-12

Table 2.5.1 Applied displacement versus computed far-field J-integral (Participant Number 5) 2-14

Table 3.4.1 Summary of finite element models used (Participant Number 4) 3-8

Table 5.1 Variables used in the round-robin finite element analysis of the 10T compact specimen (Problem A) 5-2

Table 5.2 Variables used in the round-robin finite element analysis of the 16-inch (406 mm) pipe (Problem B) 5-3

LIST OF FIGURES

		Page
Figure 2.1	Geometry of the 1.0-inch (25.4-mm) thick 10T C(T) specimen	2-17
Figure 2.2	Experimental load versus load-point displacement for the 10T C(T) Type 304 stainless steel specimen at 550 F (288 C)	2-18
Figure 2.3	Crack extension versus applied displacement for the nonside-grooved 10T C(T) Type 304 stainless steel 1-inch (25.4-mm) thick specimen	2-19
Figure 2.4	Engineering stress versus strain for Type 304 stainless steel at 550 F (288 C) used in 10T C(T) specimen test	2-20
Figure 2.5	Uniaxial true stress versus true strain for Type 304 stainless steel at 550 F (288 C) used in 10T C(T) specimen test	2-21
Figure 2.1.1	Finite element mesh and J-contours (dashed lines) for the 10T C(T) specimen analysis (Participant 1)	2-22
Figure 2.1.2	Schematic representation of crack advance modeling method (Participant 1)	2-23
Figure 2.1.3	Crack extension versus applied displacement for the nonside-grooved 10T C(T) Type 304 stainless steel 1-inch (25.4-mm) thick specimen (Participant 1)	2-24
Figure 2.1.4	Computed Load versus J up to crack initiation (Participant 1)	2-25
Figure 2.1.5	Computed load versus load-point displacement (Participant 1)	2-26
Figure 2.1.6	Computed J versus applied load-point displacement (Participant 1)	2-27
Figure 2.1.7	Computed near- and far-field J as a function of crack extension (Participant 1)	2-28

BEST COPY AVAILABLE

LIST OF FIGURES

Page

Figure 2.1.8 Crack-tip-opening angle (CTOA) obtained from The finite element displacement solution (Participant 1) 2-29

Figure 2.2.1 Finite element model for one half of the C(T) specimen and paths along which J-integral is evaluated (Participant 2) 2-30

Figure 2.2.2 Calculated load versus displacement curve compared with the experimental data (Participant 2) 2-31

Figure 2.2.3 Calculated load versus J curves (Participant 2) 2-32

Figure 2.2.4 Calculated J versus displacement curves (Participant 2) 2-33

Figure 2.2.5 Calculated J versus Δa curves (Participant 2) 2-34

Figure 2.2.6 Calculated crack-opening angle versus crack extension curve (Participant 2) 2-35

Figure 2.3.1 FE mesh for initial crack length with two outermost J-integration rings indicated (Participant 3) 2-36

Figure 2.3.2 Load versus load-point displacement (Participant 3) 2-36

Figure 2.3.3 J versus load-point displacement up to crack initiation (Participant 3) 2-37

Figure 2.3.4 J versus Load up to crack initiation (Participant 3) 2-37

Figure 2.3.5 CTOD versus load-point displacement up to crack initiation (Participant 3) 2-38

Figure 2.3.6 J versus crack extension (Participant 3) 2-38

Figure 2.3.7 CTOD versus crack extension (Participant 3) 2-39

Figure 2.3.8 Distribution of the stress perpendicular to the crack in the ligament at applied displacement level (Participant 3) 2-39

BEST COPY AVAILABLE

LIST OF FIGURES

Page

Figure 2.3.9 Distribution of the stress perpendicular to the crack in the ligament at applied displacement level 90 mm (Participant 3) 2-40

Figure 2.3.10 Distribution of the stress perpendicular to the crack in the ligament at applied displacement level (Participant 3) 2-40

Figure 2.4.1 C(T) specimen: 2-D modelling, Model 1 (Participant 4) 2-41

Figure 2.4.2 C(T) specimen: Details about the 2-D FE analysis, Model 2 (Participant 4) 2-41

Figure 2.4.3 C(T) specimen: 2-D modelling, Model 3 (Participant 4) 2-41

Figure 2.4.4 C(T) specimen: Experimental load point displacement versus crack extension (Participant 4) 2-42

Figure 2.4.5 C(T) specimen: Load versus load point displacement, Model 1 (experimental and FE results) (Participant 4) 2-42

Figure 2.4.6 C(T) specimen: Load versus load point displacement, Model 2 (Experimental and FE results) (Participant 4) 2-42

Figure 2.4.7 C(T) specimen: Load versus load point displacement, Model 3 (experimental and FE results) (Participant 4) 2-43

Figure 2.4.8 C(T) specimen: Load versus load point displacement, Models 1 and 2 (experimental and FE results) (Participant 4) 2-43

Figure 2.4.9 C(T) specimen: J-integral versus path size, Model 2 (Path 1 to Path 7) (Participant 4) 2-43

Figure 2.4.10 C(T) specimen: J-integral versus path size, Model 2, load point displacement until 214 mm (Participant 4) 2-44

Figure 2.4.11 C(T) specimen: J-integral versus path size, Model 1 (Path 1 to Path 5) (Participant 4) 2-44

LIST OF FIGURES
(Continued)

Page

Figure 2.4.12 C(T) specimen: J-integral versus path size, Model 1 load point displacement until 221 mm (Participant 4) 2-44

Figure 2.4.13 C(T) specimen: J-integral versus path size, Model 3 (Path 1 to Path 5) (Participant 4) 2-45

Figure 2.4.14 C(T) specimen: Load versus J up to crack initiation, Model 2 (Participant 4) 2-45

Figure 2.4.15 C(T) specimen: Load versus J up to crack initiation, Model 1 (Participant 4) 2-45

Figure 2.4.16 C(T) specimen: Load versus J, Model 3 (Participant 4) 2-46

Figure 2.4.17 C(T) specimen: Calculated J versus load point displacement, Model 2 (Participant 4) 2-46

Figure 2.4.18 C(T) specimen: Calculated J versus load point displacement, Model 2 (Path 4 and Path 7) (Participant 4) 2-46

Figure 2.4.19 C(T) specimen: Calculated J versus load point displacement, Model 1 (Path 4 and 5) (Participant 4) 2-47

Figure 2.4.20 C(T) specimen: Calculated J versus load point displacement, Model 2 (Path 5 and 6) (Participant 4) 2-47

Figure 2.4.21 C(T) specimen: Calculated J versus crack growth, Model 2 (Participant 4) 2-47

Figure 2.4.22 C(T) specimen: Calculated J versus crack growth (Path 4 and 7), Model 2 (Participant 4) 2-48

Figure 2.4.23 C(T) specimen: Calculated J-R curve, Model 1 (Participant 4) 2-48

Figure 2.4.24 C(T) specimen: Calculated J-R curve, Model 1 (Participant 4) 2-48

Figure 2.4.25 C(T) specimen: Calculated J-R Curve, Model 3 (Participant 4) 2-49

LIST OF FIGURES
(Continued)

Page

Figure 2.4.26 C(T) specimen: Calculated J-R curve, Model 2 (Participant 4) 2-49

Figure 2.4.27 C(T) specimen: Deformation at the crack extension of 157 mm, Model 2 (Participant 4) 2-49

Figure 2.4.28 C(T) specimen: Development of crack opening angle (A), Model 2 (Participant 4) 2-50

Figure 2.4.29 C(T) specimen: Development of crack opening angle (B), Model 2 (Participant 4) 2-50

Figure 2.4.30 C(T) specimen: Development of crack opening angle (C), Model 2 (Participant 4) 2-50

Figure 2.4.31 C(T) specimen: Calculated crack opening angle versus crack extension, Model 2 (Participant 4) 2-51

Figure 2.4.32 C(T) specimen: Calculated crack opening angle versus crack extension, Model 1 (Participant 4) 2-51

Figure 2.4.33 C(T) specimen: Comparison between J_R- and J_M- curve, Model 1 (Participant 4) 2-51

Figure 2.4.34 C(T) specimen: Comparison of J_R curves from Model 1 and Model 2 to the J_M curve (Participant 4) 2-52

Figure 2.4.35 C(T) specimen: Load versus J, Model 2 Participant 4) 2-52

Figure 2.4.36 C(T) specimen: Load versus crack growth, Model 2 (experimental and calculation) (Participant 4) 2-52

Figure 2.4.37 C(T) specimen: Stress distribution in Z direction along the crack front (Δa about 94 mm), Model 2 (Participant 4) 2-53

Figure 2.4.38 C(T) specimen: Stress distribution in Y direction along the crack front (Δa About 94 mm), Model 2 (Participant 4) 2-53

Figure 2.4.39 C(T) specimen: Stress distribution in Z direction along the crack front (Δa About 157 mm), Model 2 (Participant 4) 2-53

LIST OF FIGURES
(Continued)

Page

Figure 2.4.40 C(T) specimen: Effective stress distribution along the crack front (Δa about 157 mm), Model 2 (Participant 4) 2-54

Figure 2.4.41 C(T) specimen: Strain distribution in Z direction along the crack front (Δa about 157 mm), Model 2 (Participant 4) 2-54

Figure 2.4.42 C(T) specimen: Strain distribution in Y direction along the crack front (Δa about 157 mm), Model 2 (Participant 4) 2-54

Figure 2.5.1 FE-mesh for C(T) specimen (Participant 5) 2-55

Figure 2.5.2 Calculated load versus load point displacement (Participant 5) 2-56

Figure 2.5.3 Calculated J versus load point displacement up to crack initiation (Participant 5) 2-57

Figure 2.5.4 Calculated J versus load point displacement (Participant 5) 2-58

Figure 2.5.5 Calculated load versus J up to crack initiation (Participant 5) 2-59

Figure 2.5.6 Calculated J_R-curve, crack initiation at J_C = 1,6 MN/m (Participant 5) 2-60

Figure 3.1 The apparatus and cracked pipe geometry for 16-inch (406.4-mm) nominal diameter pipe bending experiment 3-13

Figure 3.2 Bending load versus load-line displacement during experiment 8T (406.4-mm O.D. by 26.16-mm thick stainless steel pipe. Initial crack length = 484 mm) 3-14

Figure 3.3 Longitudinal engineering stress versus strain curve for 16-inch (406.4-mm) diameter Type 304 stainless steel pipe material at room temperature 3-15

LIST OF FIGURES
(Continued)

Page

Figure 3.4 Longitudinal true stress-true strain curve for 16-inch (406.4-mm) diameter Type 304 stainless steel pipe material at room temperature (large strains) 3-16

Figure 3.1.1 Finite elements used in calculation (Participant 1) 3-17

Figure 3.1.2 Finite element subdivision (extended in circumferential direction) (Participant 1) 3-18

Figure 3.1.3 Stress-strain curve used in calculation (Participant 1) 3-19

Figure 3.1.4 Relationship between crack length and load-point displacement (Participant 1) 3-20

Figure 3.1.5 Virtual crack extension for J-integral evaluation (Participant 1) 3-21

Figure 3.1.6 Total load versus load point displacement curve (Participant 1) 3-22

Figure 3.1.7 Total load versus crack extension curve (Participant 1) 3-23

Figure 3.1.8 Ovalization factor versus load-point displacement (Participant 1) 3-24

Figure 3.1.9 Total load versus J-integral curve (Participant 1) 3-25

Figure 3.1.10 J-integral versus load-point displacement curve (Participant 1) 3-26

Figure 3.1.11 J-integral resistance curve (Participant 1) 3-27

Figure 3.1.12 Crack opening profile before and after crack growth (Participant 1) 3-28

Figure 3.1.13 Variation of crack tip opening angle with crack extension (Participant 1) 3-29

LIST OF FIGURES
(Continued)

Page

Figure 3.2.1 Pipe: Three-dimensional FE-model of the pipe (Participant 2) 3-30

Figure 3.2.2 Deformed pipe with 0.65 inch (16.4 mm) of crack growth (Participant 2) 3-31

Figure 3.2.3 Pipe: Load versus load-point displacement (Participant 2) 3-32

Figure 3.3.4 Pipe: Two paths for J-integral calculation (Participant 2) 3-33

Figure 3.2.5 Pipe: J-integral versus path size (Participant 2) 3-34

Figure 3.2.6 Pipe: J-integral versus path size (Participant 2) 3-35

Figure 3.2.7 Pipe: J-integral versus load-point displacement (Participant 2) 3-36

Figure 3.2.8 Pipe: J-integral versus load (Participant 2) 3-37

Figure 3.2.9 Pipe: Calculated crack resistance curve (J_R) (Participant 2) 3-38

Figure 3.3.1 Analytical model and boundary conditions (Participant 3) 3-39

Figure 3.3.2 Load versus load-point displacement curve (Participant 3) 3-40

Figure 3.3.3 The J-integral versus load-point-displacement curve (Participant 3) 3-41

Figure 3.3.4 The J-integral versus load curve (Participant 3) 3-42

Figure 3.3.5 The J-integral versus crack extension curve (Participant 3) 3-43

Figure 3.3.6 Crack-tip-opening angle versus crack extension curve (Participant 3) 3-44

LIST OF FIGURES
(Continued)

Page

Figure 3.3.7 Crack-tip-opening displacement versus crack extension curve (Participant 3) 3-45

Figure 3.4.1 Shell finite element model (Participant 4) 3-46

Figure 3.4.2 Twenty-node brick (3-dimension) finite element model (Participant 4) 3-47

Figure 3.4.3 Computed load as a function of applied displacement (Participant 4) 3-48

Figure 3.4.4 Computed load versus J (Participant 4) 3-49

Figure 3.4.5 Computed J versus applied displacement (Participant 4) 3-50

Figure 3.4.6 Growth of plastic zone with increasing applied displacement (Participant 4) 3-51

Figure 3.5.1 Finite element mesh with virtual crack extension elements (Participant 5) 3-52

Figure 3.5.2 Load versus load-line displacement for 16-inch (406-mm) diameter stainless steel pipe (Participant 5) 3-53

Figure 3.5.3 Load versus J for 16-inch (406-mm) diameter stainless steel pipe (Participant 5) 3-54

Figure 3.5.4 J versus load-line displacement for 16-inch (406-mm) diameter stainless steel pipe (Participant 5) 3-55

Figure 3.5.5 J-R curve for 16-inch (406-mm) diameter stainless steel pipe (Participant 5) 3-56

Figure 3.5.6 An exaggerated pipe deformation at an early stage of bending 3-57

Figure 3.5.7 Contour of plastic zone and its growth on the crack plane section during bending 3-58

Figure 3.5.8 Contour of plastic zone and its growth on the crack plane section during bending 3-59

LIST OF FIGURES
(Continued)

Page

Figure 3.5.9 Plastic zone extended over the pipe surfaces 3-60

Figure 4.1.1 J_M and J_D versus Δa for the 10T C(T) planform specimen used in Problem A 4-4

Figure 4.2.1 J and J_M- resistance curves obtained by analyzing the 16-inch (406-mm) diameter through-wall cracked pipe data (Problem B) by the J-estimation formula 4-5

Figure 5.1 Comparison of the finite element analysis results for the C(T) specimen (Problem A) with experimental data 5-6

Figure 5.2 Comparison of the computed J (far-field) versus crack growth for the C(T) specimen (Problem A) 5-7

Figure 5.3 Comparison of the J (far-field) versus crack growth curves computed by finite element analysis with the J_D and J_M resistance curves (Problem A) 5-8

Figure 5.4 Schematics of load versus load-point displacement corrections taking account of pipe weight and wire rope compliance 5-9

Figure 5.5 Comparison of the finite element analysis results for Problem B with experimental data. (Note, experimental load-displacement record was corrected for dead-weight load of the pipe, but not for the compliance of the test system. Data in Table B-3 of Appendix A did not account for pipe dead-weight load for test system compliance) 5-10

LIST OF FIGURES
(Continued)

Page

Figure 5.6 J versus load-line displacement computed by finite element analyses and J-estimation scheme 5-11

Figure 5.7 Load versus J computed by finite element analyses and by J-estimation scheme 5-12

Figure 5.8 The J versus crack growth computed by finite element analysis, and by a J-estimation scheme (Problem B) 5-13

Executive Summary

An important task in the Degraded Piping Program - Phase II is to assess the accuracy of the analysis procedures being used by Battelle to interpret experimental data. As part of this effort Battelle has organized two international round-robins involving elastic-plastic finite element analyses of experimental data supplied by Battelle. The results of the first such round-robin are compiled in this report. The problems were selected in order to address the following technical subjects: a) Analysis of data from a fracture mechanics specimen test, and b) Analysis of data from a pipe fracture experiment. Both problems have been analyzed by Battelle and by participants from Japan, West Germany, France, and Finland. The results of these analyses were first presented at the 1985 Pressure Vessel and Piping Conference of the American Society of Mechanical Engineers held in New Orleans, Louisiana. Subsequently, the participants supplied to us their results in writing. In this report, Battelle has compiled these contributions. The report provides a comparative assessment of the results. In addition, it provides a discussion on the significance of the results to the end users of the technology - regulators, licensors, and the nuclear power industry.

ELASTIC-PLASTIC FINITE ELEMENT ANALYSIS OF CRACK GROWTH IN LARGE COMPACT TENSION AND CIRCUMFERENTIALLY THROUGH-WALL CRACKED PIPE SPECIMEN--RESULTS OF THE FIRST BATTELLE/NRC ANALYSIS ROUND ROBIN

by

J. Ahmad, M. Nakagaki,
V. Papaspyropoulos, and
G. Wilkowski

1. INTRODUCTION

This report contains the results of the First Finite Element Analysis Round Robin organized by Battelle under the auspices of the United States Nuclear Regulatory Commission (USNRC) as part of the Degraded Piping Program - Phase II (DP^3II). A key objective of the DP^3II program is to quantify the margin of safety in applying the state-of-the-art elastic-plastic fracture mechanics (EPFM) techniques to structural integrity assessments of nuclear power-plant piping. The main focus is on the J-integral-based EPFM approach to predict conditions for initiation, stable growth, and the onset of instability of cracks in nuclear power-plant piping. This approach is often referred to as the J-integral/tearing modulus (J/T) theory. A detailed description of this theory can be found in Reference 1.1.

Essential to the success of the J/T approach is an analysis method for accurate determination of J as a function of crack extension (Δa). In most practical applications, this is done by using simple J-estimation formulas. Several J-estimation formulas for a variety of fracture mechanics test specimen geometries, as well as cracked pipe geometries, are reported in the literature (see Reference 1.1). Typically, the derivation of these formulas requires making simplifying assumptions to avoid elaborate and expensive numerical solution techniques. For example, idealization of the material's stress-strain behavior is a quite common assumption. Such assumptions can often lead to large inaccuracies in calculated J-values. To avoid this source of error in the application of the J/T theory, Battelle's approach is to assess the accuracy of selected J-estimation formulas by performing elastic-plastic finite element method (FEM) analyses. However, because it is possible that the FEM solutions may also be inaccurate, independent assessment of these solutions is desirable. The focus of this round robin was to examine solutions to two specific problems. These are described below.

1.1 Description of Problems

The first problem (Problem A) involved computing J as a function of Δa for a large Type 304 stainless steel compact (tension) [C(T)] specimen.

The specimen was 1 inch (25.4 mm) thick, but the planar dimensions were those of a 10T specimen. An experiment using this specimen was performed by Battelle at a temperature of 550 F (288 C). In the experiment, load-line displacement (δ) and load (P) were monitored as a function of crack extension (Δa). The maximum crack extension length in the experiment was 6.19 inches (157.23 mm). In addition to generating these data, Battelle performed uniaxial tensile tests to obtain the engineering as well as true stress-true strain curves of the material at 550 F (288 C).

The data from these tests, along with detailed drawings of the specimen, were supplied to the fracture mechanics analysis group at Battelle and to a number of potential round-robin participants located in the U.S. and abroad. The participants were requested to use these data to perform elastic-plastic finite element analyses in which crack growth should be modeled in accordance with the supplied δ (or P) versus Δa data. This type of computation is called the generation phase analysis. No restrictions were placed as to the refinement of the finite element model, choice of crack-growth modeling technique, or nonlinear solution procedure. The participants were, however, asked to present their results in a consistent manner. The key results included computed near-field and far-field values of J-integral as functions of crack extension, and the P versus δ curves. Note that, depending on whether P versus Δa or δ versus Δa data are used as input, either δ or P can be computed by FEM analysis. The other problem details and reporting requirements supplied to the participants are contained in Appendix A under Problem Statements.

The second problem (Problem B) involved computing J as a function of Δa for a 16-inch (406.4-mm) nominal diameter Type 304 stainless steel pipe containing a through-wall circumferential flaw and subject to four-point bending. An experiment using this specimen at room temperature was performed by Battelle under a research program funded by the Electric Power Research Institute. The experimental data in the form of P versus δ and δ versus Δa records were provided to the participants as well as the engineering and true stress-true strain curves of the material at room temperature. Details of Problem B are given in Appendix A.

As in Problem A, no restrictions were placed on the potential participants regarding the type of computational techniques they could use in their solutions to Problem B. The key results requested were the computed J versus Δa and P versus δ curves. Other reporting requirements for the participants appear in Appendix A.

1.2 Presentation of Results

A total of five organizations provided solutions to Problem A. These organizations are: Battelle Columbus, Technical Research Center of Finland, Gesellschaft für Reaktorsicherheit m.b.H. (West Germany), University of Tokyo and Yokohama National University (Japan), and Materialprüfungsanstalt Stuttgart (West Germany). At their request, the solutions (contained in Section 2 of this report) are not identified by the participating organizations' names.

For Problem B, the participating organizations were Battelle Columbus, Central Research Institute of Electric Power (Japan), Gesellschaft für Reaktorsicherheit m.b.H. (West Germany), Kawasaki Heavy Industries (Japan), and Commissariat à l'Energie Atomique (France). The solutions provided by the above organizations make up Section 3.

In addition to the elastic-plastic finite element analysis results provided by the participating organizations, estimates of J versus Δa for both Problem A and Problem B were obtained by Battelle using available engineering estimation formulas. Results of these analyses are presented in Section 4. A comparison of these results with the various finite element analysis results is presented in Section 5. Section 5 also contains a comparison of the computed P and δ with the corresponding experimental data for each problem, as well as conclusions.

The solutions contributed by the participating organizations were first presented at the 1985 Pressure Vessels and Piping Conference of the American Society of Mechanical Engineers held in New Orleans, Louisiana. Battelle expresses appreciation for the presentations and for the active and enthusiastic participation of the contributors. Their names and organizations are provided in Table 1.1.

References for Section 1

1.1 "The Development of a Plan for the Assessment of Degraded Nuclear Piping by Experimentation and Tearing Instability Fracture Mechanics Analysis", by Battelle-Columbus Laboratories, NUREG/CR-3142, report to the U.S. Nuclear Regulatory Commission, June 1983.

TABLE 1.1. List of participants and affiliations

Technical Research Center, Finland

Dr. K. Ikonen
Mr. T. Mikkola
Dr. H. Talja

Commissariat à l'Energie Atomique, Cadarache, France

Dr. E. de Langre

Gesellschaft für Reaktorsicherheit m.b.H., West Germany

Dr. D. Azodi

Materialprüfungsanstalt Stuttgart, West Germany

Mr. K-H. Herter
Dr. A. Sauter

University of Tokyo, Japan

Prof. T. Miyoshi
Prof. Y. Yoshida

Central Research Institute of Electric Power, Japan

Dr. K. Kashima
Dr. Y. Takahashi

Kawasaki Heavy Industries, Japan

Mr. T. Shimakawa

Yokohama National University, Japan

Prof. M. Shiratori

Battelle Columbus Division, USA

Dr. J. Ahmad
Mr. N. Ghadiali
Dr. M. Nakagaki
Ms. V. Papaspyropoulos
Mr. G. Wilkowski

BEST COPY AVAILABLE

2. FEM SOLUTIONS OF THE C(T) SPECIMEN PROBLEM (PROBLEM A)

In EPFM practice, analyses of crack-growth data from tests on small laboratory specimens are used to establish the J-integral versus Δa, or the J-resistance curve of the material. The J-resistance curve is assumed to be a material property, independent of the specimen geometry and loading. However, there is ample evidence in the literature to suggest that this assumption is questionable. Especially as the crack extension (Δa) increases, the J-resistance curve is known to become increasingly geometry-dependent. From a practical viewpoint, this fact is discomforting. Without a geometry-independent J-resistance curve, accurate prediction of crack-growth behavior in nuclear power-plant piping and other engineering structures becomes difficult. As an expedient, J-resistance curves obtained from bend-type or C(T) specimens are used. For many applications, the calculated J-R curves from these specimen types tend to provide lower-bound (conservative) J-resistance curves.

Another concern is based on the use of J-resistance curves obtained from small-specimen data. These data can be used to develop J-resistance curves only for a limited amount of crack extension. In nuclear power-plant pipes, existing cracks may grow stably for a relatively large distance before instability may occur. Therefore, to predict the conditions for crack-growth instability in nuclear power-plant pipes, J-resistance curves for large values of Δa are needed. However, based on theory, there are valid reasons for being cautious when using the J-resistance curve approach to predict crack-growth instability conditions if the stable crack extension amount is large. The J-integral has its basis in the deformation theory of plasticity, that is, nonlinear elasticity. The deformation theory cannot properly describe the stress-strain behavior of a material if unloading occurs after the material has yielded. Consequently, J becomes increasingly inapplicable as crack extension length becomes larger. This is due to stress unloading in the wake of the propagating crack tip. Beyond a certain amount of crack extension, J loses meaning as a crack tip characterizing parameter. A good account of the limits of applicability of J can be found in Reference 2.1.1. In terms of finite element analysis results, a measure of the extent of crack growth over which J can be used with confidence is the crack advance length over which J remains path-independent. This crack advance length is determined by using more than one contour to compute J during the finite element analysis.

But even if the above concerns can be overlooked to satisfy the immediate need for a conservative methodology to predict crack-growth behavior in nuclear power-plant pipes, a hindrance still exists. This is the calculation of J(Δa). In practice, the use of detailed elastic-plastic finite element analyses in every laboratory experiment to develop a J-resistance curve is not economically feasible. Therefore, simple methods have been developed to calculate approximately J(Δa) using experimental P versus δ and δ versus Δa measurements. For example, ASTM Standard E813-81 provides a simple formula to calculate J using C(T)

5

specimen data. The derivation of this formula is possible only if certain assumptions are made to simplify mathematical operations. One, the material is assumed to be elastic-perfectly plastic; that is, there is no strain-hardening. Also, the uncracked ligament of the specimen is assumed to be fully yielded for the calculation of the plastic contribution to J. Depending upon the material, these assumptions are sometimes invalid. Consequently, acceptable accuracy of the J-resistance curves established by using such J-estimation formulas cannot always be ascertained.

A common practice for assessing the accuracy of a particular J-estimation method is to perform elastic-plastic finite element generation-phase analyses of some of the experiments. Then, a direct comparison is made between J-resistance curves calculated by the J-estimation formula and those calculated by the finite element method.

Several different approaches are used for a nonlinear (elastic-plastic) finite element modeling of crack growth. For example, there are different approaches to modeling plastic flow behavior. Also, numerical integration of the nonlinear governing equations can be performed using any of the several techniques available, and with different prescribed criteria for solution convergence. Additionally, simulation of crack growth in the finite element analysis can be performed in several different ways. Finally, the J-integral computation using finite element analysis results can also be performed in several different ways.

The specific choices made in the finite element analysis* can significantly affect the accuracy of the computed J-resistance curves. Thus, Problem (A), described in detail in Appendix A, was presented to the technical community in the field and solutions were solicited. The specimen drawing and the curves representing P versus δ, δ versus Δa, engineering stress versus strain, and true stress-true strain are shown in Figures 2.1 through 2.5. The results obtained by the five participating organizations are presented below. No significant editorial changes in the written contributions received from the participants were made.

2.1 Solution By Participant Number 1

The computations were performed using in-house nonlinear finite element analysis code on the CYBER mainframe computer. This code is primarily a fracture mechanics analysis code with elastic-plastic crack-growth modeling capability. It can be used for both generation phase computations (in which an experimental P or δ versus Δa record is provided as part of the input, and a resistance curve is computed), and application phase computations (in which crack advance occurs according to a prescribed resistance curve). During the analysis, the J-integral values are computed using the path-independent contour integral definition (Ref. 2.1.2) for plane-stress and plane-strain problems, and the virtual crack extension (VCE) method (Ref. 2.1.3) for three-dimensional problems. The code contains several different constitutive models for elastic-plastic analysis. The nonlinear solution procedures include the tangent modulus method and the modified and full Newton-Raphson iteration techniques. The code contains a large-deformation and finite strain analysis capability. The element library in the code includes linear and quadratic one-, two-, and three-dimensional isoparametric elements, doubly curved shell isoparametric elements, and a general elastic stiffness element. Crack propagation is modeled by gradually releasing the initial coupled set of nodes along the projected crack propagation path.

---

* Various participants abbreviated finite element analysis as FEM or FE.

For the present analysis of the C(T) specimen geometry, the finite element model (Figure 2.1) included 263 eight-node isoparametric elements and 879 nodal points. A 3x3 Gaussian quadrature was used for stiffness generation. The modified Newton-Raphson iteration method was selected for equilibrium compensation and, because of the large ductility of Type 304 stainless steel, the analysis allowed for finite deformations and finite strains. The hardening was assumed isotropic and the J_2 flow theory was used in the constitutive model. The material's behavior was modeled by a multilinear representation of the stress-strain curve. Analyses were performed using the true stress versus true strain curve (for the entire range of crack growth), as well as the engineering stress-strain curve (up to crack initiation). The J-integral was computed using a near-field contour and a far-field contour as indicated in Figure 2.1.1. During crack-growth modeling, the far-field contour was kept fixed. The near-field contour was moved with the crack tip approximately maintaining its initial shape and size.

In the analysis, double nodes were used at all node point locations along the uncracked specimen ligament. These double nodes were coupled using spring elements having a stiffness which was several orders of magnitude larger than the Young's modulus for 304 stainless steel. A schematic drawing is shown in Figure 2.1.2.

The analysis started by applying displacement at the node located at the top of the pinhole. Beyond the first occurrence of the effective stress reaching the prescribed yield stress, further displacement was applied in small increments until the prescribed displacement corresponding to crack-growth initiation was achieved. At this point, the gradual node release process was started, and the experimental δ versus Δa record shown in Figure 2.1.3 was followed. The arrows in Figure 2.1.3 indicate the location of the corner nodes (not the midside nodes) of the elements along the uncracked ligament. Each of these nodes was released in 10 equal increments.

The results of the analysis are summarized in Table 2.1.1. The load, J (near-field), and J (far-field) are the computed values. The crack length and load-point displacement are the input data to the analysis.

1

Table 2.1.1 Summary of computed 10T CT results

				Calculated Values					
Crack Length		Load-Point Displacement		Load		J (Near Field)		J (Far Field)	
inch	mm	inch	mm	lb	kN	in-lb/in²	kN/m	in-lb/in²	kN/m
10.11	257	0.0108	0.27	7085	31	10	1.75	10	1.75
"	"	0.03426	0.87	21115	94	93	16.28	95	16.63
"	"	0.05776	1.47	31279	139	234	40.97	234	40.97
"	"	0.0812	2.06	37506	165	393	68.81	387	67.76
"	"	0.1122	2.85	41380	184	559	97.88	554.5	97.09
"	"	0.1282	3.26	43935	195	736	128.87	733	128.34
"	"	0.1516	3.85	45878	204	938	164.24	934	163.54
"	"	0.1752	4.45	47414	210	1152	201.72	1142	199.96
"	"	0.1986	5.04	48762	216	1380	241.64	1364	238.83
"	"	0.222	5.64	49968	222	1617	283.14	1599	279.98
"	"	0.2456	6.24	51065	227	1867	326.91	1847	323.40
"	"	0.2691	6.84	52080	231	2132	373.31	2113	369.98
"	"	0.2925	7.43	53021	235	2405	421.12	2386	417.78
"	"	0.31603	8.03	53910	239	2682	469.62	2656	465.06
"	"	0.3395	8.62	54748	243	2987	523.02	2949	516.36
"	"	0.3629	9.22	55556	247	3312	579.93	3266	571.87
"	"	0.3865	9.82	56333	250	3640	637.36	3589	628.43
"	"	0.4099	10.41	57088	253	3938	689.54	3882	679.73
"	"	0.4334	11.01	57821	257	4240	742.42	4174	730.86
"	"	0.4569	11.61	58538	260	4545	795.83	4469	782.52
"	"	0.4804	12.20	59230	263	4854	849.94	4768	834.88
"	"	0.5038	12.79	59910	266	5171	905.44	5075	888.6
"	"	0.52735	13.39	60574	269	5494	961.99	5388	943.44
"	"	0.5508	13.99	61225	272	5824	1019.78	5709	999
"	"	0.5743	14.59	61866	275	6167	1079.84	6041	1057.78
"	"	0.5976	15.18	62496	278	6510	1139.9	6373	1116
"	"	0.6212	15.78	63114	280	6856	1200.49	6710	1175
"	"	0.6447	16.38	63722	283	7205	1261.59	7055	1235
"	"	0.6681	16.97	64318	286	7548	1321.65	7394	1295
"	"	0.6917	17.57	64906	289	7892	1381.89	7738	1355
"	"	0.7152	18.17	65487	291	8245	1443.69	8084	1416
"	"	0.7386	18.76	66058	294	8601	1506.04	8435	1477
"	"	0.7621	19.36	66617	296	8961	1569.07	8791	1539
"	"	0.7855	19.95	67165	299	9325	1632.81	9156	1603
"	"	0.8091	20.55	67707	301	9693	1697.24	9523	1667
"	"	0.8325	21.15	68240	303	10067	1761.73	9886	1731
"	"	0.856	21.74	68779	306	10447	1829.27	10257	1796
"	"	0.8795	22.34	69286	308	10825	1895.46	10623	1860
"	"	0.90303	22.94	69797	310	11203	1961.64	10984	1923
"	"	0.9265	23.53	70300	313	11586	2028.71	11351	1988
"	"	0.95	24.13	70799	315	11971	2096.12	11718	2052

Table 2.1.1 (Continued)

Crack Length		Load-Point Displacement		Calculated Values					
				Load		J (Near Field)		J (Far Field)	
inch	mm	inch	mm	lb	kN	$\frac{in\text{-}lb}{in^2}$	kN/m	$\frac{in\text{-}lb}{in^2}$	kN/m
10.55	268	1.9	48	78164	347	23258	4072	23468	4109
10.99	279	2.54	64	80248	357	31998	5603	33589	5881
11.44	290	3.2	81	81082	361	41402	7249	44810	7846
11.88	302	3.6	91	76286	339	39359	6892	50206	8791
12.32	313	4.09	104	72592	323	42061	7365	57854	10130
12.76	324	4.5	114	67014	298	40268	7051	63413	11104
13.20	335	4.92	125	61393	273	38917	6814	68792	12045
13.65	347	5.4	137	56413	251	39226	6868	75156	13160
14.09	358	5.9	150	51393	228	38984	6826	81417	14256
14.53	369	6.3	160	45222	201	34649	6067	85054	14893
14.97	380	6.8	173	40231	179	33951	5945	90269	15806
15.42	392	7.4	188	36001	160	35533	6222	96906	16968
15.86	403	8	203	31587	140			102890	18016
16.3	414	8.8	223	28131	125			111660	19552

9

BEST COPY AVAILABLE

Note that the near-field J values corresponding to the last two crack lengths are absent from the table. This is because the model did not allow for the near-field contour to be of its initial shape and size beyond 15.42 inch (391.7 mm) of crack length.

The analysis results contained in Table 2.1.1 were obtained by using the true stress versus true strain curve of the material. Results up to crack initiation were also obtained using the engineering stress versus strain curve. A comparison of these two types of calculations in terms of computed J versus load values up to crack initiation is shown in Figure 2.1.4. Since no discernable difference was found, the analysis using engineering stress versus strain curve was discontinued.

A comparison of the computed load versus displacement with the experimental load versus displacement curve is shown in Figure 2.1.5. The computed J versus applied displacement, and J versus Δa results are shown in Figures 2.1.6 and 2.1.7, respectively. Both the far-field and near-field J values are included in these figures.

Figures 2.1.4 and 2.1.7 show that the path-independence of J is maintained up to about 1.25 inches (31.75 mm) of crack extension. This is 12.5 percent of the initial uncracked ligament. It is seen that beyond this crack extension the near-field J assumes a more or less constant value, while the far-field J keeps rising. It is of interest to note that another near-field parameter, the crack tip opening angle (CTOA), calculated using the finite element displacement solution, also seems to reach a constant value for large amounts of crack extension. This is shown in Figure 2.1.8. The CTOA was calculated by using the displacement of the closest corner node behind the instantaneous crack tip.

2.2 Solution by Participant Number 2

Figure 2.2.1 shows the element breakdown of one-half of the specimen. Due to symmetry one-half of the specimen was analyzed. The point force, P, was applied at the point on the edge of the pinhole indicated in the figure. Two-dimensional triangular elements with linear shape functions were used. Numbers of elements and nodes are 327 and 201, respectively.

The constitutive model used in the analysis is J_2 flow theory, i.e., Prandtl-Reuss flow rule coupled with von Mises yield criterion. Further, isotropic hardening model with true stress versus true strain curve (see Appendix A) was assumed. No finite deformation nor finite strain analysis was carried out. The r_{min} method proposed by Yamada, et al. (Ref. 2.2.1) was used in the incremental scheme of the elastic-plastic analysis.

The method of crack extension was based upon uncoupling nodal points ahead of the crack tip by relaxing incrementally the forces holding them together. The J-integral was evaluated through the contour integral. Figure 2.2.1 shows the two paths along which the contour integrals were calculated. One of the paths is notified with "near field" and the other "far field".

Figure 2.2.2 shows the load-versus-displacement curves. The figure shows that reasonable coincidence is obtained between the calculated and experimental results although the calculated values of load are a little higher than the experimental.

Figures 2.2.3 to 2.2.5 show load-versus-J, J-versus-displacement, and J-versus-Δa curves, respectively. In these figures, dotted lines correspond to those whose J-values are evaluated along the path indicated by "near-field" in Figure 2.2.1 while solid lines "far-field". The results of these figures show that something is wrong if the J-integral is evaluated along the near-field path in the range of large-scale yielding, especially after crack extension has occurred. Therefore, J should be evaluated along the far-field path.

Figure 2.2.6 shows the crack opening angle (COA) versus amount of crack extension, Δa. The figure shows that COA is nearly constant through the whole range of Δa analyzed.

2.3 Solution by Participant Number 3

The calculations are carried out by using 2-dimensional FE-models. We investigated earlier some specimen geometries and materials and compared the results with experiments. We concluded from the results that if the material is very ductile as stainless steel, 2-dimensional analyses give fairly good results. Because of this and the thinness of this specimen compared to other dimensions, plane-stress modeling was thought to be enough, though 3D-analysis could have been performed.

Because our present computer codes cannot simulate crack growth, the calculations have been made for five different crack lengths ranging from initial to final length (Table 2.3.1). The FE-mesh for initial crack length is shown on Figure 2.3.1. Eight-node isoparametric elements with 3x3 Gaussian integration have been used. The crack tip has been modeled using seven collapsed elements with 15 independent crack tip nodes, thus giving the 1/r-singularity.

Table 2.3.1. Crack lengths used in the calculations
(Participant Number 3)

Crack Length, a	Mesh				
	1	2	3	4	5
inch	10.11	11.66	13.99	14.75	16.30
mm	256.7	296.1	355.4	374.7	414.0

The nodes in the ligament located on the axis of symmetry are not allowed to move in the z-direction. One of the crack tip nodes is also fixed in the y-direction. The load is given as a point load affecting at the top of the hole.

In the analyses we used ADINA code for stress and strain calculations. Only the material nonlinearity has been taken into consideration in the calculations. The initial yield has been defined by von Mises criterion and after that isotropic hardening has been assumed. For calculating J-integral we used our virtual crack extension post processor, which can calculate J-integral in 2- and 3-dimensional cases, and is based on virtual crack extension method (deLorenzi formulation).

The J-integral values reported are calculated as averages from four integration elements rings (Figure 2.3.1). The innermost integration ring (length of elements of 0.12 inch [3 mm]) can be considered to give a near-field J-value and the outermost ring a far-field J, respectively. The J-value deviation from these rings was below 5 percent of the average in all calculations.

Least squares fitting lines have been to calculate CTOD-values at the instantaneous crack tip location.

The results (Figures 2.3.2 to 2.3.7 and Table 2.3.2) are constructed as follows: values up to the measured maximum load have been chosen from curves calculated for the initial crack length in spite of actual slight crack extension. After that the points corresponding to the measured dependence between displacement and crack extension have been chosen from the other calculated curves. Normally this interpolation should be made based on experimental J_R-curve.

All calculated values seemed to be in good agreement with the experimental results. The deviation in the results was remarkable only when the final crack length was considered. This is intelligible because the geometric effects have a growing importance when the crack length increases.

Thus, it seems not to be necessary to actually simulate the crack growth to do reasonable fracture assessments. The procedure of different crack lengths is expected to be advantageous in 3-D cases as well. The local Δa values could then be evaluated using local J-values and J_R-curve.

On Figures 2.3.8 to 2.3.10, the distribution of the stress component perpendicular to the crack in the ligament is shown approximately at applied displacement levels 0.79, 3.54, and 6.69 inch (20, 90, and 170 mm).

In the calculations, only material nonlinearity was taken into consideration. To describe crack growth, five different crack lengths were considered.

12

Table 2.3.2. Summary of results (Participant Number 3)

Displ., mm	Load, kN	J, kJ/m^2	Crack Ext., mm	CTOD, mm
0.0	0.0	0.0	0.0	0.00
0.51	50.0	4.2	0.0	0.05
1.16	100.0	19.7	0.0	0.15
2.33	150.0	66.0	0.0	0.39
3.40	175.0	119.7	0.0	0.63
5.15	200.0	219.0	0.0	1.03
7.25	220.0	355.0	0.0	1.54
10.53	240.0	600.3	0.0	2.37
13.97	255.0	869.5	0.0	3.23
18.27	270.0	1235.0	0.0	4.32
21.70	280.0	1536.0	0.0	5.18
24.13	286.3	1758.0	0.0	5.79
36.50	324.3	3331.0	3.8	9.75
87.84	273.6	7999.0	39.3	19.92
125.40	190.5	9816.0	78.6	22.67
169.50	116.6	10219.0	117.9	22.72
225.00	59.0	9544.0	157.3	20.54

2.4 Solution by Participant Number 4

The computations have been performed with a modified version of the Finite Element Code ADINA (Automatic Dynamic Incremental Nonlinear Analysis).

Three different kinds of 2D-finite element (FE) meshes (Figures 2.4.1 to 2.4.3) were performed for the 10T compact (tension) specimen. All three FE-models consisted of eight node isoparametric elements, the number of elements and nodes are tabulated in Table 2.4.1.

The FE analysis was performed by using true stress versus true strain curve, see Appendix A.

The constitutive model based on the incremental theory of plasticity and von Mises initial yield criterion with isotropic hardening were considered. The modified Newton iteration method was selected for equilibrium compensation and because of the large ductility of Type 304 stainless steel the analysis was made for plane-stress conditions.

✓3

Table 2.4.1. FE-Models (Participant Number 4)

Models	Number of Elements	Number of Nodes	Degrees of Freedom
Model 1	80	305	579
Model 2	208	687	1362
Model 3	482	1552	3074

To calculate J, the "virtual crack extension" method was employed. The J-integral was computed using several contours, among others near-field and far-field contours.

$$J = \frac{1}{A_C} \int_V [\sigma_{ij} \frac{\partial U_j}{\partial x_k} - W\delta_{ik}] \frac{\partial \Delta X_k}{\partial X_i} dV$$

No special treatment of the crack tip singularity was needed, since in the plastic region, the actual crack tip singularity would be a function of the strain hardening.

The FE analysis for compact tension involved modeling crack advance according to the prescribed displacement versus crack extension record.

One of the modifications implemented into the ADINA CODE are subroutines for J-integral calculations and simulation of stable crack growth by the procedure called "node shift and node release" technique.

A number of finite element runs were made for three finite element meshes to establish the adequate model for this experiment.

The numerical simulation of the experiments have been conducted by using the relation between the load-point displacement and the crack propagation as observed in the experiment (Figure 2.4.4), as input for the finite element analysis in order to calculate:

- Load versus load-point displacement curve, Figures 2.4.5 to 2.4.8
- J-integral versus path size, Figures 2.4.9 to 2.4.13
- J-integral load up to crack initiation, Figures 2.4.14 to 2.4.16
- J versus load-point displacement, Figures 2.4.17 to 2.4.20

- J versus crack growth, Figures 2.4.21 to 2.4.26
- Deformation at crack extension of 6.18 inches (157 mm), Figure 2.4.27
- Development of crack tip opening angle, Figures 2.4.28 to 2.4.30
- Calculated crack tip opening angle versus crack extension, Figures 2.4.31 to 2.4.32
- Comparison between J_R- and J_M-curves, Figures 2.4.33 and 2.4.34
- Load versus J, Figure 2.4.35
- Load versus crack growth, Figure 2.4.36
- Stress and strain distribution in z- and y-direction, Figures 2.4.37 to 2.4.42.

The primary reason for the variation of the finite element meshes was based on the lack of appropriate agreement between the FE-Model 1 (Figure 2.4.1) results of load versus load-point displacement (P-δ) and the experimental curve. Generally, in case of plane stress calculation for a compact tension, one expects that the FE-results of P-δ curve should never exceed the experimental data, but it was the case concerning the results of FE-Model 1. So we refined and varied the finite element meshes (Model 2 and 3, Figures 2.4.2 and 2.4.3), in order to find better agreement, but unfortunately we did not succeed (Figures 2.4.5 to 2.4.8). So we believe the possible reasons for this overestimation were:

1. Uncertainties regarding 2D-Model instead of a 3D-modeling
2. Uncertainties regarding the experimental measurement.

We hope to find an adequate answer by a 3D-numerical simulation of the C(T) specimen soon.

Further discussion and consideration is mainly based on FE-Model 2, because we believed this FE-mesh is as fine as necessary in order to determine reliable J-integral-values and other fracture mechanics results, and last but not least, because of lower computer costs--compared with the FE-Model 3.

Nevertheless, we presented and compared most of the time the results of other FE-Models as well. In case of FE-Model 3, we cut off with further investigations after reaching about 90-mm crack opening.

Besides the problem mentioned before, we found reasonable agreement for all other FE-analysis results, which are shown in Figures 2.4.14 to 2.4.42, e.g., see Tables 2.4.2 and 2.4.3. The computed load versus

15

Table 2.4.2. Crack initiation results (Participant Number 4).

Procedure	J, (N/mm)	Load, (kN)	J-Deviation From ASTM-Value, (%)	Load Deviation From Experiment, (%)
FE-Model 2	2052	309.0	6	2
FE-Model 1	2178	301.4	13	4
FE-Model 3	2060	318.7	6	1
	ASTM-Value	Experiment		
	1934.7	315	-	-

Table 2.4.3. Calculated maximum load compared with experimental data (Participant Number 4)

Procedure	Load, (kN)	Deviation From Experiment, (%)
FE-Model 2	350	8
FE-Model 1	350	8
FE-Model 3	357	10
Experiment	324	--

load-point displacement was compared with the experimental record and was higher in comparison, see the comment before.

All values of J-integral contours are reported to indicate the effect of the influence on path size.

The deviation between the near-field and far-field J-integral contour from about 1-inch (25.4-mm) crack growth on was remarkable, since the geometric effects have growing influence when crack length increases.

In summary, J-integral (energy release rate) provided the ability to predict the J-resistance curve, even for a large stable crack growth. The influence of the path size was demonstrated.

2.5 Solution by Participant Number 5

The crack-growth experiment to be analyzed was a 10T (stainless steel) C(T) specimen test. The size of the specimen was 10T in planar dimension and 1.0 inch (25.4 mm) in thickness.

The experimental data given by Battelle such as true-stress-strain curve, crack extension versus applied displacement, and the material properties Young's modulus and Poisson's Ratio for the test temperature of 550 F (288 C), had to be used as input to the FE analysis (see Appendix A).

In the FE discretization for the computer code ADINA (Ref. 2.5.1) a 2-dimensional structure representation using 488 eight-node isoparametric elements (1592 nodal points) under plane stress.

The constitutive model for representing the highly ductile material deformation behavior followed small strain incremental plasticity using J_2 flow theory together with isotropic hardening on von Mises initial yield surface. The stiffness matrix generation has been performed by a 2x2 Gaussian integration scheme.

The BFGS matrix update method was selected for equilibrium compensation.

The crack extension was simulated by shifting of nodal points. These nodes are then released when the crack growth becomes equal to the original length of the element side.

For the evaluation of the J-integral, the energy release rate under virtual crack extension (Refs. 2.5.2, 2.5.3) has been used.

The complete loading history had been divided into 225 loading steps for the ADINA run. After each load step a stiffness reformation had been performed.

The total CPU time on a CRAY-1/M machine was 6 hours 36 minutes.

After 158 load steps the far-field J-integral reached a maximum value; during further loading with increasing load-point displacement the decreasing far-field J-value lost path independence.

Therefore reporting of J-results has been limited up to this load step, see Table 2.5.1.

The near-field J-value corresponds to the far-field value only up to crack initiation. Then both values started deviating. The crack initiation value of J is approximately 1.6 MN/m. This number is a mean value of the initiation values according to the experimental load-point displacement at initiation on the one hand and the experimental load value at initiation on the other hand.

Table 2.5.1. Applied displacement versus computed far-field J-integral (Participant Number 5)

Load Step	Load-Point Displacement, mm	J-Integral (Far-Field), kN/m
1	1,218	11,691
2	2,488	21,005
3	3,072	25,651
4	3,658	30,529
5	4,394	37,516
7	5,410	48,715
9	6,578	62,895
11	8,052	84,537
13	9,524	113,508
15	10,262	129,633
17	11,734	167,314
20	14,656	267,256
23	17,602	383,553
26	20,522	506,147
29	23,470	629,339
30	24,130	658,795
43	41,528	1,665,429
52	49,838	2,336,500
62	58,984	3,055,667
72	68,788	3,895,778
79	77,674	4,544,667
85	86,588	5,267,125
92	92,208	5,445,714
99	98,557	5,774,667
107	106,628	6,314,400
114	114,186	7,186,250
121	120,904	7,338,000
131	129,844	7,626,000
139	139,496	8,193,251
151	150,398	8,457,667
158	160,198	8,971,001

18

The FE mesh used is shown in Figure 2.5.1.

The results of the analysis are given as calculated load versus load-point displacement, Figure 2.5.2, calculated far-field J versus load-point displacement up to crack initiation, Figure 2.5.3, calculated far-field J versus total load-point displacement, Figure 2.5.4, calculated load versus far-field J up to crack initiation, Figure 2.5.5, and calculate J-R curve using the far-field J-values, Figure 2.5.6.

The agreement in the load versus load-point displacement behavior between analysis and experiment seems to be fairly good.

The calculated maximum load occurs at a larger load-point displacement with only a slightly higher load value compared to the experiment. This indicates that the structural stiffness of the FE model underestimates the specimen behavior to some extent. As a matter of fact, this is what one should expect from a plane-stress analysis.

Besides serious objections against the computed J-values because of the restrictions to small crack extensions for a J-dominance in the crack tip field there are some other concerns.

The large deformations in the specimen should be accounted for using large deformation algorithms; this was not done here because small strain theory is implied in the J-integral derivation.

Further, the appearance of the crack surface of the specimen with large shear lips and some amount of crack tunneling also gives rise to some doubts if a 2D plane-stress analysis would be able to reproduce experimentally determined J-integral values.

Therefore, there is a chance that more light is brought into these problems by the final evaluation of the round-robin results.

2.6 References for Section 2

2.1.1 Shih, C. F., de Lorenzi, H. G., and Andrews, W. R., "Studies on Crack Initiation and Stable Crack Growth", Elastic-Plastic Fracture, ASTM STP 668, American Society for Testing and Materials, 1979, pp. 65-120.

2.1.2 Rice, J. R., "A Path Independent Integral and the Approximate Analysis of Strain Concentration by Notches and Cracks", J. Applied Mechanics, Vol. 40, 1973.

2.1.3 De Lorenzi, H. G., "3-D Elastic-Plastic Fracture Analysis with ADINA", Computers and Structures, Vol. 13, 1981.

2.2.1 Yamada, Y., et al., International Journal of Mechanical Science, Vol. 10, 1968, pp. 343-354.

2.5.1 Bathe, K.J., Mass. Inst. Tech. Report, No. 824481-1, 1975.

2.5.2 De Lorenzi, H. G., "Energy Release Rate by the Finite Element Method", GE CR & D, Rep. No. 80 CRD 113, June 1980.

2.5.3 Kussmaul, K., Sauter, A., 10th MPA-Seminar, Stuttgart, 1984.

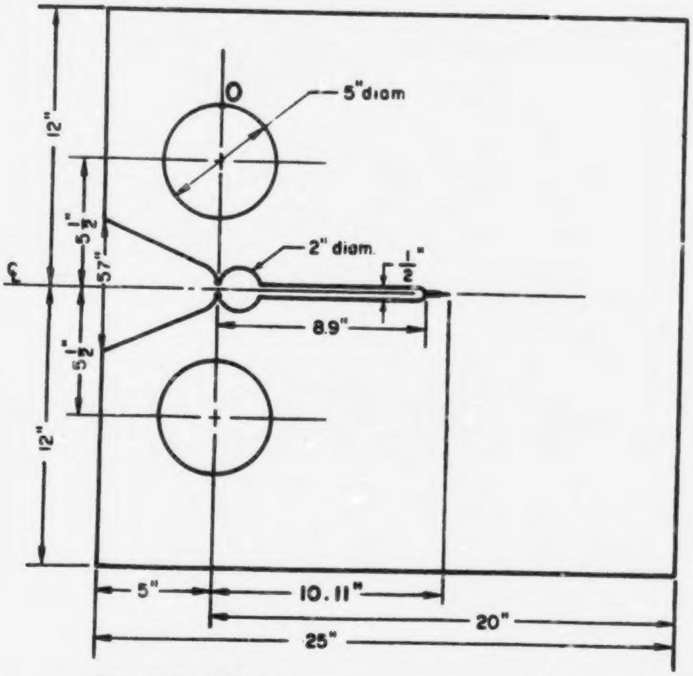
O
5" diam
2" diam
1/2"
℄
12"
5 1/2"
5.7"
5 1/2"
8.9"
12"
5"
10.11"
20"
25"

Note: 1 inch = 25,4 mm

Figure 2.1 Geometry of the 1.0-inch (25.4-mm) thick 10T C(T) specimen.

T-4573-F2.1

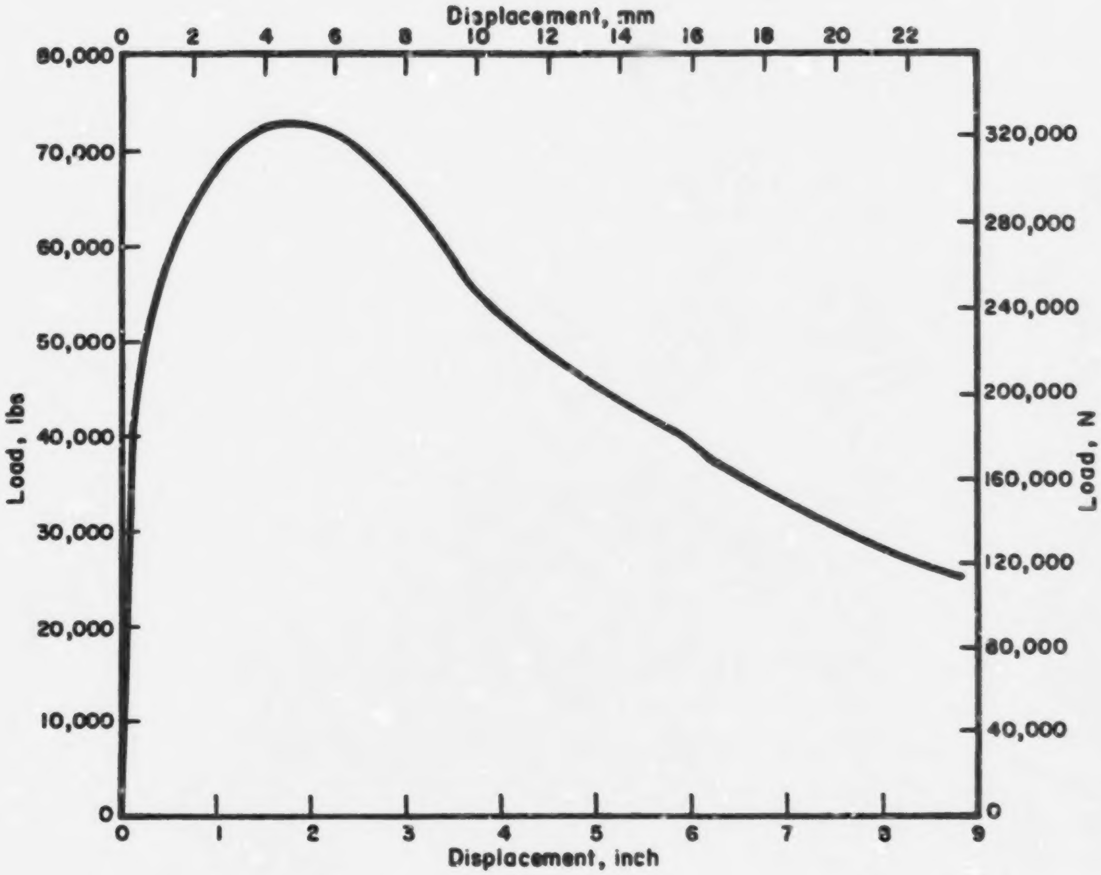

Figure 2.2 Experimental load versus load-point displacement for the 10T C(T) Type 304 stainless steel specimen at 550 F (288 C).

T-4573-F2.2

22

BEST COPY AVAILABLE

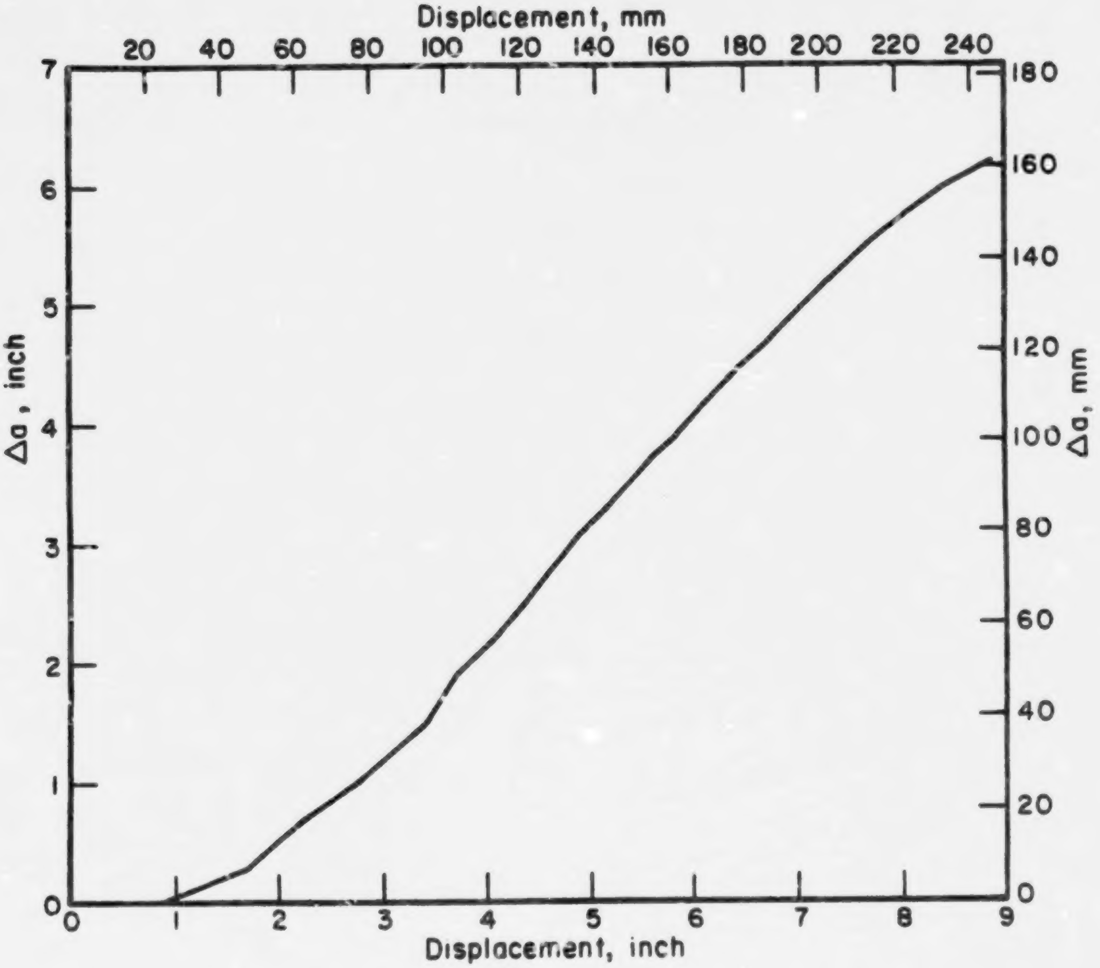

Figure 2.3 Crack extension versus applied displacement for the 10T C(T) Type 304 stainless steel 1-inch (25.4-mm) thick specimen.

T-4573-F2.3

23

BEST COPY AVAILABLE

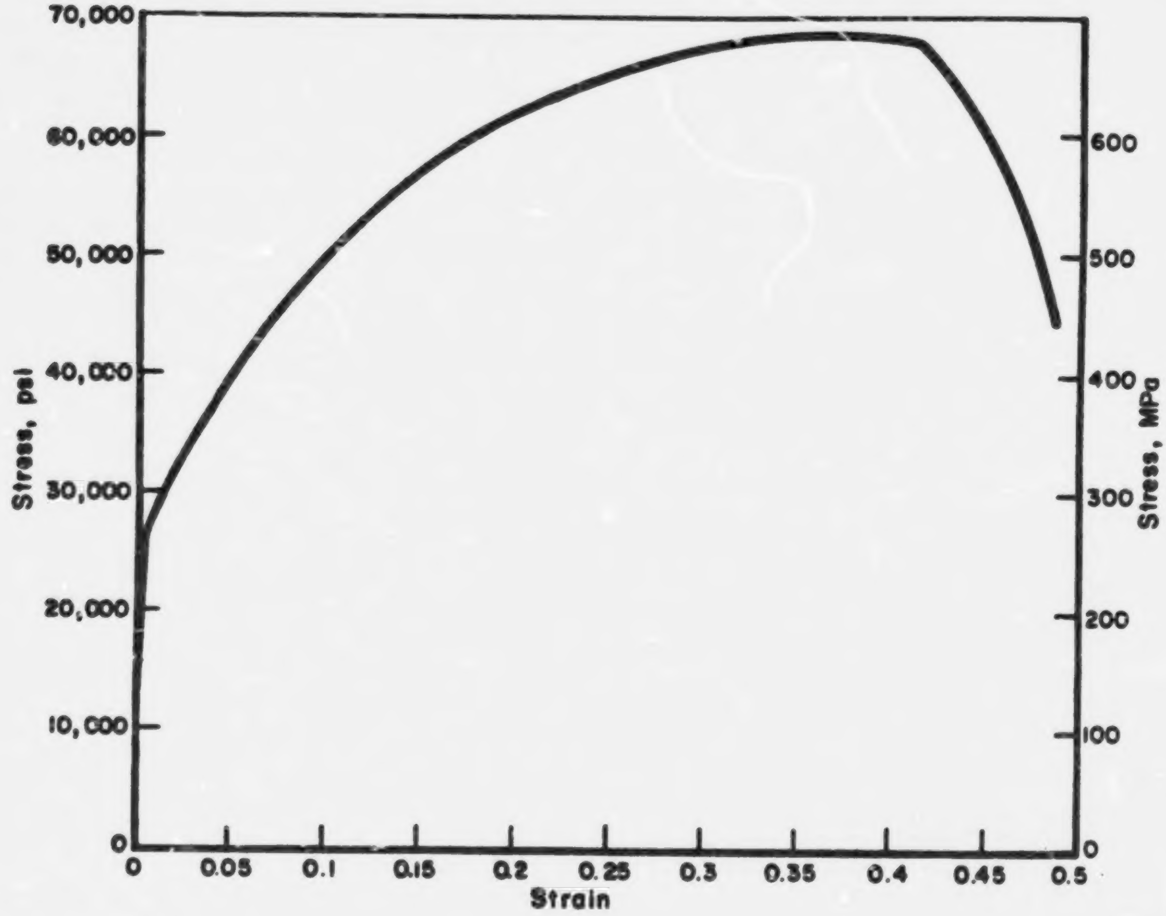

Figure 2.4 Engineering stress versus strain for Type 304 stainless steel at 550 F (288 C) used in 10T C(T) specimen test.

T-4573-F2.4

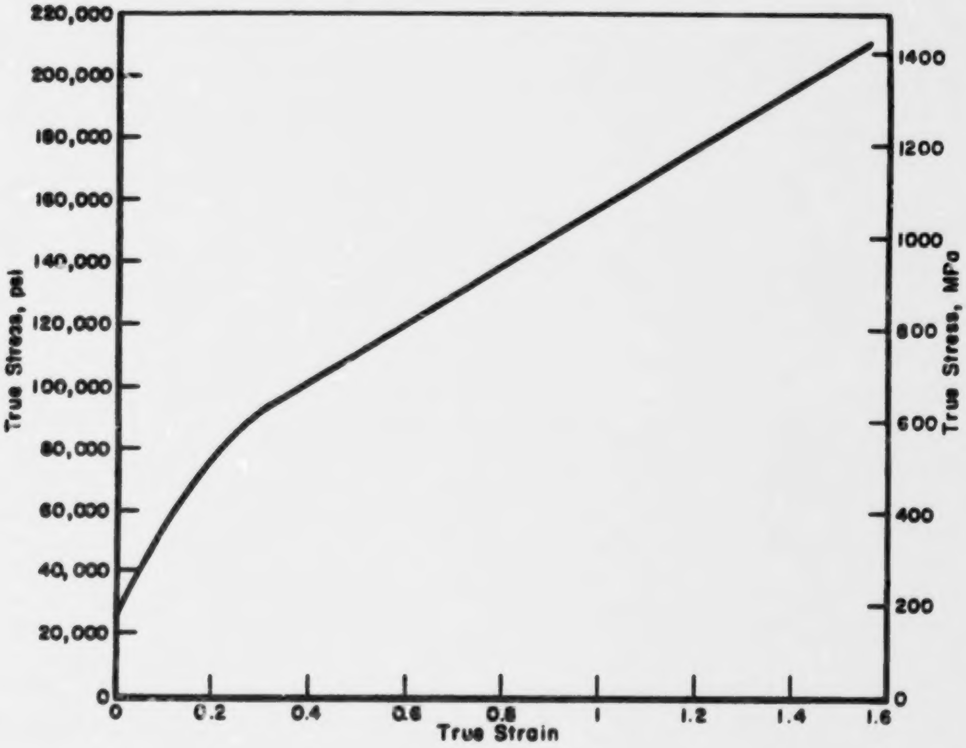

Figure 2.5 Uniaxial true stress versus true strain for Type 304 stainless steel at 550 F (288 C) used in 10T C(T) specimen test.

T-4573-F2.5

BEST COPY AVAILABLE

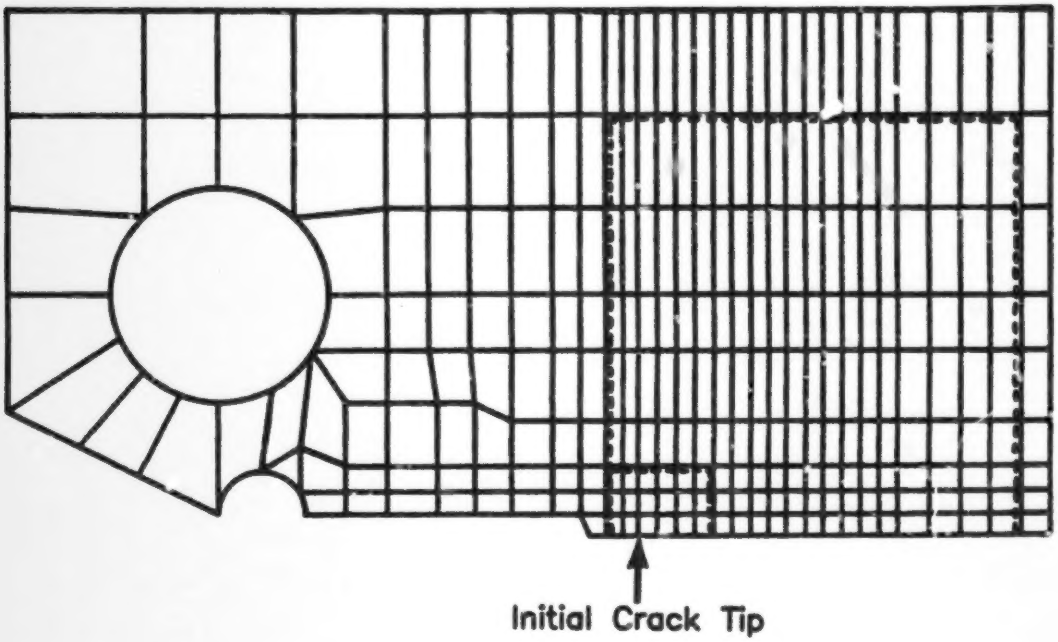
Initial Crack Tip

Figure 2.1.1 Finite element mesh and J-contours (dashed lines) for the 10T C(T) specimen analysis. (Participant 1.)

T-4573-F2.1.1

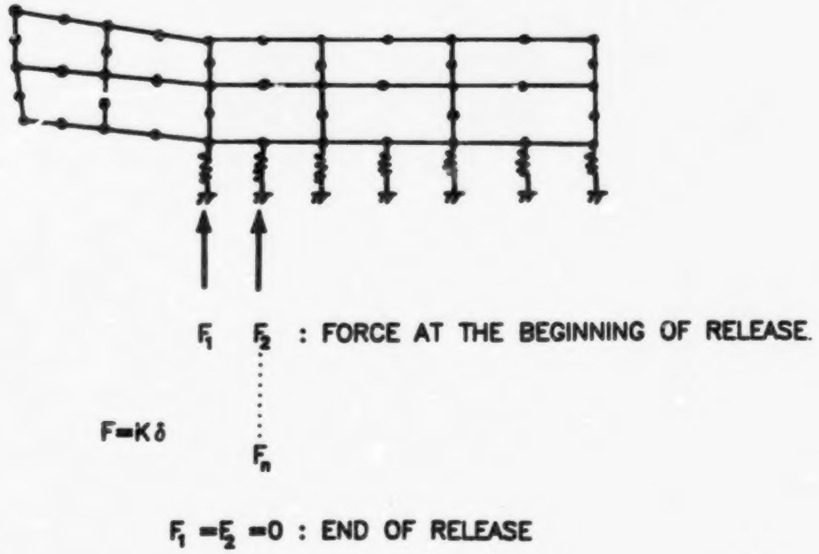
F_1 F_2 : FORCE AT THE BEGINNING OF RELEASE.
$F = K\delta$
F_n
$F_1 = F_2 = 0$: END OF RELEASE

Figure 2.1.2 Schematic representation of crack advance modeling method. (Participant 1.)

T-4573-F2.1.2

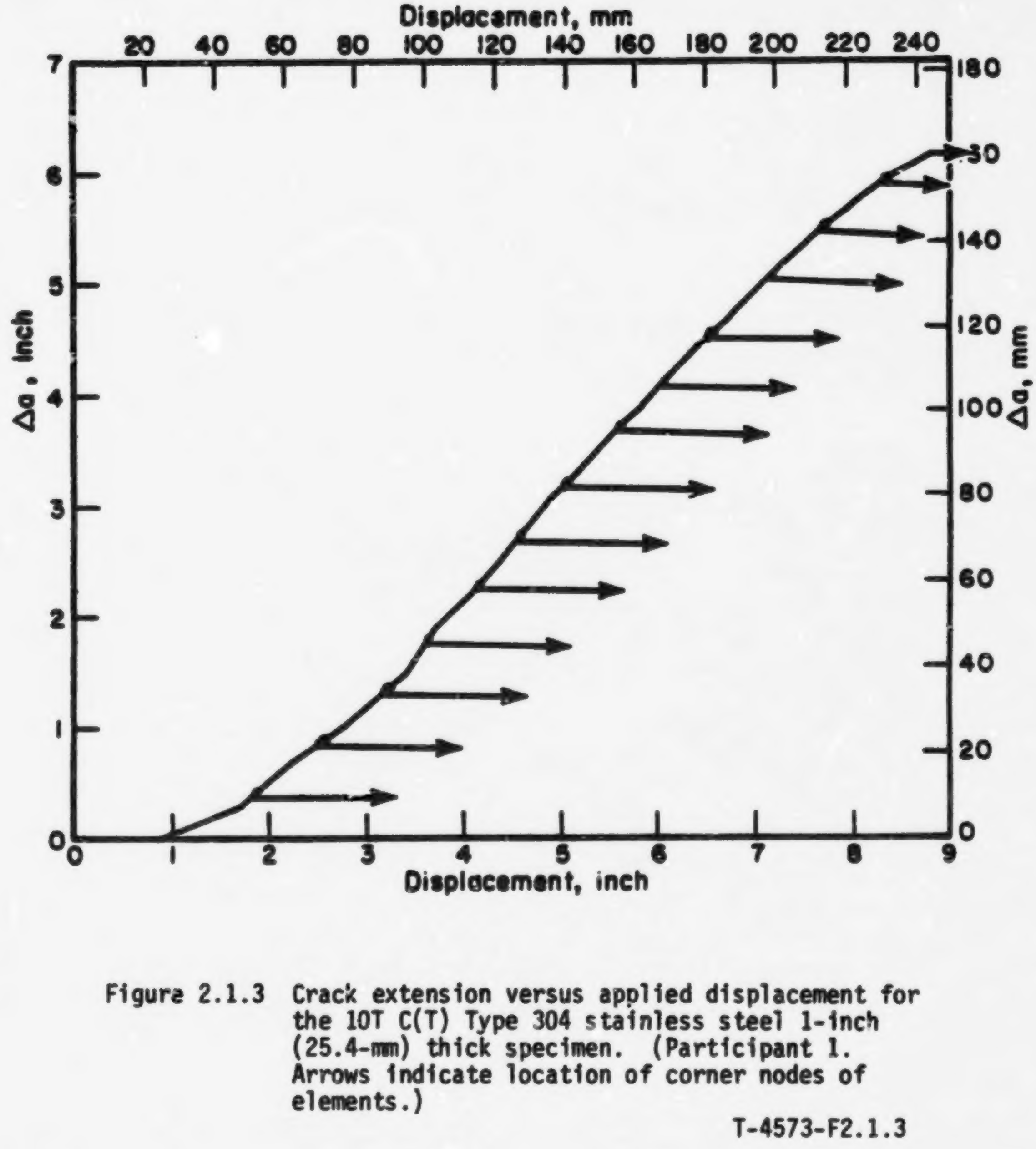

Figure 2.1.3 Crack extension versus applied displacement for the 10T C(T) Type 304 stainless steel 1-inch (25.4-mm) thick specimen. (Participant 1. Arrows indicate location of corner nodes of elements.)

T-4573-F2.1.3

BEST COPY AVAILABLE

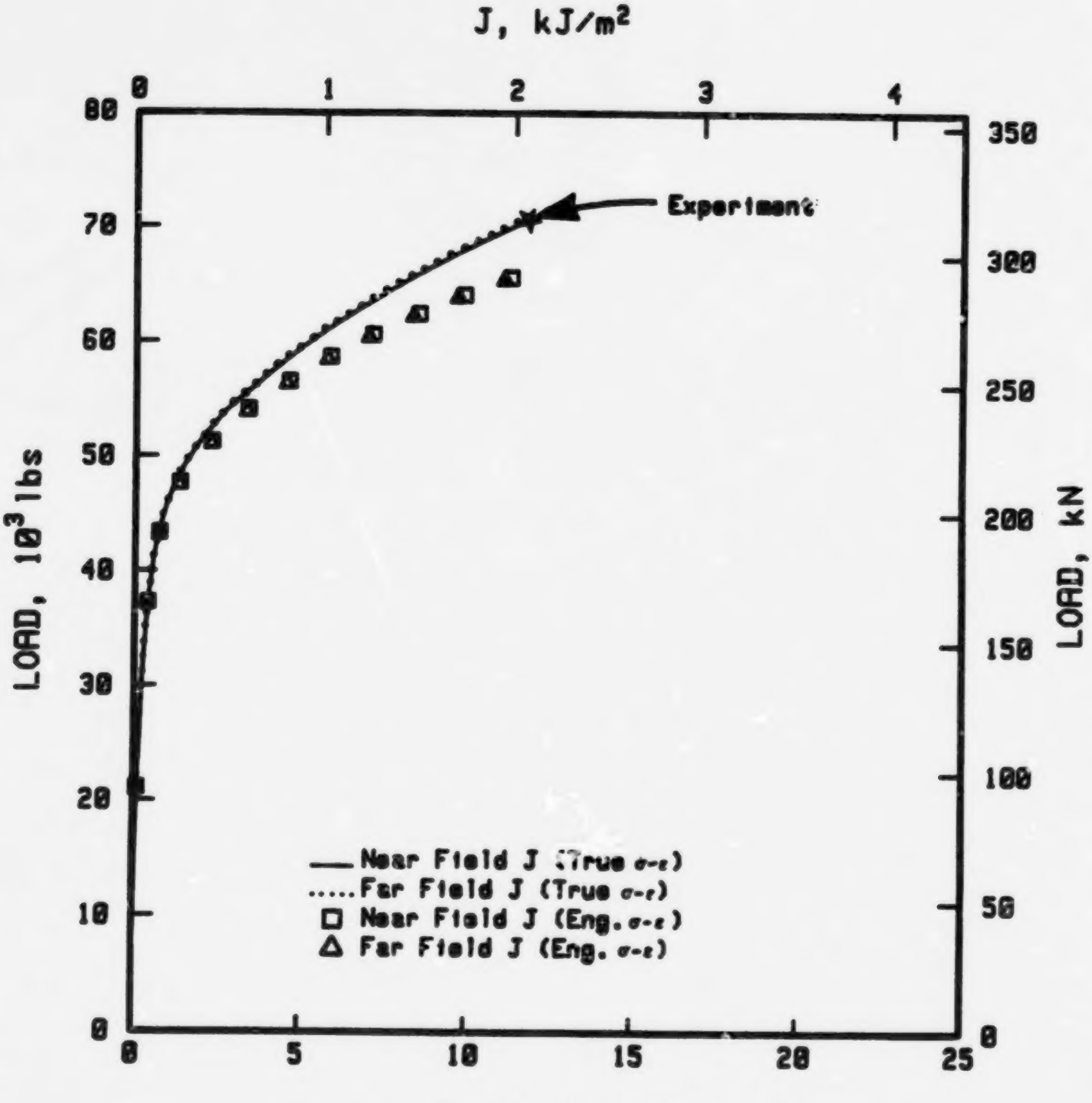

Figure 2.1.4 Computed load verus J up to crack initiation. (Participant 1.)

T-4573-F2.1.4

29

BEST COPY AVAILABLE

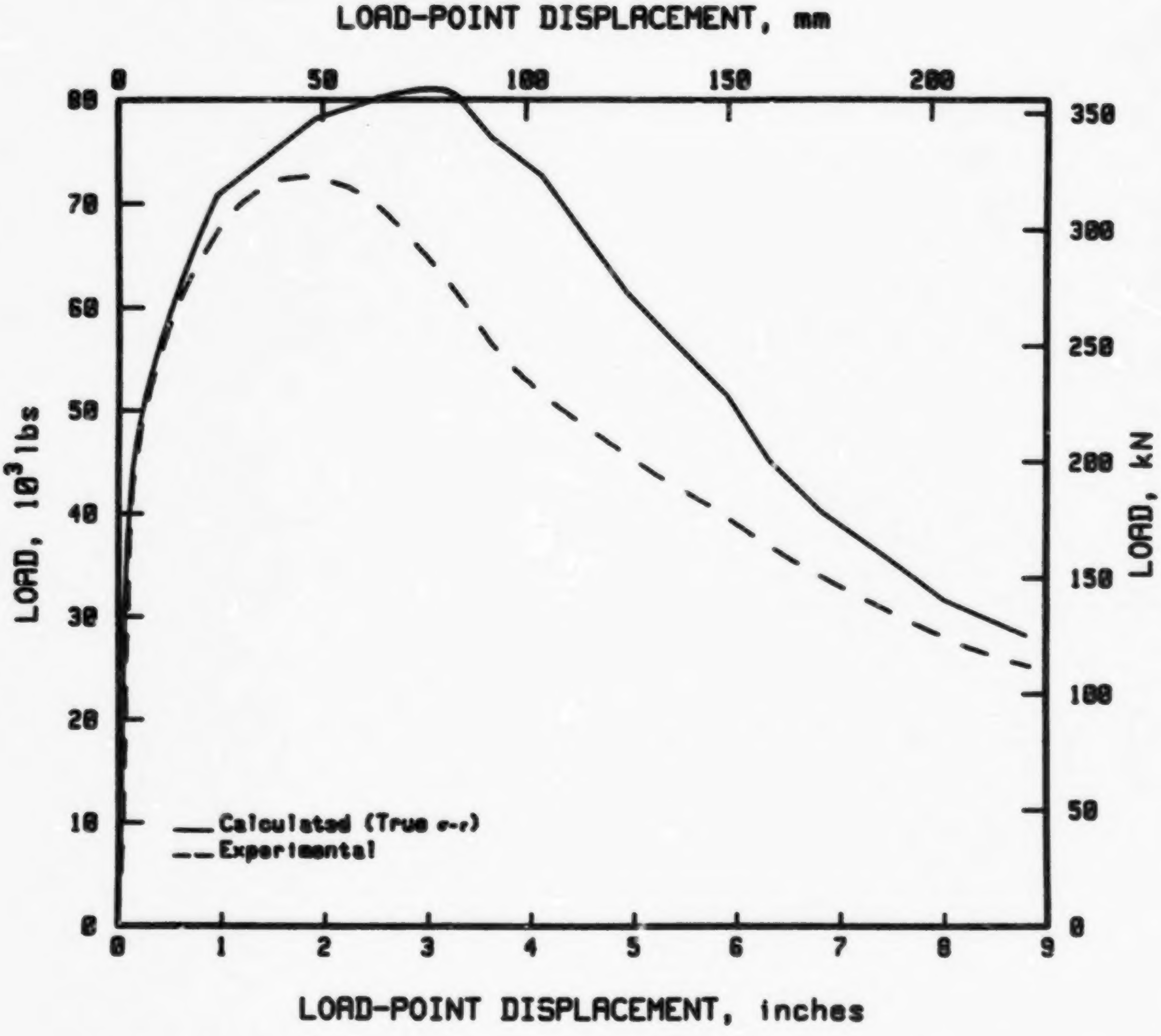

Figure 2.1.5 Computed load versus load-point displacement. (Participant 1.)

T-4573-F2.1.5

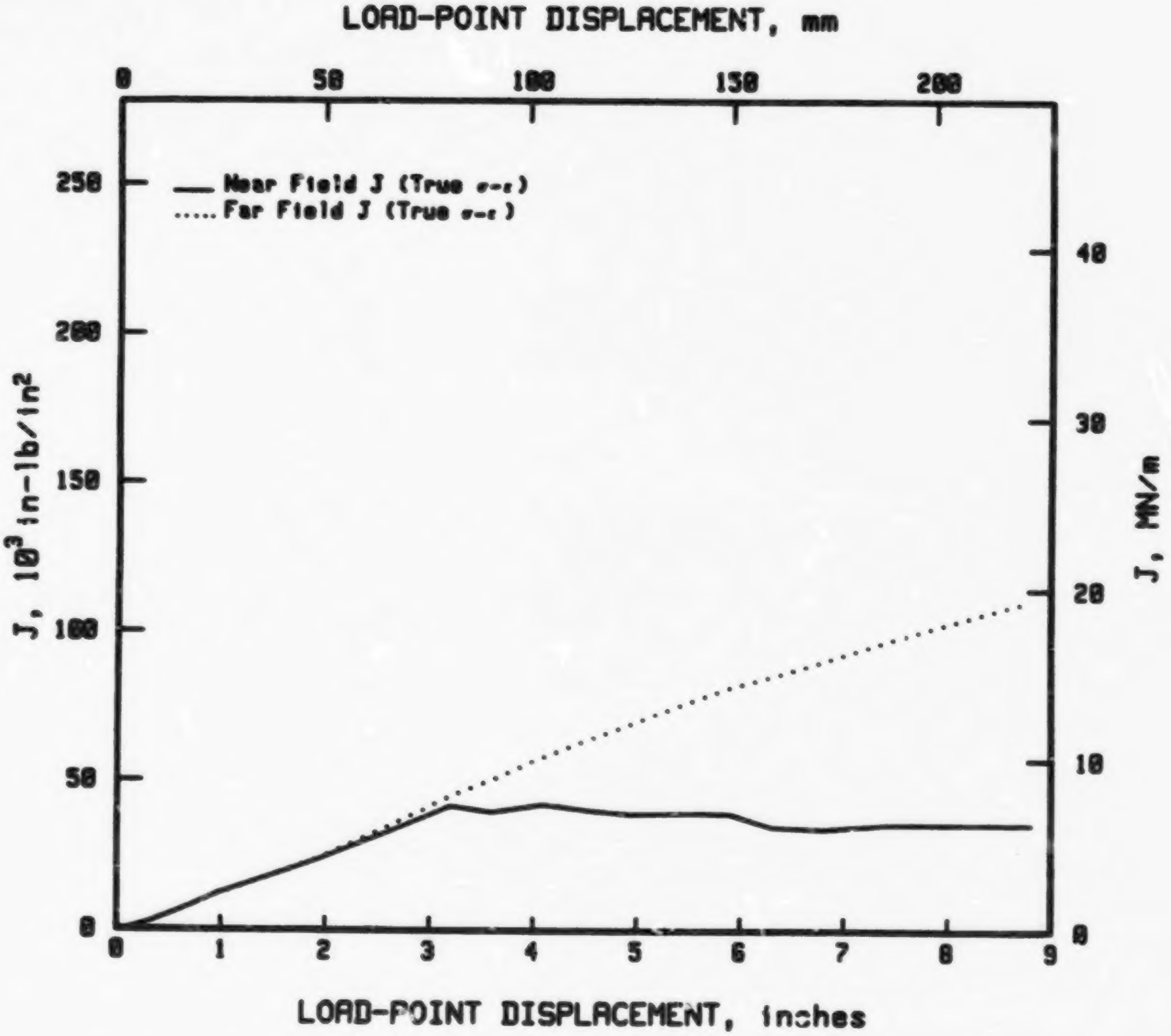

Figure 2.1.6 Computed J versus applied load-point displacement. (Participant 1.)

T-4573-F2.1.6

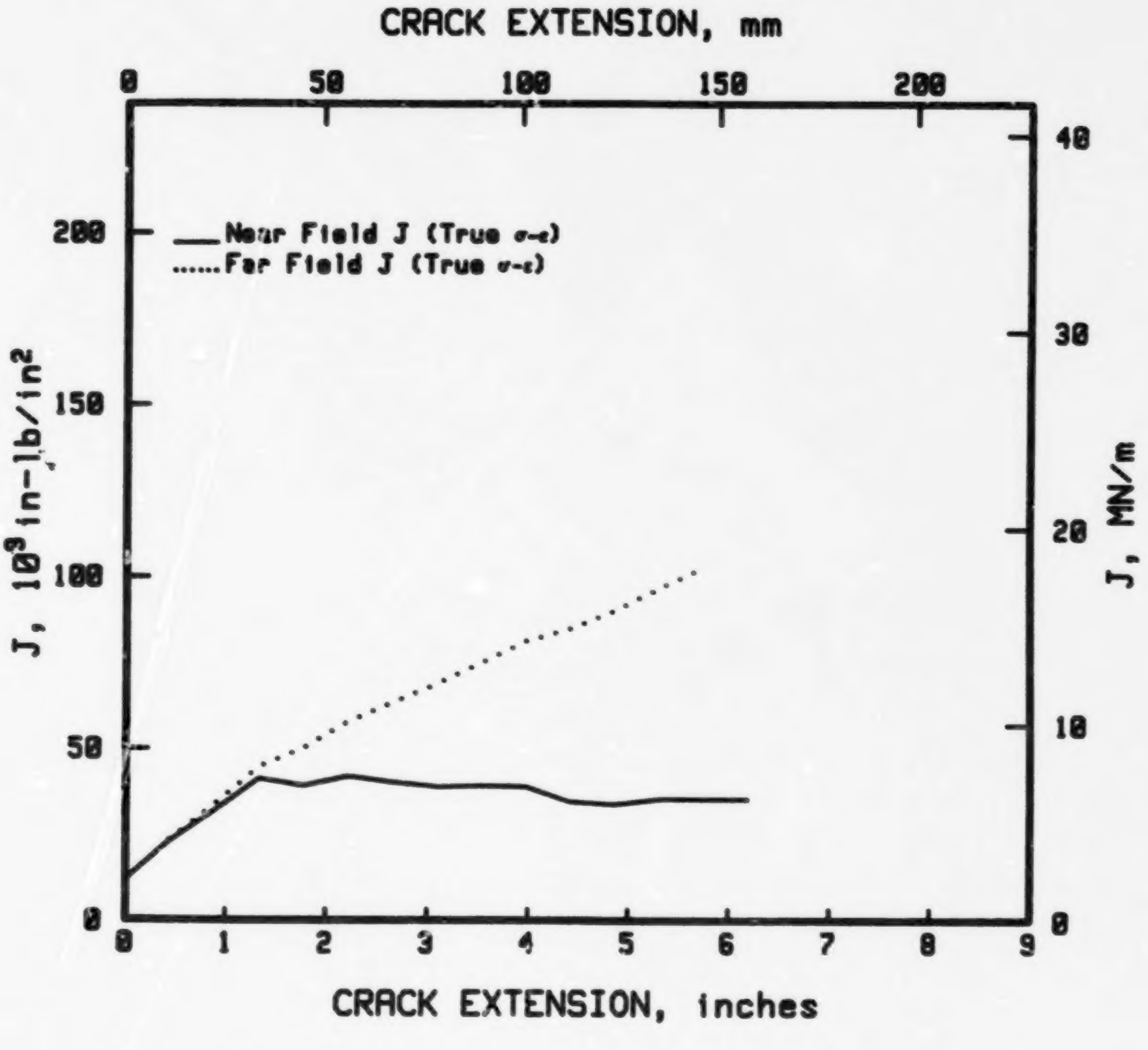

Figure 2.1.7 Computed near- and far-field J as a function of crack extension. (Participant 1.)

T-4573-F2.1.7

32

BEST COPY AVAILABLE

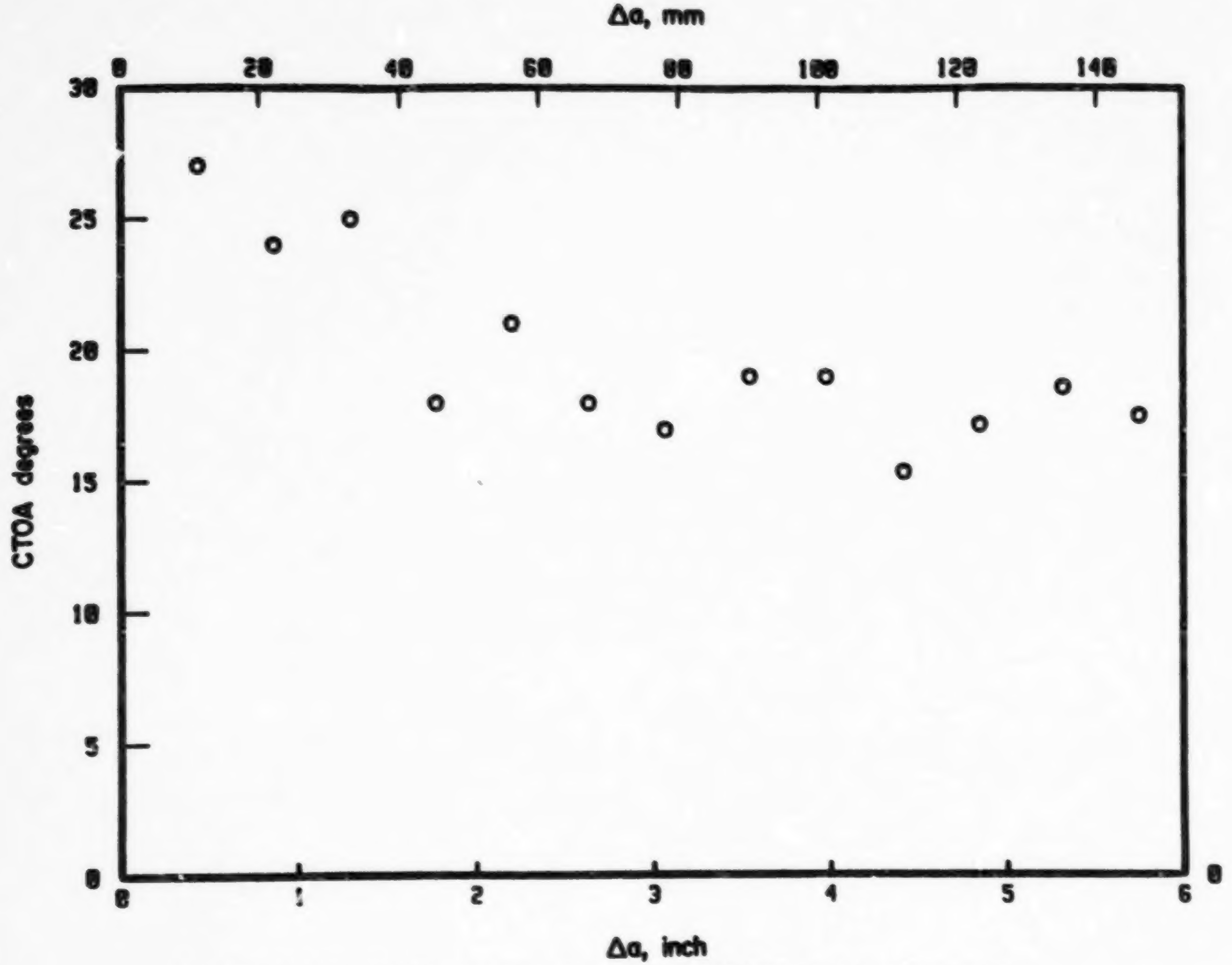

Figure 2.1.8 Crack-tip-opening angle (CTOA) obtained from the finite element displacement solution. (Participant 1.)

T-4573-F2.1.8

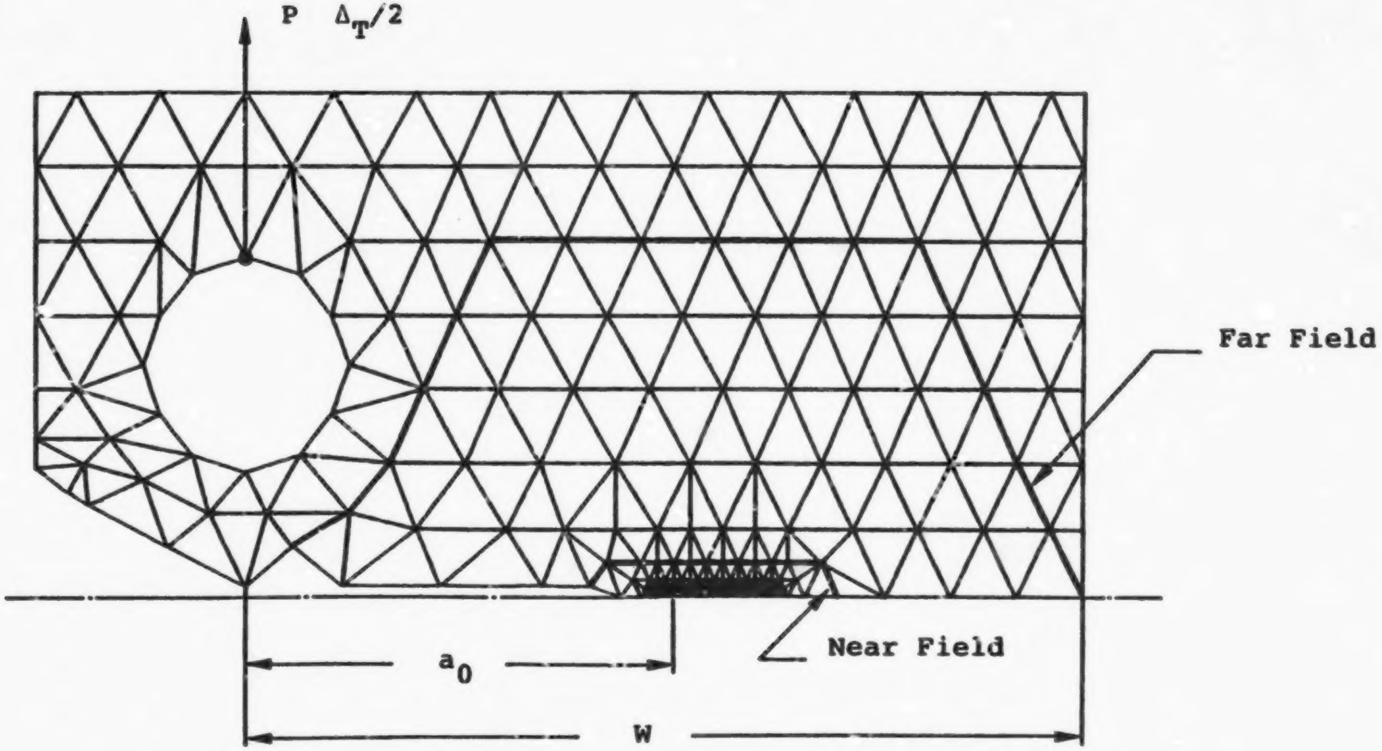
P $\Delta_T/2$
Far Field
Near Field
a_0
W

Figure 2.2.1 Finite element model for one half of the C(T) specimen and paths along which J-integral is evaluated. (Participant 2.)

T-4573-F2.2.1

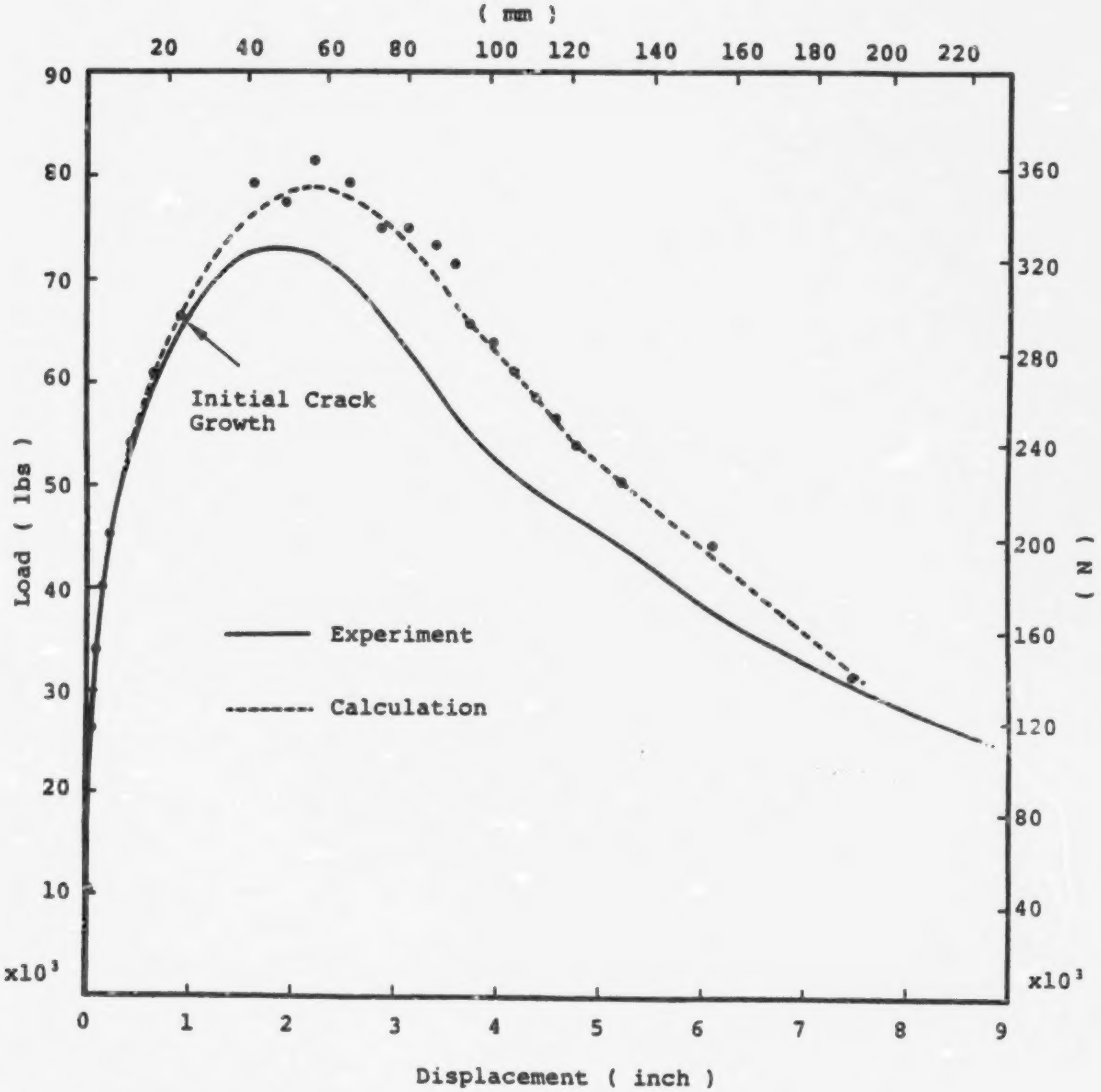

Figure 2.2.2 Calculated load versus displacement curve compared with the experimental data. (Participant 2.)

T-4573-F2.2.2

BEST COPY AVAILABLE

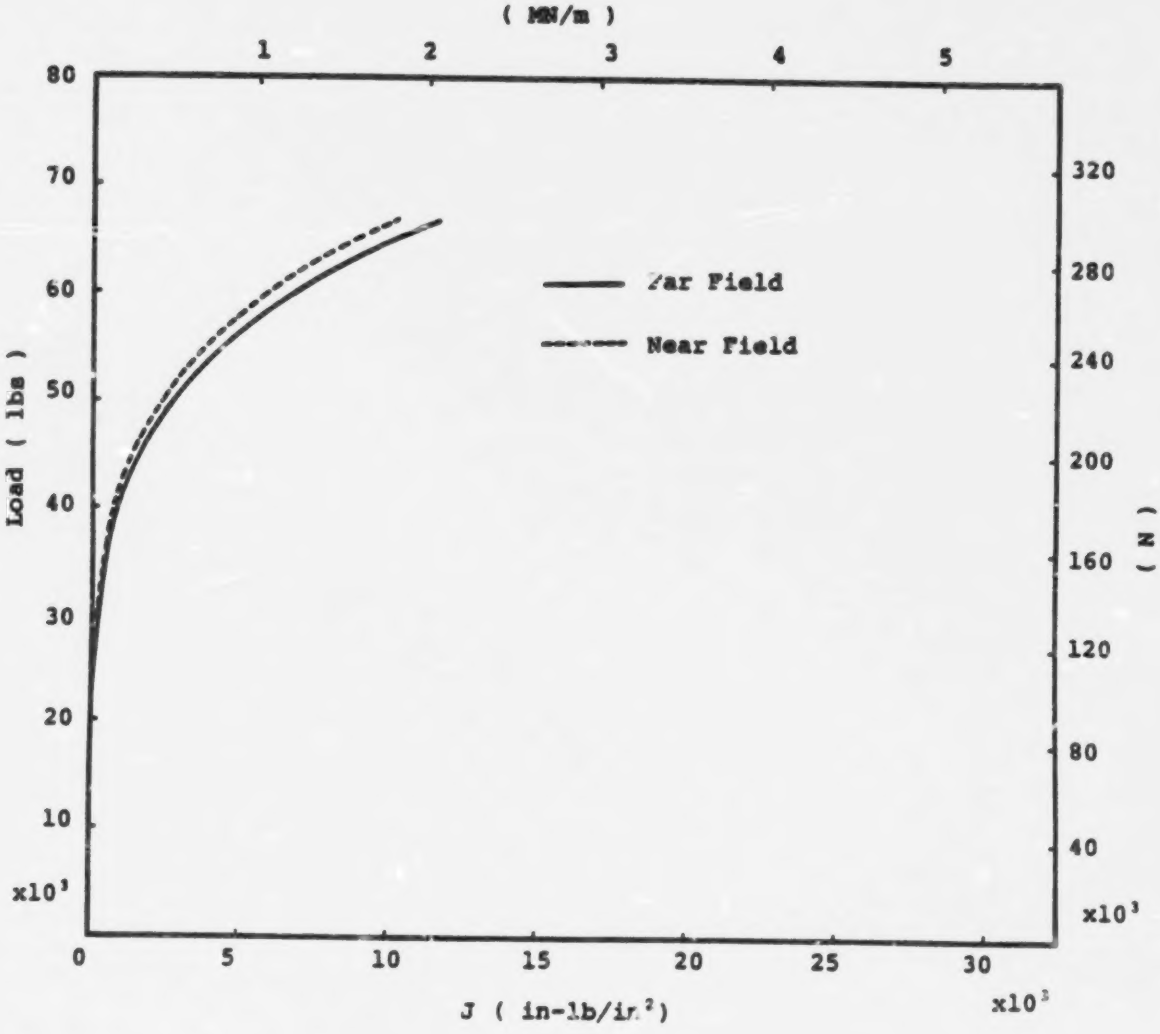

Figure 2.2.3 Calculated load versus J curves. (Participant 2.)

T-4573-F2.2.3

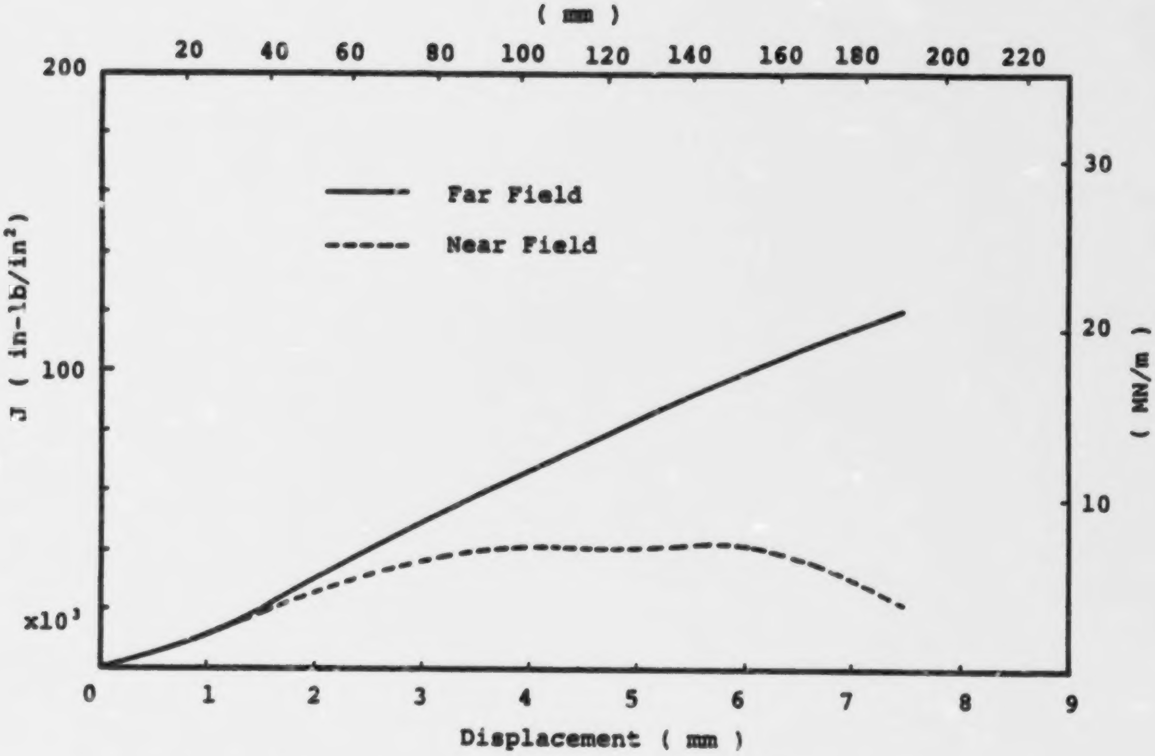

Figure 2.2.4 Calculated J versus displacement curves. (Participant 2.)

T-4573-F2.2.4

37

BEST COPY AVAILABLE

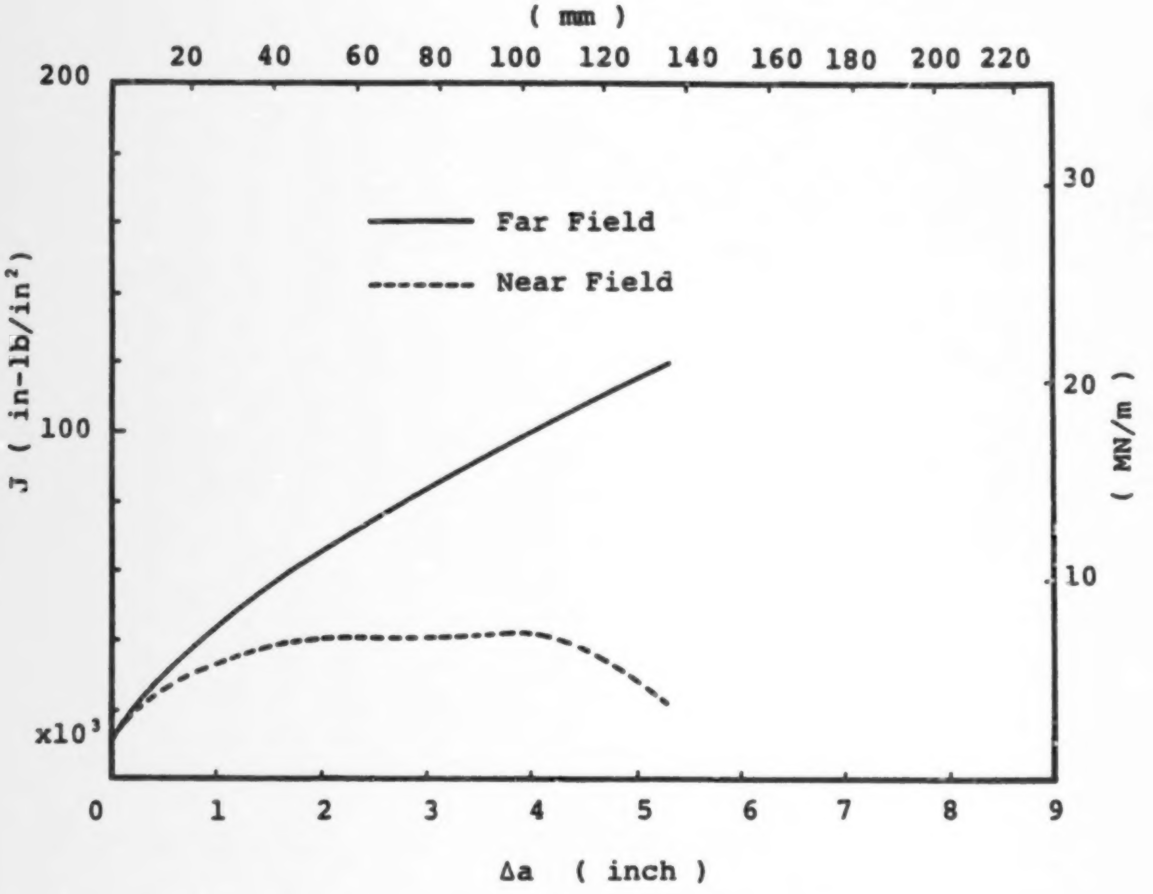

Figure 2.2.5 Calculated J versus Δa curves. (Participant 2.)

T-4573-F2.2.5

38

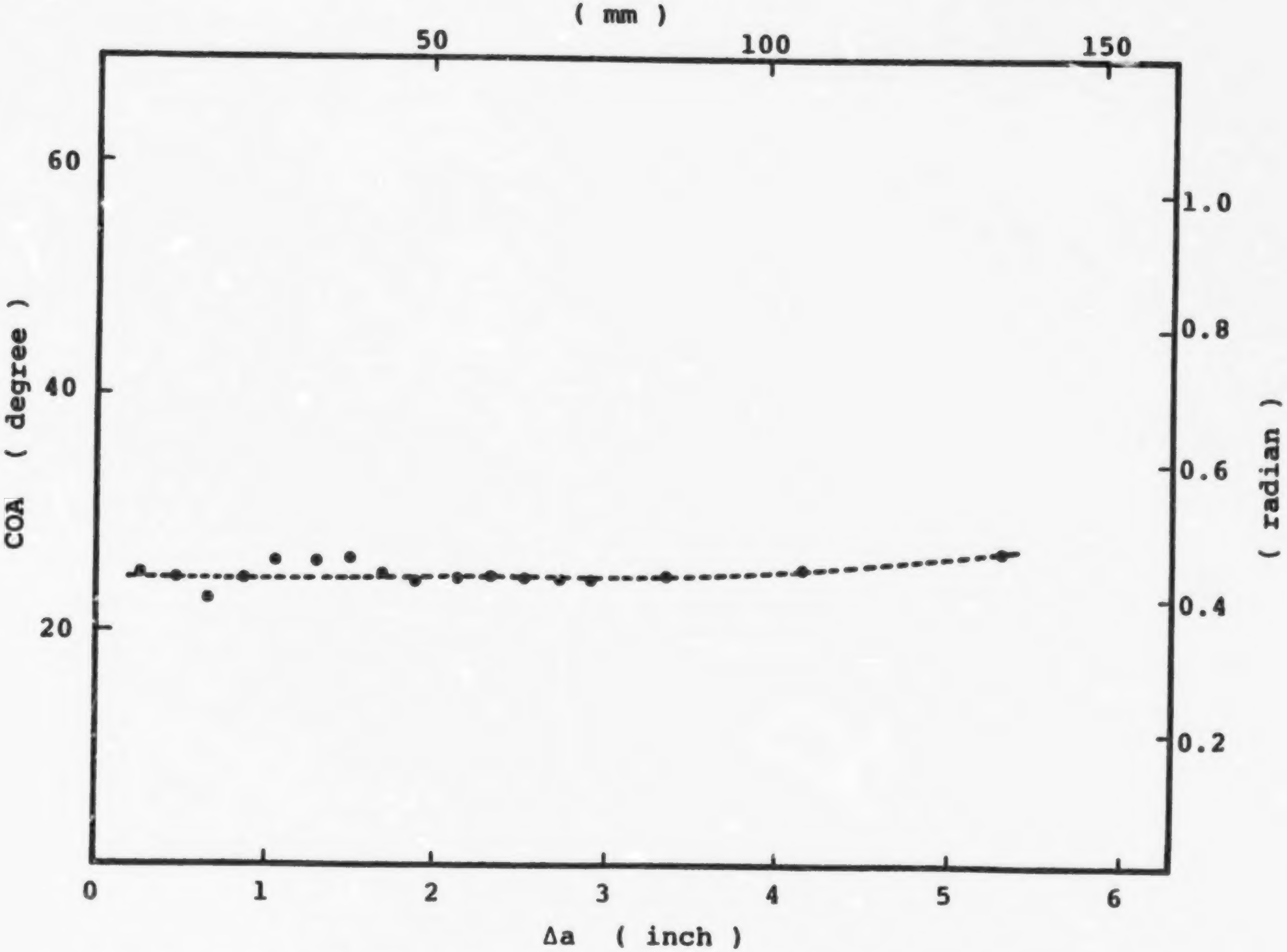

Figure 2.2.6 Calculated crack-opening angle versus crack extension curve. (Participant 2.)

T-4573-F2.2.6

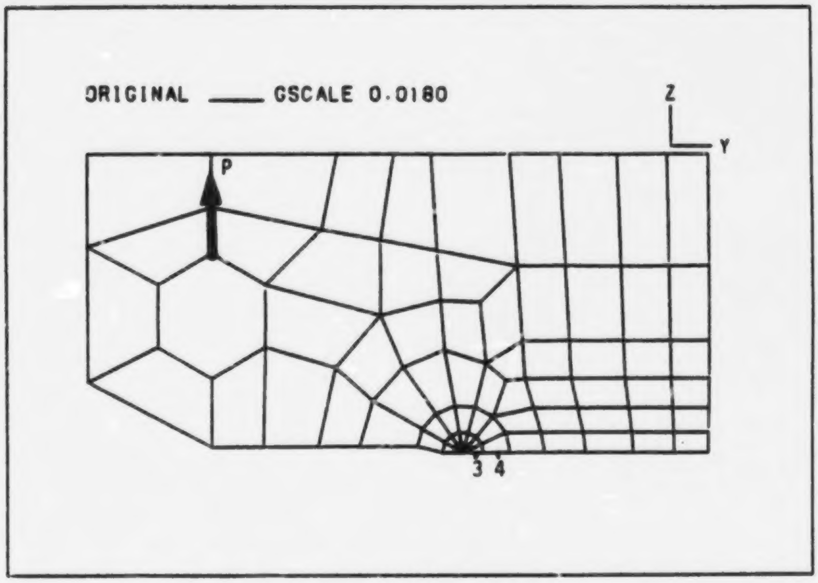
ORIGINAL ____ GSCALE 0.0180
Z
Y
P
3 4

Figure 2.3.1 FE mesh for initial crack length with two outermost J-integration rings indicated. (Participant 3.)

T-4573-F2.3.1

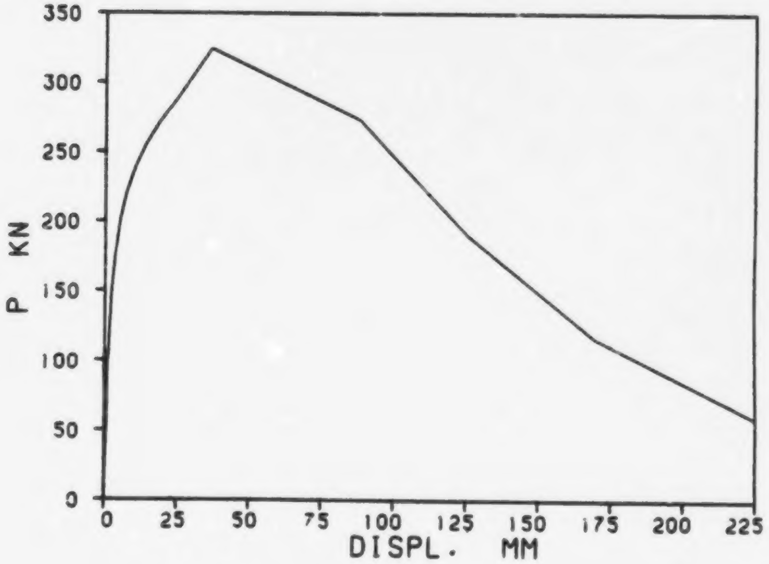

Figure 2.3.2 Load versus load-point displacement. (Participant 3.)

T-4573-F2.3.2

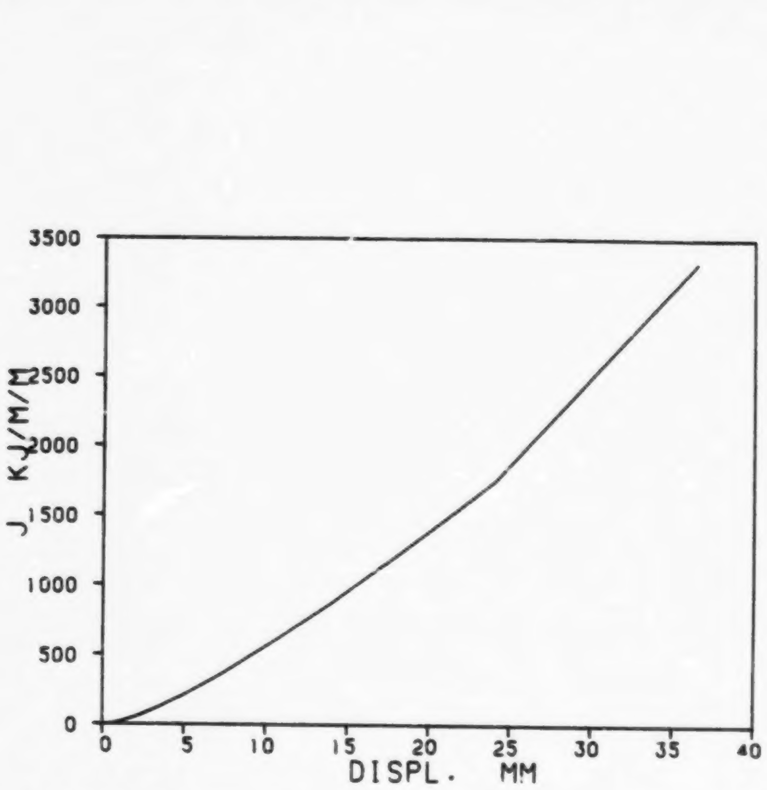

Figure 2.3.3 J versus load-point displacement up to crack initiation. (Participant 3.)

T-4573-F2.3.3

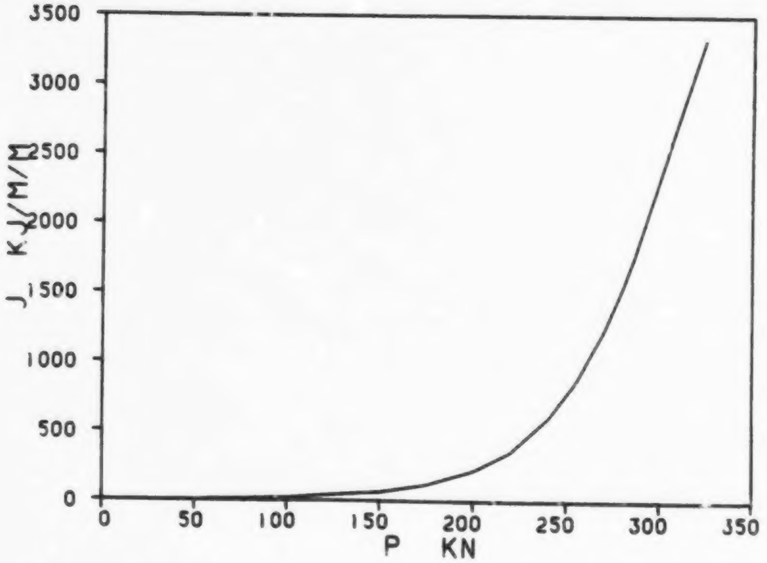

Figure 2.3.4 J versus load up to crack initiation. (Participant 3.)

T-4573-F2.3.4

41

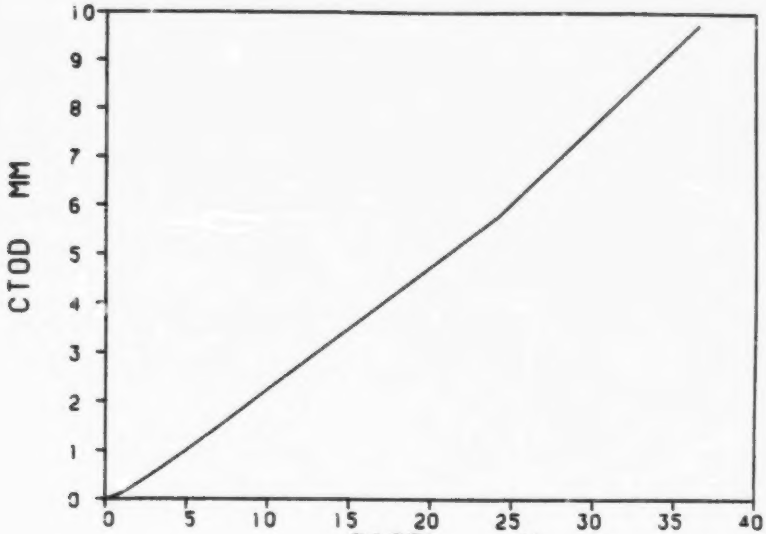

Figure 2.3.5 CTOD versus load-point displacement up to crack initiation. (Participant 3.)

T-4573-F2.3.5

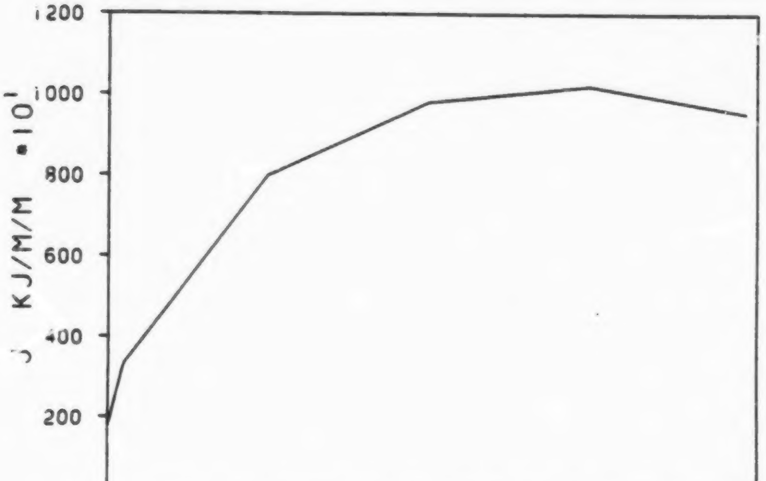

Figure 2.3.6 J versus crack extension. (Participant 3.)

T-4573-F2.3.6

42

BEST COPY AVAILABLE

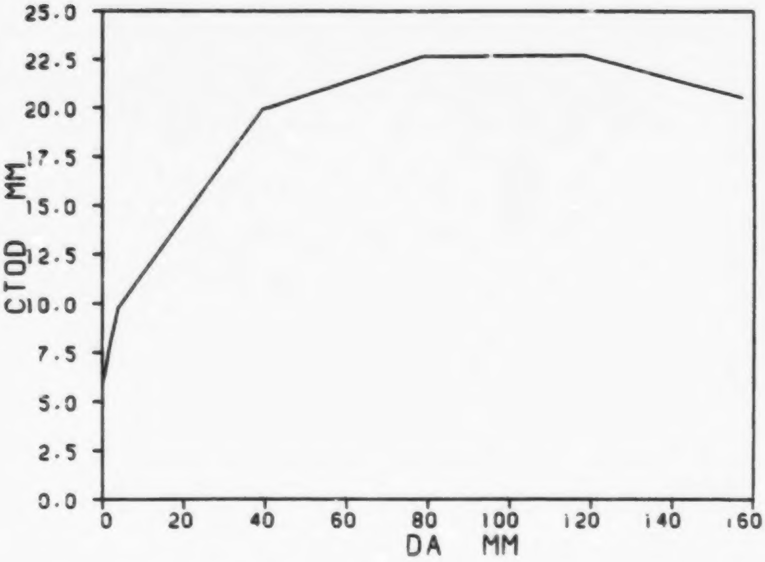

Figure 2.3.7 CTOD versus crack extension. (Participant 3.)

T-4573-F2.3.7

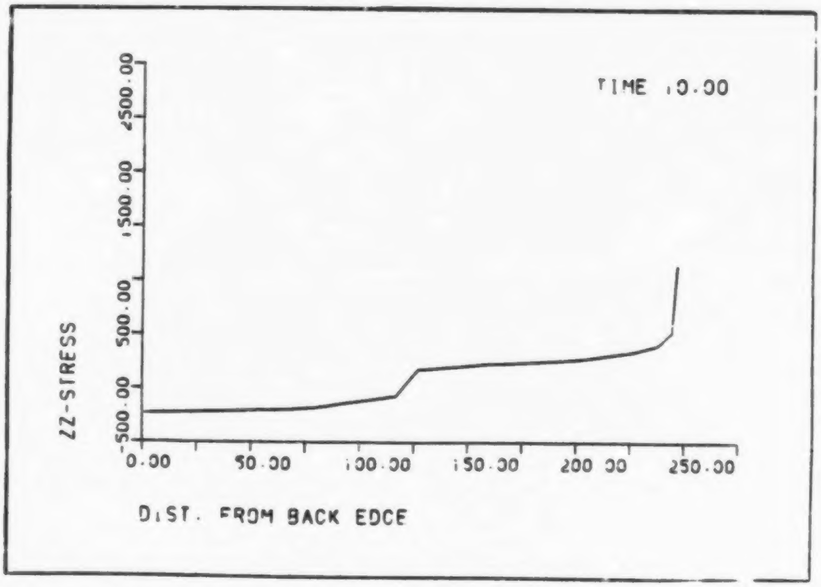

Figure 2.3.8 Distribution of the stress perpendicular to the crack in the ligament at applied displacement level. (Participant 3.)

T-4573-F2.3.8

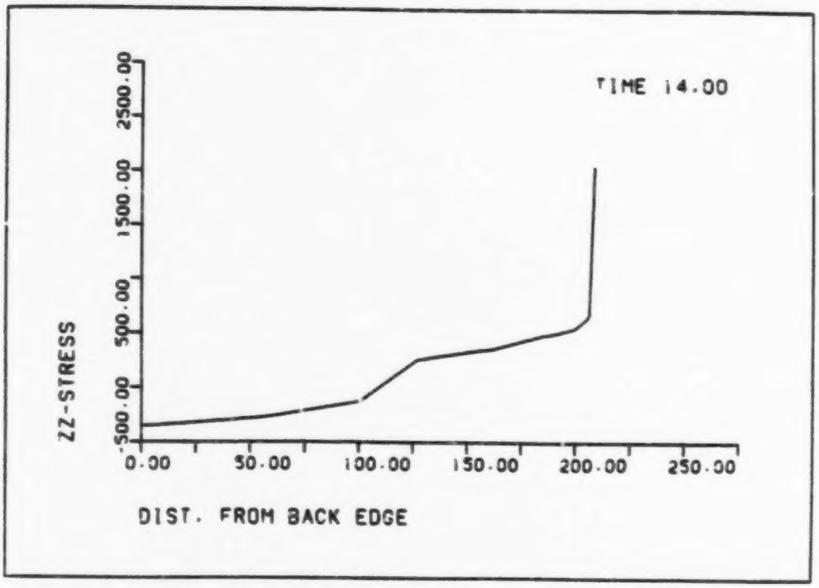

Figure 2.3.9 Distribution of the stress perpendicular to the crack in the ligament at applied displacement level 90 mm. (Participant 3.)

T-4573-F2.3.9

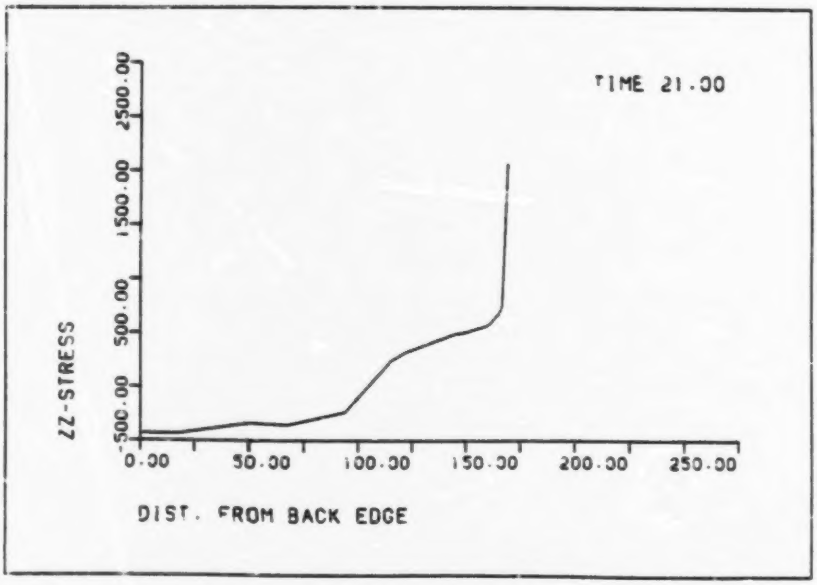

Figure 2.3.10 Distribution of the stress perpendicular to the crack in the ligament at applied displacement level. (Participant 3.)

T-4573-F2.3.10

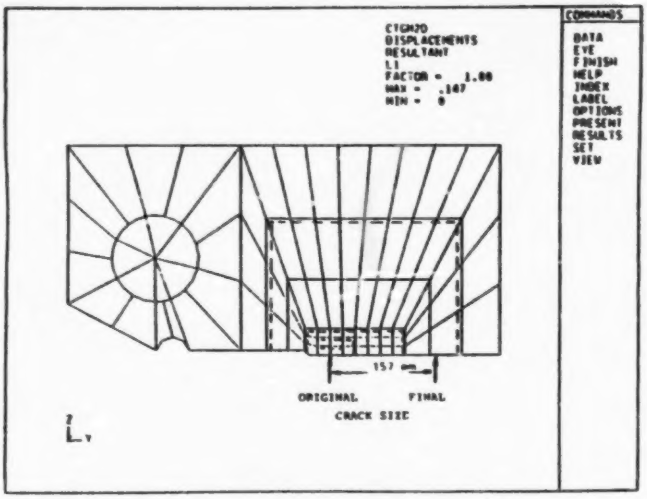
CTGM20
DISPLACEMENTS
RESULTANT
L1
FACTOR = 1.00
MAX = .147
MIN = 0
COMMANDS
DATA
EYE
FINISH
HELP
INDEX
LABEL
OPTIONS
PRESENT
RESULTS
SET
VIEW
157 mm
ORIGINAL
FINAL
CRACK SIZE
Z
Y

Figure 2.4.1 C(T) specimen: 2-D modelling, Model 1. (Participant 4.)

T-4573-F2.4.1

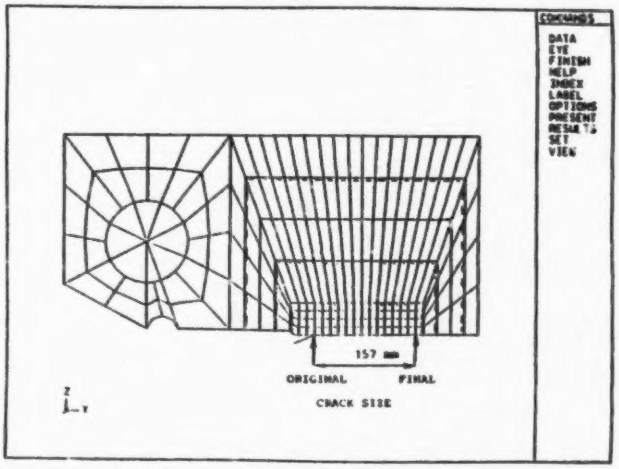
COMMANDS
DATA
EYE
FINISH
HELP
INDEX
LABEL
OPTIONS
PRESENT
RESULTS
SET
VIEW
157 mm
ORIGINAL
FINAL
CRACK SIZE
Z
Y

Figure 2.4.2 C(T) specimen: Details about the 2-D FE analysis, Model 2. (Participant 4.)

T-4573-F2.4.2

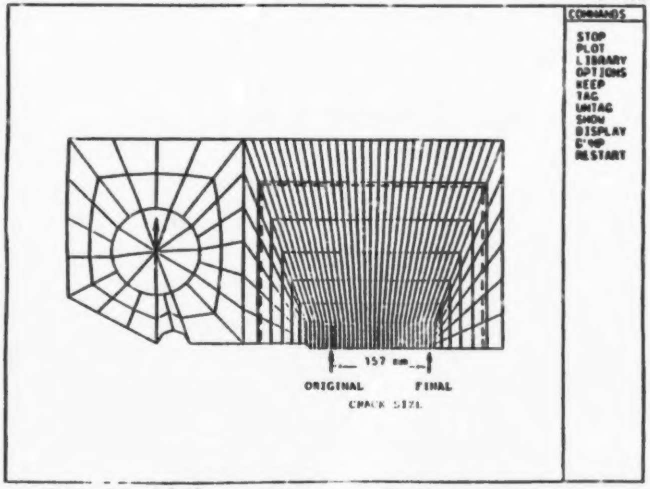
COMMANDS
STOP
PLOT
LIBRARY
OPTIONS
KEEP
TAG
UNTAG
SHOW
DISPLAY
G'MP
RESTART
157 mm
ORIGINAL
FINAL
CRACK SIZE

Figure 2.4.3 C(T) specimen: 2-D modelling, Model 3. (Participant 4.)

T-4573-F2.4.3

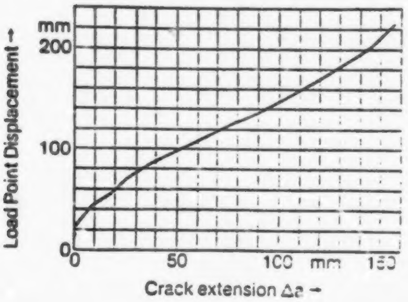

Figure 2.4.4 C(T) specimen: Experimental load point displacement versus crack extension. (Participant 4.)

T-4573-F2.4.4

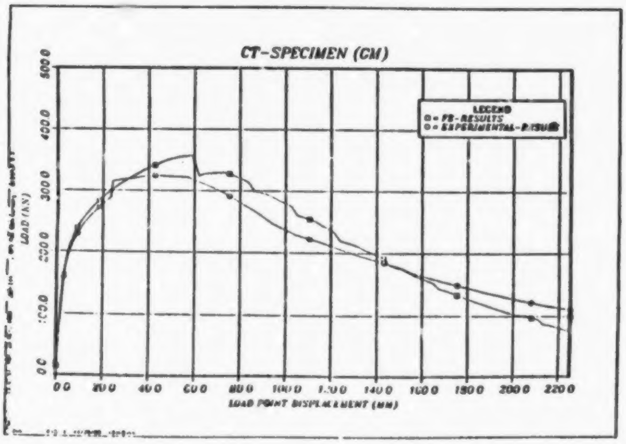

Figure 2.4.5 C(T) specimen: Load versus load point displacement, Model 1 (experimental and FE results). (Participant 4.)

T-4573-F2.4.5

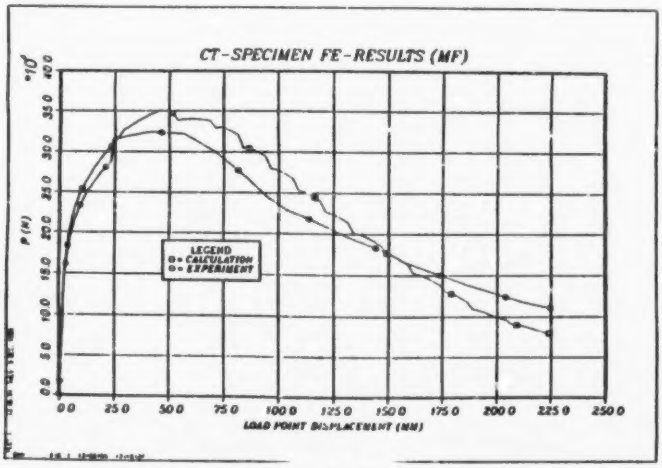

Figure 2.4.6 C(T) specimen: Load versus load point displacement, Model 2 (experimental and FE results). (Participant 4.)

T-4573-F2.4.6

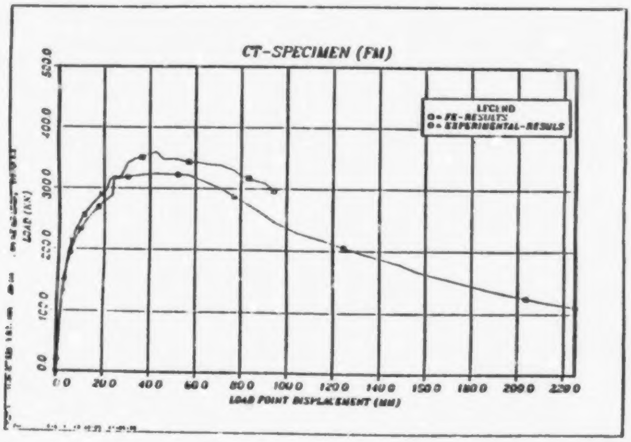

Figure 2.4.7 C(T) specimen: Load versus load point displacement, Model 3 (experimental and FE results.) (Participant 4.)

T-4573-F2.4.7

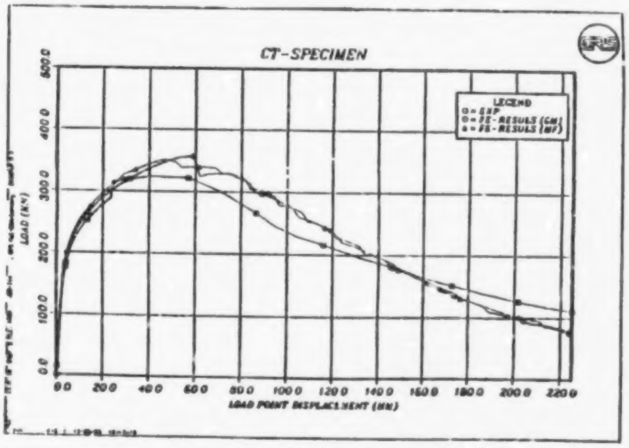

Figure 2.4.8 C(T) specimen: Load versus load point displacement, Models 1 and 2 (experimental and FE results). (Participant 4.)

T-4573-F2.4.8

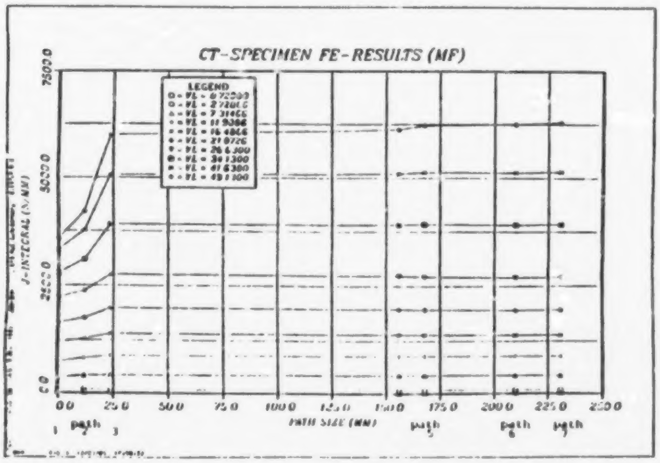

Figure 2.4.9 C(T) specimen: J-integral versus path size, Model 2 (Path 1 to Path 7). (Participant 4.)

T-4573-F2.4.9

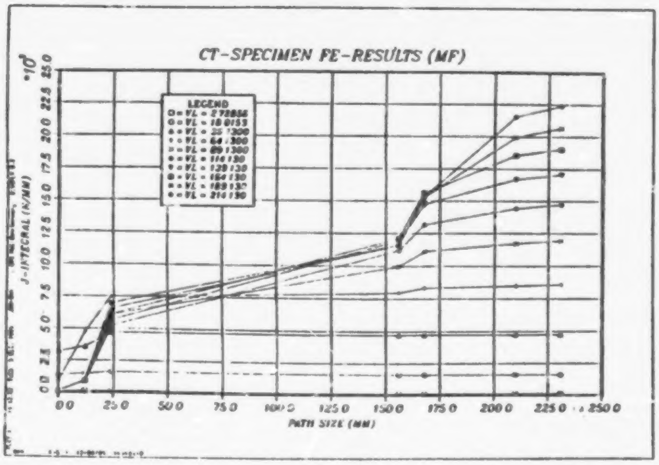

Figure 2.4.10 C(T) specimen: J-integral versus path size, Model 2, load point displacement until 214 mm. (Participant 4.)

T-4573-F2.4.10

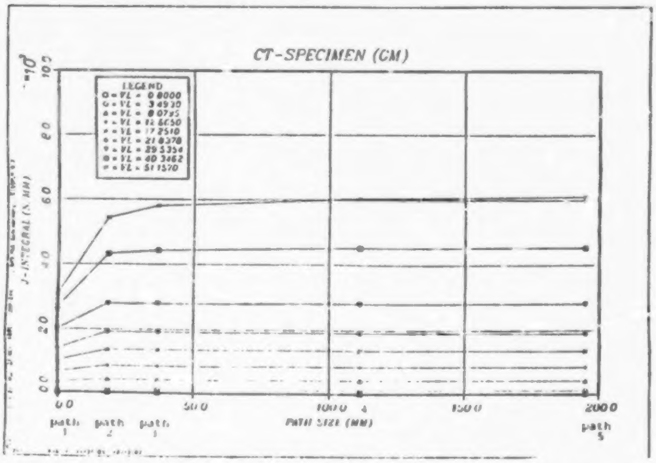

Figure 2.4.11 C(T) specimen: J-integral versus path size, Model 1 (Path 1 to Path 5). (Participant 4.)

T-4573-F2.4.11

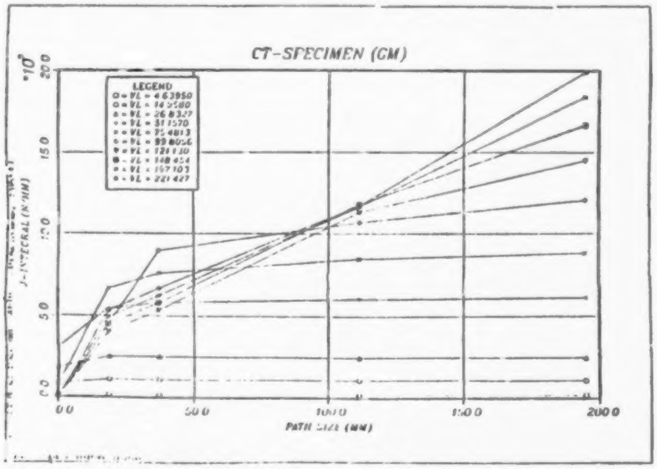

Figure 2.4.12 C(T) specimen: J-integral versus path size, Model 1, load point displacement until 221 mm. (Participant 4.)

T-4573-F2.4.12

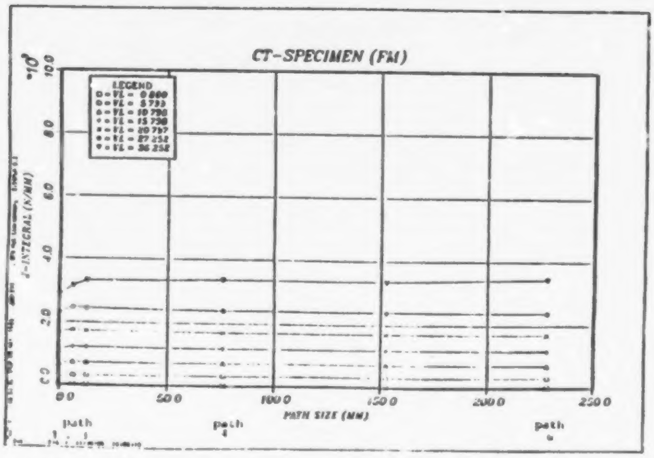

Figure 2.4.13 C(T) specimen: J-integral versus path size, Model 3 (Path 1 to Path 5). (Participant 4.)
T-4573-F2.4.13

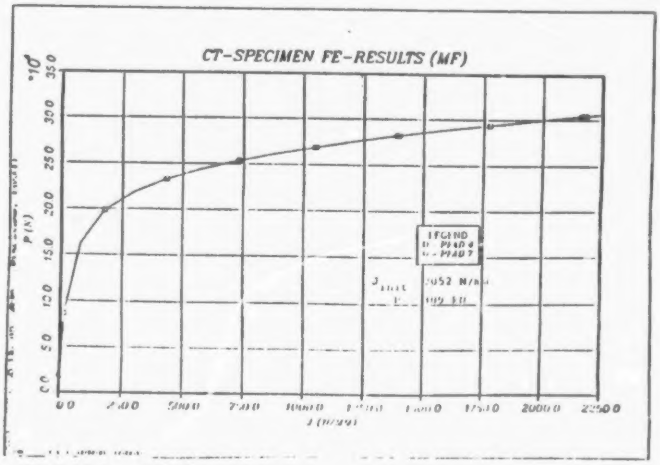

Figure 2.4.14 C(T) specimen: Load versus J up to crack initiation, Model 2. (Participant 4.)
T-4573-F2.4.14

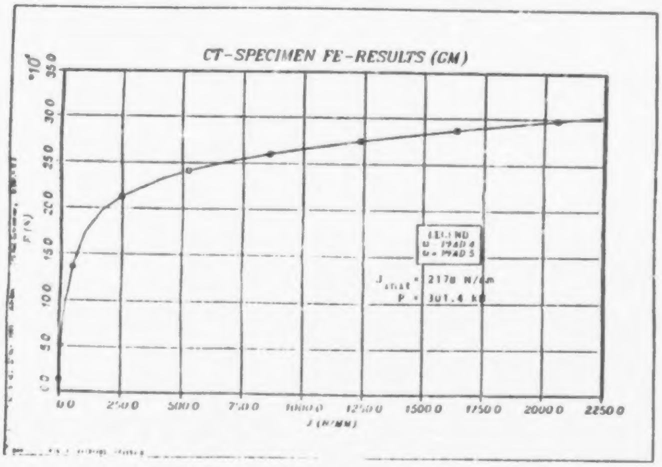

Figure 2.4.15 C(T) specimen: Load versus J up to crack initiation, Model 1. (Participant 4.)
T-4573-F2.4.15

49

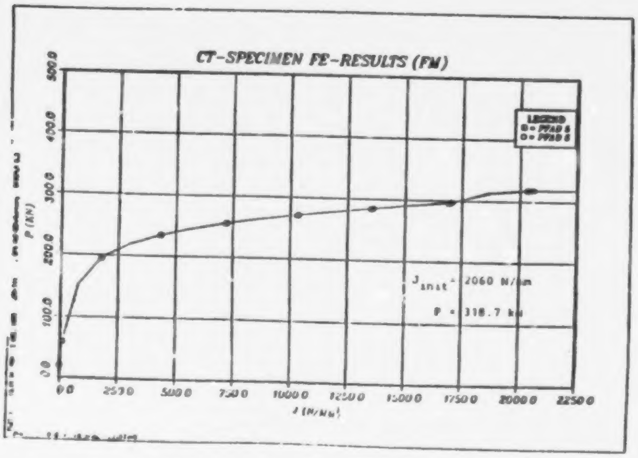

Figure 2.4.16 C(T) specimen: Load versus J, Model 3. (Participant 4.)

T-4573-F2.4.16

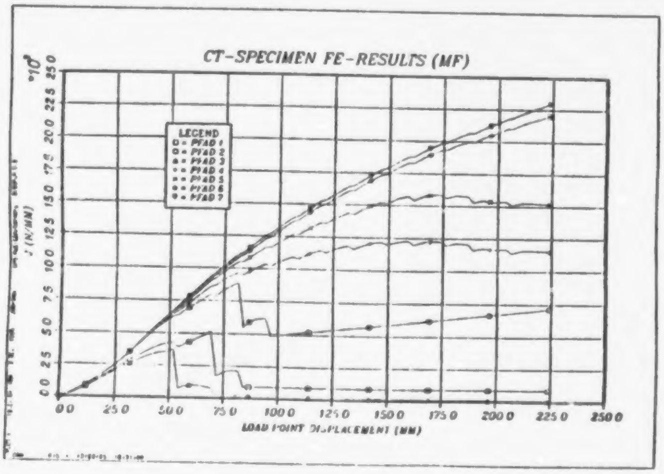

Figure 2.4.17 C(T) specimen: Calculated J versus load point displacement, Model 2. (Participant 4.)

T-4573-F2.4.17

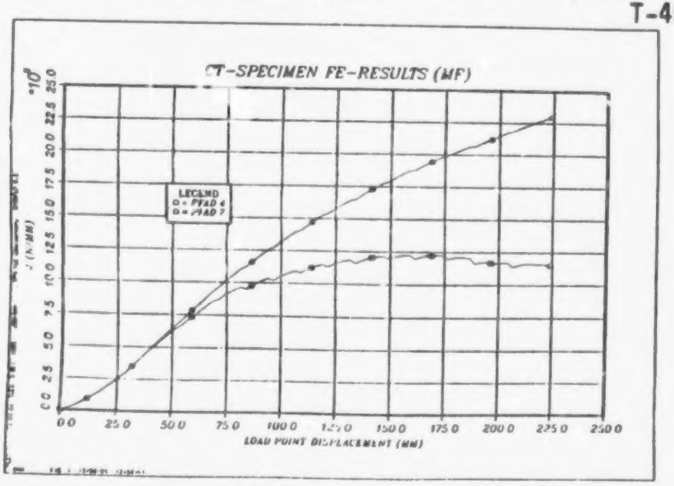

Figure 2.4.18 C(T) specimen: Calculated J versus load point displacement, Model 2 (Path 4 and Path 7). (Participant 4.)

T-4573-F2.4.18

50

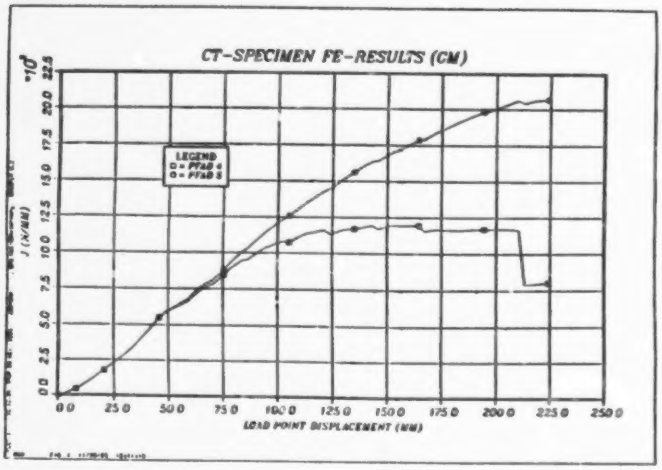

Figure 2.4.19 C(T) specimen: Calculated J versus load point displacement, Model 1 (Path 4 and 5). (Participant 4.)

T-4573-F2.4.19

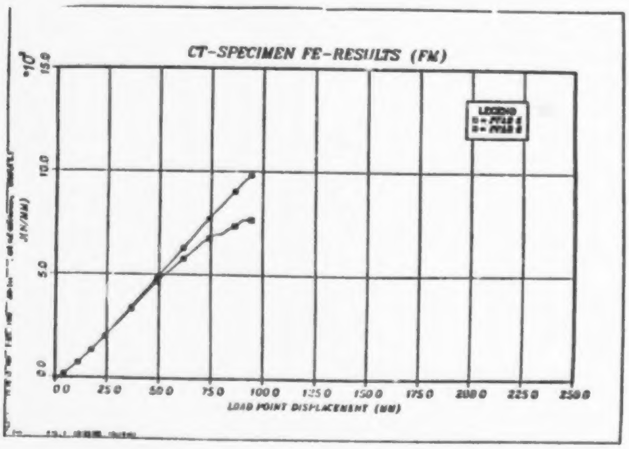

Figure 2.4.20 C(T) specimen: Calculated J versus load point displacement, Model 2 (Path 5 and 6). (Participant 4.)

T-4573-F2.4.20

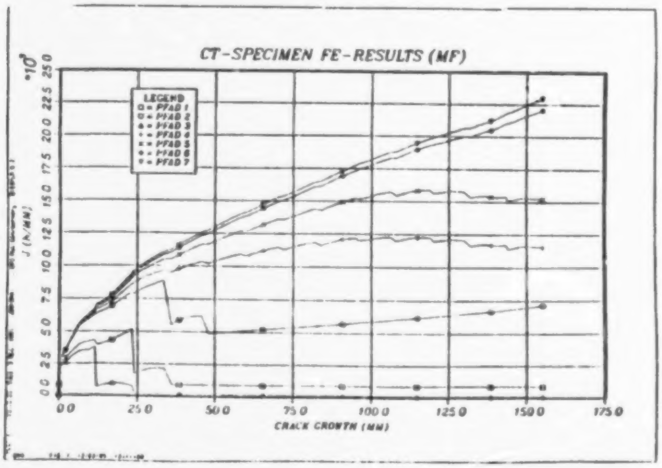

Figure 2.4.21 C(T) specimen: Calculated J versus crack growth, Model 2. (Participant 4.)

T-4573-F2.4.21

51

BEST COPY AVAILABLE

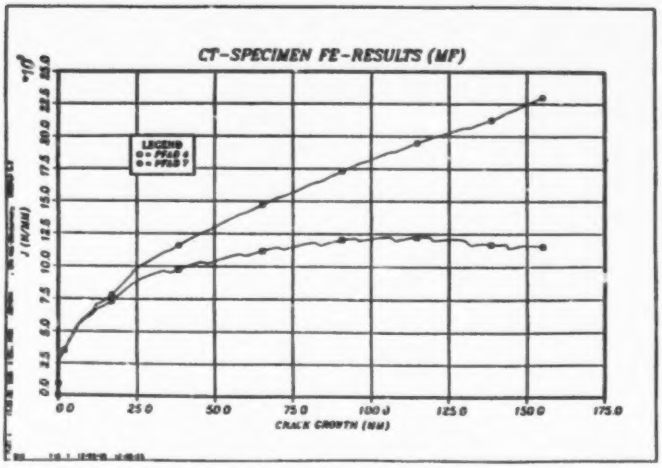

Figure 2.4.22 C(T) specimen: Calculated J versus crack growth (Path 4 and 7), Model 2. (Participant 4.)

T-4573-F2.4.22

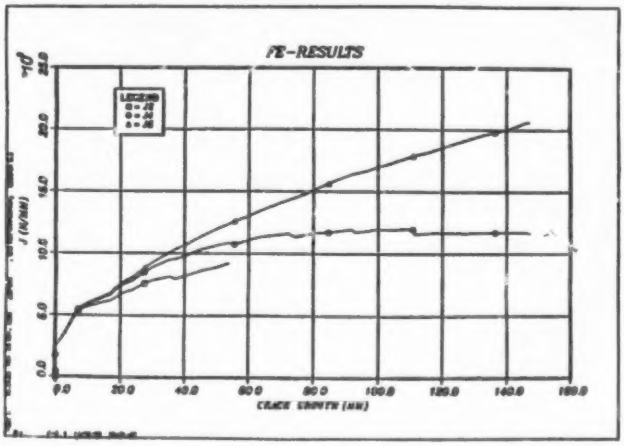

Figure 2.4.23 C(T) specimen: Calculated J-R curve, Model 1. (Participant 4.)

T-4573-F2.4.23

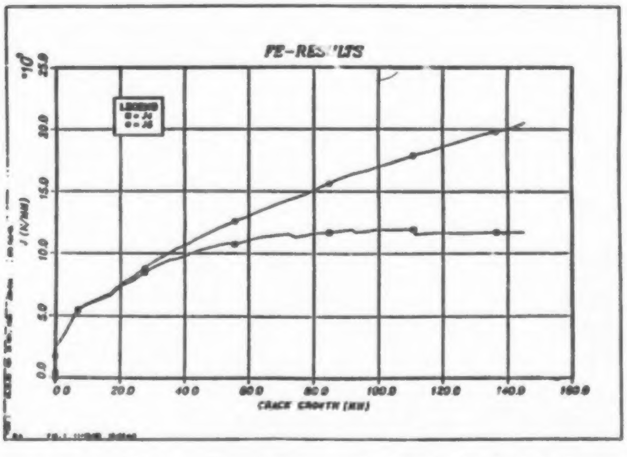

Figure 2.4.24 C(T) specimen: Calculated J-R curve, Model 1. (Participant 4.)

T-4573-F2.4.24

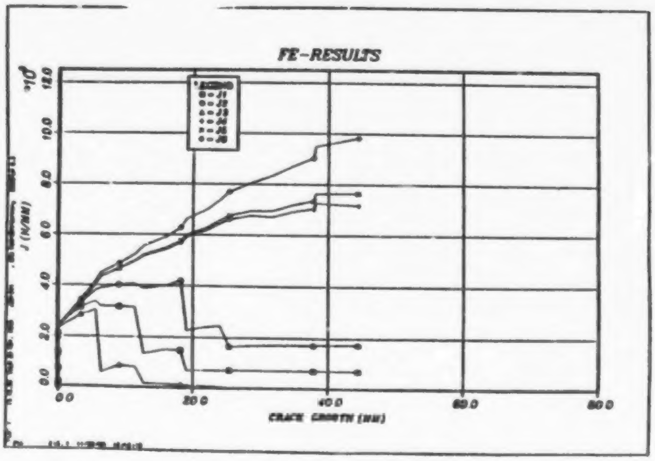

Figure 2.4.25 C(T) specimen: Calculated J-R curve, Model 3. (Participant 4.)

T-4573-F2.4.25

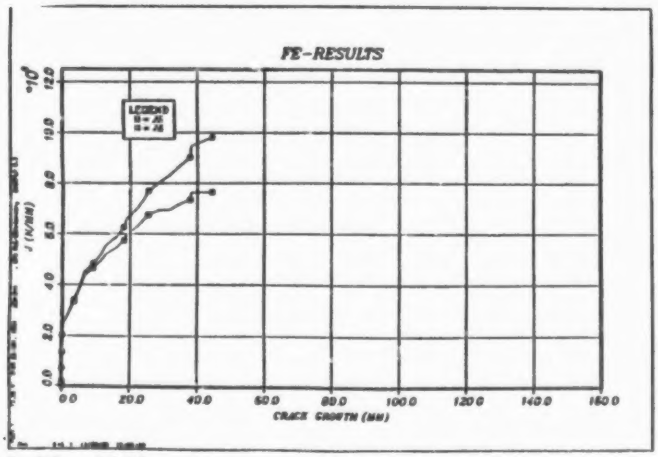

Figure 2.4.26 C(T) specimen: Calculated J-R curve, Model 3. (Participant 4.)

T-4573-F2.4.26

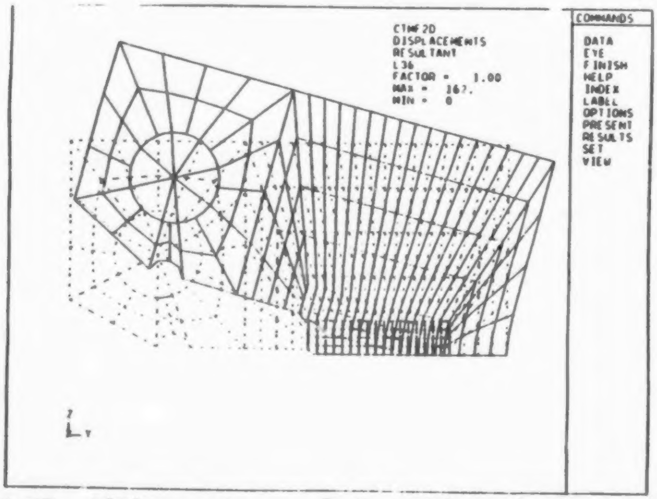
CTMF2D
DISPLACEMENTS
RESULTANT
L36
FACTOR = 1.00
MAX = 167.
MIN = 0
COMMANDS
DATA
EYE
FINISH
HELP
INDEX
LABEL
OPTIONS
PRESENT
RESULTS
SET
VIEW

Figure 2.4.27 C(T) specimen: Deformation at the crack extension of 157 mm, Model 2. (Participant 4.)

T-4573-F2.4.27

BEST COPY AVAILABLE

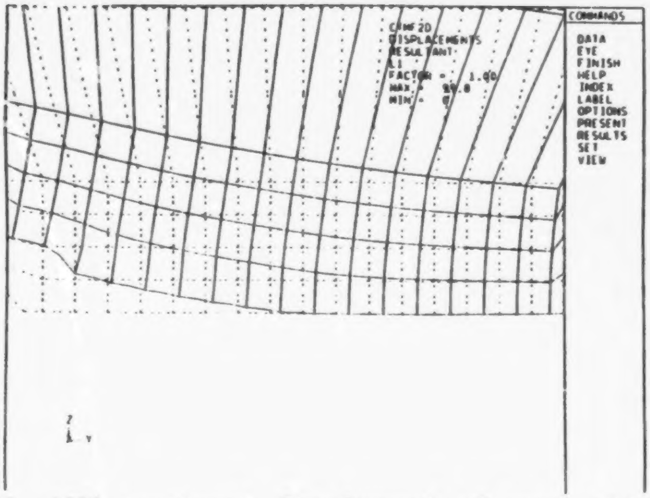
CTMF 2D
DISPLACEMENTS
RESULTANT
L1
FACTOR = 1.00
MAX =
MIN = 0
COMMANDS
DATA
EYE
FINISH
HELP
INDEX
LABEL
OPTIONS
PRESENT
RESULTS
SET
VIEW
Z
Y

Figure 2.4.28 C(T) specimen: Development of crack opening angle (A), Model 2. (Participant 4.)

T-4573-F2.4.28

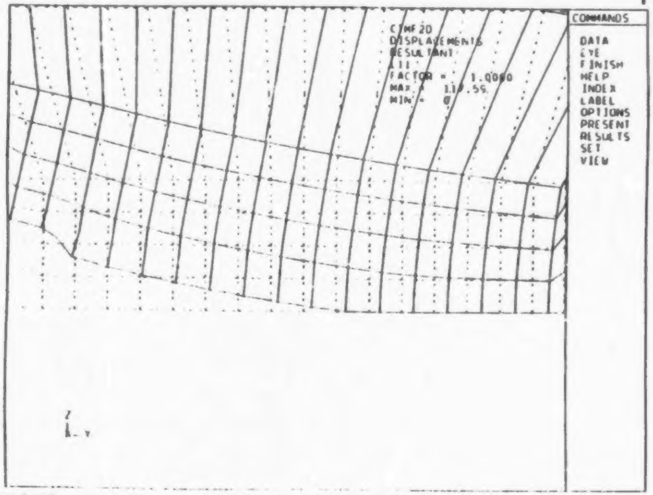
CTMF 2D
DISPLACEMENTS
RESULTANT
L11
FACTOR = 1.0000
MAX =
MIN = 0
COMMANDS
DATA
EYE
FINISH
HELP
INDEX
LABEL
OPTIONS
PRESENT
RESULTS
SET
VIEW
Z
Y

Figure 2.4.29 C(T) specimen: Development of crack opening angle (B), Model 2. (Participant 4.)

T-4573-F2.4.29

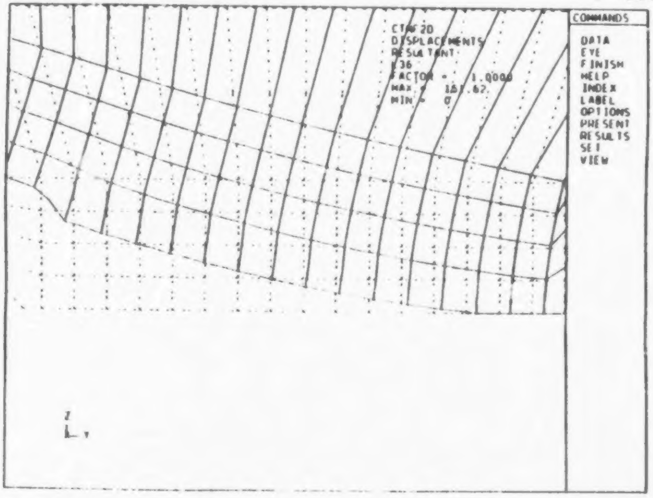
CTMF 2D
DISPLACEMENTS
RESULTANT
L36
FACTOR = 1.0000
MAX =
MIN = 0
COMMANDS
DATA
EYE
FINISH
HELP
INDEX
LABEL
OPTIONS
PRESENT
RESULTS
SET
VIEW
Z
Y

Figure 2.4.30 C(T) specimen: Development of crack opening angle (C), Model 2. (Participant 4.)

T-4573-F2.4.30

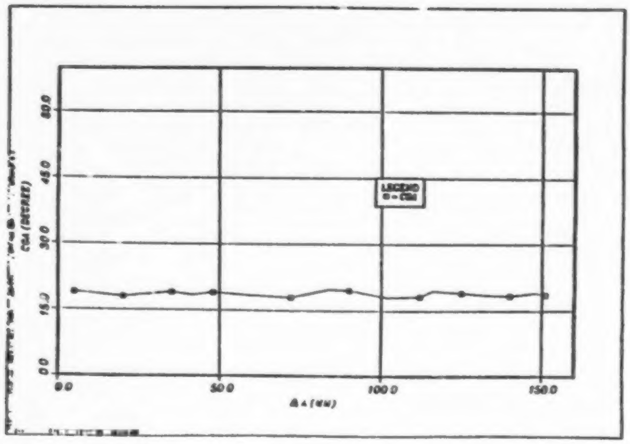

Figure 2.4.31 C(T) specimen: Calculated crack opening angle versus crack extension, Model 2. (Participant 4.)
T-4573-F2.4.31

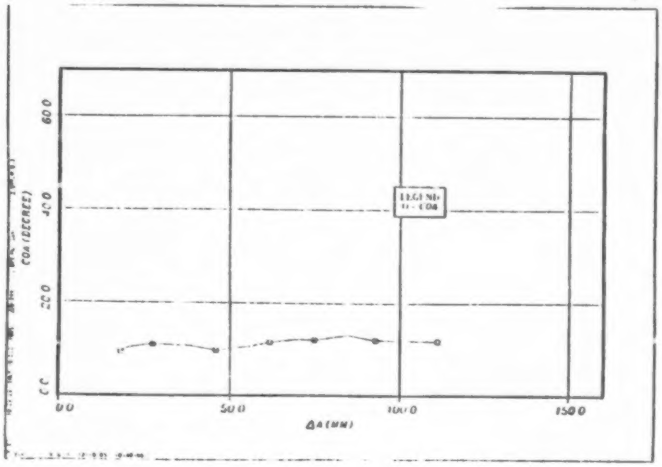

Figure 2.4.32 C(T) specimen: Calculated crack opening angle versus crack extension, Model 1. (Participant 4.)
T-4573-F2.4.32

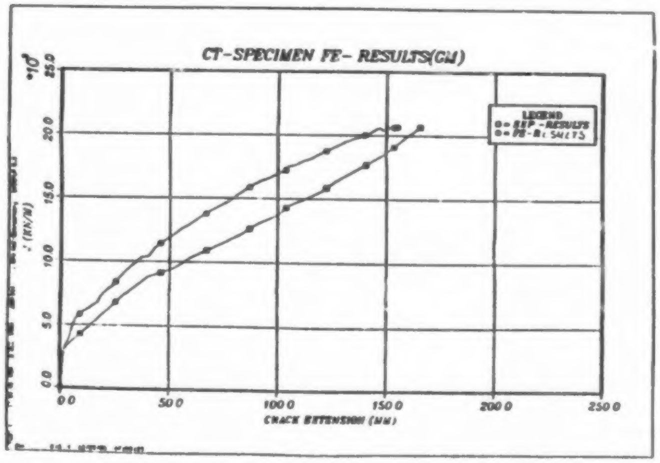

Figure 2.4.33 C(T) specimen: Comparison between J_R- and J_M-curve, Model 1. (Participant 4.)
T-4573-F2.4.33

55

BEST COPY AVAILABLE

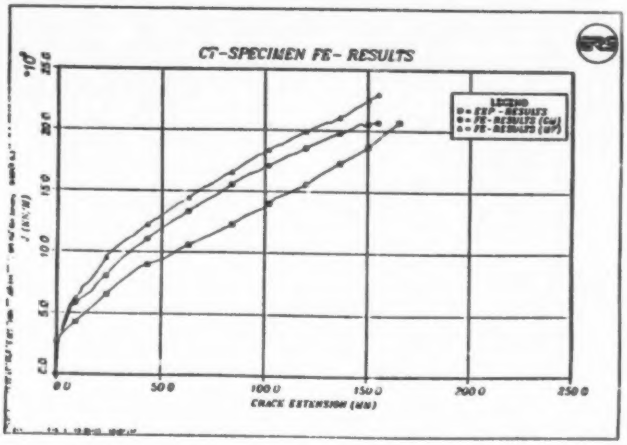

Figure 2.4.34 C(T) specimen: Comparison of J_R curves from Model 1 and Model 2 to the J_M curve. (Participant 4.)

T-4573-F2.4.34

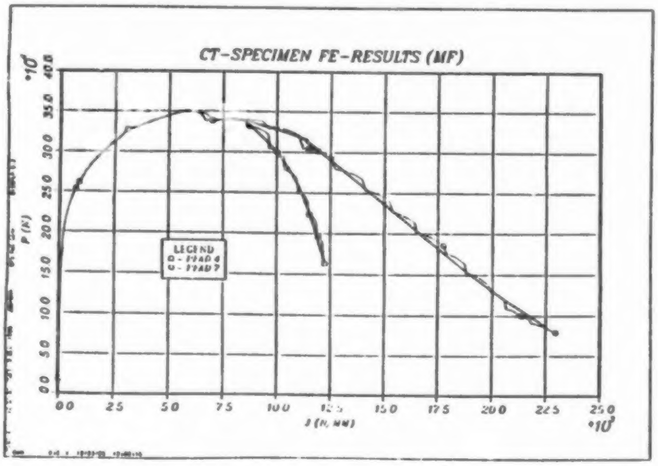

Figure 2.4.35 C(T) specimen: Load versus J, Model 2. (Participant 4.)

T-4573-F2.4.35

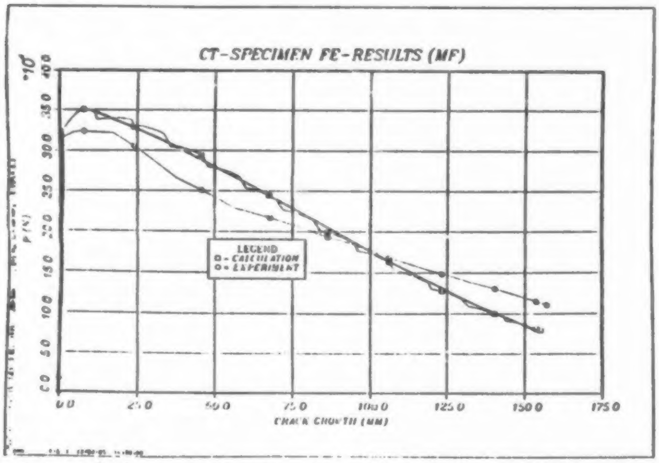

Figure 2.4.36 C(T) specimen: Load versus crack growth, Model 2 (experimental and calculation). (Participant 4.)

T-4573-F2.4.36

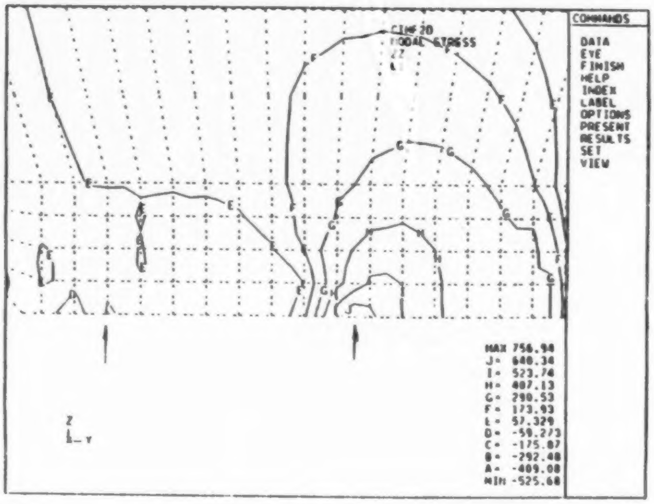

Figure 2.4.37 C(T) specimen: Stress distribution in Z direction along the crack front (Δa about 94 mm), Model 2. (Participant 4.)
T-4573-F2.4.37

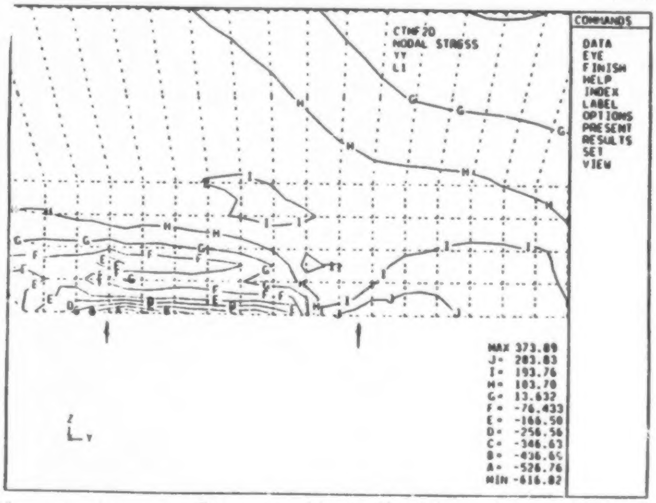

Figure 2.4.38 C(T) specimen: Stress distribution in y direction along the crack front (Δa about 94 mm), Model 2. (Participant 4.)
T-4573-F2.4.38

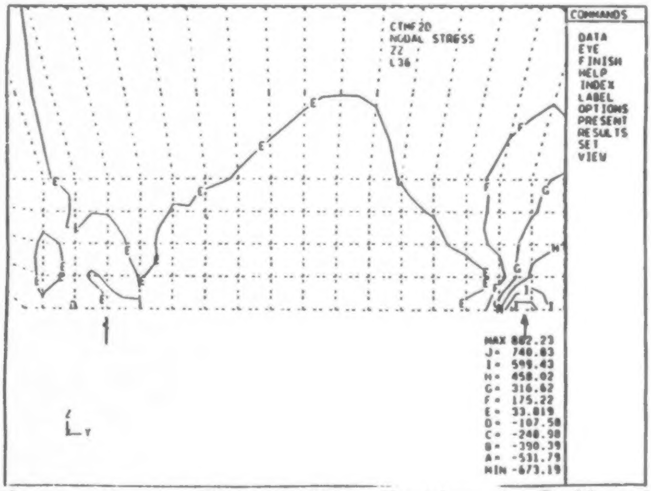

Figure 2.4.39 C(T) specimen: Stress distribution in Z direction along the crack front (Δa about 157 mm), Model 2. (Participant 4.)
T-4573-F2.4.39

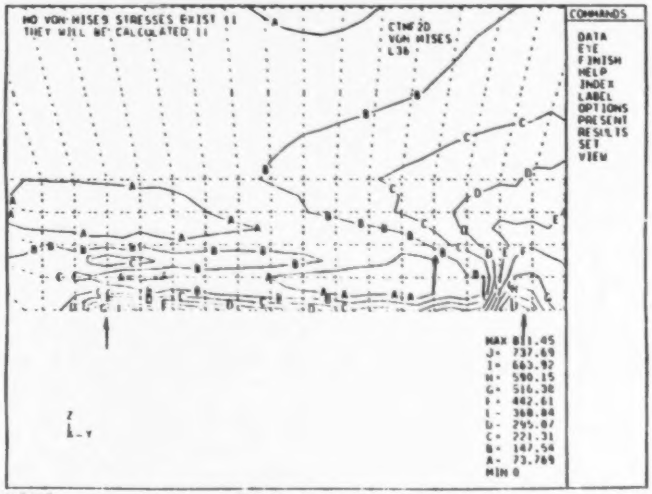

Figure 2.4.40 C(T) specimen: Effective stress distribution along the crack front (Δa about 157 mm), Model 2. (Participant 4.)
T-4573-F2.4.40

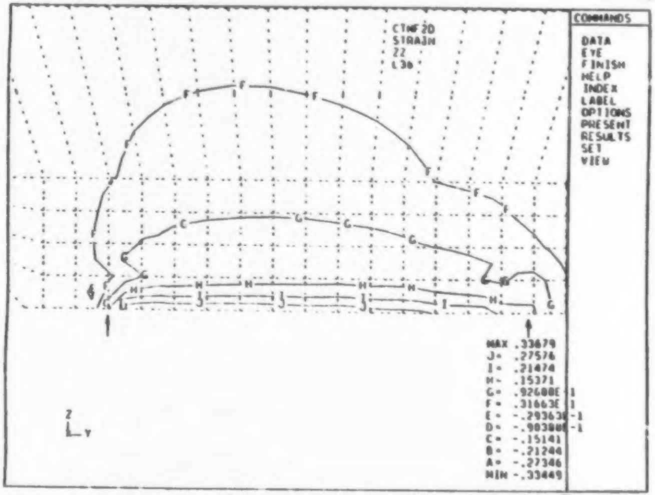

Figure 2.4.41 C(T) specimen: Strain distribution in Z direction along the crack front (Δa about 157 mm), Model 2. (Participant 4.)
T-4573-F2.4.41

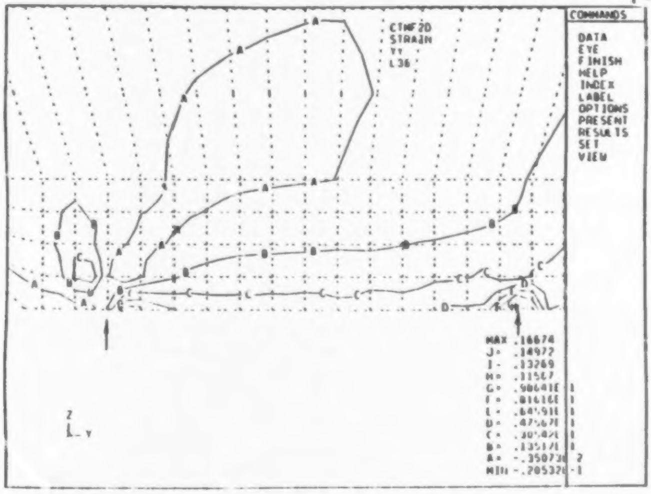

Figure 2.4.42 C(T) specimen: Strain distribution in y direction along the crack front (Δa about 157 mm), Model 2. (Participant 4.)
T-4573-F2.4.42

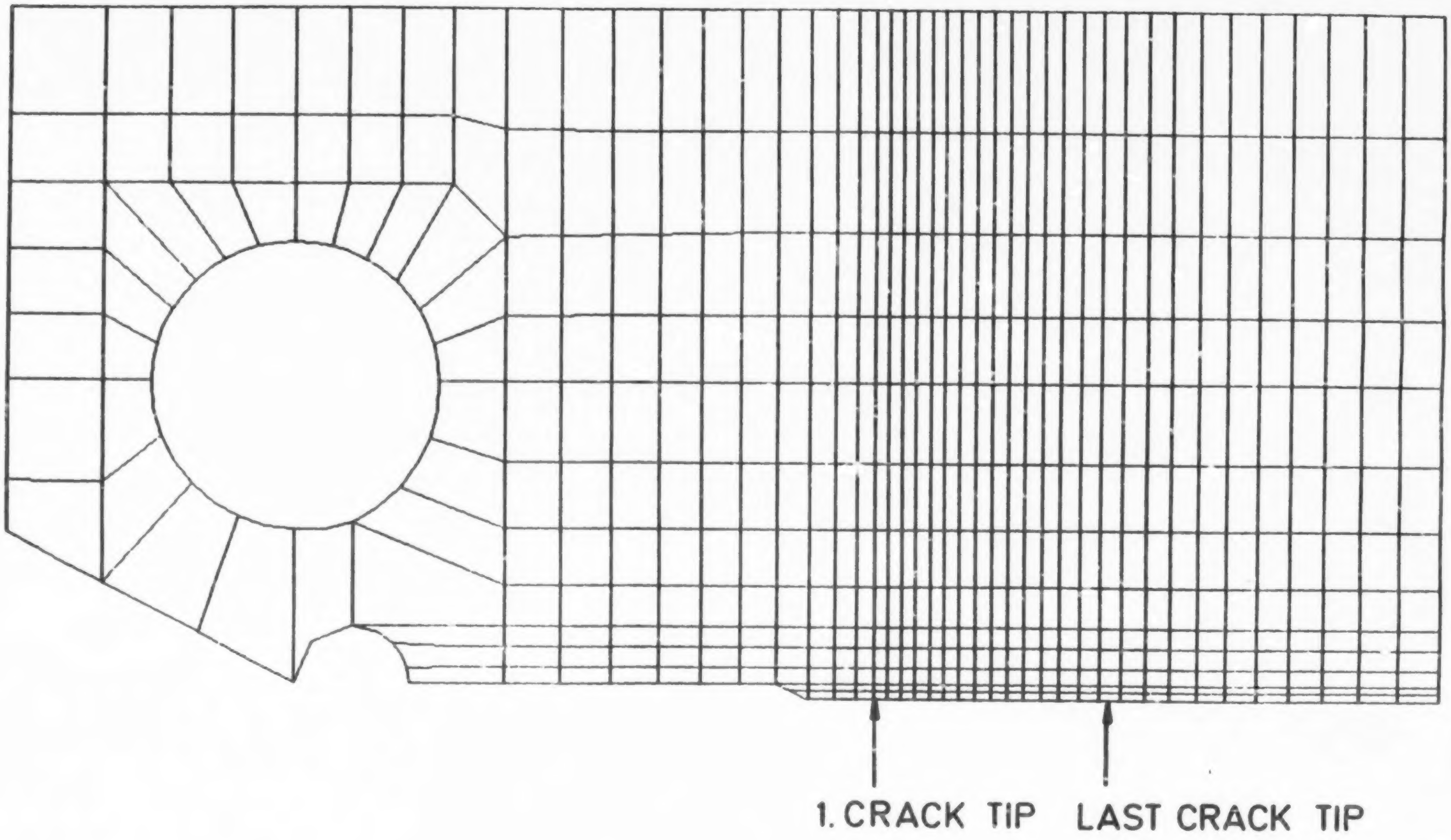
1. CRACK TIP
LAST CRACK TIP

Figure 2.5.1 FE-mesh for C(T) specimen. (Participant 5.)

T-4573-F2.5.1

59

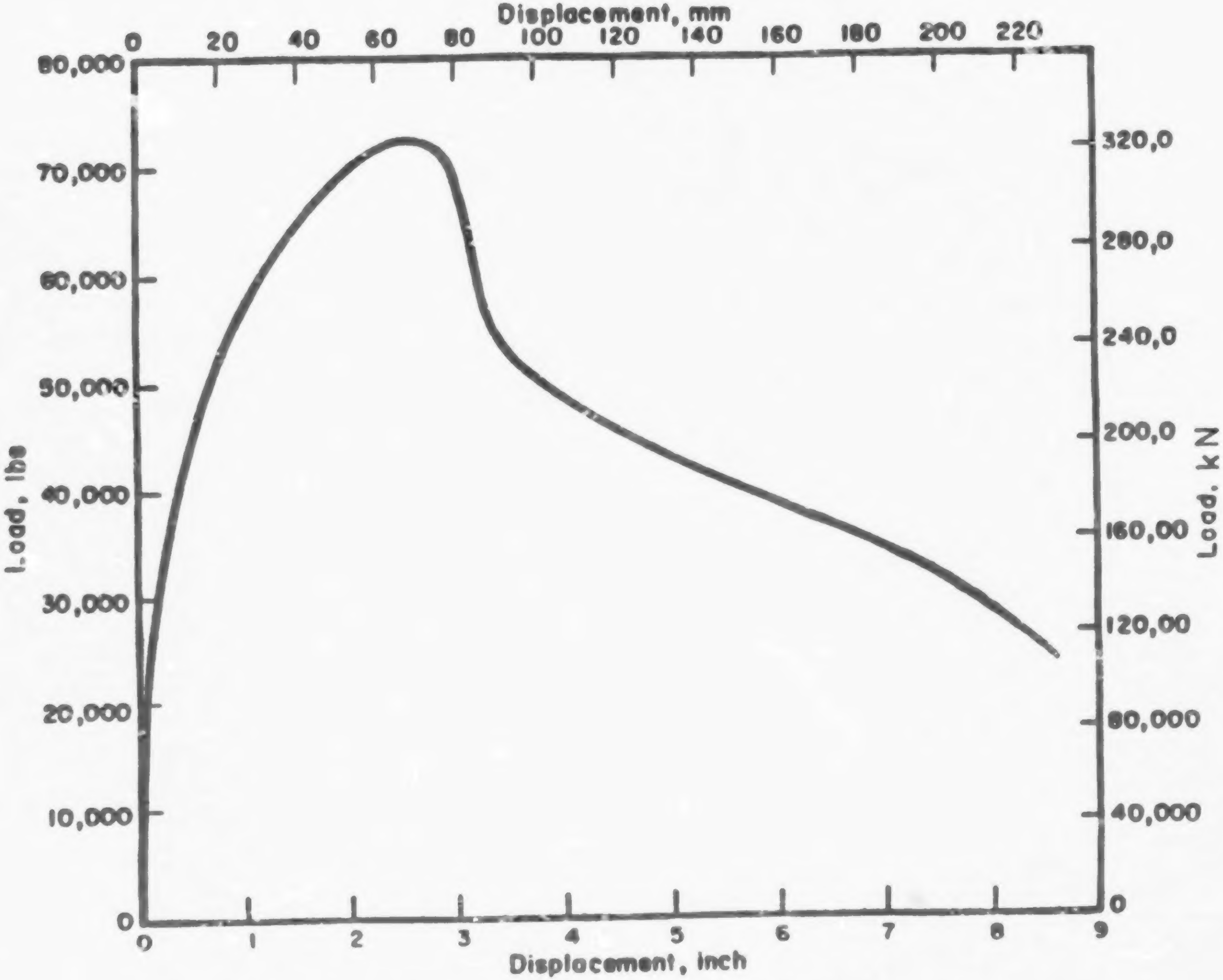

Figure 2.5.2 Calculated load versus load-point displacement. (Participant 5.)

T-4573-F2.5.2

60

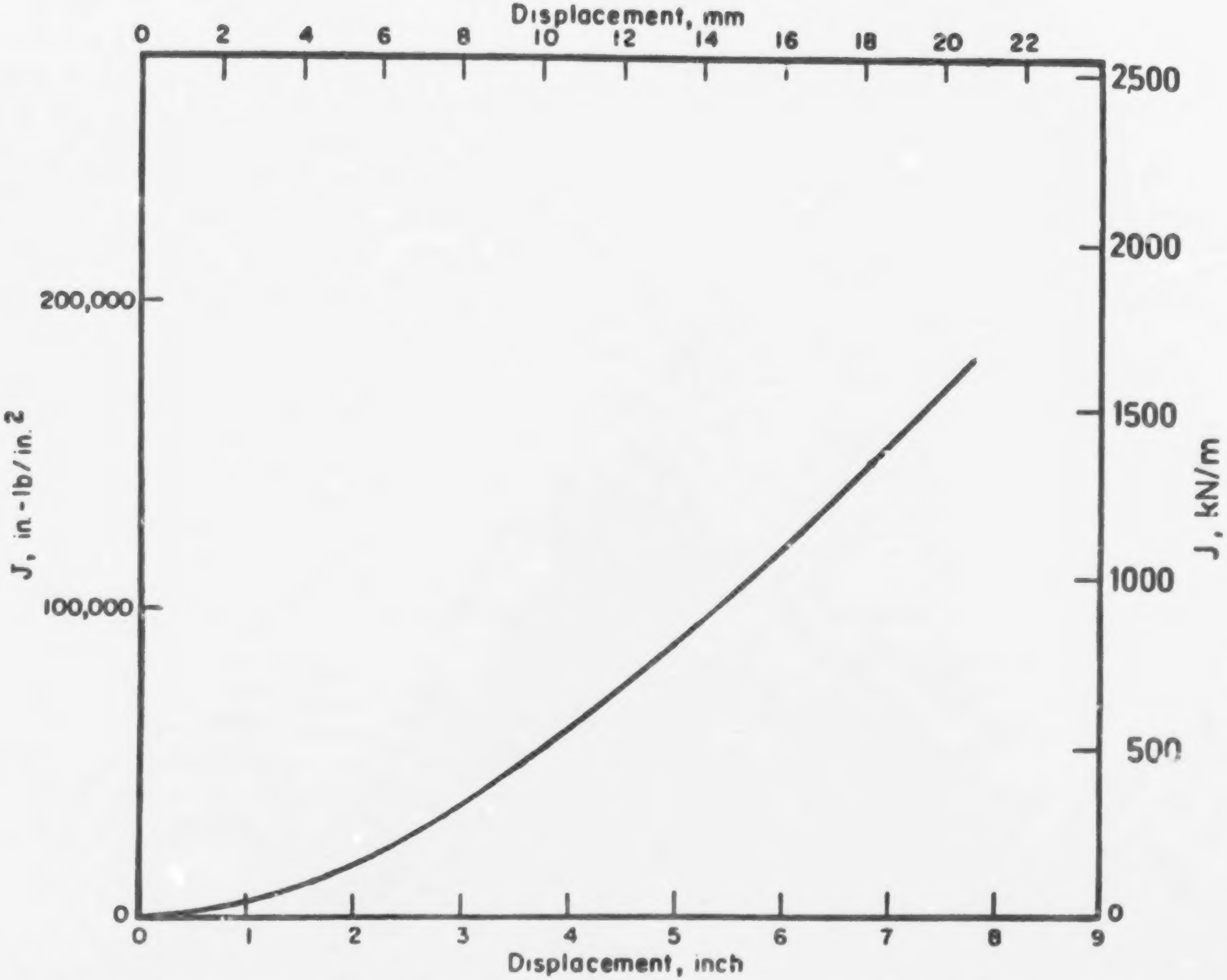

Figure 2.5.3 Calculated J versus load point displacement up to crack initiation. (Participant 5.)

T-4573-F2.5.3

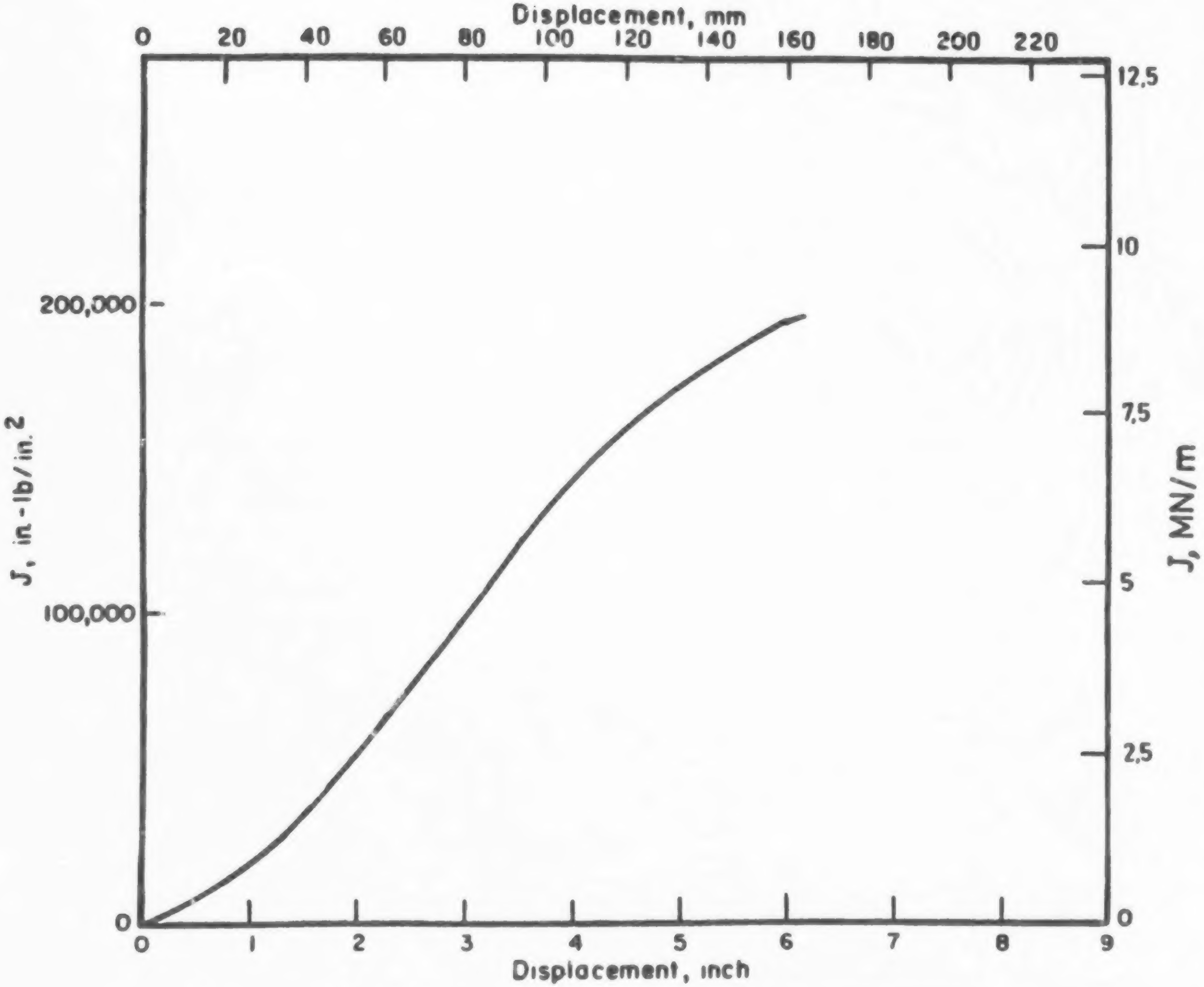

Figure 2.5.4 Calculated J versus load point displacement. (Participant 5.)

T-4573-F2.5.4

62

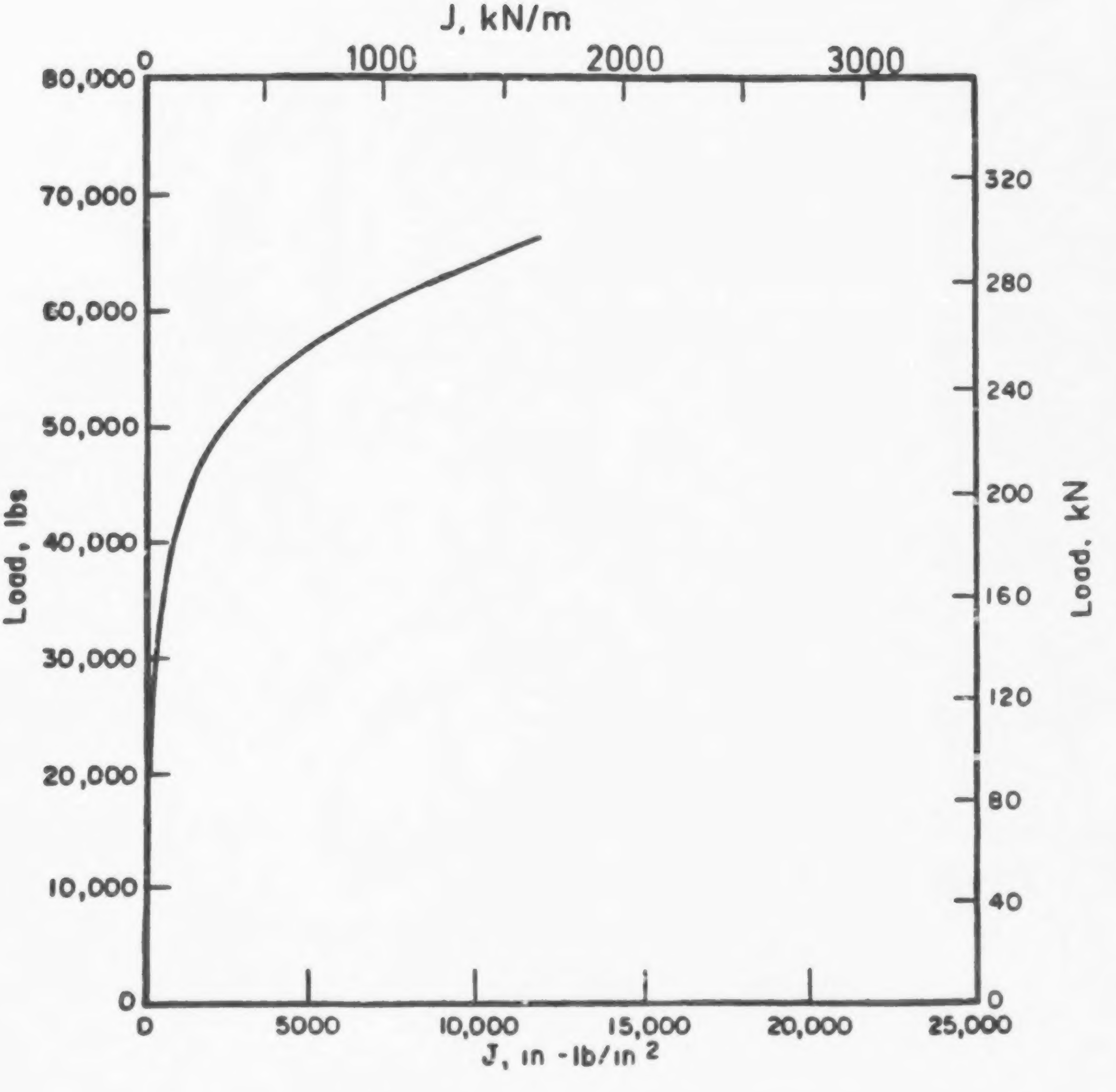

Figure 2.5.5 Calculated load versus J up to crack initiation. (Participant 5.)

T-4573-F2.5.5

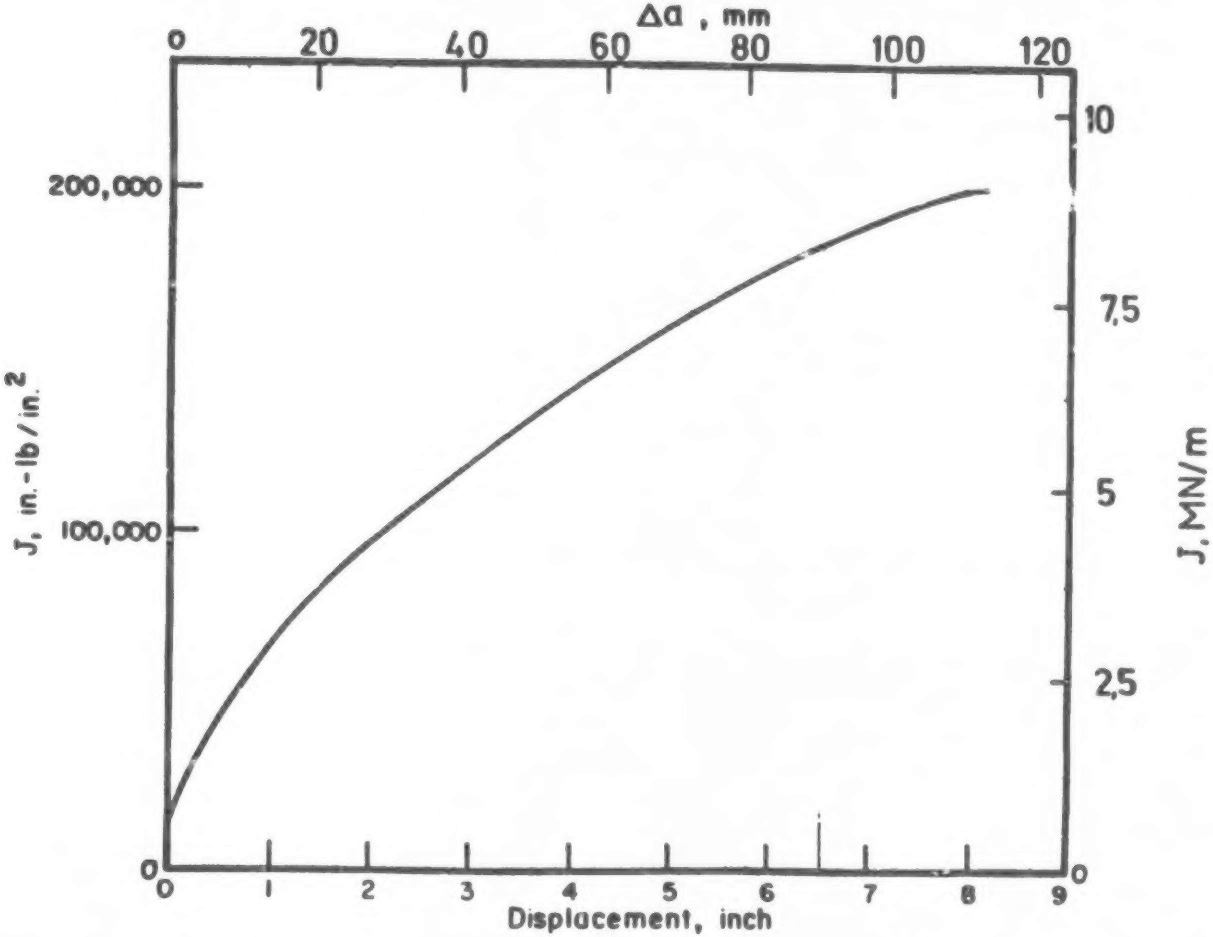

Figure 2.5.6 Calculated J_R-curve, crack initiation at J_c = 1,6 MN/m. (Participant 5.)

T-4573-F2.5.6

3. FEM SOLUTIONS OF THE PIPE PROBLEM

In common EPFM applications to assess integrity of nuclear power-plant piping, the J-resistance curve of a material is obtained by analyzing data from small-sized specimens, rather than data from large pipe experiments. However, because of the suspected geometry dependence of the J-resistance curve (discussed in Section 2), analyses are being performed of large-scale pipe experiments (Degraded Piping Program - Phase II) to calculate J-resistance curves. Typically, this is done by using J-estimation formulas. The data required for these calculations are the load versus load-point displacement, load-point displacement versus crack extension, and sometimes (depending upon the estimation formula used) the stress versus strain curve of the material.

As discussed in Section 2, the J-estimation formulas are based on several simplifying assumptions. Therefore, the J-resistance curves obtained by using these formulas need to be assessed for accuracy. In the Degraded Piping Program, this is being done by performing elastic-plastic finite element analyses of a selected number of experiments to obtain the J-resistance curves. But since nonlinear finite element analyses of crack growth also involve assumptions and judgments on the part of the analyst, the accuracy of these assumptions and judgments should also be tested. With this as the rationale, the second problem (Problem B) in the round robin was selected.

The problem involved a 16-inch (406.4-mm) nominal diameter Type 304 stainless steel pipe containing a through-wall circumferential crack. The pipe was loaded in four-point bending at room temperature. The pipe and crack dimensions and the loading arrangement are shown in Figure 3.1. The experiment was performed by Battelle under a research project funded by the Electric Power Research Institute. The load versus load-line displacement and the corresponding crack-growth values obtained from the experiment are shown in Figure 3.2. The engineering stress versus strain and true stress-true strain curves of the material are shown in Figures 3.3 and 3.4. These data were supplied to potential round-robin participants in the form described in Appendix A. The participants were requested to perform a generation phase elastic-plastic finite element analysis. No restrictions were made as to the refinement of finite element mesh, element type, constitutive model choice, or any other computational modeling aspect. However, there were requirements regarding the form in which results would be presented. These are described in detail in Appendix A. The key results of the analyses were to include the computed J versus Δa curve and the computed load-versus-applied-displacement curve. The results obtained by the five participating organizations, including Battelle-Columbus, are presented below. Note that not all the participants who supplied the solution to Problem B are the same as those who supplied the solution to Problem A.

3.1 Solution by Participant Number 1

Calculation was performed by the finite element code specially developed for the purpose of pipe crack-growth analysis. This code utilizes the 16-node isoparametric three-dimensional solid elements shown in Figure 3.1.1. They have one midside node along circumferential as well as axial directions, but no midside node along the thickness direction of the pipe. As can be seen in Figure 3.1.1, 3x3x2 Gaussian integration points are arranged for the construction of the element stiffness matrices.

Finite element subdivision for one quarter of the pipe is shown in Figure 3.1.2, extended in the circumferential direction. One layer of the elements was arranged in the pipe thickness direction. Total number of elements and that of nodes of this model are 142 and 974, respectively. As indicated in the figure, one node at the pipe end, denoted by A, was constrained in the loading direction, while the forced displacement was given to the node point B.

Conventional J_2-flow theory was used in the elastic-plastic computation with the isotropic hardening law. Based on the uniaxial engineering stress and strain curve given in the problem, multilinear modeling was made for the input of the calculation, within the strain range less than 10 percent, as shown in Figure 3.1.3. No consideration was made for the nonlinearity due to the geometry changes.

Tangent stiffness method was employed for the nonlinear calculation with the residual load correction function. Total 78 loading steps were applied with equal displacement increment of 0.394 inch (10 mm) at point B.

The crack was forced to grow after some deformation according to the relationship between the load-point displacement and crack length, given in the program description. Figure 3.1.4 shows that the calculation follows the prescribed relation with good accuracy. Crack extension was simulated by the nodal releasing technique, where nodal reaction forces were released in three increments in each extension step.

The J-integral was computed by the virtual crack extension method using the deformed element ring shown in Figure 3.1.2 by a broken line. The nodes located at the inner- and outer-pipe surfaces were moved by the same angle ($\Delta\alpha = 10^{-7}$ radian) in the circumferential direction as shown in Figure 3.1.5. The estimation of the J-integral was made by

$$J = - \frac{\Delta\Pi}{R_m t \Delta\alpha} \tag{3.1.1}$$

66

where Π, R_m and t represent the potential energy stored in the pipe, pipe mean radius and pipe thickness, respectively. $\Delta\Pi$ can be obtained by the following formula:

$$\Delta\Pi = \sum_n \sum_l (W \, \Delta \det J + \sigma_{ij} \, \Delta B_{ijk} \, u_k \, \det J) \, H_l \qquad (3.1.2)$$

where

$\sum_n$ and $\sum_l$ represent the summations on the deformed elements and on the integration points, respectively,

W = strain energy density

$\det J$ = Jacobian

σ_{ij} = stresses

B_{ijk} = strain-nodal displacement matrix coefficients

u_k = nodal displacements

H_l = integration weight coefficients.

The values obtained in this way can be regarded as the average of the pointwise J-integral along the crack front.

Total load versus load-point displacement curve is shown in Figure 3.1.6. Good agreement with the experimental record was achieved. Figure 3.1.7 shows the variation of the applied load during ductile crack extension. According to the present calculation, maximum load was attained at the crack extension of 0.831 inch (21.1 mm) and then the load decreased gradually with the crack extension. The load at the onset of ductile crack extension was 98.6 percent of the maximum load.

The ovalization factor represented by the ratio of in-plane diameter to out-of-plane diameter is shown in Figure 3.1.8 as a function of load-point displacement. The ovalization factor increases almost linearly with the load-point displacement and reaches about 1.08 in the present analysis regime.

Calculated load versus J-integral relation up to crack initiation is shown in Figure 3.1.9. The value of the J-integral began to increase rapidly at the load level about 40,000 lbs (178 kN), where the fully plastic state was achieved. J-integral versus load-point displacement relation and J-integral-resistance curve are shown in Figures 3.1.10 and 3.1.11.

Crack opening profile before and after crack growth is shown in Figure 3.1.12. It can be seen that the opening displacement at inner surface is larger than that at outer surface in the neighborhood of the crack tip but smaller near the center of the crack. Finally, crack tip opening angle (CTOA) at inner and outer surfaces is shown in Figure 3.1.13. It should be noted that the crack tip opening angle at the inner surface is nearly twice as that at the outer surface.

From the comparison of calculated and experimental results on global deformation behavior, overall deformation behavior of the cracked pipe seemed to be simulated in a reasonable accuracy by the present analysis method. Because the J-integral value was evaluated at the elements relatively far from the crack tip, the value can be also regarded as the global quantity.

On the other hand, because the CTOA was evaluated at the location very close to the crack tip. effect of the geometrical nonlinearity is expected to be larger. This may account for the fact that the value of the CTOA obtained by the present calculation seemed rather small compared to the available past data. The effect of the difference in the hardening law, i.e., isotropic versus kinematic, on the near tip quantities should be examined in detail.

3.2 Solution by Participant Number 2

The computations have been performed with a version of the Finite Element Code ADINA modified by subroutines for J-Integral calculation and simulation of stable crack growth using the elastic-plastic model with von Mises yield condition, isotropic hardening and total Lagrangian analysis.

The numerical simulation of the pipe bending experiment, described in Appendix A, has been conducted by using the uniaxial true stress versus true strain curve and the relation between the load-point displacement and the crack propagation observed in the experiment as input for the Finite Element analysis in order to predict the crack resistance curve and the load displacement behavior. The input data are described in detail in the statement of Problem B in Appendix A.

The 3-D-finite-element grid of the pipe model shown in Figure 3.2.1 consists of 1133 nodes and 130 twenty-node isoparametric elements with 3000 degrees of freedom. The bending load is realized with a fixity at the end of the modelled pipe and prescribed displacements at the marked node.

Figure 3.2.2 shows the typical shape of the pipe deformation due to the bending load especially at a load-point displacement of 18.1 inch (460 mm), where crack growth of 0.65 inch (16.4 mm) has already taken place. The crack growth is determined by the experimental curve of load-point displacement versus crack growth. The comparison between the experimental measured total load (i.e., twice the load at each of the load points) and the calculated load versus the load-point displacement (Figure 3.2.3) shows some differences which are not yet fully

68

BEST COPY AVAILABLE

understood. Maybe some experimental effects in connection with the kind of loading and the counter weight realized by wire ropes have not been taken into account.

In the frame of the fracture mechanics analysis, the path dependence of the calculated J-integral has been investigated. Figure 3.2.4 shows two of the selected node blocks for application of the virtual crack extension method. As measure of the path size, the square root of the outer node block surface is used. The curves of the calculated J-integral versus the path size (Figures 3.2.5 and 3.2.6) dependent on the load-point displacement show in all cases the largest J-values with path size of about 2.95 inch (75 mm), i.e., path No. 6 and smaller values for far-field paths (path No. 8).

This behavior is negligible up to load-point displacement of 3.9 inch (100 mm), i.e., in this region the calculated J-values are path independent, but results in a discrepancy of about 40 percent in J_{Ic} between path No. 6 and No. 8. The same effect is also demonstrated in Figures 3.2.7 and 3.2.8 where the calculated J-values versus load-point displacement and the load respectively are plotted for the two selected integral paths.

The unusual path dependence of J-Integral results from the following aspects:

The coarse mesh in the crack front region effects that the stress singularity has not been considered very well. Therefore the J-values evaluated with paths close to the crack front seem to be too small.

In a further calculation it is planned a finer FE mesh with cubic elements near the crack front and an appropriate transition to coarser regions. Furthermore it has to be mentioned that in the present fracture mechanics version of ADINA it is only possible to displace regions of the structure around the crack front virtually into a fixed direction. Concerning with curved crack front regions as in this analysis the J-calculation with paths extended beyond large angles (path No. 7,8) is falsified. It is planned to improve the fracture mechanics options of the used ADINA-version and to analyse the pipe once more.

In the frame of the analysis documented in this report the path dependence of J-Integral is assessed as a scatter band. The J-values of paths 4 to 6 seem to be most reliable because of the considerations mentioned above.

The details of experimental results gave information that the initiation value ranges about 3,027 lb/inch (5.3 kN/mm), which is in our proposed scatter band. The predicted J-R curve up to 1.57 inch (40 mm) crack growth, i.e., about 12 degree angle increase of the half slit is shown in Figure 3.2.9 dependent on the path size.

3.3 Solution by Participant Number 3

Description of the Cracked Pipe Finite Element Model:

a. Analytical model and boundary conditions:	Figure 3.3.1
b. Number of elements:	304
c. Number of nodes:	337
d. Element type:	4 node thick shell
e. Integration:	1 gauss
f. Crack extension:	Node release
g. Equilibrium correction:	Newton-Raphson
h. Yield surface:	Von Mises
i. Hardening:	Kinematic
j. Stress-strain:	True stress-strain
k. Finite deformation:	N/A
l. The J-integral:	VCE

Pipe Analysis Results:

a. Load (P) versus load-point displacement (δ) curve:	Figure 3.3.2
b. The J-integral (J) versus δ curve:	Figure 3.3.3
c. J versus P curve:	Figure 3.3.4
d. J versus crack extension (Δa) curve:	Figure 3.3.5
e. Crack tip opening angle (CTOA) versus Δa curve:	Figure 3.3.6
f. Crack tip opening displacement (CTOD) versus Δa curve:	Figure 3.3.7

Discussion of Pipe Results

The discussion of results could be as follows:

a. Load (P) decreases gradually during the crack extension	Figure 3.3.2

while the J-integral increases monotonically: Figure 3.3.3

b. Kinematic hardening rule is adopted in this analysis, so CTOD/2 and/or CTOA/2 are expected to be higher than the others.

3.4 Solution by Participant Number 4

Description of the cracked pipe finite element model:

Three different finite element models were used for the calculations. The first two (model 1 and 2) were those presented at the 1985 PVP meeting, while model 3 was used afterwards.

Their main characteristics are summarized in Table 3.4.1.

a. Mesh

A shell mesh with 1107 3-noded plane thin shell elements was used in Model 1 and 2 (Figure 3.4.1).

A brick mesh with 40 20-noded isoparametric brick elements was used in Model 3 (Figure 3.4.2).

This second mesh was chosen to be quite coarse because it was mainly used to check various numerical procedures.

b. Nonlinearities

In all the models, true stress-strain curve (10 points and parabolic interpolation) with isotropic hardening and von Mises criteria were considered.

Finite deformations (in model 2), but no finite strain effects, were taken into account.

c. Load and boundary conditions

Problem symmetries were modeled through appropriate boundary conditions, and two different analyses of wire rope and hydraulic ram contact were used.

In the first analysis (model 1 and 2) vertical displacement (OY axis) was prescribed in semicircumferential lines both at pipe end (zero displacement) and at saddle point O (input growing displacement).

These semicircumferential lines (180 degrees) were chosen to prevent excessive local yielding and ovalization.

Table 3.4.1 Summary of finite-element models used (Participant 4).

Model	1	2	3
Elements	1107 shell	1107 shell	40 Brick
Nodes	616	616	343
Degrees of freedom	3696	3696	1029
Finite deformation	No	Yes	No
Boundary conditions	180°	180°	0°

In the second analysis (model 3), those displacements were only prescribed at single points, 0 at saddle location, A at pipe end (0 degree).

In both analyses load-point displacement growth was made through 15 steps from zero to 368 mm (fourteen 25 mm steps and one 18 mm step).

d. J-integral computation

J-integral estimation was calculated with the VCE method using the following formula:

$$J = - \frac{\delta\pi}{\delta A}$$

with

$$\delta\pi = \sigma \; . \; {}^{\delta}B \cdot U$$

δA being the crack area extension due to a crack tip rotation of $\delta\theta = 5.10 \times 10^{-7} \pi$.

The J-integral results given here come from the contribution of a large set of elements, as can be seen by contours in Figure 3.4.1 and 3.4.2.

The choice of the number of elements to be taken into account was arrived at after preliminary test calculations which showed some numerical scatter in near-field J-calculation.

The same method was used even when finite deformation were taken into account.

e. Crack advance modeling

No crack advance simulation was done.

Pipe analysis results

Main results of the 3 calculations are summarized in Figures 3.4.3 to 3.4.5.

Plastic zone growth ($\sigma > 185$ MPa) is shown in the center part of the pipe for Model 2, Figure 3.4.6.

Discussion of pipe results

On the P-δ curve (Figure 3.4.3), comparison between the 3 models and the experiment shows that:

- Thin shell model underestimates load more than brick model, though the later was used with a much coarser mesh. This is mainly due to the simplified plastic shell behavior model which is not very accurate for this kind of radius to thickness ratio.

- Finite deformation analysis induces here a global stiffening of the structure (8 percent between model 1 and 2).

We can therefore assume that a calculation with brick elements (as in model 3) and finite deformation would lead to a somewhat higher P-δ curve, thus closer to the experiment.

On the J-P curve (Figure 3.4.4) and J-δ curve (Figure 3.4.5) one can see that the J-Integral results are roughly the same with the different models, within a 10 percent scatter band. They differ, on the J-P curve, more from the P calculation than from the J-estimation.

These results show that one should distinguish in cracked pipe analysis, two kinds of problems.

The first one is pipe modeling itself, which includes the choice of:

- type and number of elements

- mean of modeling the boundary conditions

- finite deformation or ovalization analysis

Analysis of the P-δ curves of the 3 models leads to the conclusion that the most appropriate pipe modeling, in this case, seems to be using brick elements, evenly distributed prescribed displacements and finite deformation.

The second problem is crack modeling which includes the choice of:

- VCE method (formula, size of extension, size of contours)

- crack advance modeling.

The best way to single out influence of these choices is J-δ and J-Δa curves analysis. Comparison between the solutions of all the participants will be of great interest on this particular point.

Interaction between the two problems is best seen on the J-P curves, which is, in some way, the user's curve.

It is of great importance to keep in mind that final comparison between the solutions (including estimation schemes) is to be made on initiation load P_i (which leads to $J = J_{Ic}$), considering degree of accuracy and conservatism compared to the experiment.

3.5 Solution by Participant Number 5

In the present analysis of the 16-inch (406.4-mm) Type 304 stainless steel pipe with a through-wall crack under the four-point bending, our in-house finite element code was used. Twenty-node brick elements with quadratic serendipity displacement were invoked. Figure 3.5.1 shows 142 elements of the type used in the analysis of a quarter of the specimen, where several collapsed elements of basically the same type are also used. Thus, the total number of nodes was 1102. The 3x3x3 Gaussian integration rule was used in the element for stiffness matrix and J-integral evaluations.

Sixty general elastic spring elements with variable stiffness were used in the area where the crack was to be extended. Incremental crack growth was simulated by gradual relaxation of the spring stiffness to zero in 10 to 15 steps per crack extension. Thus, the history-dependent loading/unloading due to the advancing crack tip area was properly followed. The finite deformation effects were not accounted for. The prescribed displacement-crack growth history was thus followed precisely in the analysis.

The constitutive model was based on the incremental theory of plasticity using the von Mises initial yield criterion with isotropic hardening. A multilinear representation of the engineering uniaxial stress-strain was used. Out of balance nodal forces due to the material nonlinearity and due to the crack geometry change were corrected by modified Newton-Raphson iteration scheme in a semi-tangent modulus approach.

The virtual crack extension method was used for calculating J. The formula is given by

$$J = \frac{1}{\delta a} \int_V [\sigma_{ij} \frac{\partial U_i}{\partial X_k} - W\delta_{jk}] \frac{\partial \Delta X_k}{\partial X_j} dV$$

where

U_i, σ_{ij}, and W are displacement, stress, and stress working density, respectively

X_i is the global coordinate

δ_{jk} is Kronecker delta

ΔX_k is the perturbation vector associated with the arbitrary virtual crack extension

δa is the virtual crack extension area.

The J was evaluated in the volume, V, inside the area indicated in Figure 3.5.1, wherein the area inside the broken line was rigidly moved within the pipe circumference. The J-integral, which is based on the

75

deformation theory of plasticity, is not path-independent after crack initiation because of the nonproportional stress-strain state occurring in the crack area. Thus, the J-values calculated in the present study may represent a far-field J which does not directly reflect the crack tip deformation state during crack growth.

The calculated load versus displacement results are shown in Figure 3.5.2 together with the experimental results. The experimental results were corrected by taking the pipe specimen weight into account and also by adjusting the elastic compliance in accordance with an average of the FE elastic compliances computed by all participants. The adjustment is due to elastic tension of the wire rope used for constraining at the ends of the pipe as shown in Figure 3.1. (See Section 5 for further discussion regarding the correction.) At crack initiation, the computed load level is 94 percent of the experimental value. However, after initiation, the computed load decreased more rapidly than the experiment.

The computed J-results over the range of loading analyzed are shown in Figures 3.5.3 through 3.5.5 as functions of load, displacement, and crack growth. Figure 3.5.6 shows exaggerated views of global and local pipe deformation at an early stage of the bending loading. The opposite trend of deformation on the longitudinal upper and lower edges of the pipe due to crack gives another view of ovalization on the crack plane.

Contour and growth of the plastic zone on the crack plane section are shown in Figures 3.5.7 and 3.5.8 for various load steps over the entire load range of the present analysis, where the yielding occurred at the equivalent stress above 44,300 psi (305.44 MPa). It is seen that the plastic zone near the crack, where the stress state is dominately tensile, proceeds faster on the inner surface than on the outer surface. The yielding in the area dominately compressive occurs at the load-point displacement δ = 10.5 inches (266.7 mm), and both the plastic zones approach each other to the neutral axis as the loading proceeds. In Figures 3.5.7 and 3.5.8, cross-sectional deformations are not represented, and the plastic zones at various load steps are not in common scale. In Figure 3.5.9, plastic zones extended over the pipe surface are shown in angled view at the load stages δ = 7.5 inches (190.5 mm), 13.5 inches (342.9 mm), and 25 inches (635 mm).

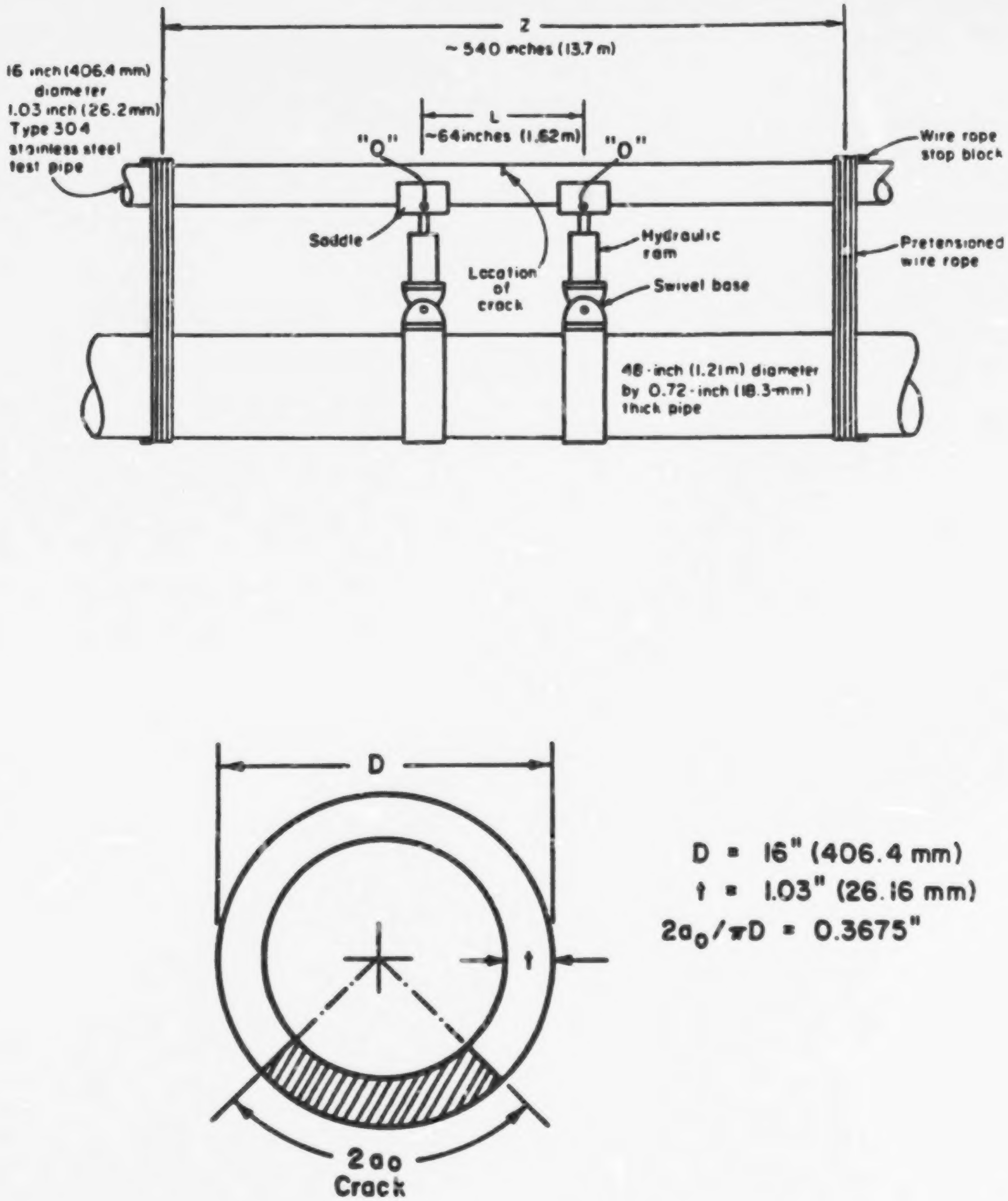
Z
~ 540 inches (13.7 m)
16 inch (406.4 mm) diameter 1.03 inch (26.2 mm) Type 304 stainless steel test pipe
L
~64 inches (1.62 m)
"O"
"O"
Wire rope stop block
Saddle
Hydraulic ram
Location of crack
Swivel base
Pretensioned wire rope
48-inch (1.21 m) diameter by 0.72-inch (18.3-mm) thick pipe
D
t
D = 16" (406.4 mm)
t = 1.03" (26.16 mm)
2a₀/πD = 0.3675"
2ao Crack

Figure 3.1 The apparatus and cracked pipe geometry for 16-inch (406.4-mm) nominal diameter pipe bending experiment.

T-4573-F3.1

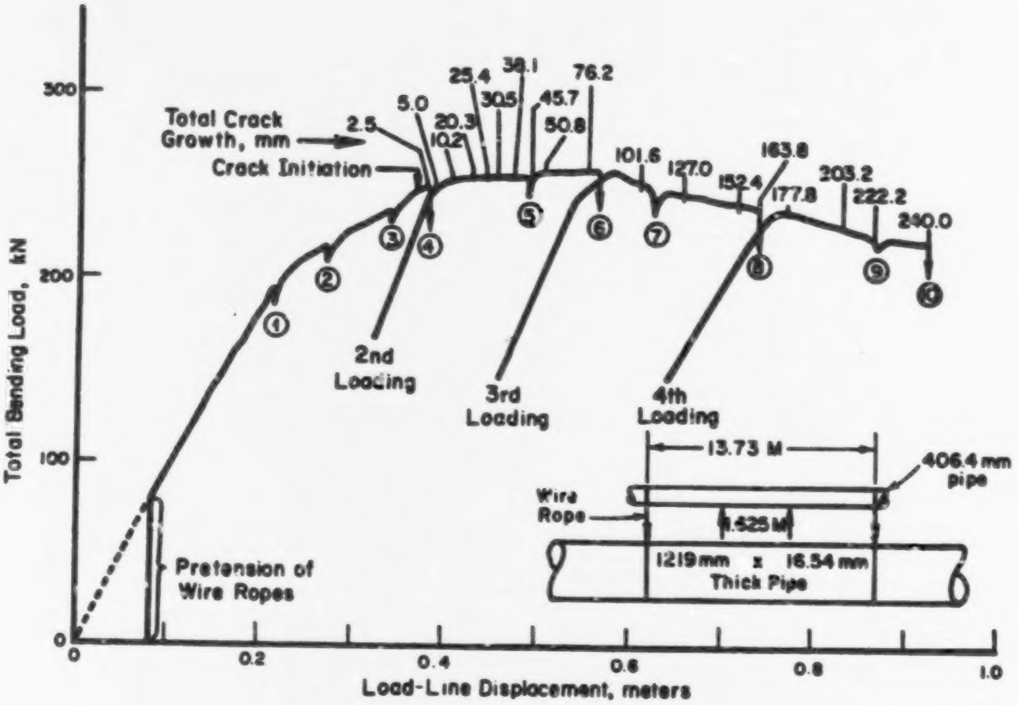

Figure 3.2 Bending load versus load-line displacement during experiment 8T (406.4-mm O.D. by 25.16-mm thick stainless steel pipe. Initial crack length = 484 mm).

T-4573-F3.2

78

BEST COPY AVAILABLE

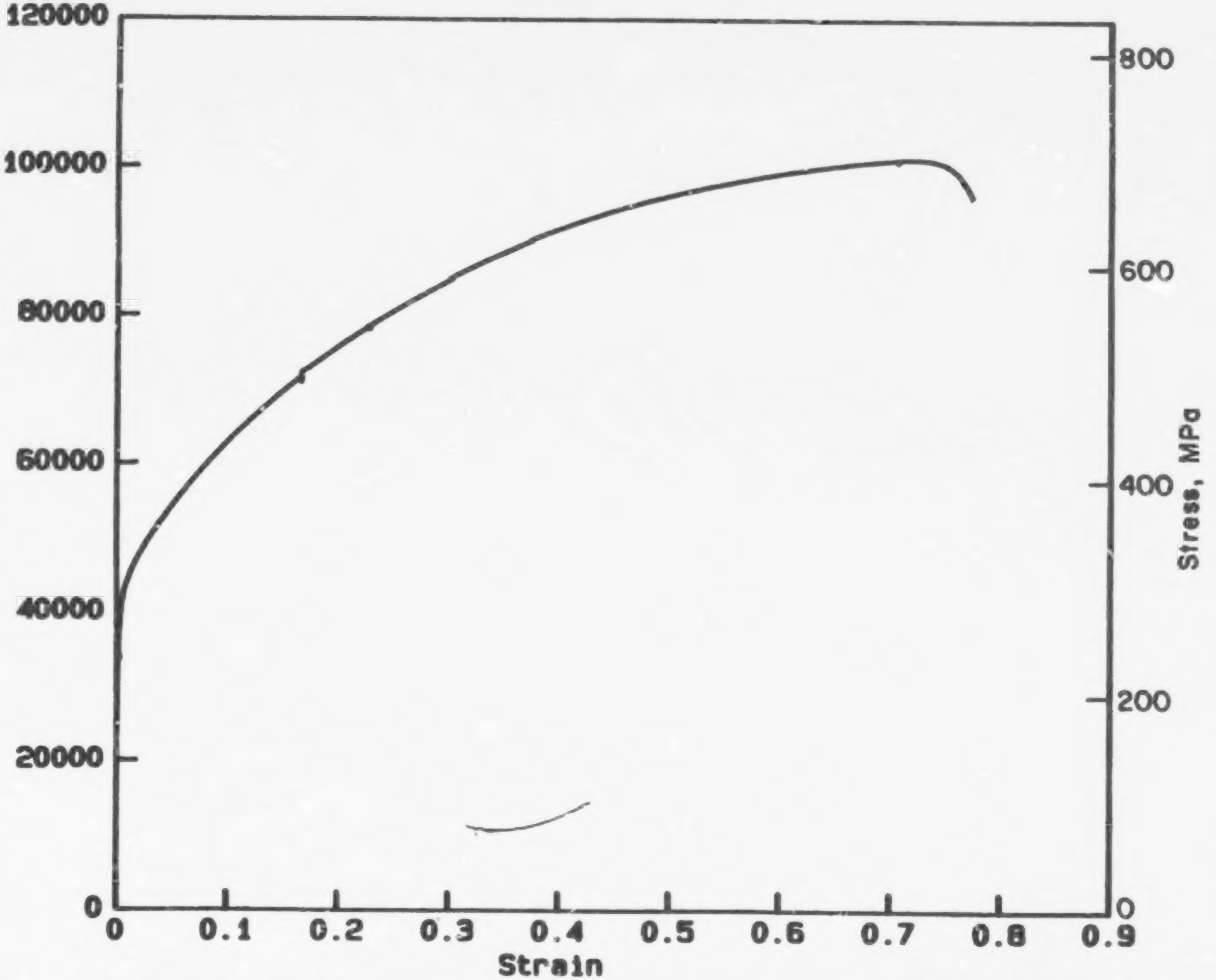

Figure 3.3 Longitudinal engineering stress versus strain curve for 16-inch (406.4-mm) diameter Type 304 stainless steel pipe material at room temperature.
T-4573-F3.3

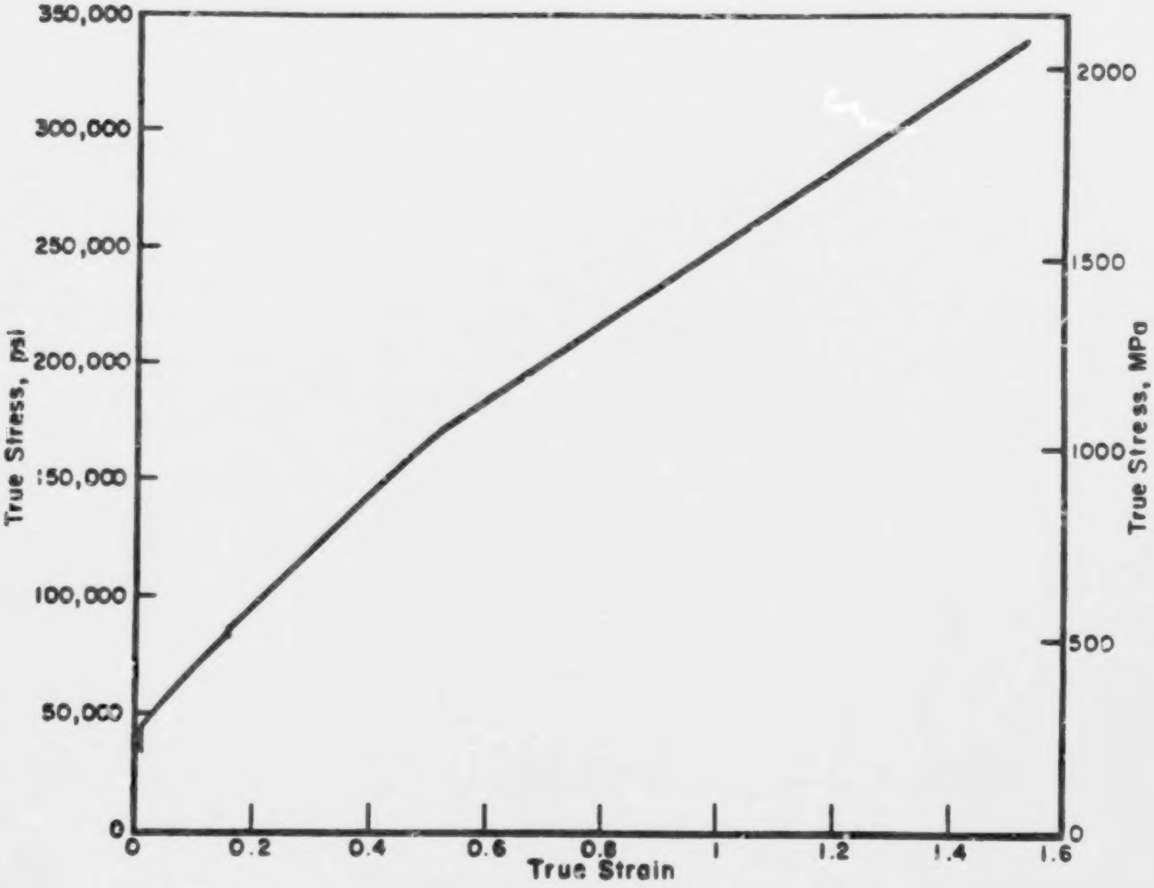

Figure 3.4 Longitudinal true stress-true strain curve for 16-inch (406.4-mm) diameter Type 304 stainless steel pipe material at room temperature (large straings).

T-4573-F3.4

80

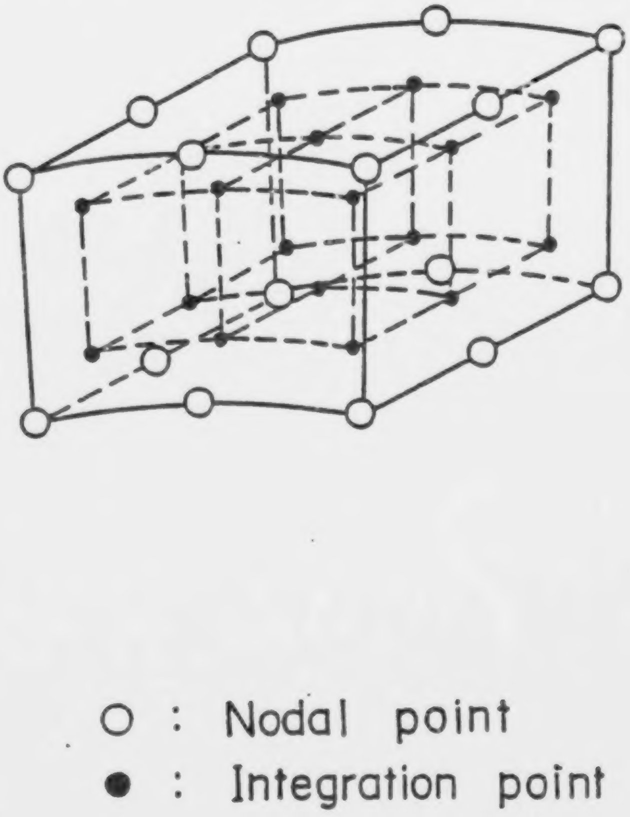
○ : Nodal point
● : Integration point

Figure 3.1.1 Finite elements used in calculation (Participant 1).

T-4573-F3.1.1

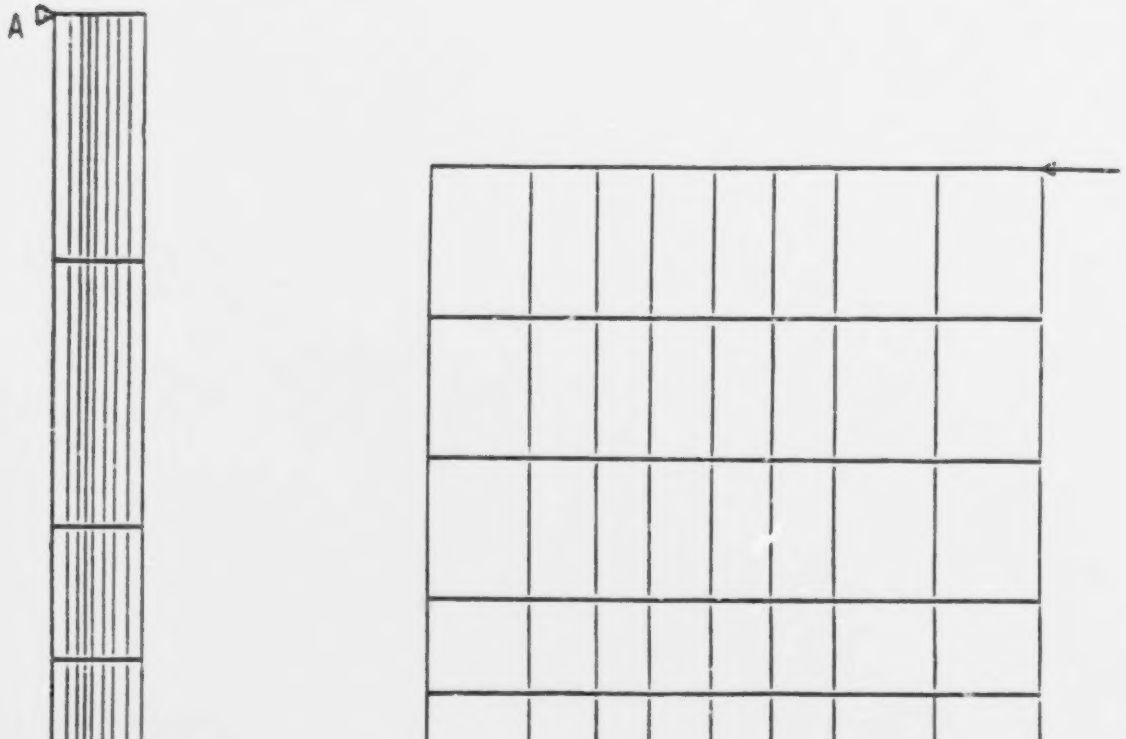
A
B
CRACK GROWTH RANGE
---- RING FOR J-INTEGRAL EVALUATION

Figure 3.1.2 Finite element subdivision (extended in circumferential direction) (Participant 1).

T-4573-F3.1.2

82

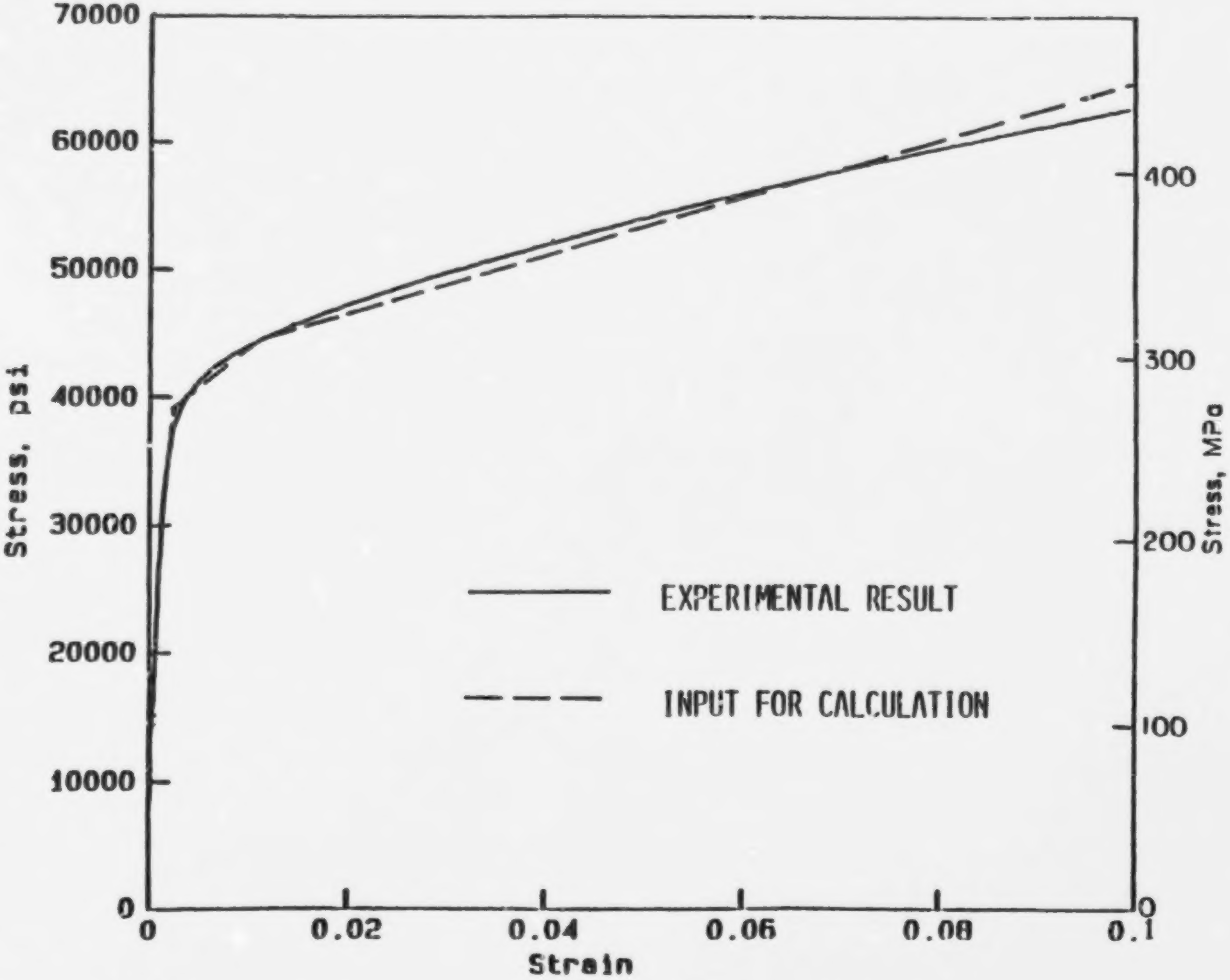

Figure 3.1.3 Stress-strain curve used in calculation. (Participant 1.)

T-4573-F3.1.3

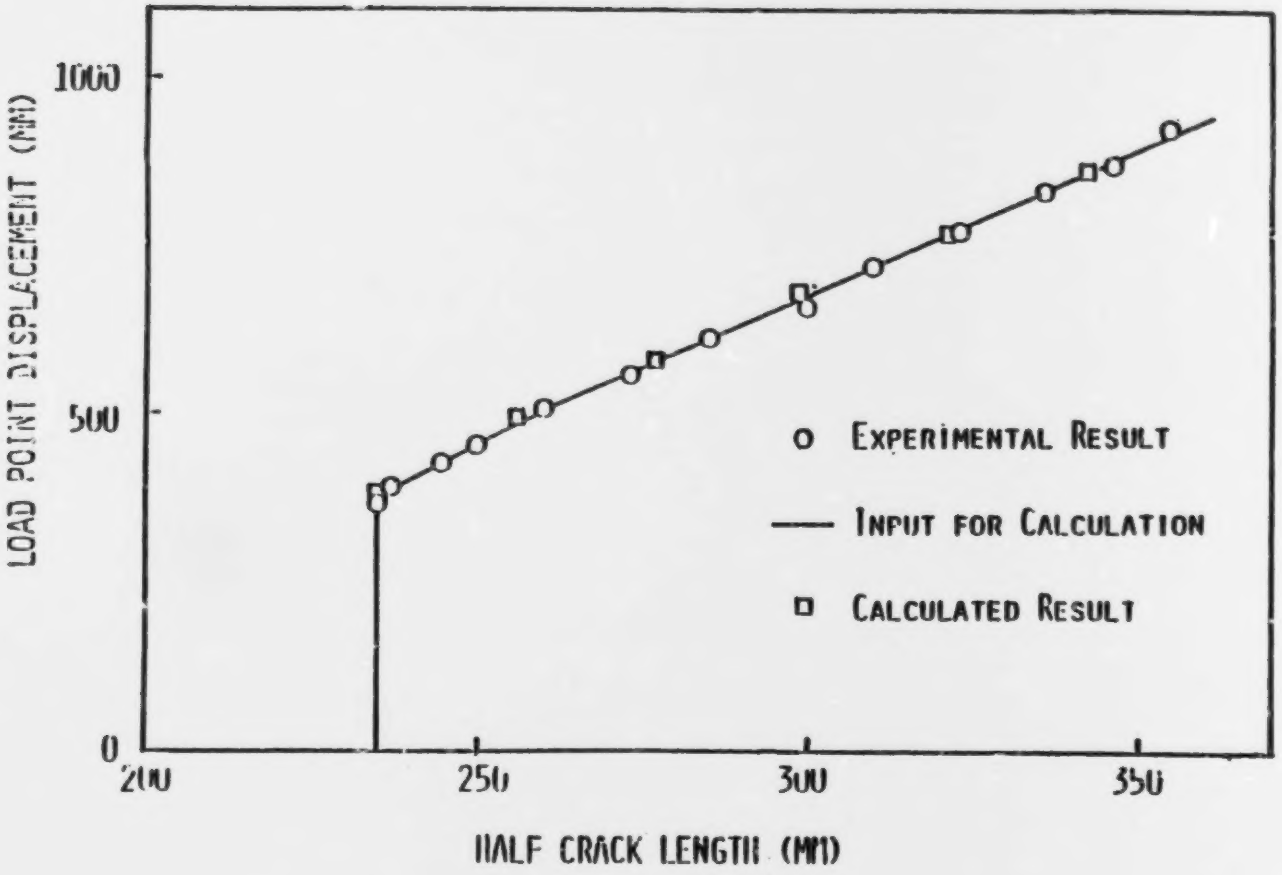

Figure 3.1.4 Relationship between crack length and load-point displacement. (Participant 1.)

T-4573-F3.1.4

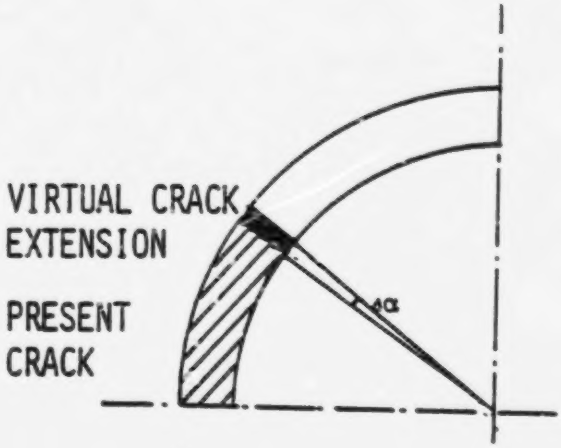
VIRTUAL CRACK EXTENSION
PRESENT CRACK
Δα

$\Delta\alpha = 10^{-7}$ RADIAN

Figure 3.1.5 Virtual crack extension for J-integral evaluation (Participant 1).

T-4573-F3.1.5

85

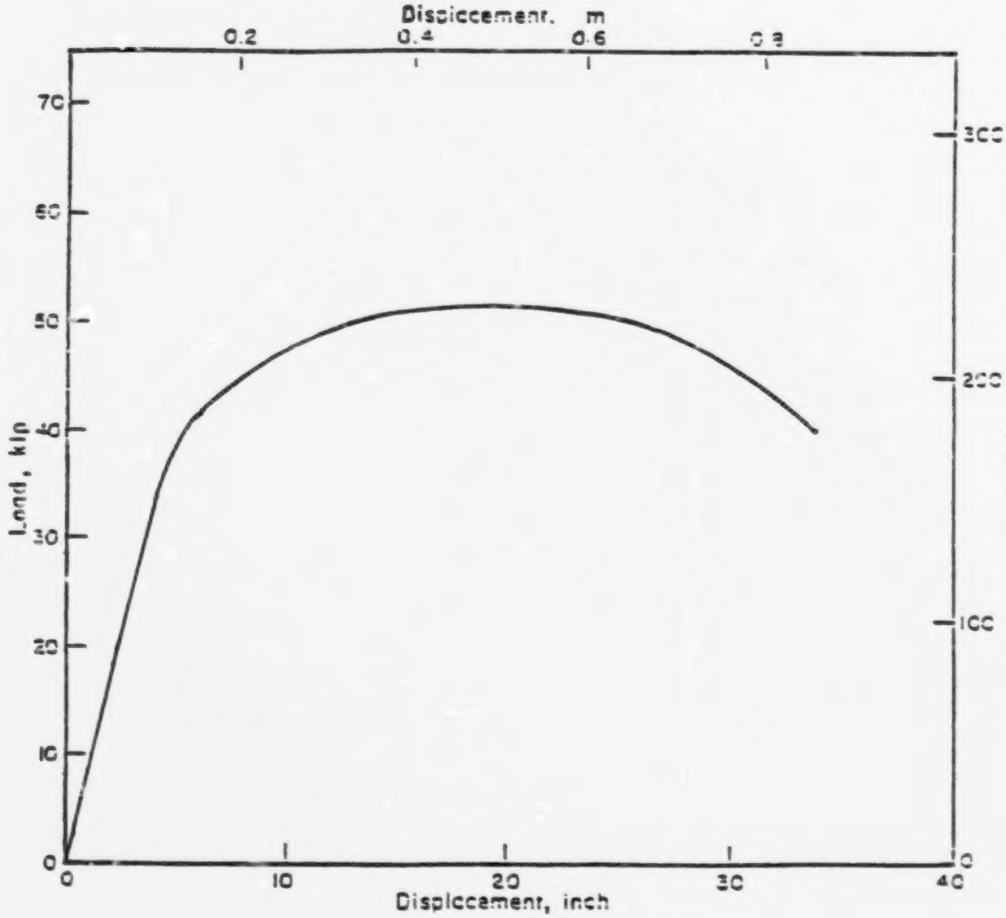

Figure 3.1.6 Total load versus load point displacement curve (Participant 1).

T-4573-F3.1.6

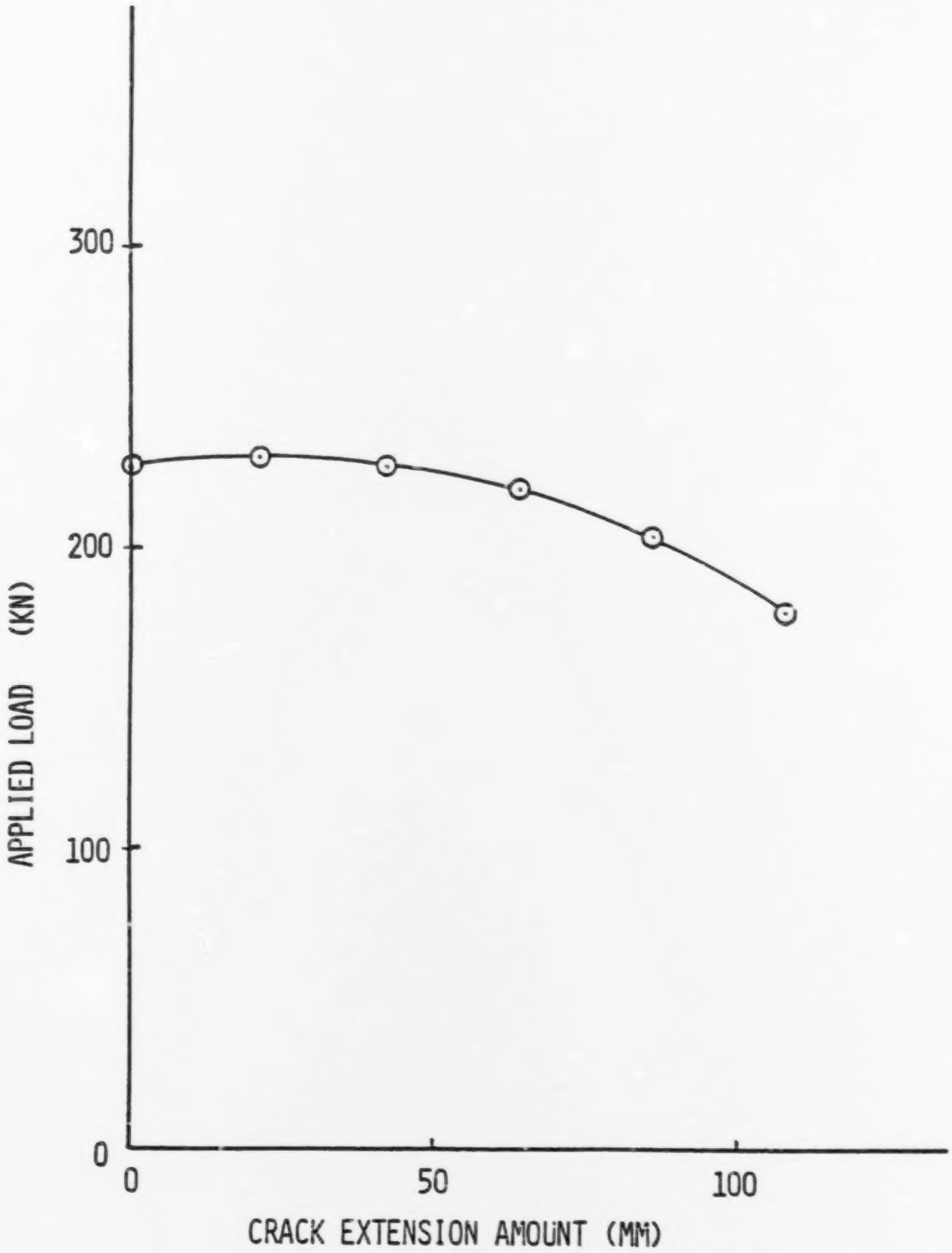

Figure 3.1.7 Total load versus crack extension curve (Participant 1).

T-4573-F3.1.7

87

BEST COPY AVAILABLE

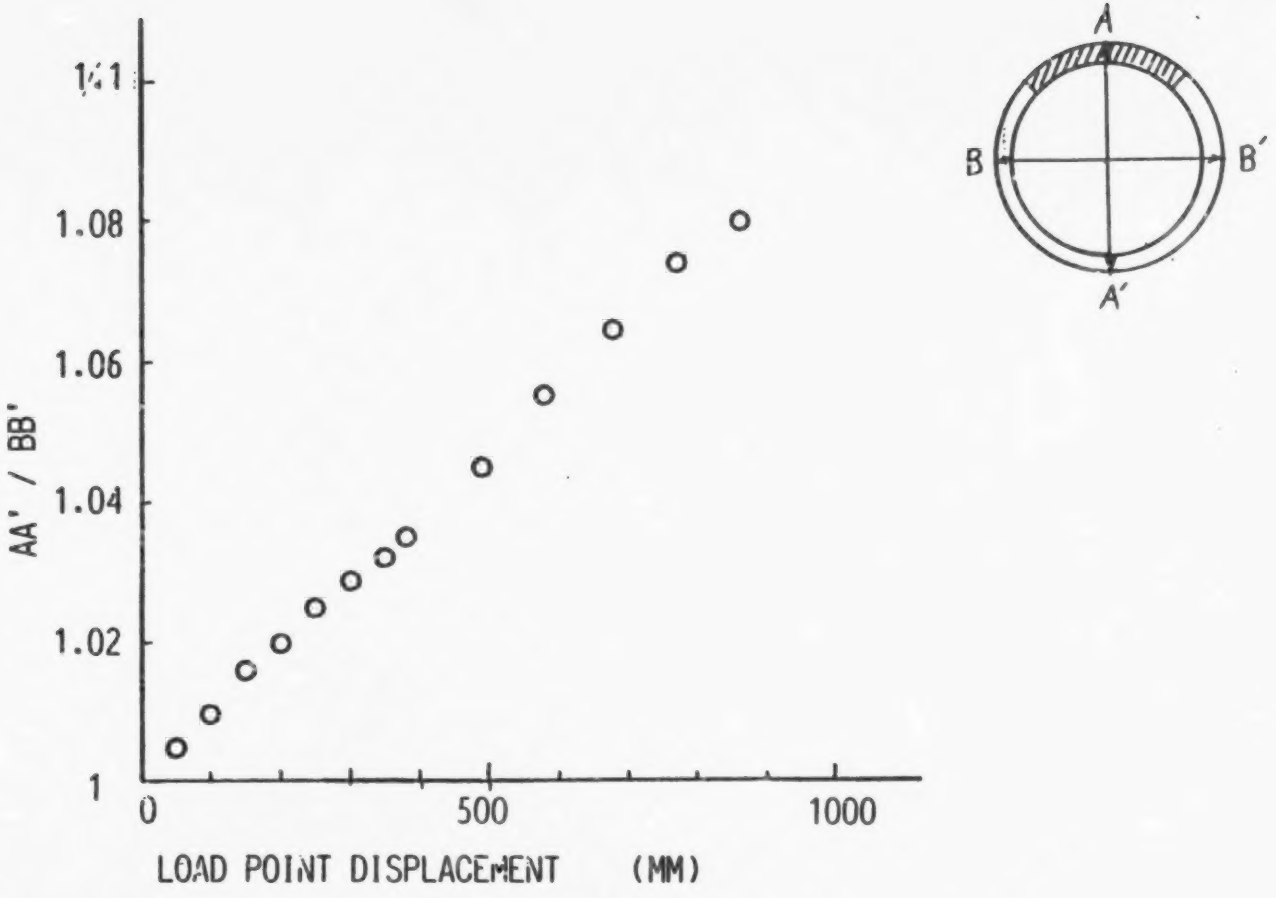

Figure 3.1.8 Ovalization factor versus load-point displacement.
(Participant 1.)

T-4573-F3.1.8

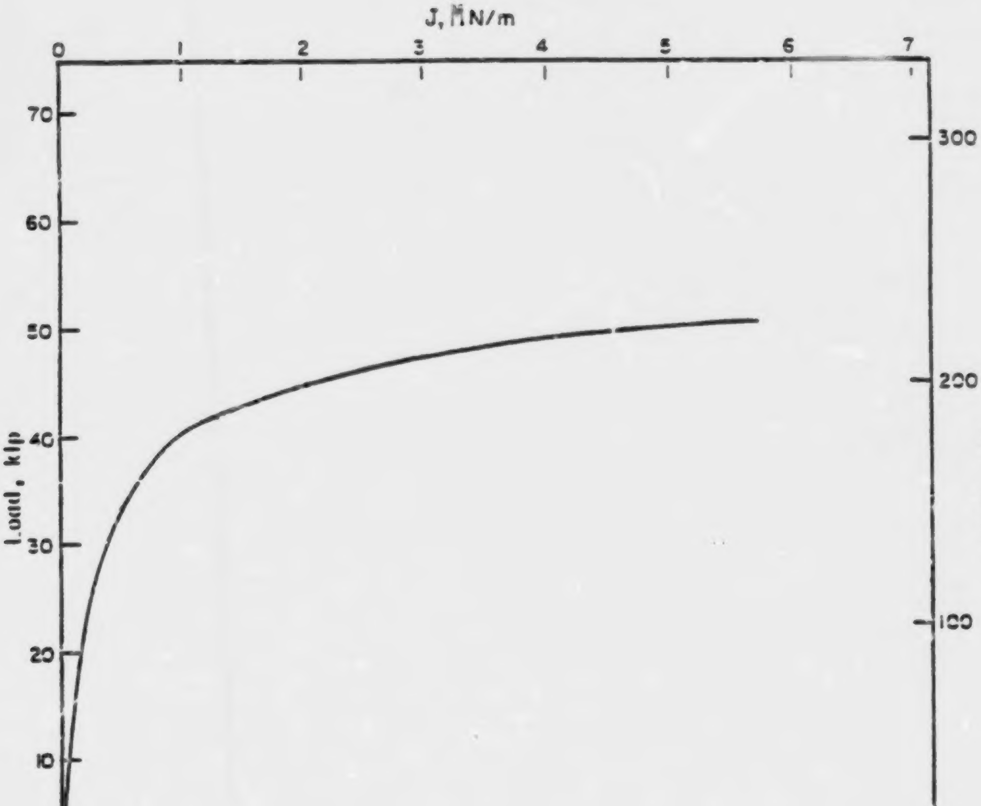

Figure 3.1.9 Total load versus J-integral curve (Participant 1).

T-4573-F3.1.9

89

BEST COPY AVAILABLE

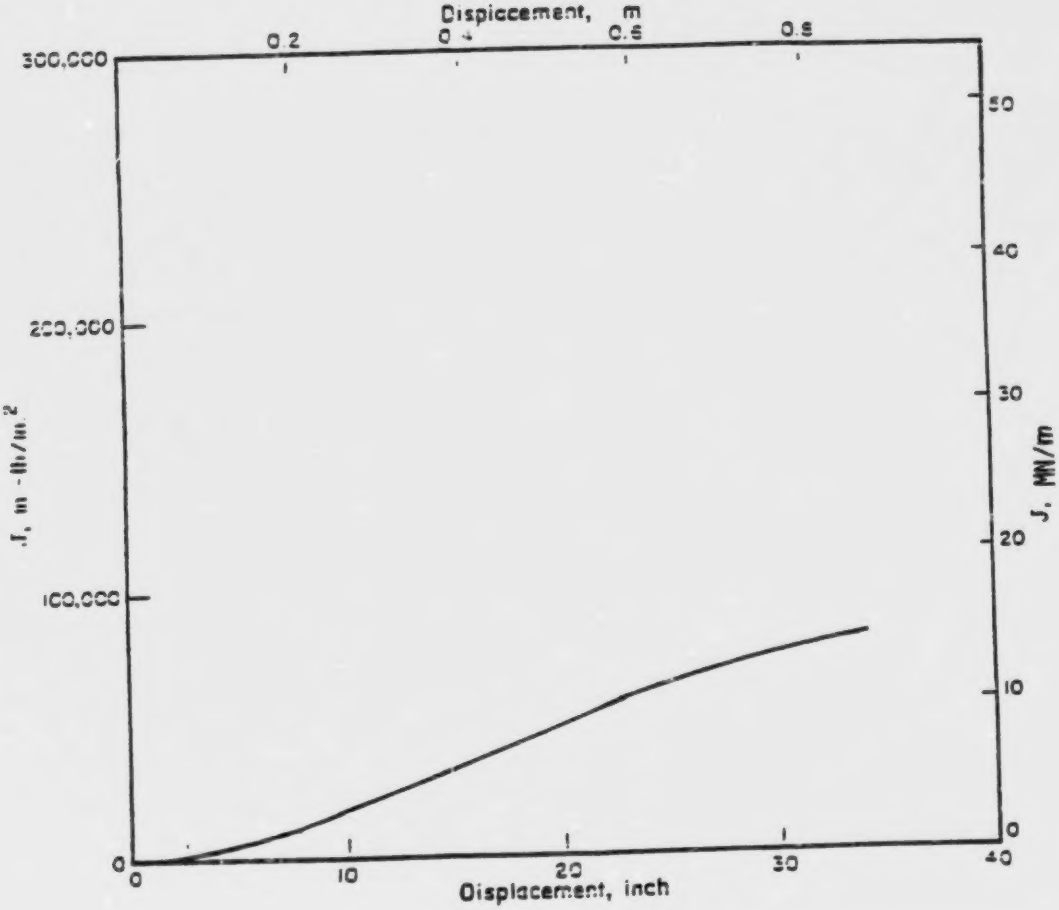

Figure 3.1.10 J-integral versus load-point displacement curve (Participant 1).

T-4573-F3.1.10

90

BEST COPY AVAILABLE

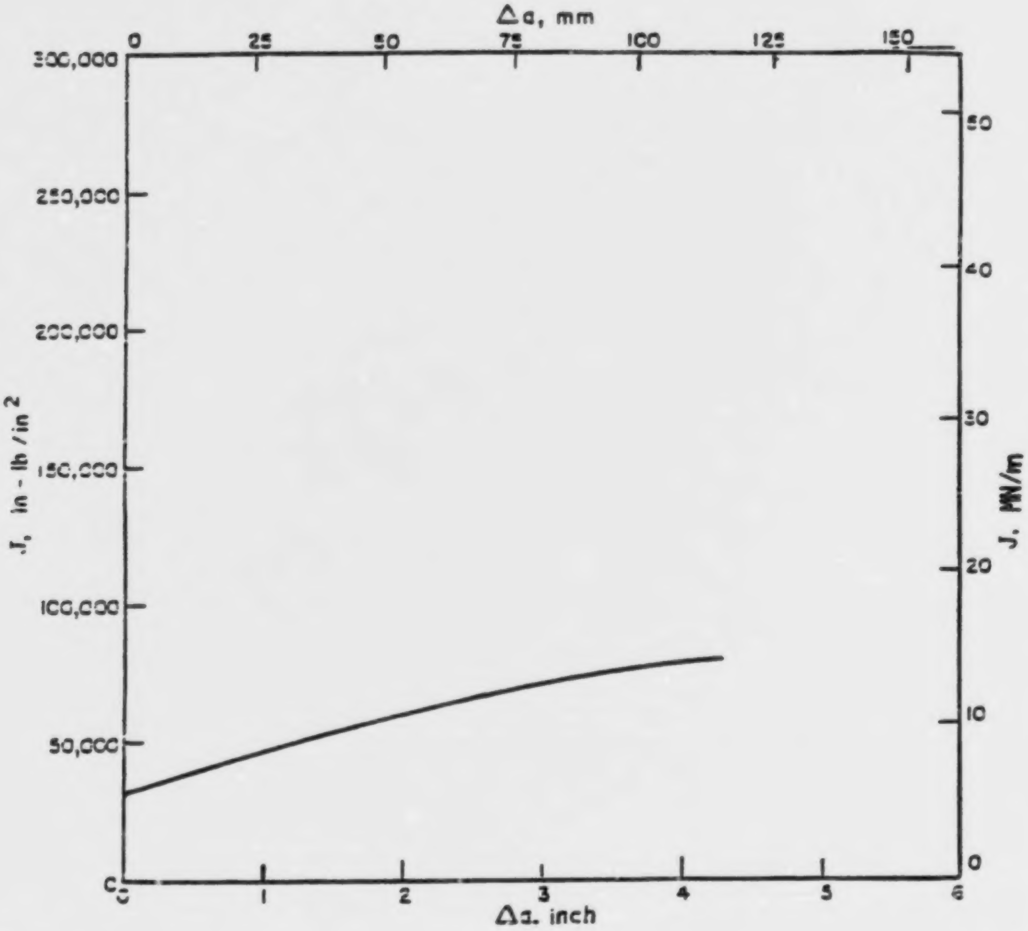

Figure 3.1.11 J-integral resistance curve (Participant 1).

T-4573-F3.1.11

BEST COPY AVAILABLE

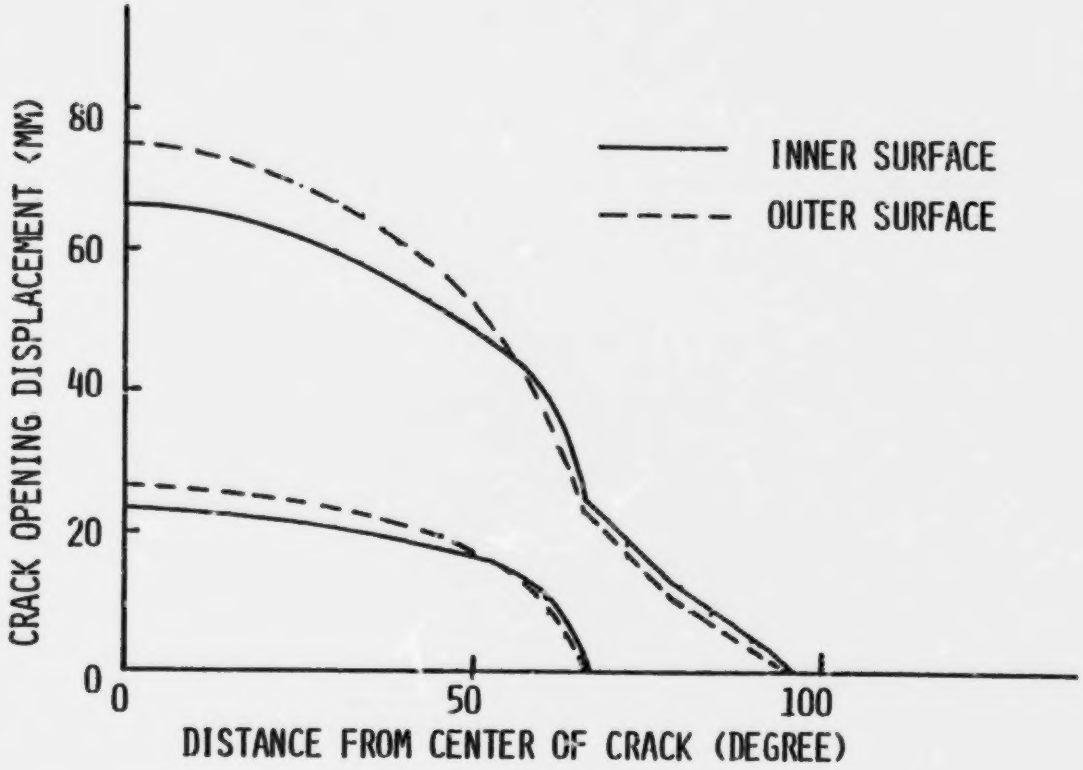

Figure 3.1.12 Crack opening profile before and after crack growth. (Participant 1.)

T-4573-F3.1.12

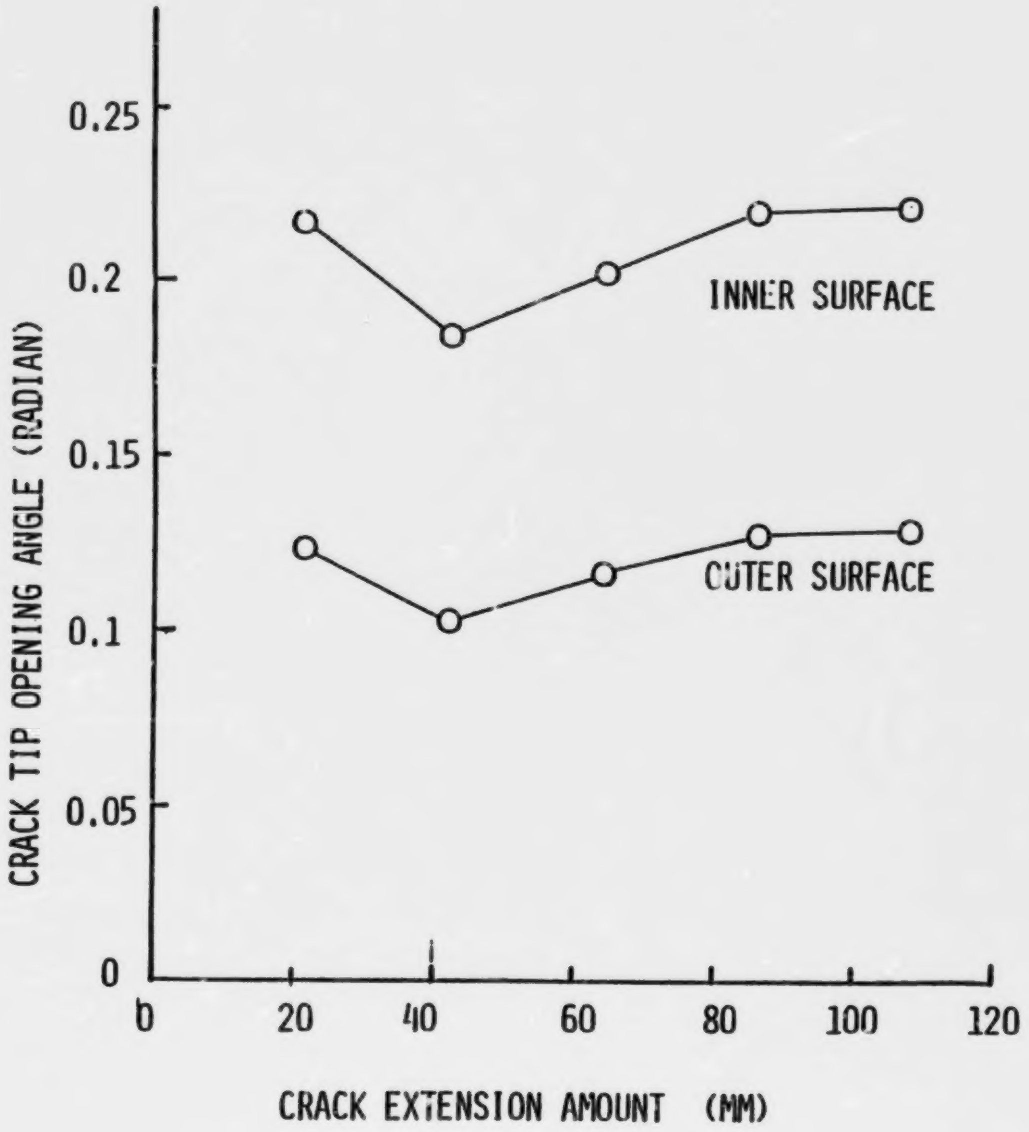

Figure 3.1.13 Variation of crack tip opening angle with crack extension (Participant 1).

T-4573-F3.1.13

BEST COPY AVAILABLE

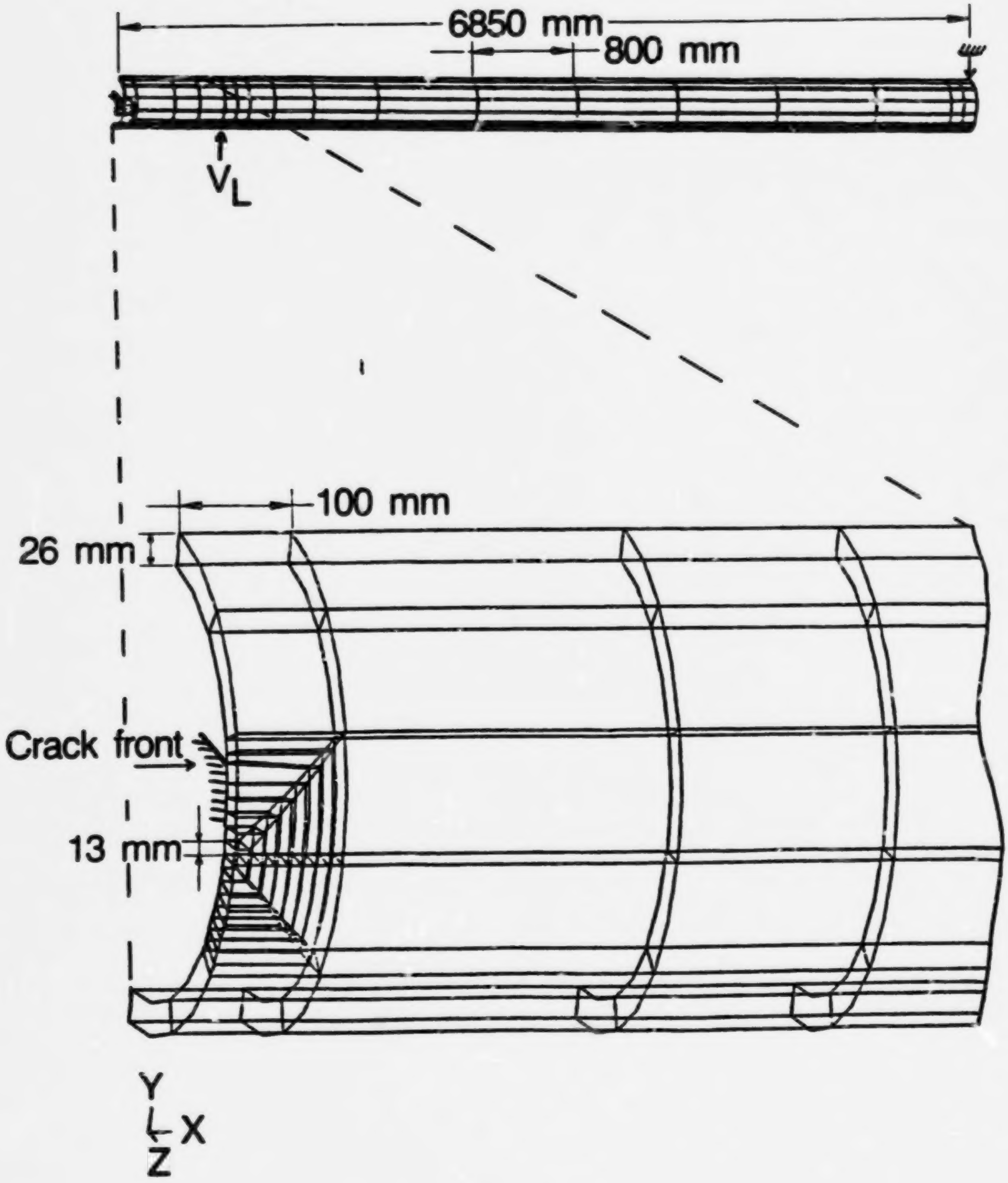
6850 mm
800 mm
V_L
100 mm
26 mm
Crack front
13 mm
Y
X
Z

Figure 3.2.1 Pipe: Three-dimensional FE-model of the pipe (Participant 2).

T-4573-F3.2.1

94

BEST COPY AVAILABLE

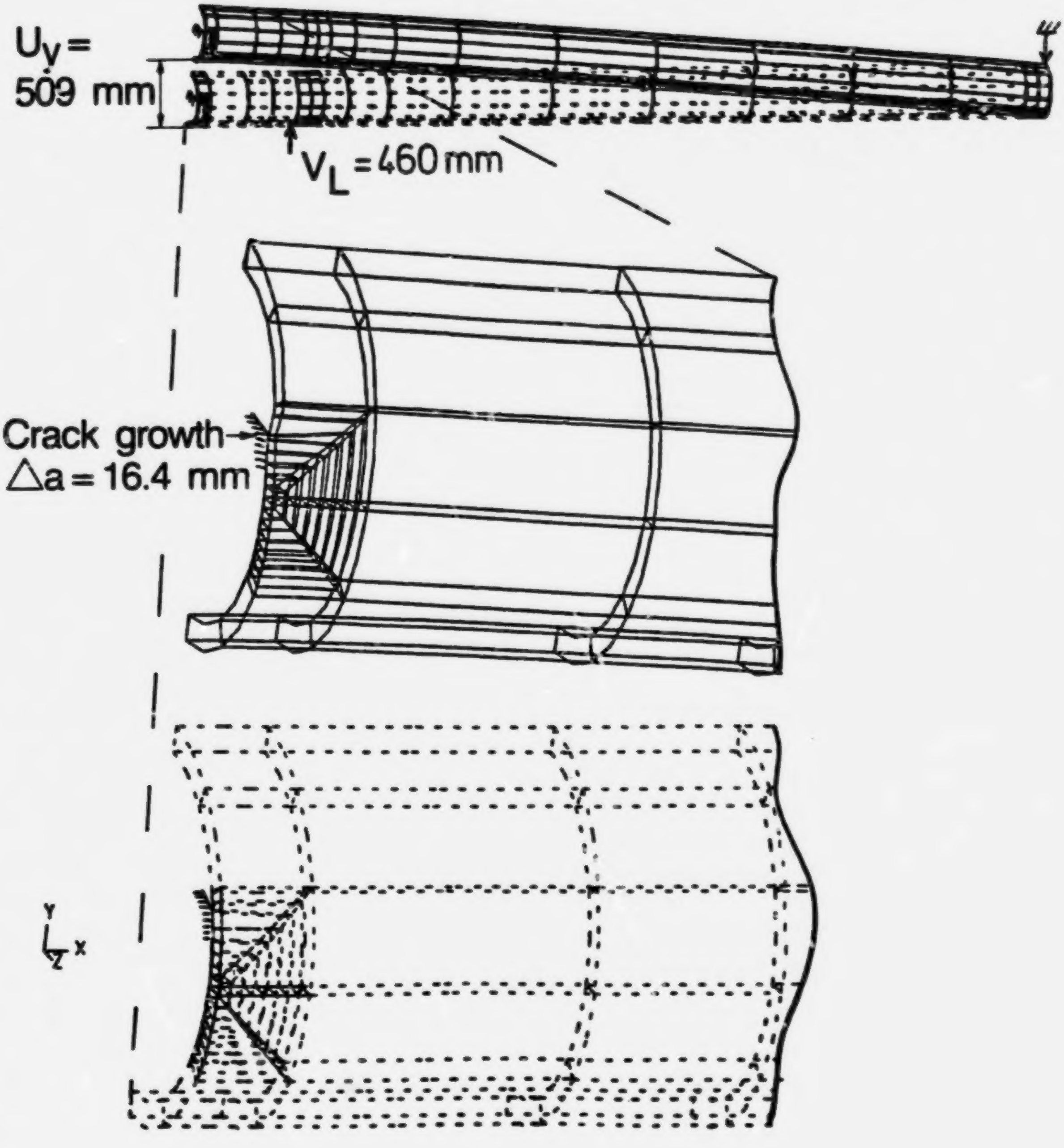
U_y =
509 mm
V_L = 460 mm
Crack growth
$\triangle a$ = 16.4 mm
Y
Z
X

Figure 3.2.2 Deformed pipe with 0.65 inch (16.4 mm) of crack growth (Participant 2).

T-4573-F3.2.2

95

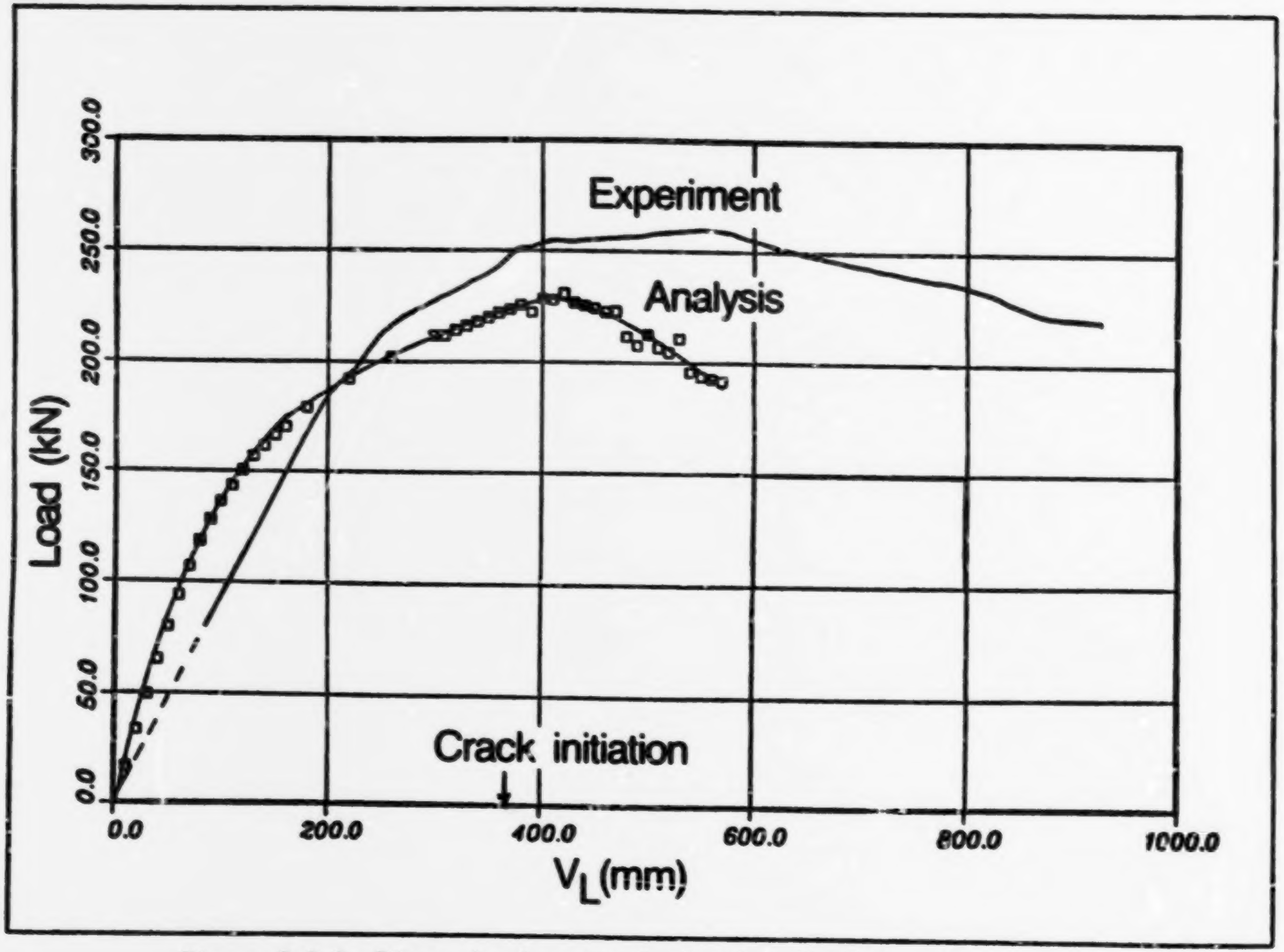

Figure 3.2.3 Pipe: Load versus load-point displacement. (Participant 2.)

T-4573-F3.2.3

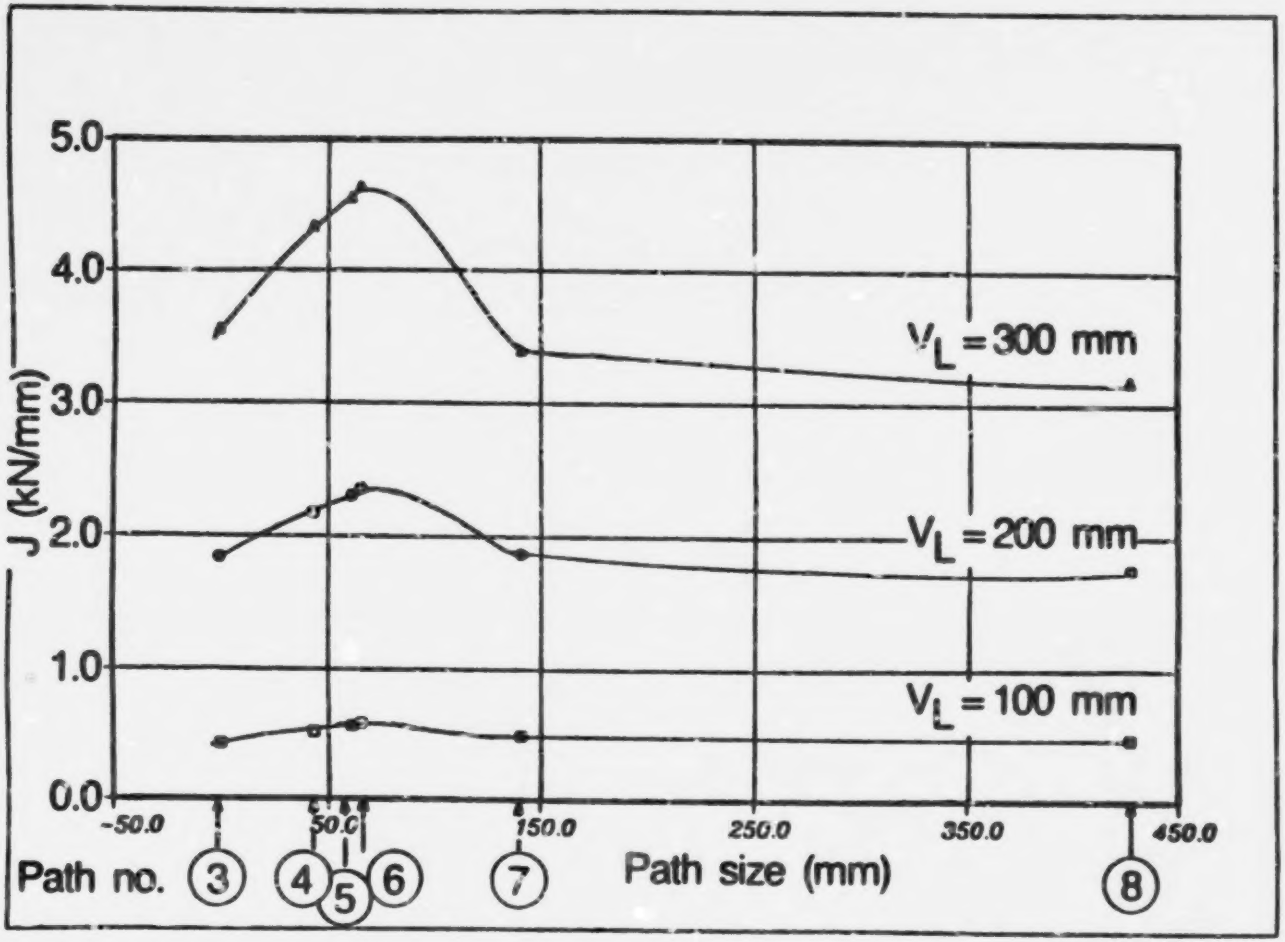

Figure 3.2.5 Pipe: J-integral versus path size. (Participant 2.)

T-4573-F3.2.5

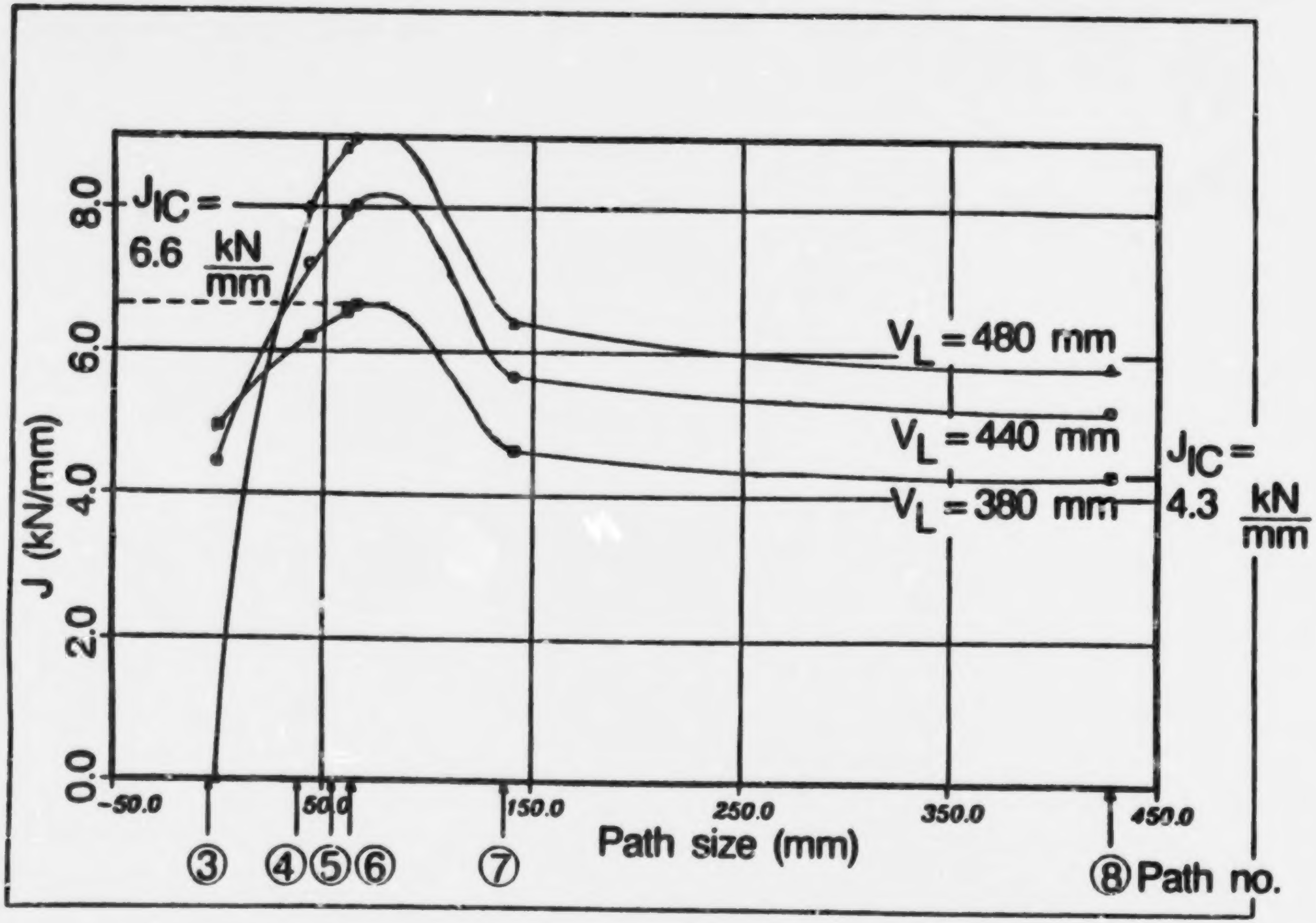

Figure 3.2.6 Pipe: J-integral versus path size. (Participant 2.)

T-4573-F3.2.6

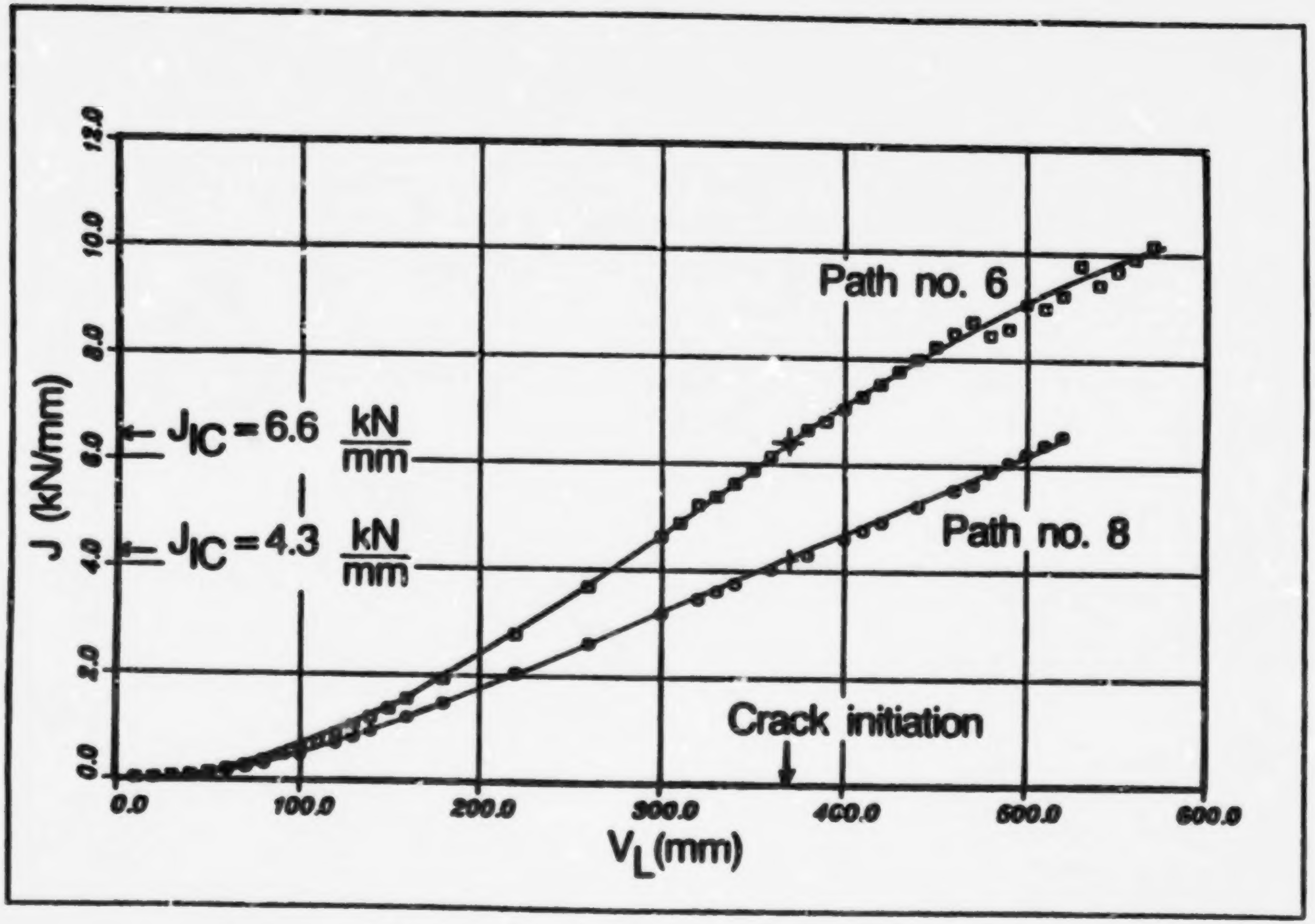

Figure 3.2.7 Pipe: J-integral versus load-point displacement. (Participant 2.)

T-4573-F3.2.7

/100

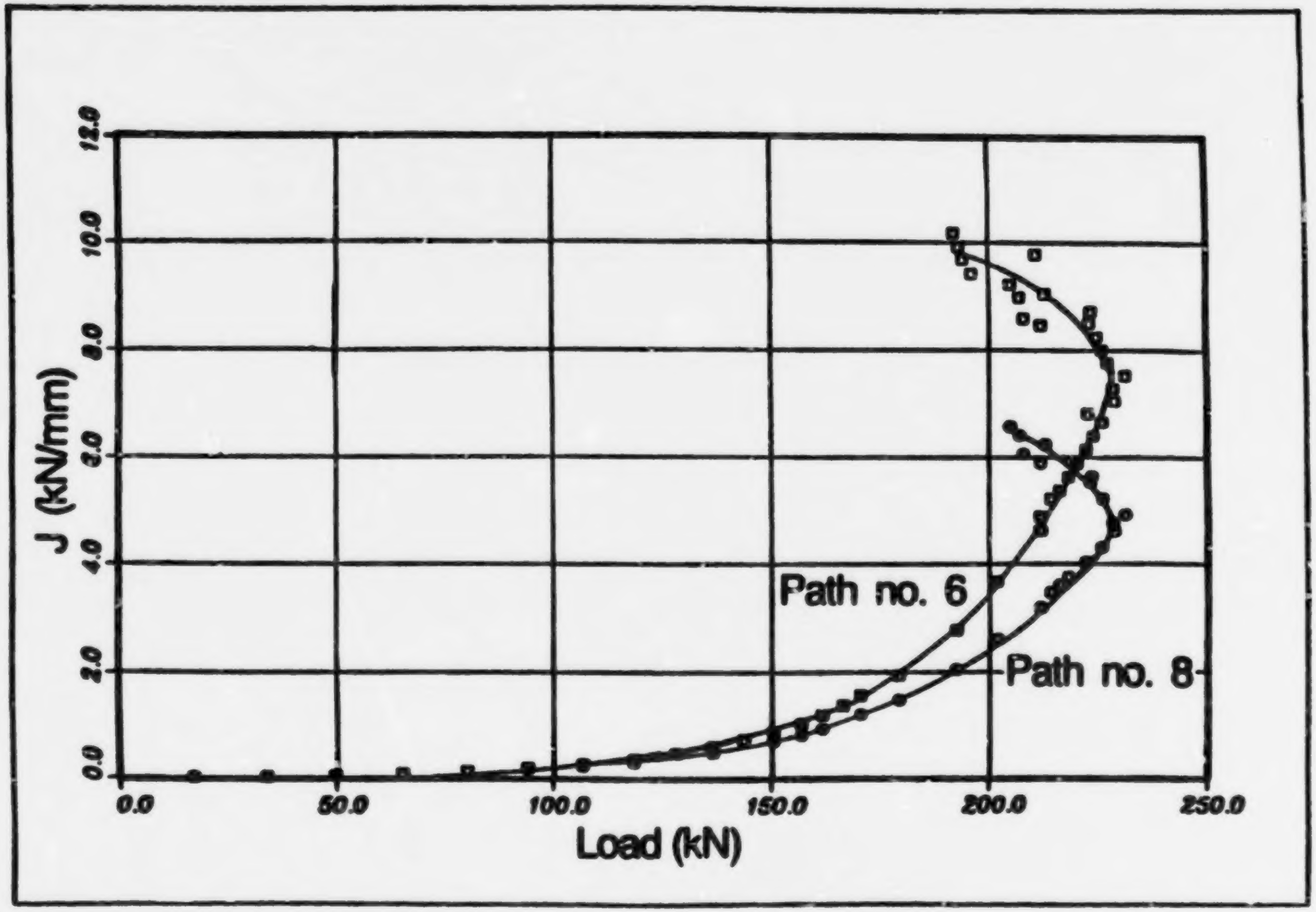

Figure 3.2.8 Pipe: J-integral versus load. (Participant 2.)

T-4573-F3.2.8

101

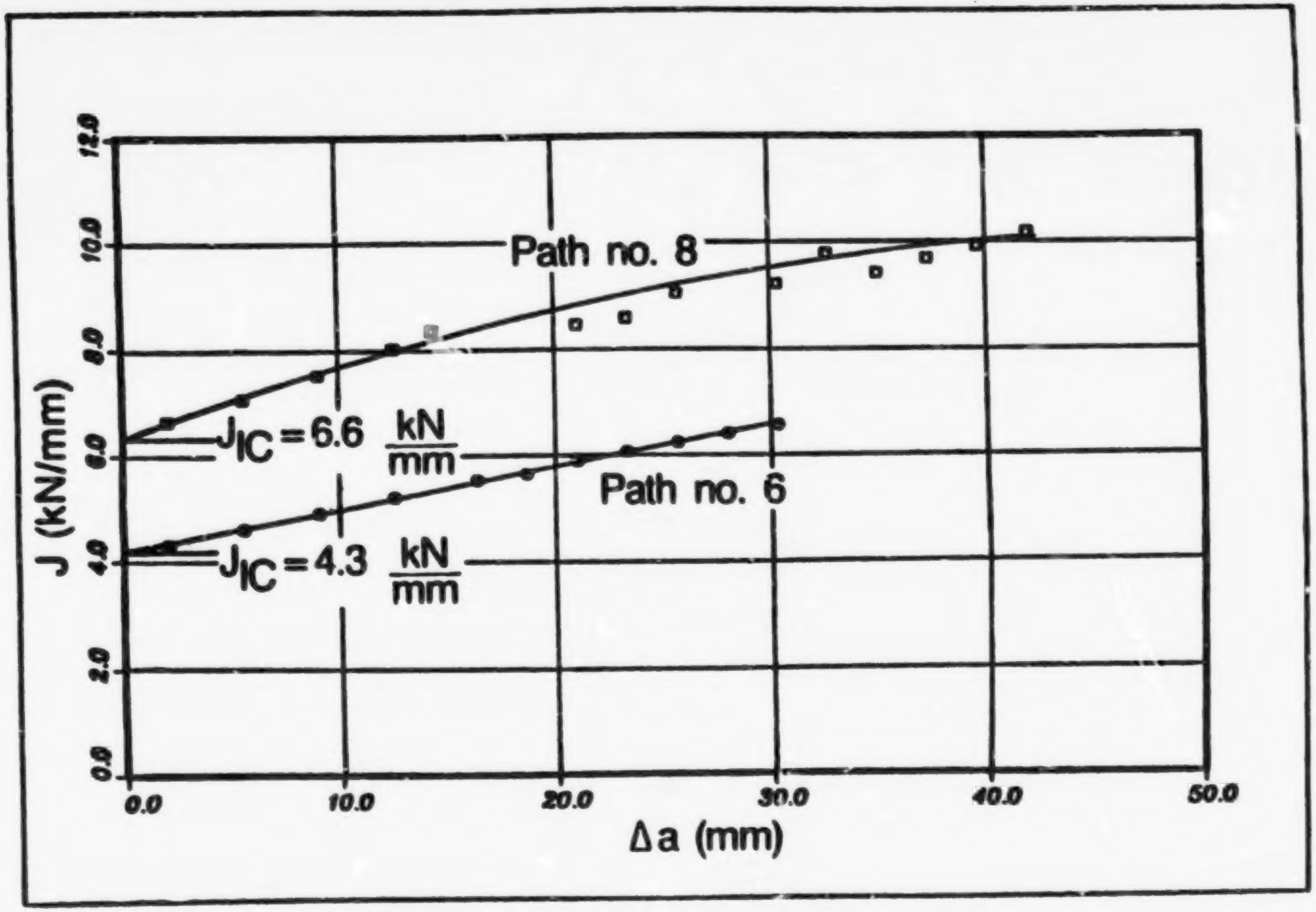

Figure 3.2.9 Pipe: Calculated crack resistance curve (J_R).
(Participant 2.)

T-4573-F3.2.9

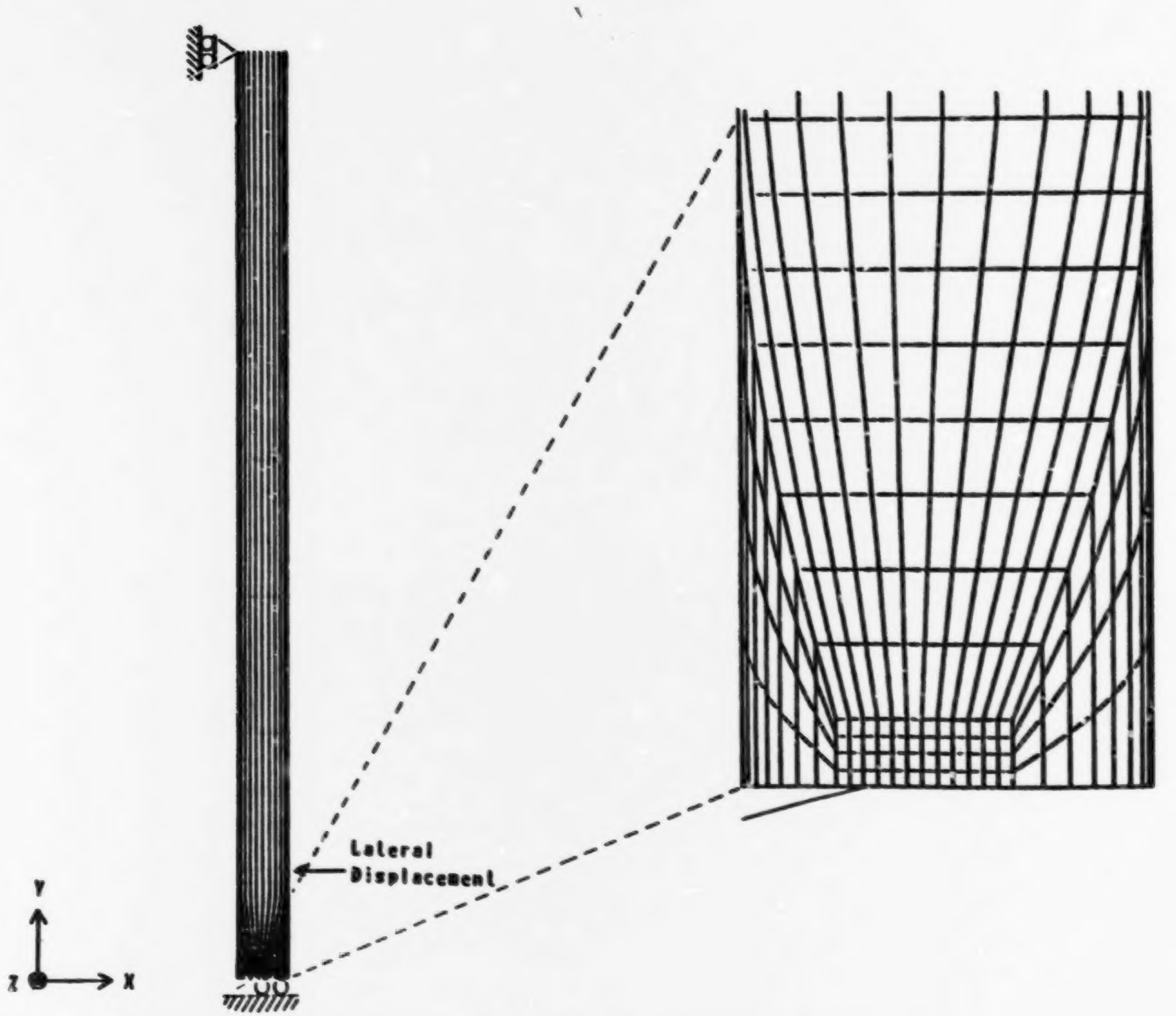
Lateral
Displacement
Y
X
Z

Figure 3.3.1 Analytical model and boundary conditions. (Participant 3.)

T-4573-F3.3.1

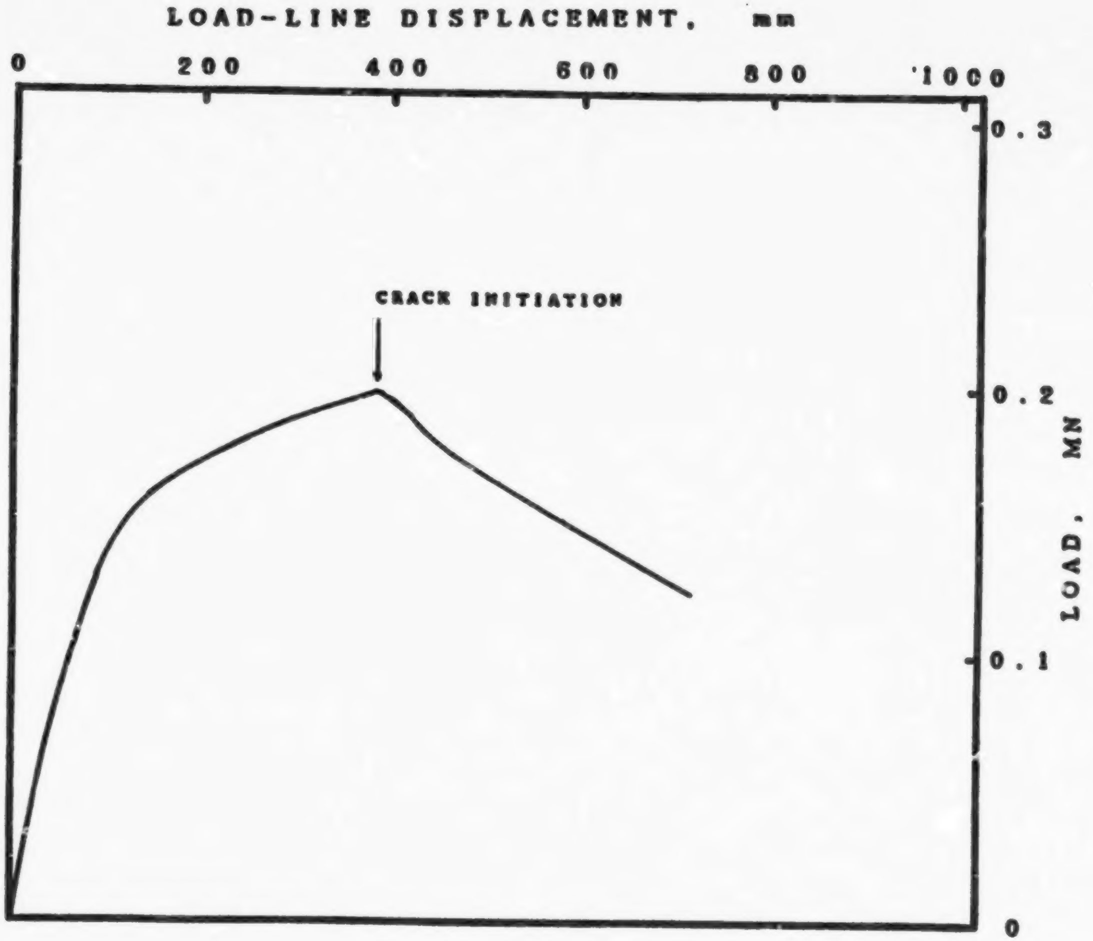

Figure 3.3.2 Load versus load-point displacement curve. (Participant 3.)

T-4573-F3.3.2

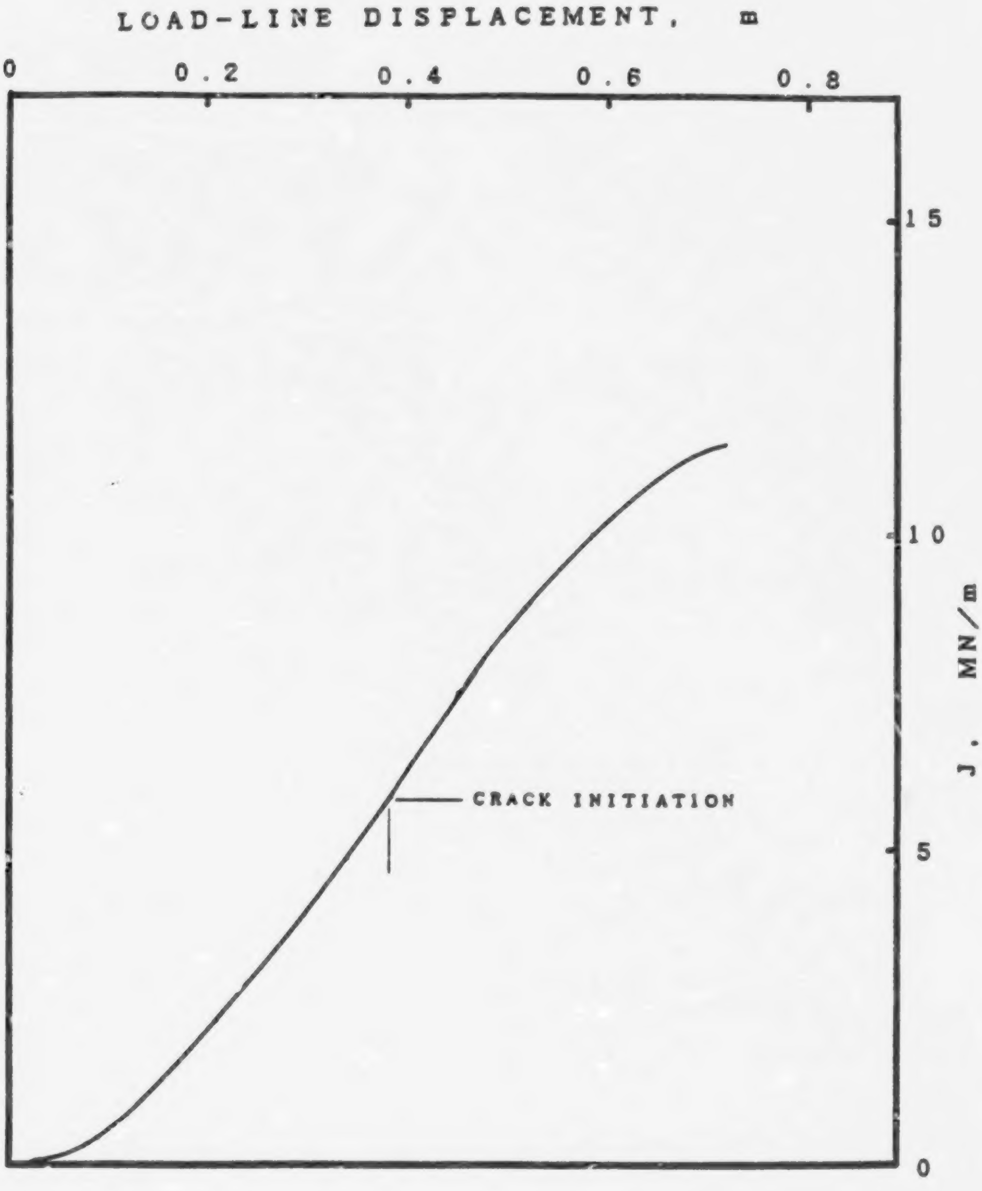

Figure 3.3.3 The J-integral versus load-point-displacement curve (Participant 3).

T-4573-F3.3.3

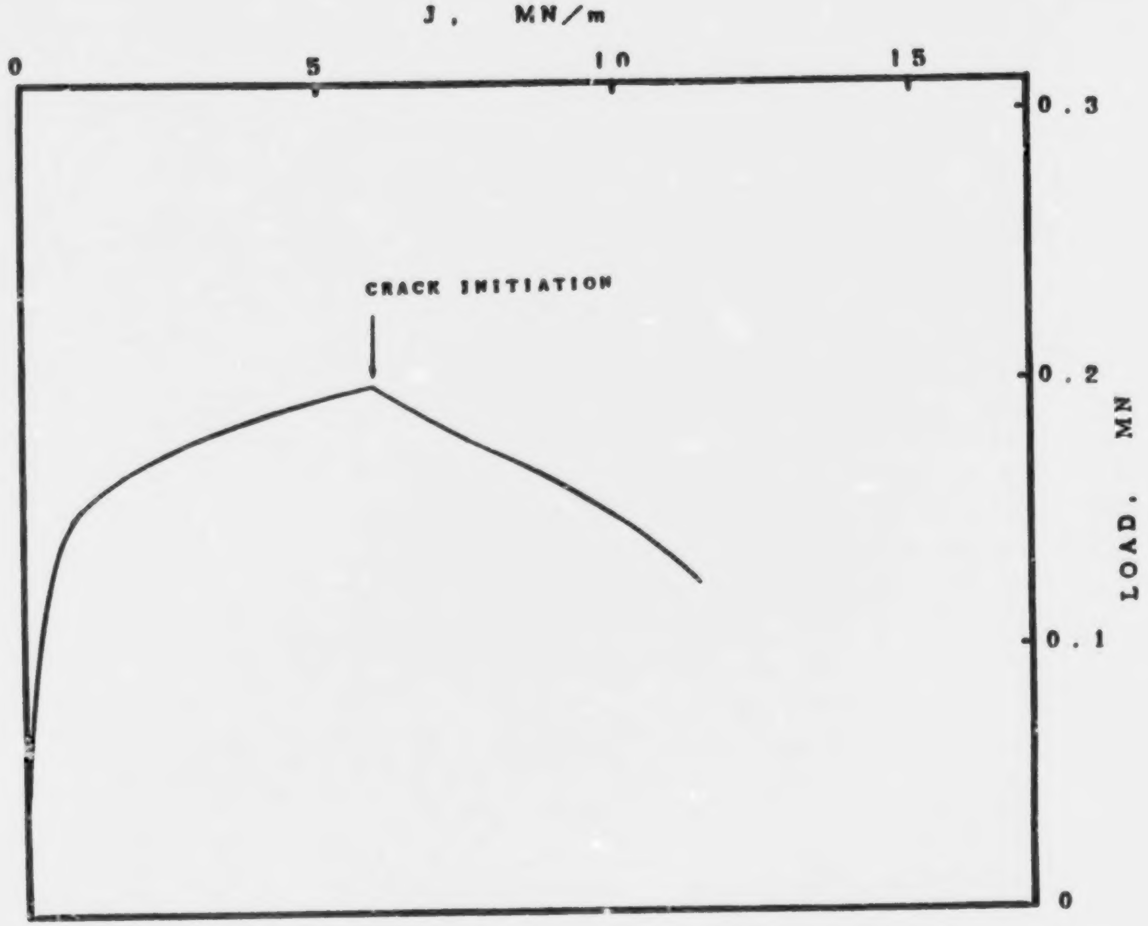

Figure 3.3.4 The J-integral versus load curve.
(Participant 3.)

T-4573-F3.3.4

106

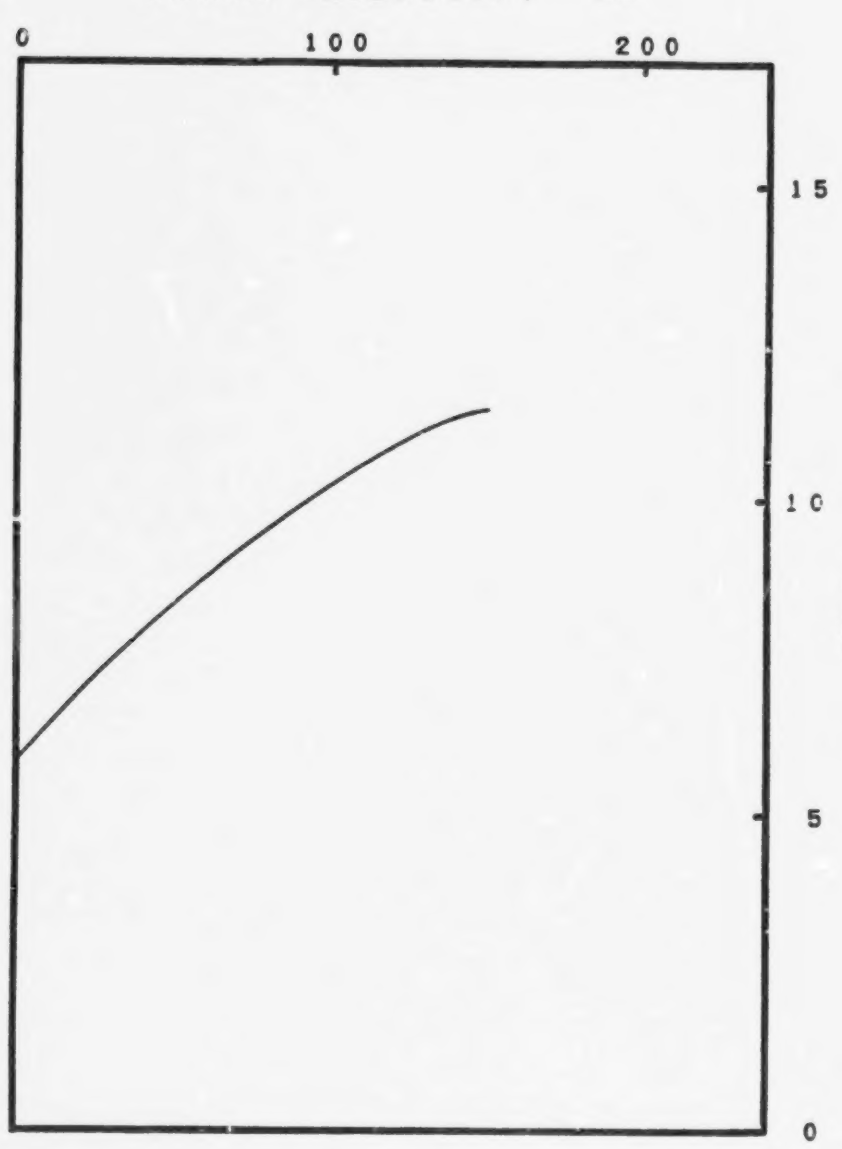

Figure 3.3.5 The J-integral versus crack extension curve (Participant 3).

T-4573-F3.3.5

107

BEST COPY AVAILABLE

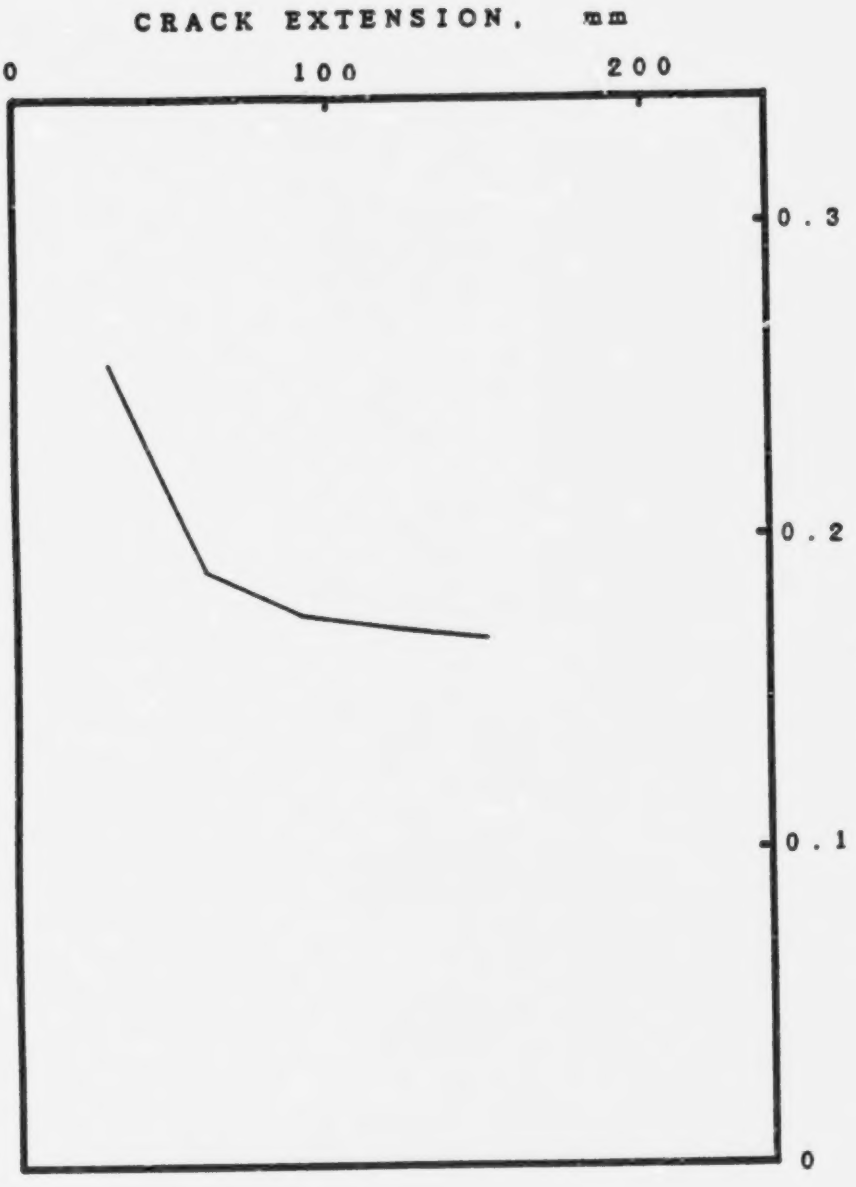

Figure 3.3.6 Crack-tip-opening angle versus crack extension curve (Participant 3).

T-4573-F3.3.6

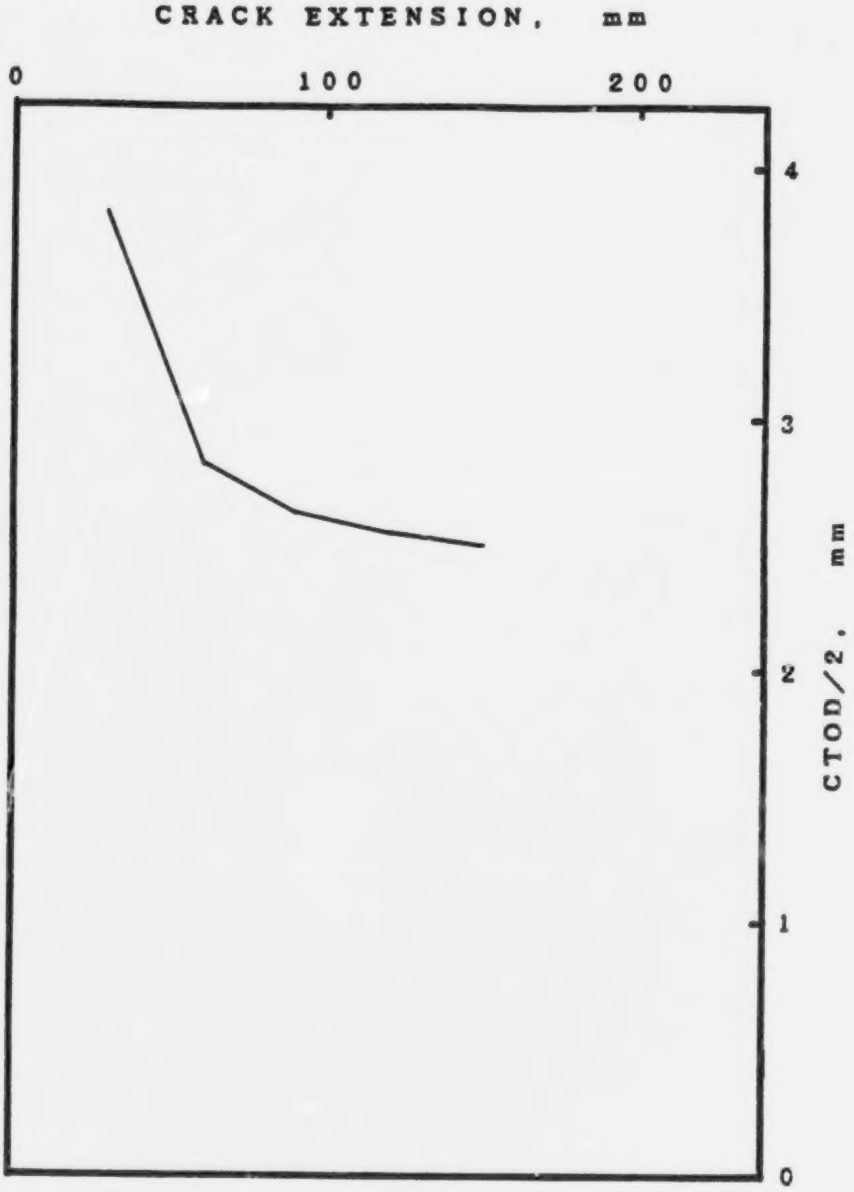

Figure 3.3.7 Crack-tip-opening displacement versus crack extension curve (Participant 3).

T-4573-F3.3.7

109

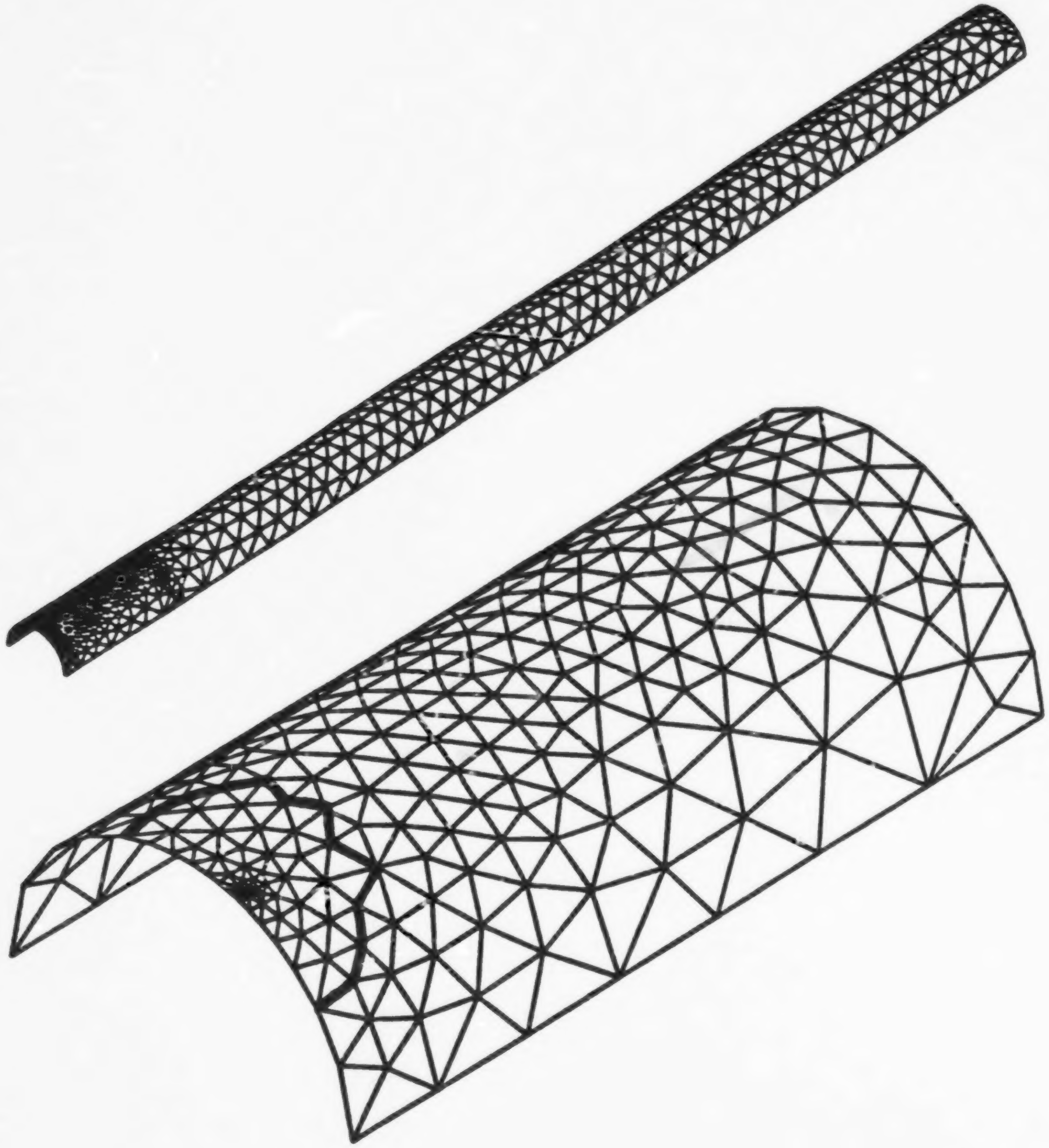

Figure 3.4.1 Shell finite element model (Participant 4).

T-4573-F3.4.1

BEST COPY AVAILABLE

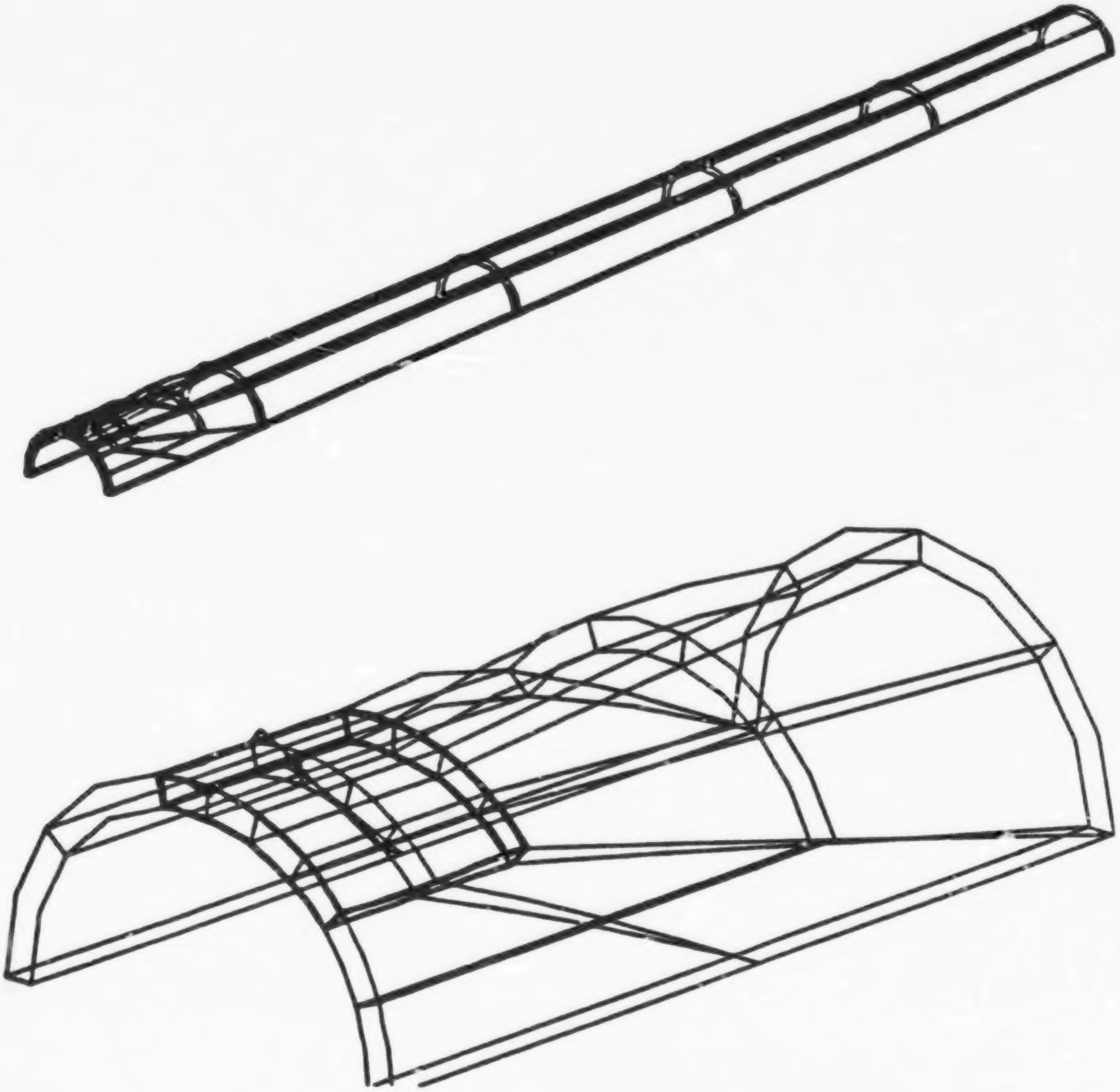

Figure 3.4.2 Twenty-node brick (3-dimension) finite element model (Participant 4).

T-4573-F3.4.2

///

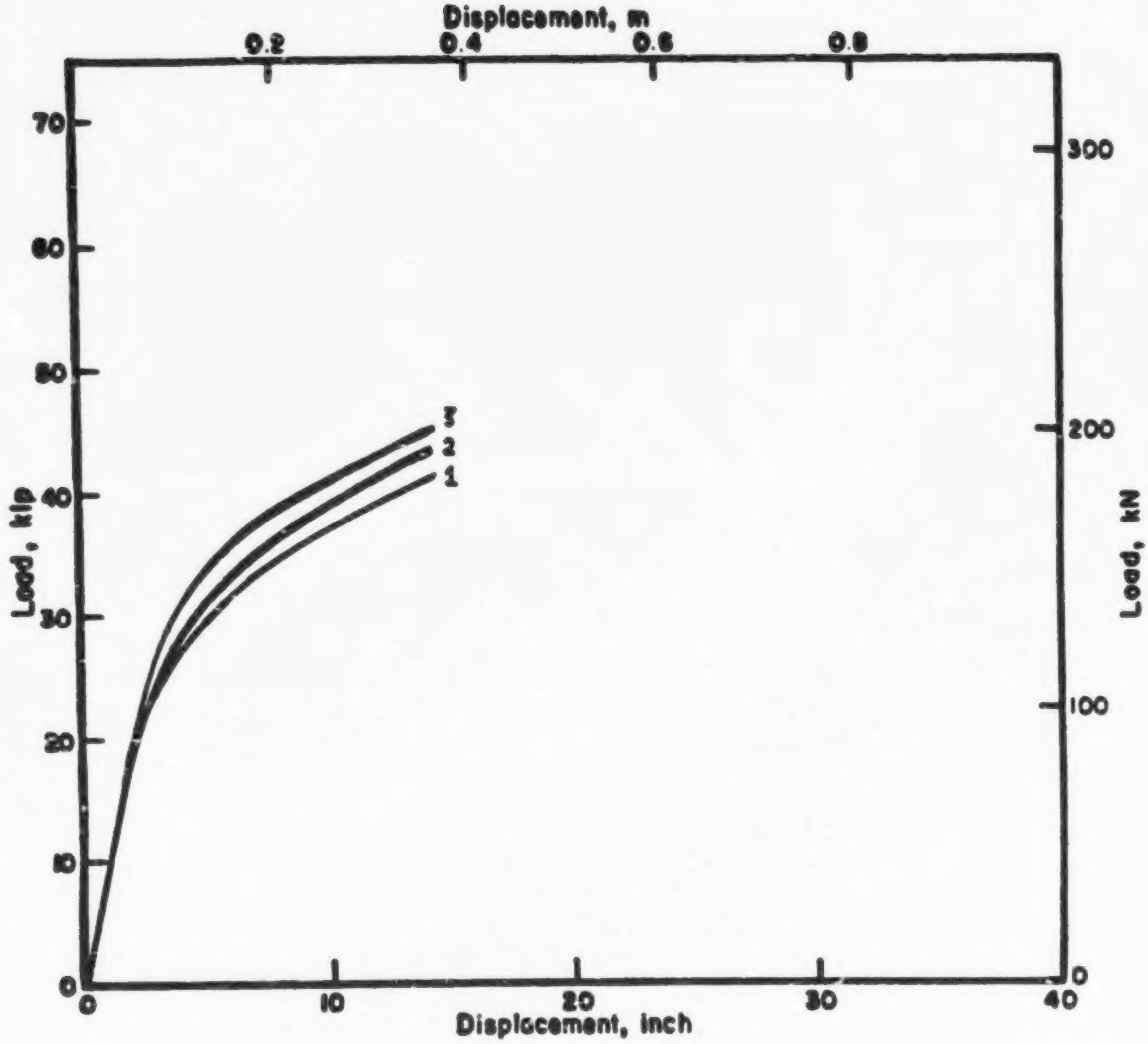

Figure 3.4.3 Computed load as a function of applied displacement (Participant 4).

T-4573-F3.4.3

112

BEST COPY AVAILABLE

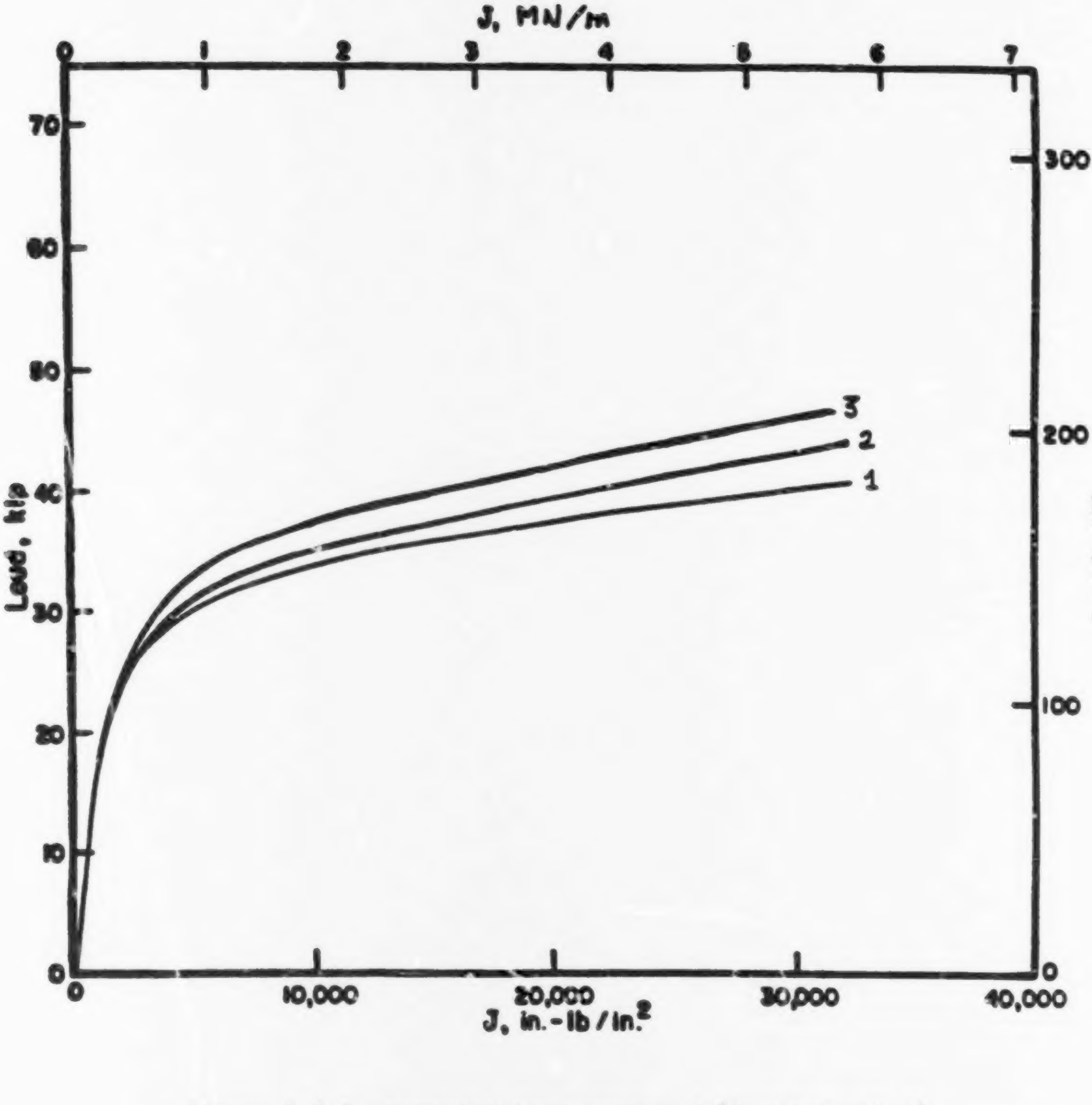

Figure 3.4.4 Computed load versus J (Participant 4).

T-4573-F3.4.4

113

BEST COPY AVAILABLE

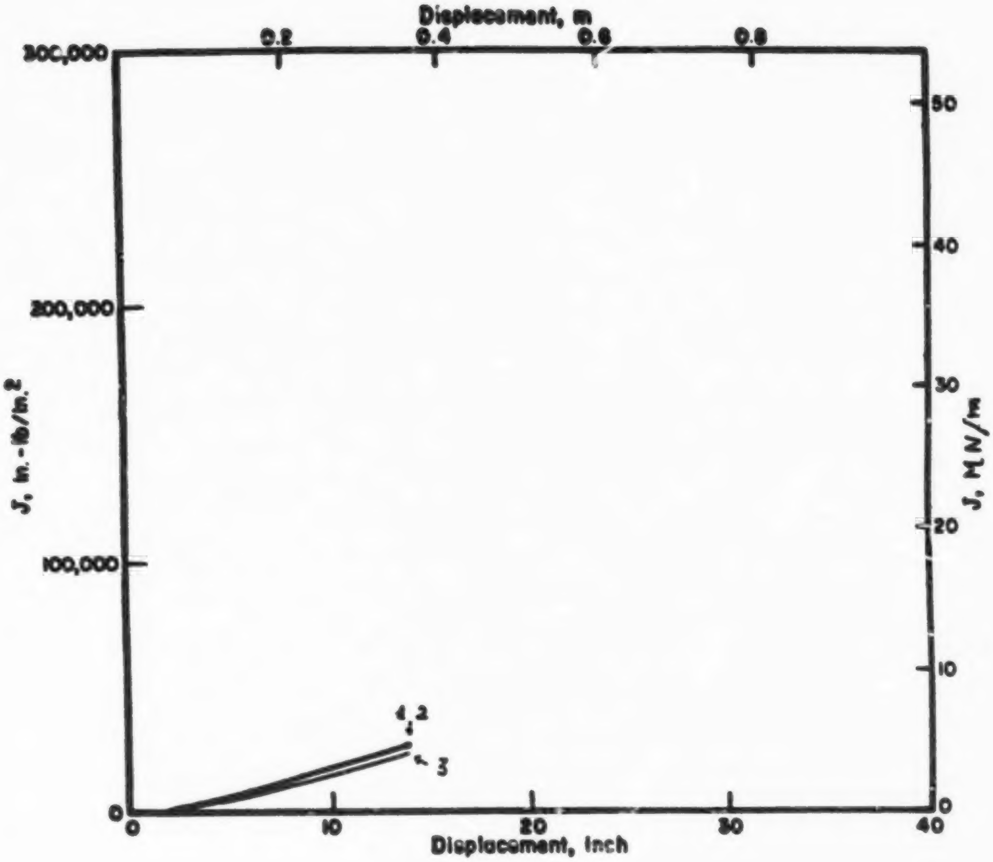

Figure 3.4.5 Computed J versus applied displacement (Participant 4).

T-4573-F3.4.5

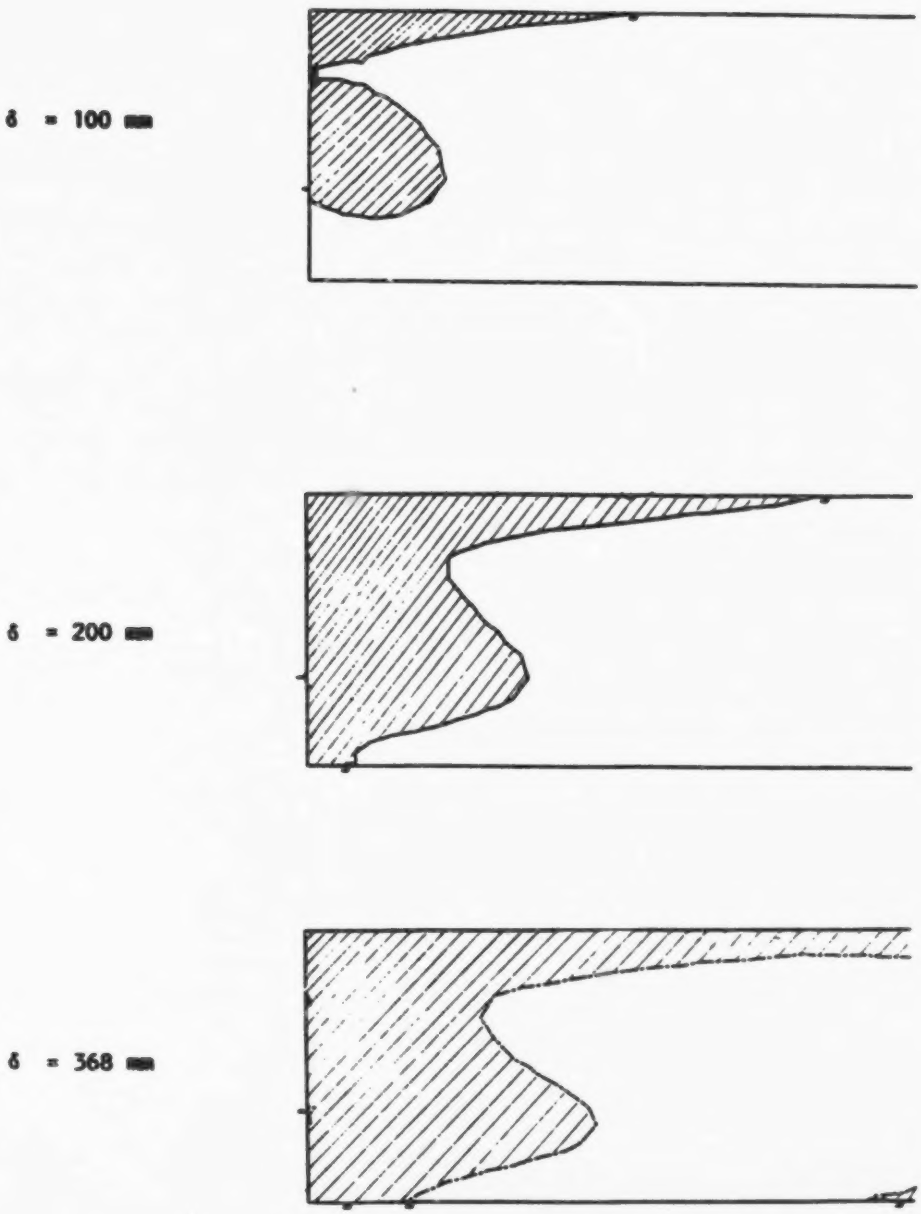
δ = 100 mm
δ = 200 mm
δ = 368 mm

Figure 3.4.6 Growth of plastic zone with increasing applied displacement (Participant 4).

T-4573-F3.4.6

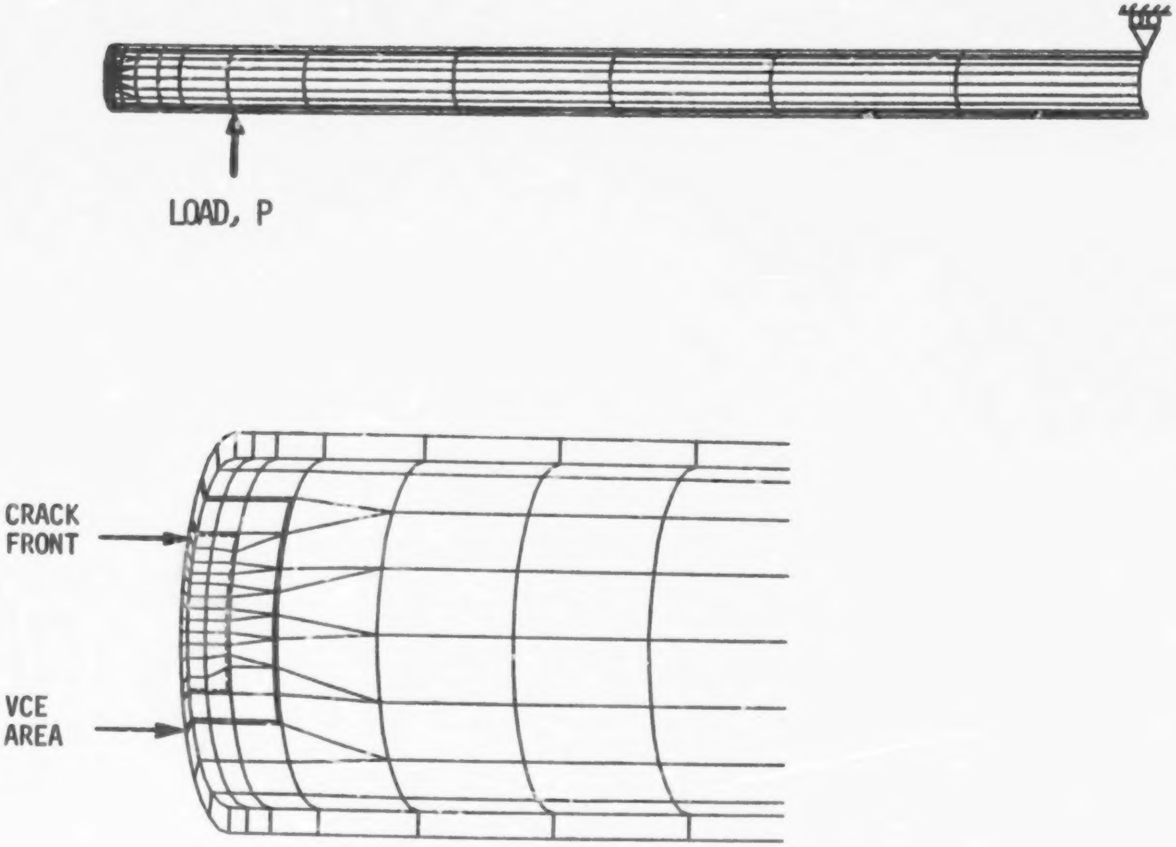
LOAD, P
CRACK FRONT
VCE AREA

Figure 3.5.1 Finite element mesh with virtual crack extension elements. (Participant 5.)

T-4573-F3.5.1

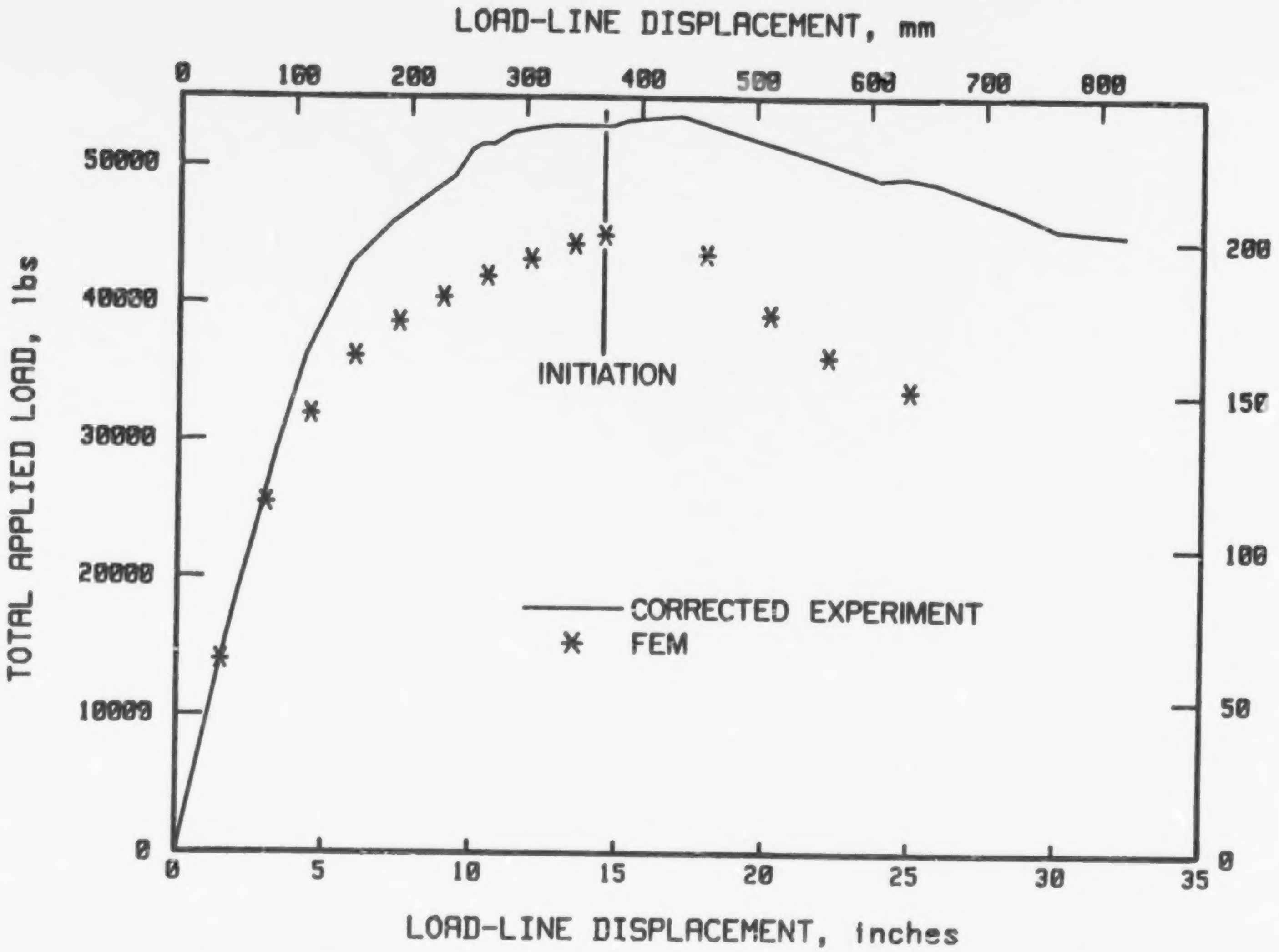

Figure 3.5.2 Load versus load-line displacement for 16-inch (406-mm) diameter stainless steel pipe. (Participant 5.)

T-4573-F3.5.2

117

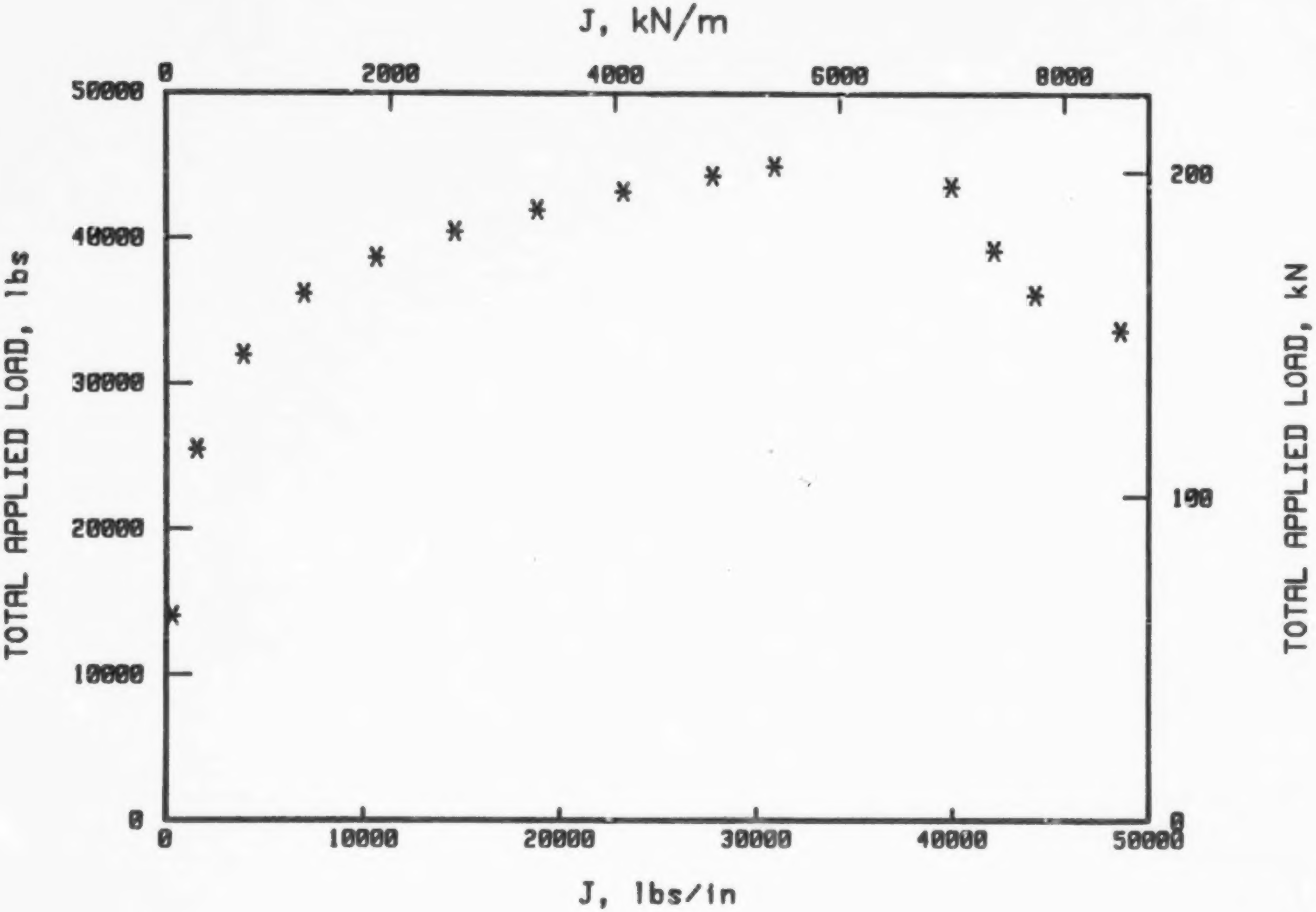

Figure 3.5.3 Load versus J for 16-inch (406-mm) diameter stainless steel pipe. (Participant 5.)

T-4573-F3.5.3

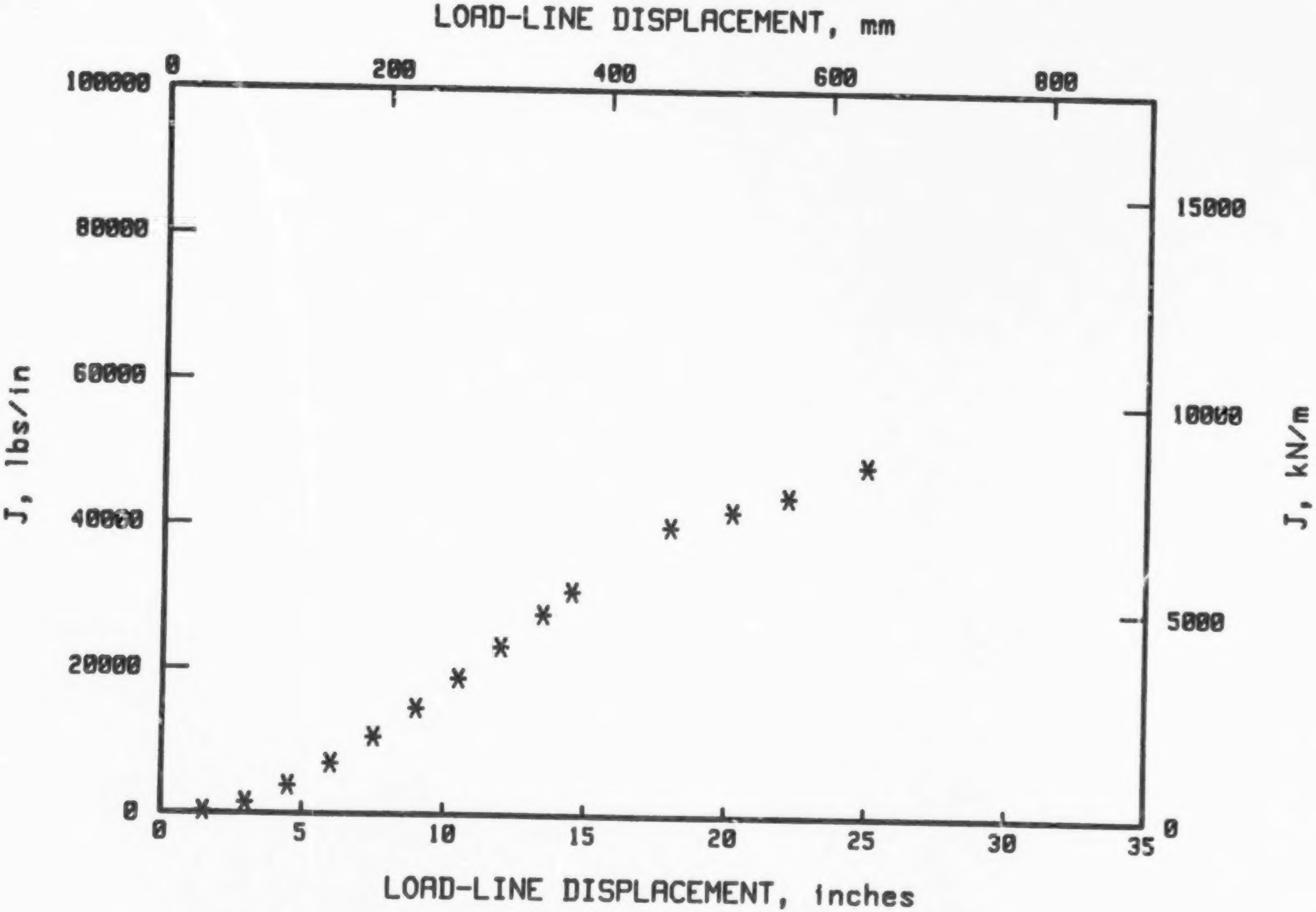

Figure 3.5.4 J versus load-line displacement for 16-inch (406-mm) diameter stainless steel pipe (Participant 5).

M-6/85-FB8

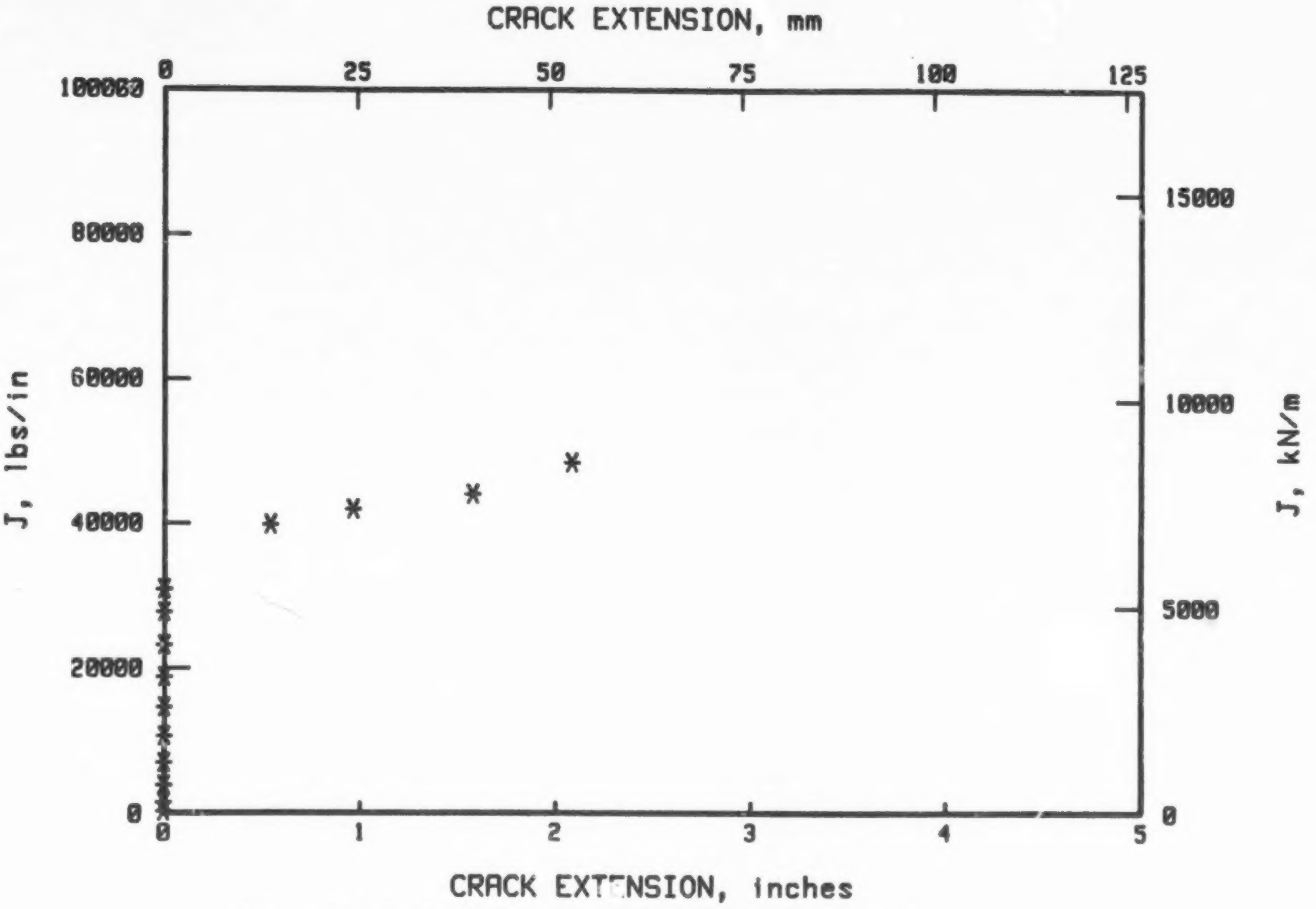

Figure 3.5.5 J-R curve for 16-inch (406-mm) diameter stainless steel pipe (Participant 5).

M-6/85-FB9

120

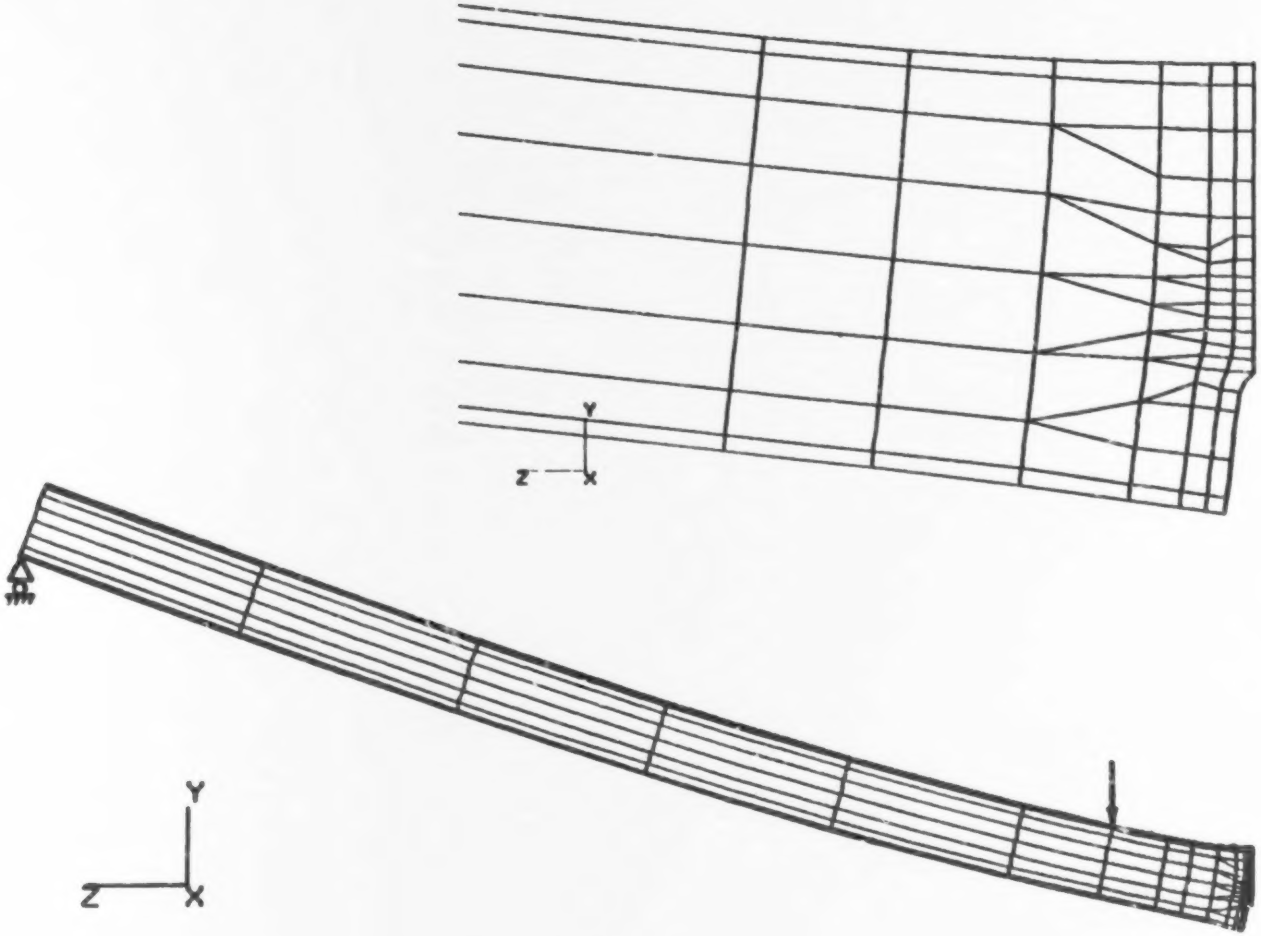

Figure 3.5.6 An exaggerated pipe deformation at an early stage of bending.

T-4573-F3.5.6

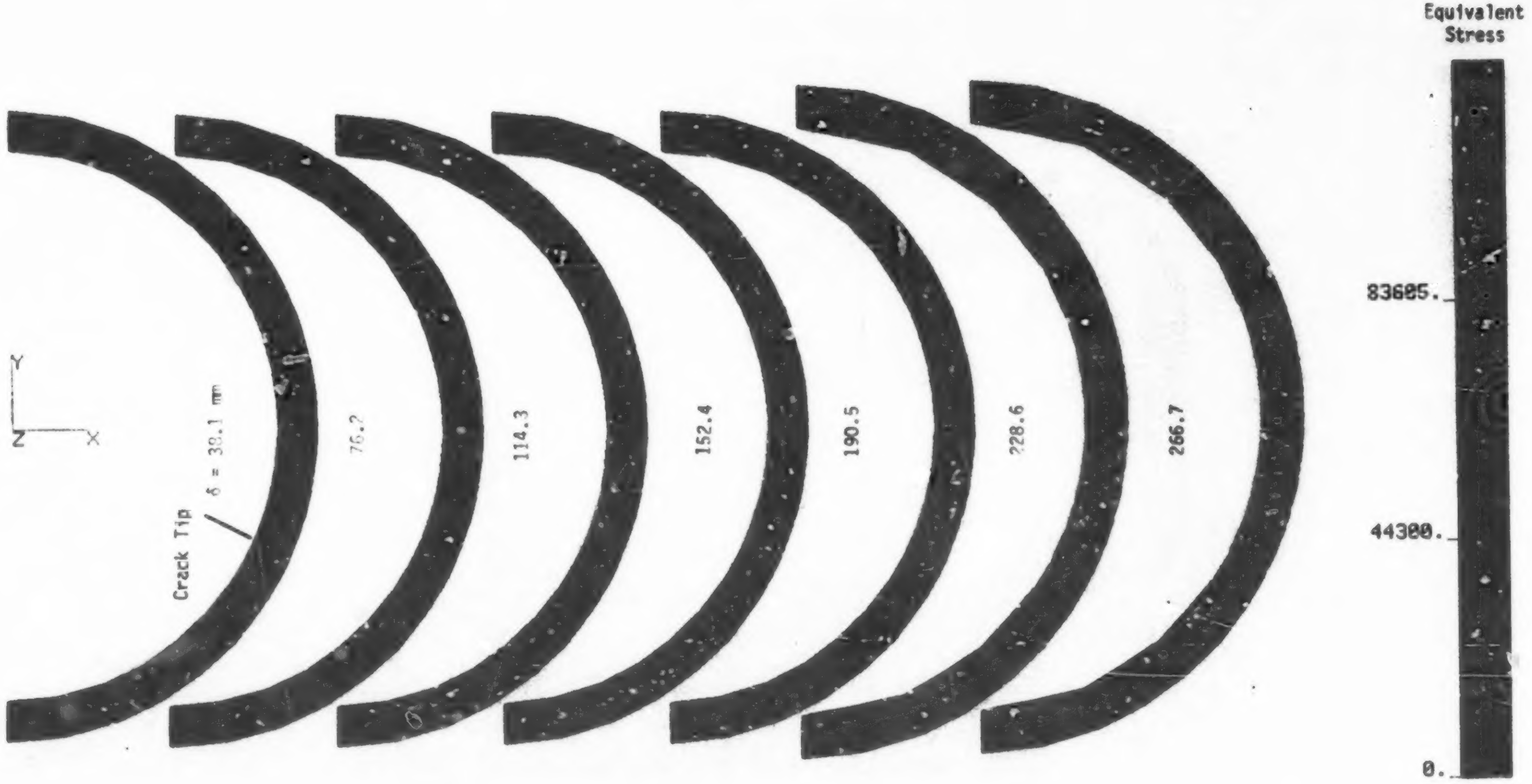
Equivalent Stress
83605.
44300.
0.
Y
Z
X
Crack Tip
δ = 38.1 mm
76.2
114.3
152.4
190.5
228.6
266.7

Figure 3.5.7 Contour of plastic zone and its growth on the crack plane section during bending.

T-4573-F3.5.7

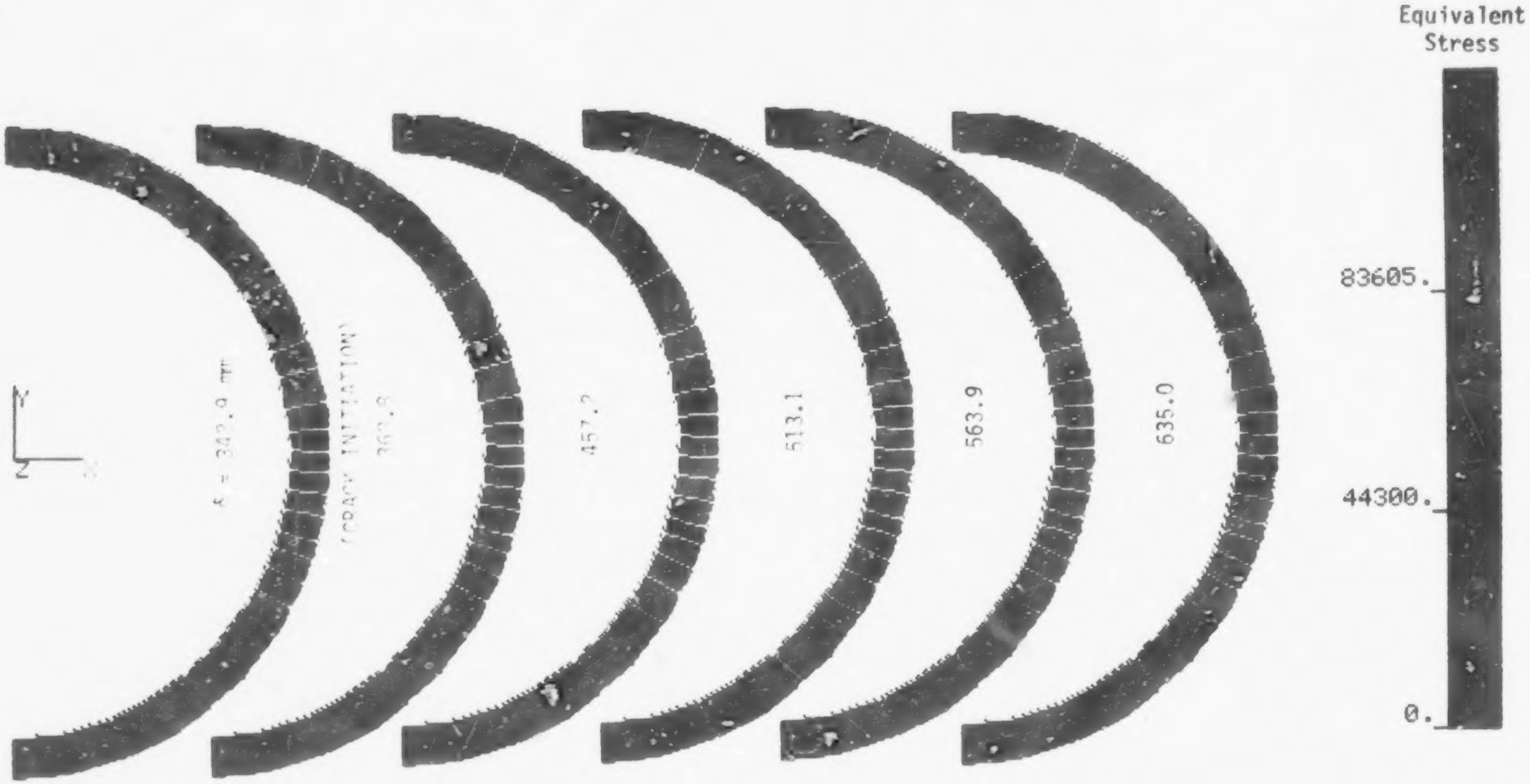

Figure 3.5.8 Contour of plastic zone and its growth on the crack plane section during bending.

T-4573-F3.5.8

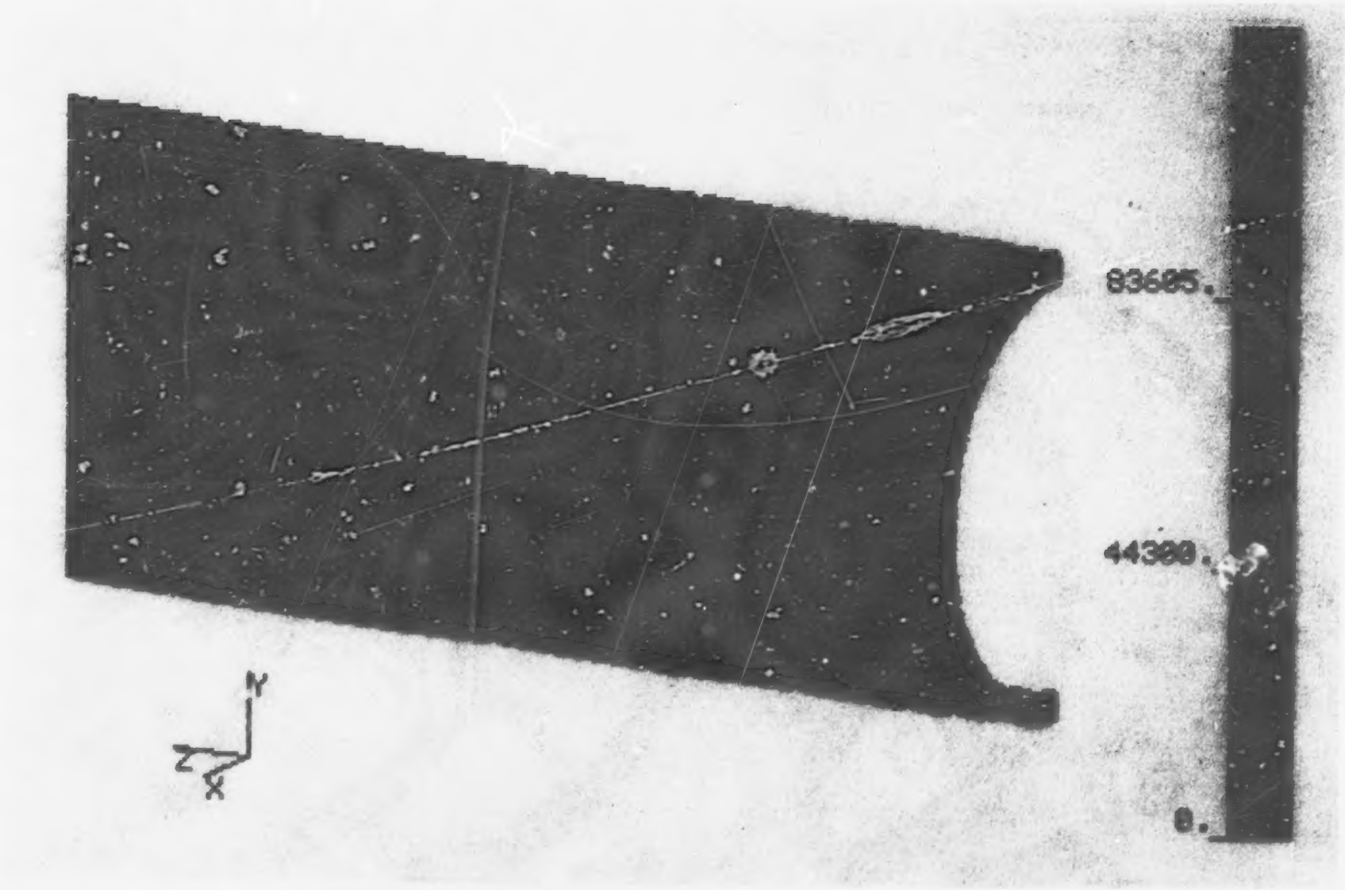

Figure 3.5.9 Plastic zones extended over the pipe surfaces.

T-4573-F3.5.9

4. J-ESTIMATION SCHEME RESULTS

In EPFM practice, J-resistance curves are commonly obtained by analyzing experimental load (P) versus load-line displacement (δ) and crack extension (Δa) records by engineering J-estimation formulas. Therefore, it is of interest to assess the accuracy of J-resistance curves obtained using an estimation formula by comparing these curves with the results of finite element analyses such as those contained in Sections 2 and 3. In this section, J-estimation analysis results for both the C(T) specimen (Problem A) and the circumferentially through-wall-cracked pipe in bending (Problem B) are presented.

4.1 Analysis of Problem A by a J-Estimation Scheme

For C(T) specimens, ASTM E813-81 provides a method for calculating J, called J_D*. The expression for J_D is given as

$$J_{D(i+1)} = [J_{D(i)} + (\frac{\eta}{b}) \frac{A_{i,i+1}}{B_N}] [1 (\frac{\gamma}{b})_i (a_{i+1} - a_i)] \qquad (4.1)$$

where A is the area under the P versus δ curve, and B_N is the thickness.

The subscripts i and i+1 relate to the test record increments and the parameters η, γ and b are updated at each increment. These parameters are defined as follows:

$\eta = 2 + 0.522 \ b/w$

$\gamma = 1 + 0.76 \ b/w$

$b = [w - (a_o + \Delta a_i)]$.

The use of Eq. 4.1 in developing a J-resistance curve requires experimental P versus δ and δ versus Δa records. For the present case, these were the same as those used in all the finite element analyses of Section 2, and contained in the statement of Problem A in Appendix A. The resulting J-resistance curve is shown in Figure 4.1.1.

An additional calculation was performed using a modified form of J, called J_M, recently proposed by Ernst (Ref. 4.1). In essence, J_M has been proposed as a crack-growth characterizing parameter for larger crack extension amounts than can be characterized by J_D. The formula for calculating J_M is as follows:

---

* In the present work, the J_D is used rather loosely. It is not meant to imply that the calculated values satisfy the validity criteria given in ASTM E813-81.

$$J_M = J_D - \int_{a_0}^{a} \left. \frac{\partial(J_D - G)}{\partial a} \right|_{\delta_p} da \tag{4.2}$$

where G is the Griffith's linear elastic energy release rate. Therefore, the quantity differentiated with respect to a is the plastic part of J_D. (δ_p) is the plastic part of the displacement. The resistance curve calculated by using Eq. 4.2 is shown in Figure 4.1.1.

4.2 Analysis of Problem B by a J-Estimation Scheme

In analyzing a pipe subjected to four-point bending and containing a through-wall circumferential crack of length 2a, a J-estimation scheme developed at Battelle (Ref. 4.2) was used. In this scheme, J is calculated using the following formula:

$$J = J_e + J_p \tag{4.3}$$

$$J_p = 2t \int_{0}^{\delta_{cp}} \beta P \, d\delta_{cp} + \int_{\phi_0}^{\phi} \gamma \, J_p d\phi \tag{4.4}$$

where

J_e = elastic component of J

J_p = plastic component of J

t = pipe thickness

ϕ = crack angle = $2a/R_m$

R_m = mean pipe radius

δ_{cp} = plastic component of load-point displacement resulting from crack

P = load acting at each load point (that is, half the total applied load)

$\beta = -\dfrac{h'}{R_m t h}$

$\gamma = \dfrac{h''}{h'}$

$h = \cos(\frac{\phi}{4}) - \frac{1}{2} \sin(\frac{\phi}{2})$

$h' = \dfrac{dh}{d\phi}$, $h'' = \dfrac{d^2 h}{d^2 \phi}$

The use of Eq. 4.4 and the analysis of the Problem B data given in Appendix A gave the resistance curve shown in Figure 4.2.1.

4.3 References for Section 4

4.1 Ernst, H. A., "Material Resistance and Instability Beyond J-Controlled Crack Growth", Elastic-Plastic Fracture: Second Symposium, Volume 1 -Inelastic Crack Analysis, ASTM STP 803, C. F. Shih and J. P. Gudas, Eds., Am. Soc. Test. Matls., 1983.

4.2 "The Development of a Plan for the Assessment of Degraded Nuclear Piping by Experimentation and Tearing Instability Fracture Mechanics Analysis", Appendix, by Battelle-Columbus Laboratories, NUREG/CR-3142, report to the U.S. Nuclear Regulatory Commission, June 1983.

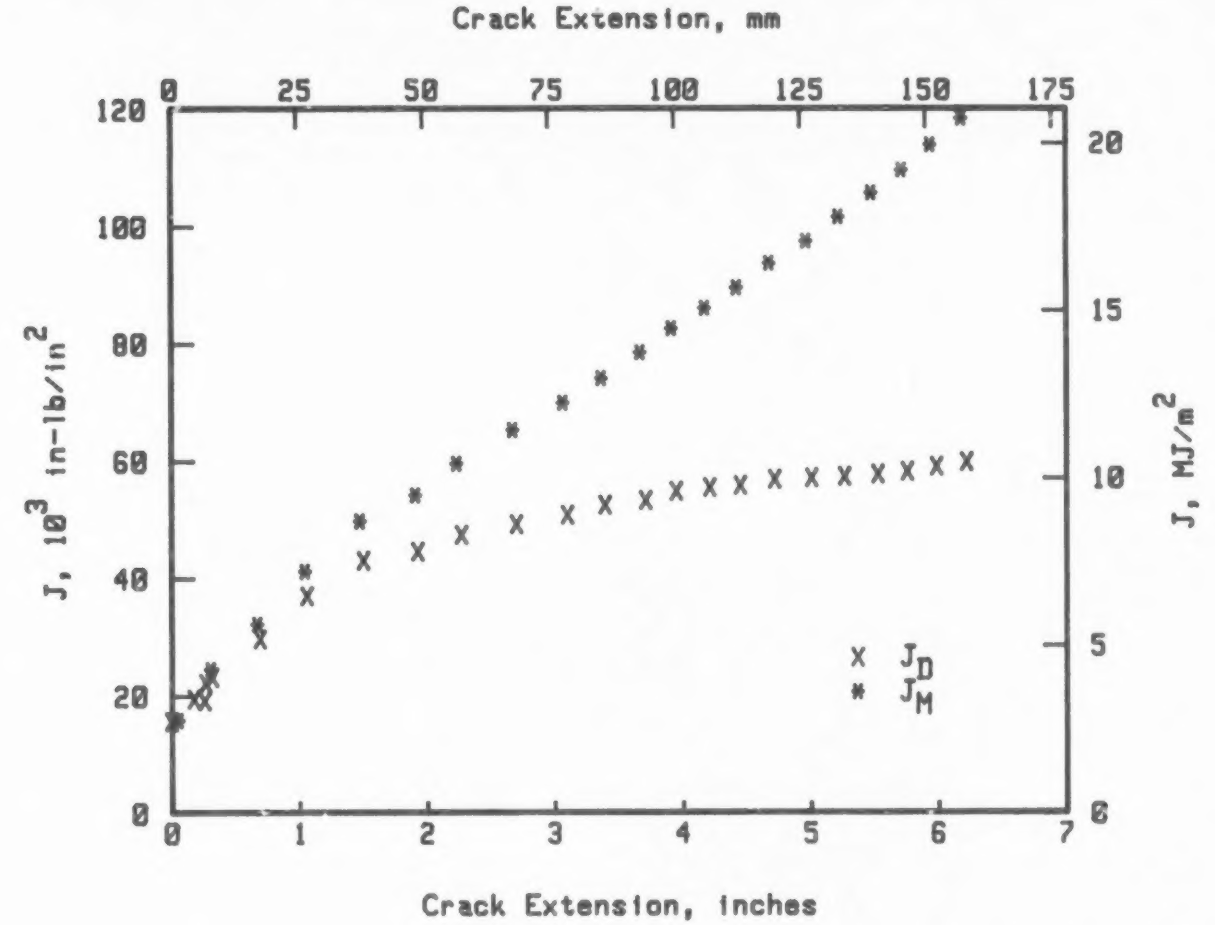

Figure 4.1.1 J_M and J_D versus Δa for the 10T C(T) planform specimen used in Problem A.

T-4573-F4.1.1

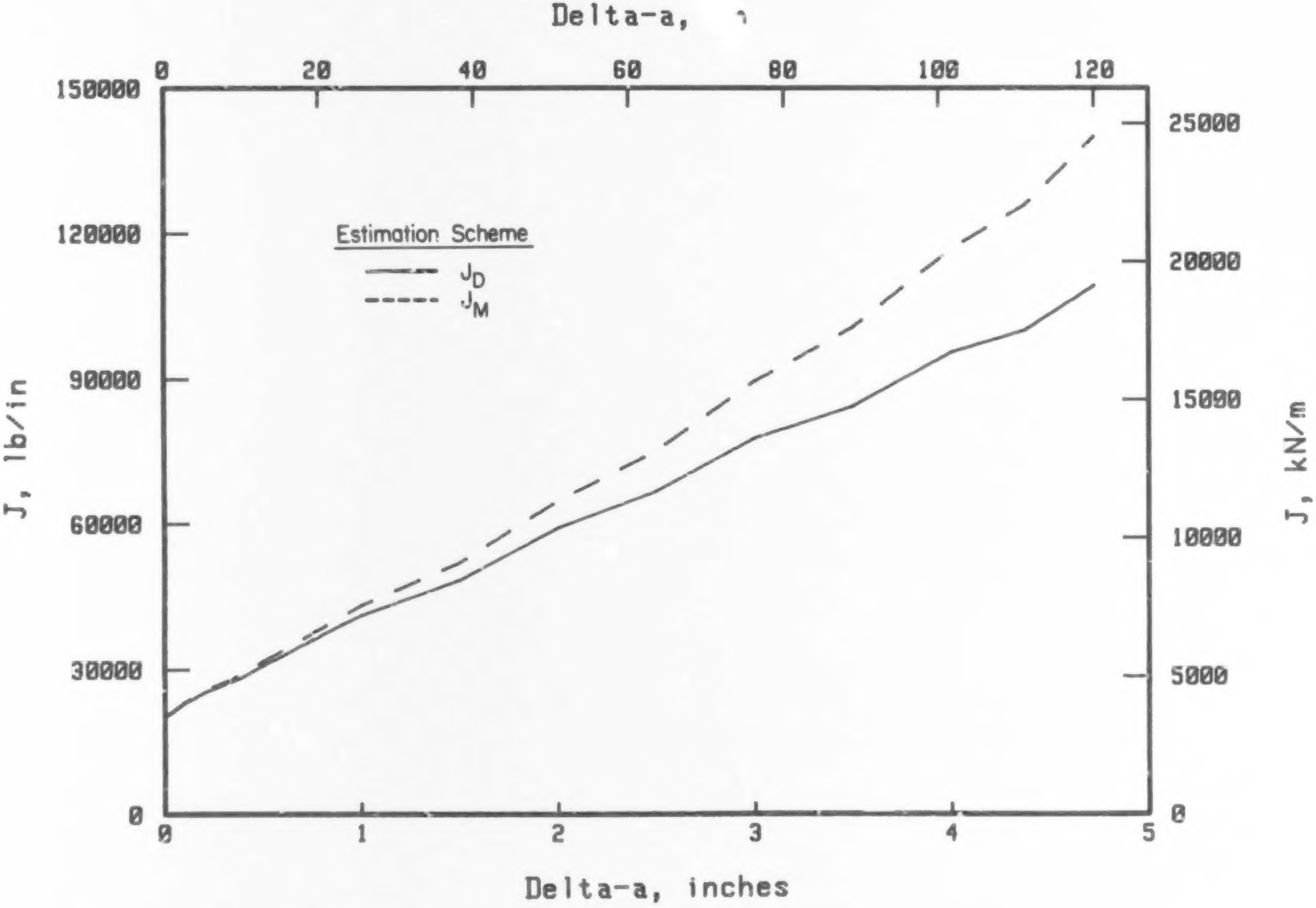

Figure 4.2.1 J- and J_M-resistance curve obtained by analyzing the 16-inch (406-mm)-diameter through-wall cracked pipe data (Problem B) by the J-estimation formula.

T-4573-F4.2.1

5. DISCUSSION OF RESULTS AND CONCLUSION

At the onset of the round-robin effort, it was expected that the participants would use widely differing modeling methods in solving the two problems. As is evident in Table 5.1 for Problem A, barring a few exceptions, the participants showed a remarkable degree of consensus in their choice of modeling techniques. Four of the five participants used plane-stress eight-node isoparametric elements. Also, all the participants chose the von Mises yield surface with isotropic hardening to model plastic deformation. There were, however, differences in the methods used to model crack propagation and in computing the J-integral.

The results for Problem A in terms of predicted load versus applied displacement are shown in Figure 5.1 with the experimentally measured load-versus-displacement curve. Considering that the problem involved gross plastic deformation and large amounts of crack extension, the agreement between the computed results is good. Also, all the predicted values are in reasonably close agreement with the experimental record. The general trend, except for the results by Participant Number 5, is that beyond crack initiation, the computed loads are higher than the experimental values. However, the agreement between the predicted and the experimental values improves for larger amounts of crack extension.

The results for Problem A in terms of far-field J versus crack extension are shown in Figure 5.2. Except for the results by Participants Number 3 and 5, the computed J-values are within about 20 percent of each other, even at 6 inches (152.4 mm) of crack extension. Note that the results of Participant Number 5 show a considerably lower J at crack initiation compared with the other solutions. This is consistent with the corresponding load-versus-displacement results (Figure 5.1) reported by Participant Number 5 as being lower than the rest of the predictions. Also note that Participant Number 3 chose to find J as a function of crack extension by performing a number of finite element analyses, each with different crack length. That is, the crack-growth process per se was not modeled. Consequently, these results do not reflect the crack-growth history dependence on the computed J-resistance curve, and may be viewed as the deformation theory J-resistance curve. Therefore, the results of Participant Number 3 would be expected to agree well with the J_D-estimation formula results of Section 4. As shown in Figure 5.3, this is the case. The other computed J-resistance curves seem to be in better agreement with the J_M, rather than the J_D, resistance curve.

A summary of the various modeling techniques used by the participants in solving Problem B is presented in Table 5.2. For this problem, the main differences in the techniques used are in the choice of elements, rather than in crack-growth modeling or in J-computation methods. The three element types used are the three-dimensional 20- and 16-node brick elements, 3-node thin-shell elements, and thick-shell elements.

In Problem B, the experimental total load and the load point displacement versus crack growth (listed in Table B.3 in Appendix A) are

Table 5.1 Variables used in the round-robin finite element analyses of the 10T compact specimen (Problem A).

Participant	(3)	(4)	(5)	(2)	(1)
No. & Type of Elements	90 8-noded isoparametric	482 8-noded isoparametric	488 8-noded isoparametric	327 constant strain triangles	263 8-noded isoparametric
No. of nodes	340	482	1592	201	879
Integration Order	3x3 Gauss	2x2 Gauss	2x2 Gauss		3x3 Gauss
Type of Analysis and Formulation	2D plane stress small deformations small strains	2D plane stress large deformations small strains	2D plane stress small deformations small strains	2D plane stress small deformations small strains	2D plane stress large deformations large strains
Equilibrium Compensation		Mod. Newton Raphson			Mod. Newton Raphson
Crack Extension Procedure	N.A.*	Node shift & node release	Node shift & node release	Nodal force release	Nodal force release
Yield Surface	Von Mises	Von Mises	Von Mises	Von Mises	Von Mises
Hardening Model	Isotropic	Isotropic	Isotropic	Isotropic	Isotropic
σ–ε Curve	Engineering	True	True	True	True
J-Computation	VCE	VCE	VCE	Contour Integral	Contour Integral

* Multiple analyses performed for 5 different crack lengths

T-4573-T5.1

Table 5.2 Variables used in the round-robin finite element analysis of the 16-inch (406-mm) pipe (Problem B).

Participant	(1)	(4)	(2)	(3)	(5)
No. & Type of Elements	142 16-node isoparametric	1107 3-node shell	130 20-node isoparametric	304 thick shell	142/60 20-node Brick/general
No. of nodes	974	616	1133	337	1102
Integration Order	3x3x2 Gauss	1 Gauss	2x2x2 Gauss	1 Gauss	3x3x3 Gauss
Finite Deformation	No	Yes Small strain	Yes Small strain	No	No
Equilibrium Compensation	Yes	No	Mod. Newton-Raphson	Newton-Raphson	Newton-Raphson
Crack Extension Procedure	Node release	No	Node shift & release	Node release	Node release
Yield Surface	Von Mises	Von Mises	Von Mises	Von Mises	Von Mises
Hardening Model	Isotropic	Isotropic	Isotropic	Kinematic	Isotropic
$\sigma-\varepsilon$ Curve	Engineering	Engineering	True	True	Engineering
J-Computation	VCE	VCE	VCE	VCE	VCE

T-4573-T5.2

the values measured at the ram. Although the experimental data prior to the crack initiation are not needed for finite element simulation, all participants in Problem B used the displacement versus crack extension data from the table. Later, it was found that the effects of the specimen weight and of the constraining wire rope compliance during the loading are significant. A portion of the upper weight, which does not contribute to opening the crack in bending, was thus subtracted for correction. As to the rope compliance, none of the rope data are retrievable. Since it is known from our prior analyses that 3-D finite element calculation in the elastic state provides fairly good correlations with experimental results, and since the present low load FEM results from all the participants agree very well with each other, the rope compliance was deduced so that the elastic portion of the corrected experimental P-δ relation matches with that of the averaged FEM results from all the participants. A schematic relation of the corrected experimental load-displacement (P_i-δ_i) represented by a broken line to the uncorrected results (P-δ curve) by a solid line is shown in Figure 5.4. In Figure 3.2.3 results of Participant Number 2 are compared with the uncorrected P-δ curve. These are recompared in Figure 5.5 with the results from all the other participants to the corrected experimental $P_i - \delta_i$ curve. As shown in Figure 5.5; only one of the five participants (Participant Number 1) obtained good agreement between the calculated load versus displacement curve and the experimental record. The rest of the calculated values (by Participants 2, 3, and 5) appear to agree fairly well with each other.

Figure 5.6 and 5.7 show, respectively, computed J versus load line displacement and J versus load by the VCE method. Also shown in the figures are calculated J and J_M by estimation method*, based on the corrected experimental load versus load point displacement record, P_i-δ_i. These figures indicate relatively consistent results for J among all the participants. However, the results deviate from the J by estimation scheme after crack initiation. The results of load-J from only Participant Number 1 in Figure 5.7 show reasonably good correlations with the estimation method J. Others obtained fairly low values, especially after crack growth initiation.

Figure 5.8 shows the finite element J versus crack growth compared with estimation method J and J_M. This figure shows a conspicuous discrepancy in J at crack initiation between the VCE computed results from the participants and the estimation method J. The opposite trend of the subsequent J-Δa slope between the two also provides a reason for concern.

---

* J was calculated using Eqs. (4.3) and (4.4). J_M was calculated using Eq. (4.3), with only the first term of Eq. (4.4) used to represent J_M.

133

In terms of the computed J versus crack-growth values (Figure 5.8), the results are consistent with the load-versus-displacement predictions. That is, in general, the J-resistance curves computed by Participants 2, 3, and 5 each have a smaller slope than that computed by Participant Number 1. The latter is found to agree well with the resistance curve obtained by the J-estimation scheme.

Overall, the results of the round robin suggest that the current elastic-plastic finite element analysis techniques for crack-growth modeling in two-dimensional problems provide both consistent and reasonably accurate results. For three-dimensional problems, the existing methods need further review and improvements.

134

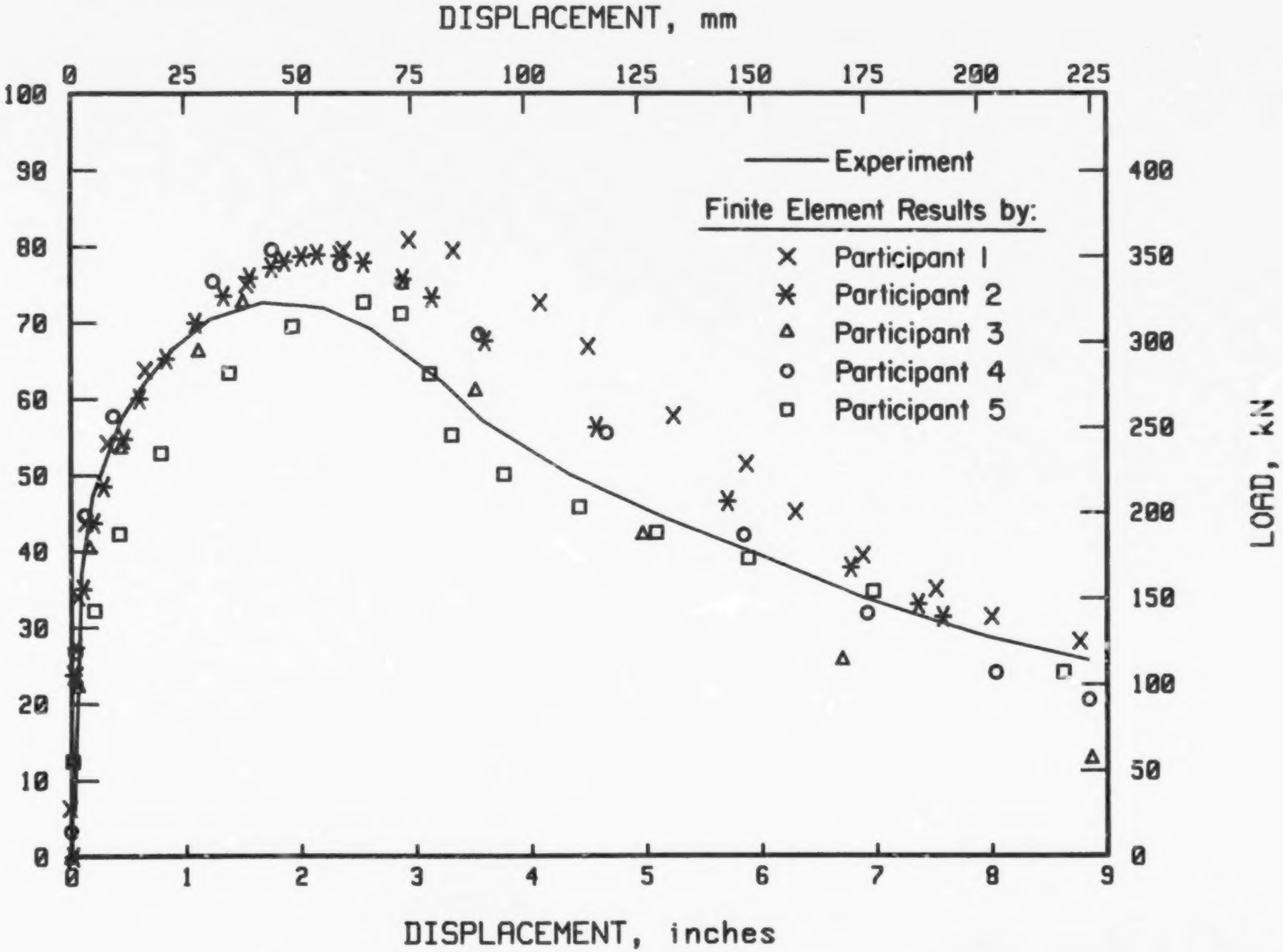

Figure 5.1 Comparison of the finite element analysis results for the C(T) specimen (Problem A) with experimental data.

135

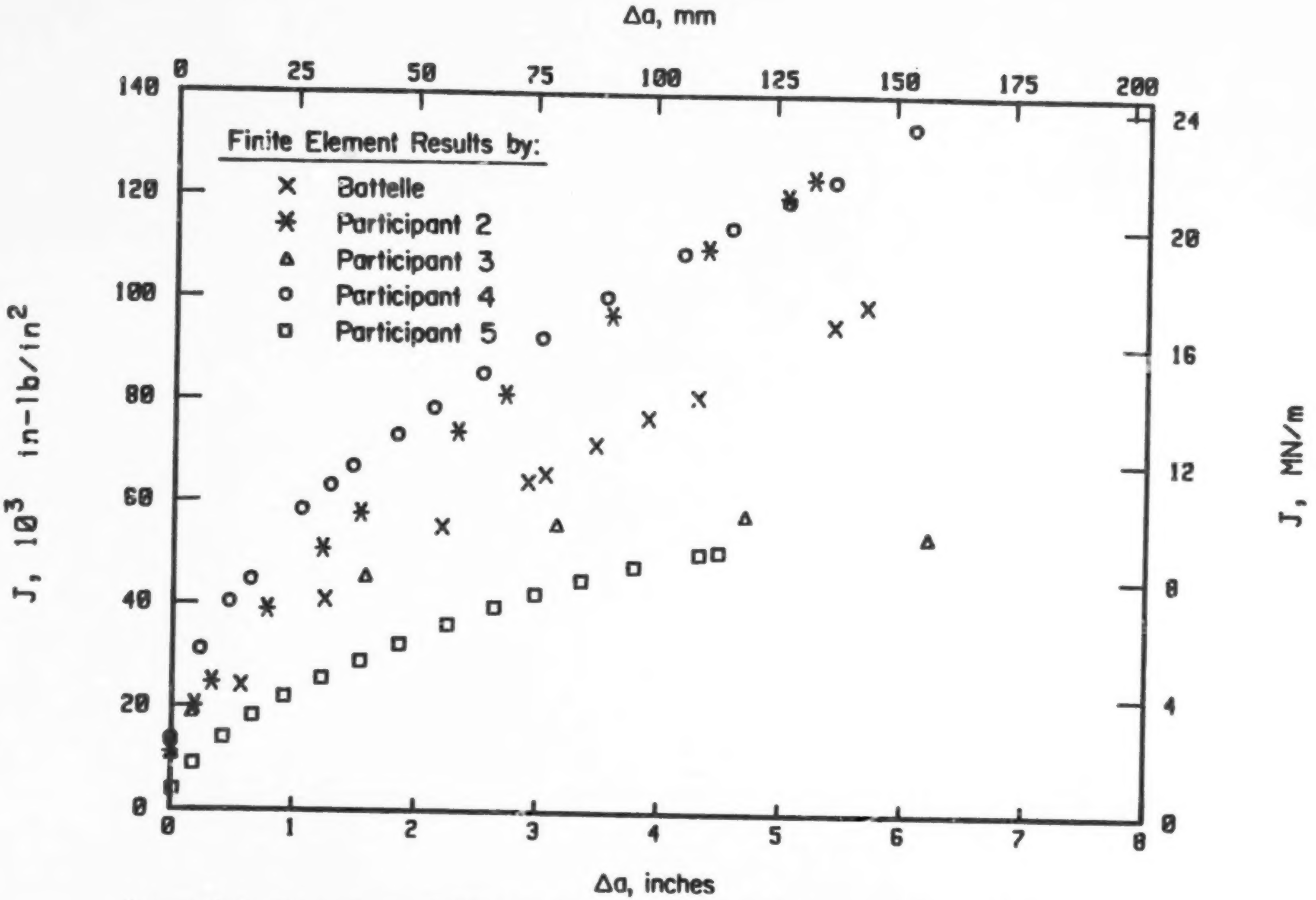

Figure 5.2 Comparison of the computed J (far-field) versus crack growth for the C(T) specimen (Problem A).

T-4573-F5.2

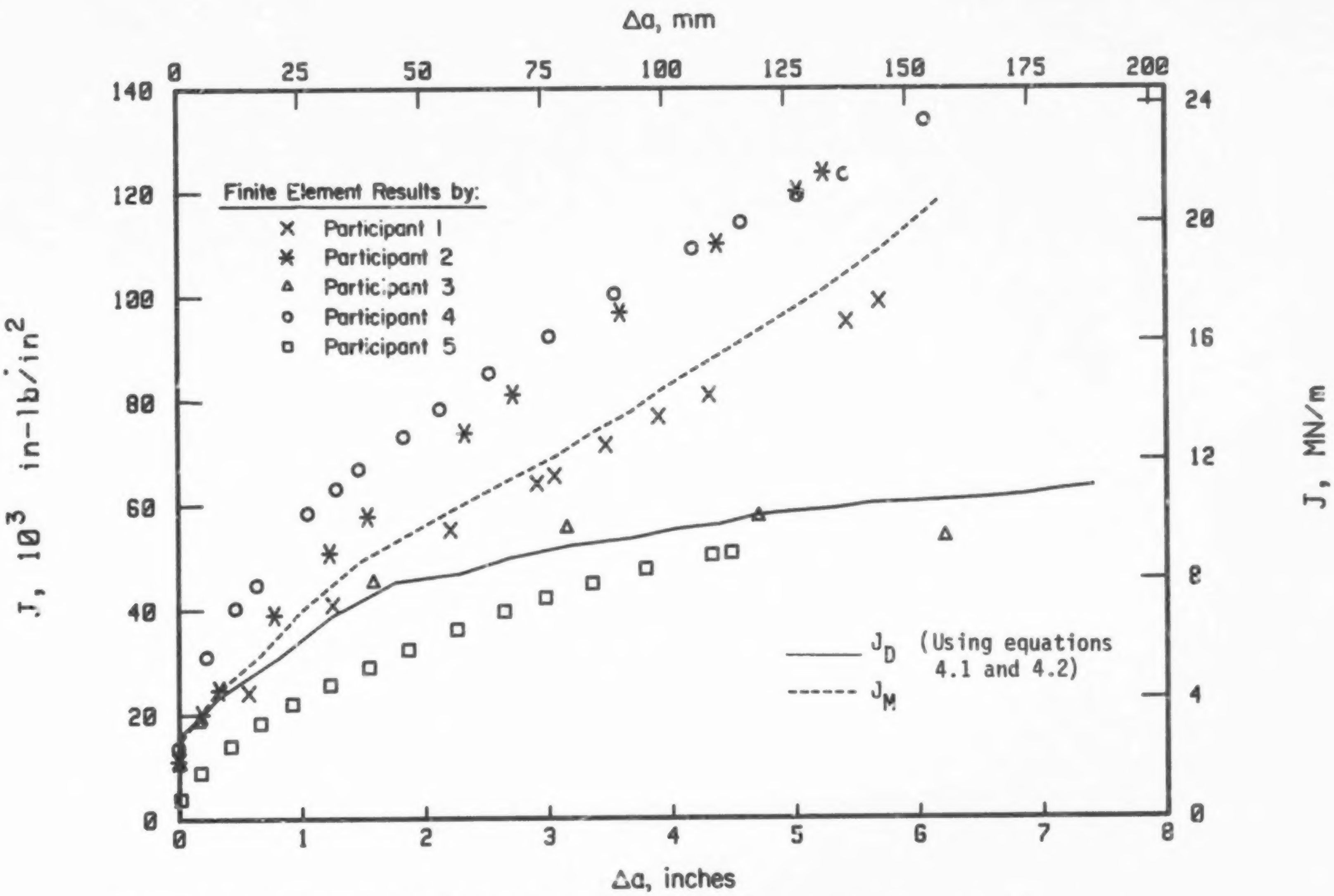

Figure 5.3 Comparison of the J (far-field) versus crack growth curves computed by finite element analysis with the J_D and J_M resistance curves (Problem A).

T-4573-F5.3

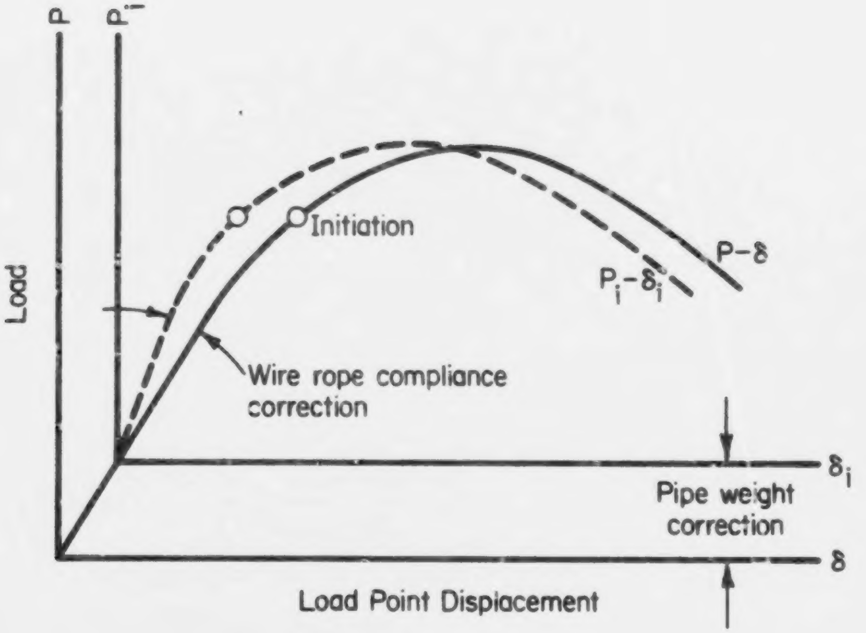
P
P_i
Load
Initiation
P-δ
$P_i-\delta_i$
Wire rope compliance correction
δ_i
Pipe weight correction
δ
Load Point Displacement

Figure 5.4 Schematic of load versus load-point displacement corrections taking account of pipe weight and wire rope compliance.

T-4573-F5.4

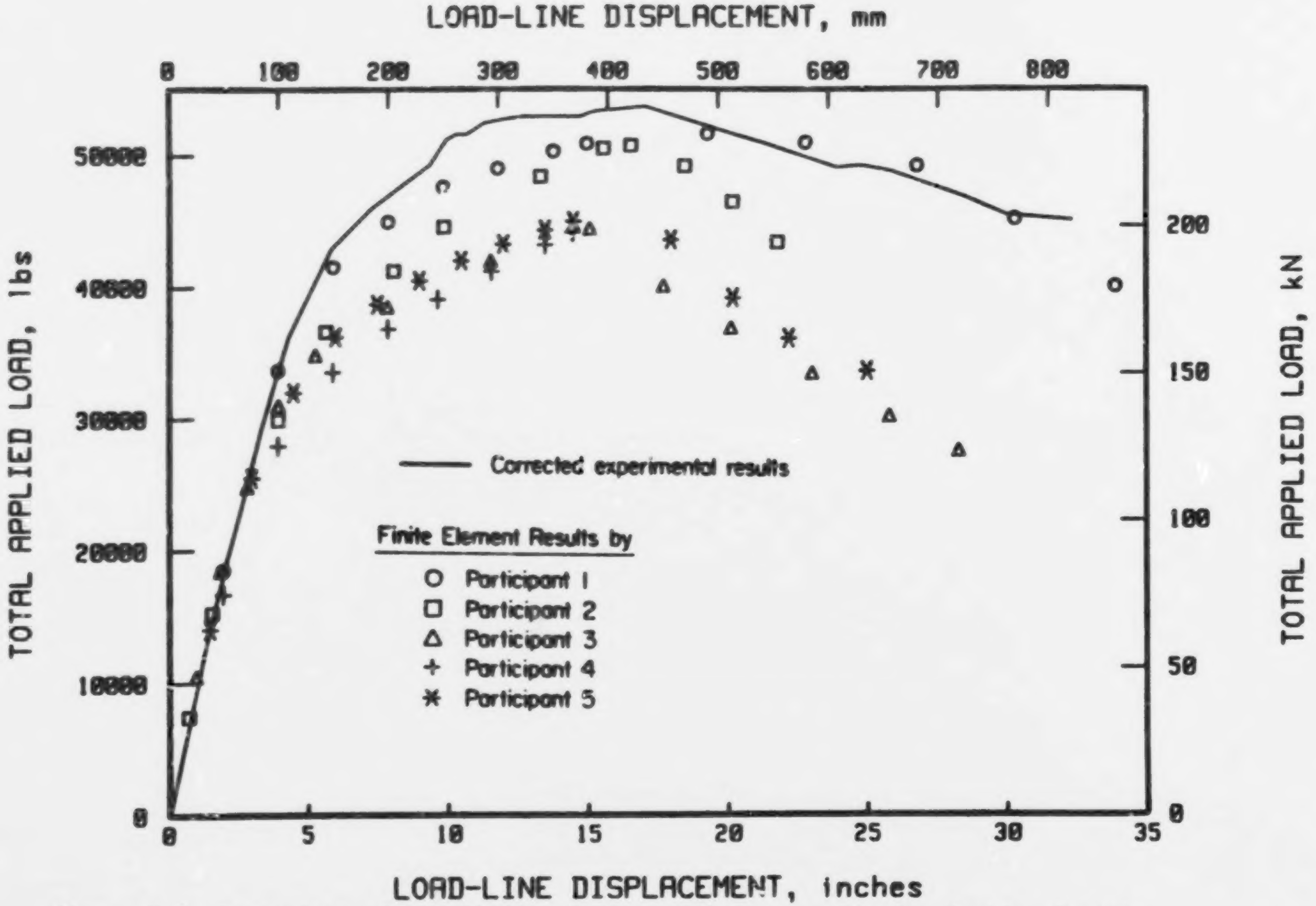

Figure 5.5 Comparison of the finite element analysis results for Problem B with experimental data. (Note, experimental load-displacement record was corrected for dead-weight load of the pipe, but not for the compliance of the test system. Data in Table B-3 of Appendix A did not account for pipe dead-weight load or test system compliance.)

T-4573-F5.5

139

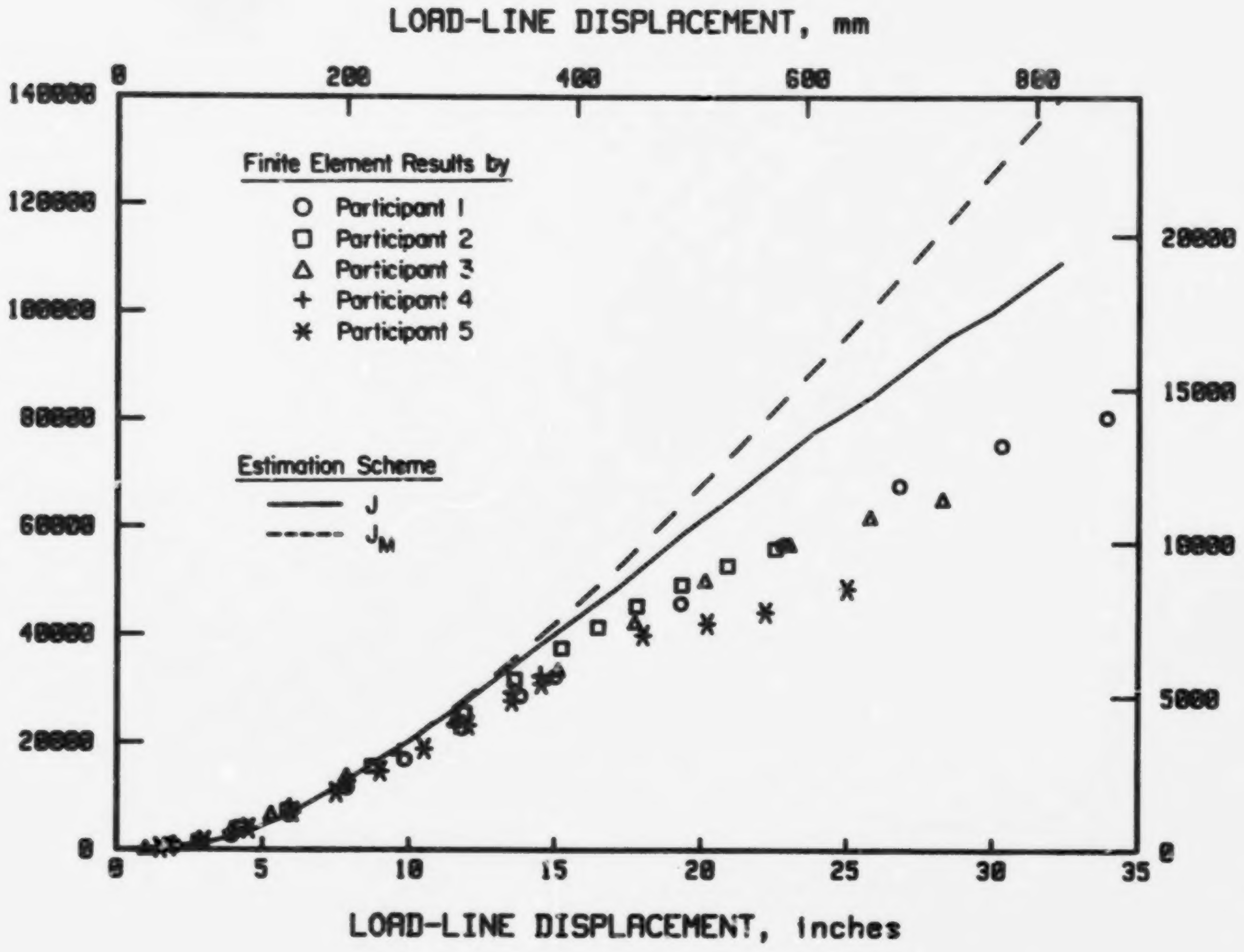

Figure 5.6 J versus load-line displacement computed by finite element analysis and by J-estimation scheme.

T-4573-F5.6

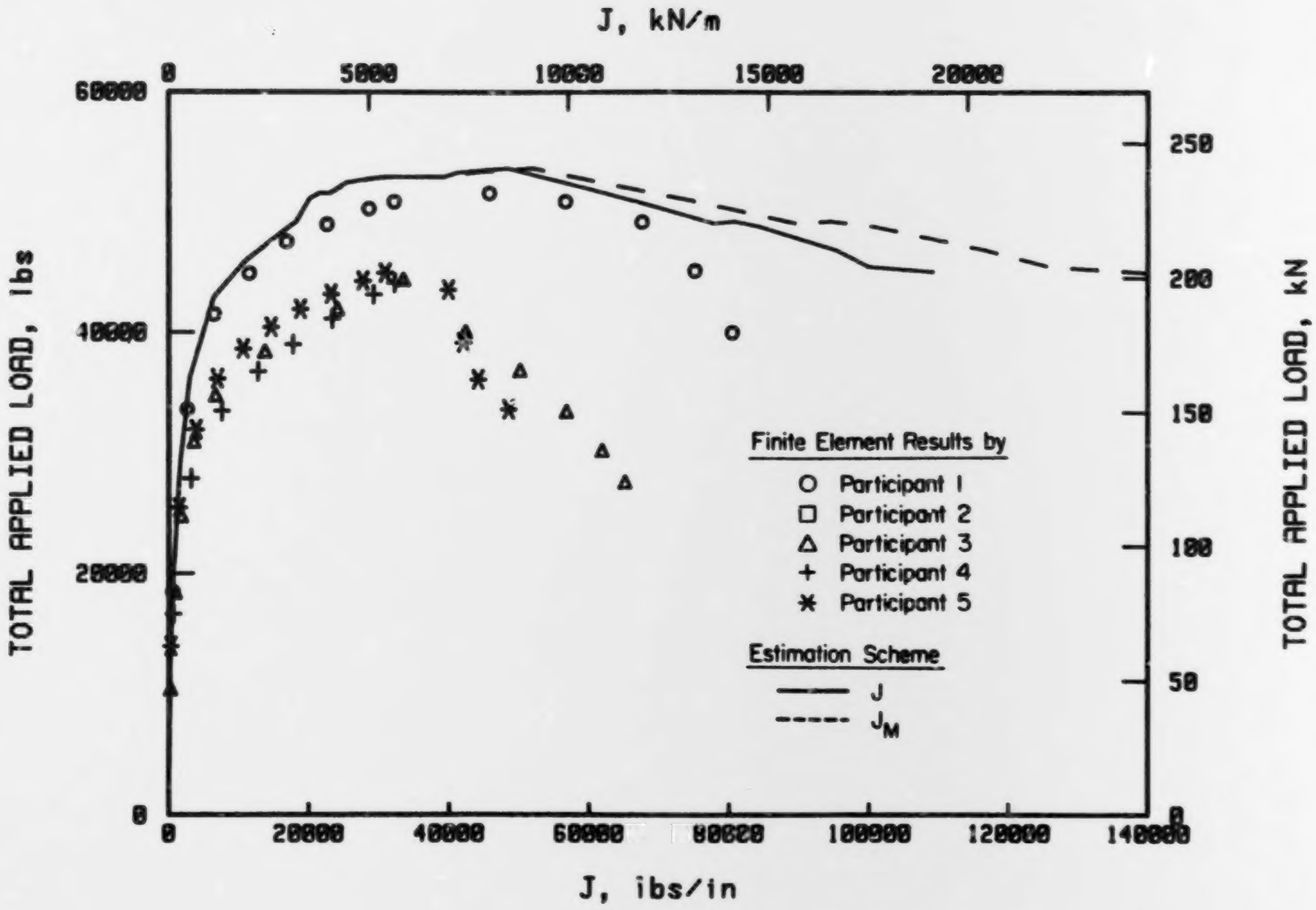

Figure 5.7 Load versus J computed by finite element analysis and by J-estimation scheme.

T-4573-F5.7

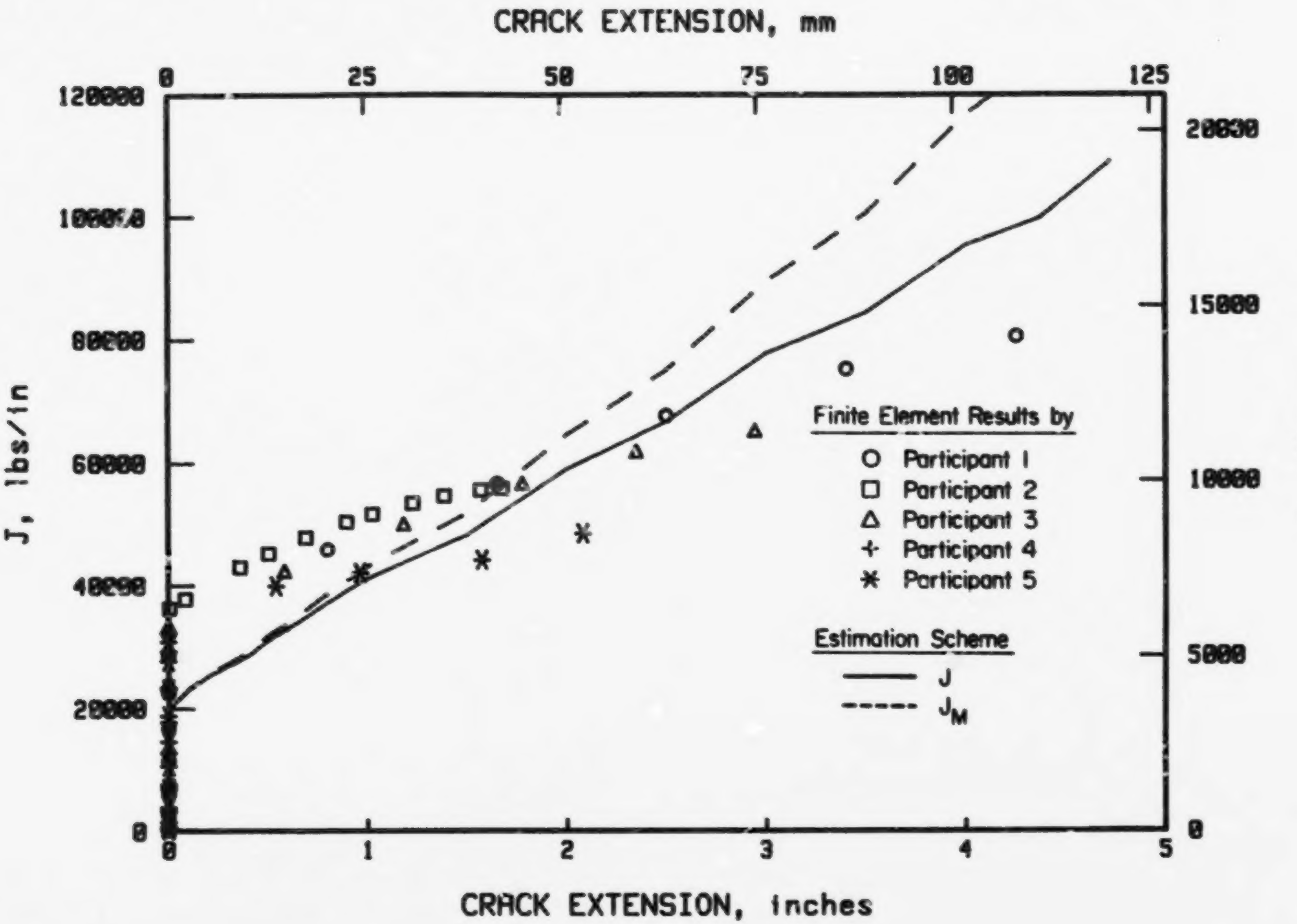

Figure 5.8 The J versus crack growth computed by finite element analysis, and by a J-estimation scheme (Problem B).

T-4573-F5.8

142

APPENDIX A

ROUND ROBIN PROBLEM STATEMENT

APPENDIX A

ROUND ROBIN PROBLEM STATEMENT

Prediction of crack growth initiation, extent of stable growth, and instability of cracks using the J-integral and tearing modulus (J/T) is hampered by two reasons. The first (and more basic) reason is that the J-integral is based on deformation theory of plasticity. If a large amount of crack extension precedes instability, nonproportionality attributable to elastic unloading in the wake of the crack tip can severely violate this implicit assumption. In such cases, instability predictions using the J/T approach become suspect.

The second (and more practical) reason is that, typically, predictions are made using estimation procedures to calculate J. These J-estimation procedures are based on simplifying assumptions to keep mathematical operations simple. The price of simplicity may be a loss in the accuracy. This would be acceptable if the nature (conservative, nonconservative) and the amount of error to be expected were known. Usually, this is not the case.

A common way of error assessment is by computing J via a nonlinear finite-element analysis, for comparison with results of estimation procedures. The implied assumption is that the finite-element results are always accurate. A critical review of this implied assumption is the objective of this round-robin exercise.

Specifically, two problems have been selected for analysis. These are labeled problem (A) and problem (B). Problem (A) is a two dimensional problem involving a compact tension [C(T)] specimen. The specimen is 10T in planar dimensions, and 1.00-inch (25.4 mm) thick. Problem (B) is a three dimensional problem involving a 16-inch (406.4 mm) diameter, 1.03-inch (26.2 mm) thick pipe with a through-wall circumferential crack. Both problems (A) and (B) are to be analyzed by elastic-plastic finite-element techniques. This includes modeling crack propagation according to prescribed (experimental) load line displacement (δ) versus crack length (a) records. Experimental load (P) versus δ records are also supplied for the purpose of comparison with computed P versus δ curves. The results of the analyses are to include the following;

(1) P versus δ
(2) J versus δ up to crack initiation
(3) J versus load up to crack initiation
(4) J versus crack extension (Δa)

The information needed to solve the two problems is described in the following pages. Note that Problem A is a two-dimensional problem using material that exhibits significant strain-hardening and with large amounts of crack growth. Problem B is a three-dimensional problem of practical concern. Solutions from various estimation schemes for both the C(T) and pipe geometries will be provided by Battelle at the PVP Meeting for comparison with the FEM results. It should be noted that while both problems involve Type 304 stainless steel, the C(T) specimen stress-strain data was obtained at 550 F (288 C) and the pipe stress-strain data was obtained at 70 F (21 C). Consequently, the material stress-strain curves for the two problems are different.

The results of these calculations will be presented at the June 1985 ASME PVP conference in New Orleans, Louisiana. Two half day sessions are reserved for the presentations; tentatively on Wednesday June 26, 1985. In the morning session the C(T) specimen results will be presented by each participant. Comparisons of these results to C(T) specimen J-estimation schemes will be made at the end of the morning by Dr. Jalees Ahmad of Battelle. The afternoon session will involve presentations of the pipe FEM results by each participant. Dr. David Broek will show comparisons of these results to pipe J-estimation scheme calculations.

The results will not be published as part of the 1985 ASME proceedings. They may be published as a NRC/CSNI report, or possibly as an ASME PVP report. Therefore, you need not have a paper written at the time of the conference. We do however, ask that you send your results (plotted on the attached figures or on the attached tables) to Battelle by May 31, 1985. This will allow us to make the appropriate comparisons in time for the conference.

145

PROBLEM A

COMPACT TENSION SPECIMEN

A-1: Geometry

The geometry and dimensions of the C(T) specimen to be analyzed are shown in Figure A-1. The initial and final crack lengths are as follows:

initial crack length (a_0) = 10.11 in, (25.67 cm)
final crack length (a_f) = 16.3 in, (41.40 cm)

A-2: Material Properties

The material of the C(T) specimen is Type 304 stainless steel. The uniaxial true stress versus true strain and engineering stress versus strain curves are shown in Figures A-2 (a,b) and A-2 (c,d) respectively. Table A-1 contains the digitized values for the stresses and strains. Other material properties to be used are:

Young's Modulus = 25000 ksi, (1.7238×10^5 MPa)
Poisson's Ratio = 0.3

A-3: Crack Extension Versus Load Point Displacement

The experimental crack extension (Δa) versus load-point displacement (δ) record is shown in Figure A-3 and are also given in Table A-2. The displacement is to be applied at point O in Figure A-1.

A-4: Load Versus Load Point Displacement

The experimental load (P) versus load-point displacement (δ) record is shown in Figure A-4. (Table A-2 also includes the load versus displacement data.) This figure is to be used for comparison with the computed P versus δ curve.

A-5: Example of Finite-Element Mesh

The finite-element mesh used by Battelle for the C(T) specimen is shown in Figure A-5. The mesh contains 879 nodes and 263 eight noded isoparametric elements of the serendipity kind. Further mesh size refinement by the participants is acceptable. If any participant wishes to model this as a 3rd problem, this is acceptable.

The broken lines in Figure A-5 represent suggested J contours. The smaller countour moves with the crack tip, but remains unchanged in size and shape for the most part of the crack growth. The larger contour remains fixed for far field J calculations.

Note that the mesh, element type, and the J countours are provided only as examples. Participants may select different models. However, near crack tip and far-field values of J must be computed. Additional contours are acceptable.

A-6: Presentation of Results

The results should be presented in both English (ft-lb) and in SI (m-N) systems of units. The conversion factors needed to convert from English to SI system are provided in Table A-3.

Presentation of results will be in the form of Figures RA-1 to RA-4, and completed Questionnaire A. The supplied sheets of graph paper should be used for completing Figures RA-1 to RA-4. This will facilitate direct comparison of results from different participants. A table of displacements, crack lengths, computed loads, and J values (near and far field) is also desireable (see Table A-4).

QUESTIONNAIRE A

1. Finite-Element Model (supply mesh picture with J-contours indicated).

    a. 2d or 3d analysis:
    b. Number of elements:
    c. Number of nodes:
    d. Type(s) of elements:
    e. Type and order of integration used for stiffness matrix generation:
    f. Crack extension procedure:
    g. Equilibrium compensation procedure:

2. Plasticity model

    a. Definition of initial yield surface:
    b. Hardening model:
    c. Stress vs. strain curve used: FIGURE A-2(a,b) FIGURE A-2(c,d) (Circle one)

3. Formulation

    a. Finite deformation analysis: YES NO (Circle one)
    b. Finite strain analysis: YES NO (Circle one)
    c. Constitutive model:

4. J-computation method:

    a. Contour Integral VCE OTHER (Circle one)
    If other, specify
    b. Define the formula used.

148

Table A.1. Material stress-strain data for Type 304 stainless steel at 550 F (288 C) used in 10T C(T) specimen.

Stress, psi	Stress, MPa	Strain	True Stress, psi	True Stress, MPa	True Strain
3038.7	20.95	0.00018	3039.2	20.95	0.00017998
6077.4	41.90	0.00036	6079.2	41.92	0.00035993
9116.1	62.85	0.00054	9121.0	62.89	0.00053985
12154.8	83.80	0.00072	12163.6	83.86	0.00071974
15193.5	104.76	0.00092	15207.5	104.85	0.00091957
18232.2	125.71	0.00124	18254.8	125.86	0.00123923
20177.0	139.12	0.00160	20209.3	139.34	0.00159872
22121.7	152.53	0.00200	22165.9	152.83	0.00199800
22972.6	158.39	0.00240	23027.7	158.77	0.00239712
24188.1	166.77	0.00320	24265.5	167.31	0.00319489
24735.0	170.54	0.00360	24824.0	171.16	0.00359354
25099.7	173.06	0.00400	25200.1	173.75	0.00399202
25464.3	175.57	0.00440	25576.3	176.35	0.00439035
25828.9	178.09	0.00480	25952.9	178.94	0.00478852
26193.6	180.60	0.00520	26329.3	181.54	0.00518653
26497.5	168.91	0.00560	26645.9	183.72	0.00558438
26922.9	185.63	0.00640	27095.2	186.82	0.00637961
27469.8	189.40	0.00720	27667.6	190.76	0.00717420
27895.3	192.34	0.00800	28118.5	193.87	0.00796817
28442.2	196.11	0.00920	28703.9	197.91	0.00915794
29110.7	200.72	0.01080	29425.1	202.88	0.01074210
29596.9	204.07	0.01216	29956.8	206.55	0.01208670
30387.0	209.52	0.01516	30847.7	212.69	0.01504620
31602.5	217.89	0.01916	32208.0	222.07	0.01897880
32818.0	226.28	0.02316	33578.1	231.52	0.02289590
34033.4	234.66	0.02716	34957.7	241.03	0.02679770
35248.9	243.04	0.03116	36347.3	250.61	0.03068440
36464.4	251.42	0.03616	37783.0	260.51	0.03552160
37679.9	259.80	0.04116	39230.8	270.49	0.04033550
38895.4	268.18	0.04616	40690.8	280.56	0.04512630
40110.8	276.56	0.05116	42162.9	290.71	0.04989430
41326.3	284.94	0.05616	43647.2	300.95	0.05463970
42541.8	293.32	0.06116	45143.7	311.26	0.05936260
44365.0	305.89	0.07016	47477.6	327.35	0.06780820
46188.2	318.46	0.07916	49844.5	343.67	0.07618300
48011.5	331.04	0.08816	52244.2	360.22	0.08448820
49834.7	343.61	0.09816	54726.5	377.34	0.09363610
51657.9	356.18	0.11020	57350.6	395.43	0.10454000
53481.1	368.75	0.12220	60016.5	413.81	0.11529100

Table A-1. (continued)

Stress, psi	Stress, MPa	Strain	True Stress, psi	True Stress, MPa	True Strain
54939.7	378.81	0.1312	62147.8	428.51	0.123279
56114.7	386.91	0.1382	63869.8	440.38	0.129448
57330.1	395.29	0.1482	65826.4	453.87	0.138195
57937.9	399.48	0.1582	67103.7	462.68	0.146867
59153.4	407.86	0.1682	69103.0	476.46	0.155464
60368.8	416.24	0.1782	71126.5	490.42	0.163988
61584.3	424.62	0.1882	73174.5	504.54	0.172440
62799.8	433.00	0.2082	75874.7	523.15	0.189132
64015.3	441.38	0.2282	78623.6	542.11	0.205550
64926.9	447.67	0.2482	81041.8	558.78	0.221703
65838.5	453.95	0.2682	83496.4	575.71	0.237599
67054.0	462.34	0.2882	86379.0	595.58	0.253246
67965.6	468.62	0.3082	88912.6	613.05	0.268652
68269.5	470.72	0.3382	91358.2	629.91	0.291325
68877.2	474.91	0.3582	93549.0	645.02	0.306160
68573.3	472.81	0.3882	211805.0	1460.39	1.558600
68269.5	470.72	0.4122			
65230.8	449.76	0.4282			
60368.8	416.24	0.4482			
53683.7	370.15	0.4682			
49429.5	340.82	0.4782			
44567.6	307.29	0.4862			

Table A.2 Experimental crack growth data from 10T C(T) specimen test at 550 F (288 C).

Load Point Displacement		Load		Crack Length	
inch	mm	lbs/10^3	Newtons x 10^3	inch	mm
0.000	0.000	0.0	0.000	10.11	256.794
0.009	0.229	5.0	22.240	10.11	256.794
0.021	0.533	10.0	44.480	10.11	256.794
0.034	0.866	15.0	66.720	10.11	256.794
0.048	1.219	20.0	88.960	10.11	256.794
0.065	1.651	25.0	111.200	10.11	256.794
0.075	1.905	27.4	121.875	10.11	256.794
0.086	2.184	30.1	133.885	10.11	256.794
0.098	2.489	32.6	145.005	10.11	256.794
0.109	2.769	34.6	153.901	10.11	256.794
0.121	3.073	36.3	161.462	10.11	256.794
0.132	3.353	38.1	169.469	10.11	256.794
0.144	3.658	39.6	176.141	10.11	256.794
0.155	3.937	40.8	181.478	10.11	256.794
0.173	4.394	42.3	188.150	10.11	256.794
0.190	4.826	43.7	194.378	10.11	256.794
0.213	5.410	45.3	201.494	10.11	256.794
0.231	5.867	46.3	205.942	10.11	256.794
0.259	6.579	47.9	213.059	10.11	256.794
0.288	7.315	49.2	218.842	10.11	256.794
0.317	8.052	50.3	223.734	10.11	256.794
0.346	8.788	51.5	229.000	10.11	256.794
0.375	9.525	52.5	233.520	10.11	256.794
0.404	10.262	53.4	237.523	10.11	156.794
0.462	11.735	55.2	245.530	10.11	256.794
0.519	13.183	56.7	252.202	10.11	256.794
0.577	14.656	58.0	257.984	10.11	256.794
0.635	16.129	59.3	263.766	10.11	256.794
0.693	17.602	60.6	269.549	10.11	256.794
0.750	19.050	61.8	274.886	10.11	256.794
0.808	20.523	62.8	279.334	10.11	256.794
0.924	23.470	64.8	288.230	10.11	256.794
0.950	24.130	65.3	290.455	10.11	256.794
1.115	28.321	68.2	303.354	10.13	257.302
1.394	35.408	71.0	315.808	10.20	259.080
1.500	38.100	72.6	322.925	10.27	261.112
1.680	42.672	72.9	324.259	10.37	263.398
1.750	44.450	72.4	322.035	10.42	264.668
2.245	57.023	70.4	313.139	10.79	274.066
2.824	71.730	67.3	299.350	11.15	283.210
3.409	86.589	59.9	266.435	11.59	294.386

Table A.2 (continued)

Load Point Displacement		Load		Crack Length	
inch	mm	lbs/10^3	Newtons x 10^3	inch	mm
3.725	94.615	55.3	245.974	12.02	305.308
4.113	104.470	51.4	228.627	12.35	313.690
4.538	115.265	48.8	217.062	12.78	324.612
4.908	124.663	46.1	205.053	13.18	334.772
5.248	133.299	43.7	194.378	13.48	342.392
5.553	141.046	41.9	186.371	13.79	350.266
5.867	149.022	40.1	178.365	14.03	356.362
6.138	155.905	37.7	167.690	14.29	362.966
6.408	162.763	36.2	161.018	14.54	369.316
6.735	171.069	34.4	153.011	14.80	375.920
7.058	179.273	32.7	145.450	15.09	383.286
7.369	187.173	31.0	137.888	15.35	389.890
7.698	195.529	29.5	131.216	15.61	396.494
8.016	203.606	28.0	124.544	15.84	402.336
8.382	212.903	26.4	117.627	16.07	408.178
8.857	224.968	24.9	110.755	16.30	414.020

Table A.3 Conversion of English unites to SI units.

To Convert	In	to	Multiply by
Energy Release Rate	Inch-pounds per square inch (in lbf/in^2)	Joule per square meter (J/m^2)	175.1
Force	Pound-force (lbf)	Newton (N)	4.448
Force per unit length	Pound-force per foot	New per meter (N/m)	14.59
J-integral	Inch-pound per square inch (lbf/in^2)	Joule per square meter (J/m^2)	175.1
Length	Foot (ft) Inch (in)	Meter (m)	0.3048 0.0254
Moment	Pound-force-foot (lbf ft)	Newton-meter (NM)	1.356
Stress (pressure)	Pound-force per square inch (lbf/in^2)	Pascal (Pa)	6.895×10^3
Stress intensity factor	Kilopound-force per inch$^{3/2}$ (kip/in$^{3/2}$)	Meganewton per meter$^{3/2}$ (MN/m$^{3/2}$)	1.099
Temperature	Fahrenheit (F)	Celsium (C)	c=5(f-32)/9

STRESS INTENSITY FACTOR CONVERSIONS

MPa=m$^{1/2}$or (MN=m$^{-3/2}$)	N=mm$^{-3/2}$	kgf-mm$^{-3/2}$	ksi=$\sqrt{in}$
1.	31.623	3.2246	0.9101
0.03162	1.	0.10197	0.0287
0.31012	9.80665	1.	0.2822
1.099	34.749	3.543	1.

Table A.4 Summary of computed 10T C(T) results

Crack Length		Load-Point Displacement		Calculated Values Load		J (Near Field)		J (Far Field)	
inch	mm	inch	mm	lb	Kn	$\frac{\text{in-lb}}{\text{in}^2}$	KN/m^2	$\frac{\text{in-lb}}{\text{in}^2}$	KN/m^2

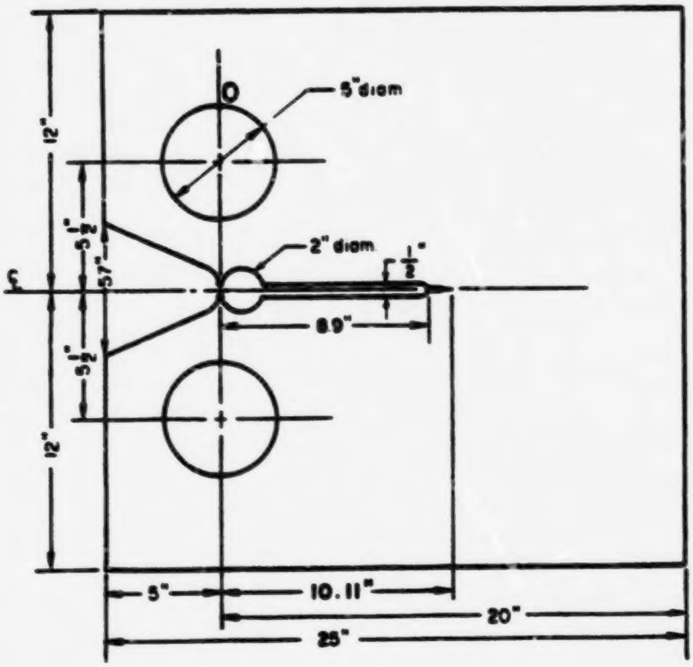
5" diam
12"
5 1/2"
5.7"
2" diam
1/2"
℄
8.9"
5 1/2"
12"
5"
10.11"
20"
25"

Note 1 inch = 25,4 mm

FIGURE A-1. GEOMETRY OF THE 1.0 INCH (25 MM) THICK 10T-C(T) SPECIMEN

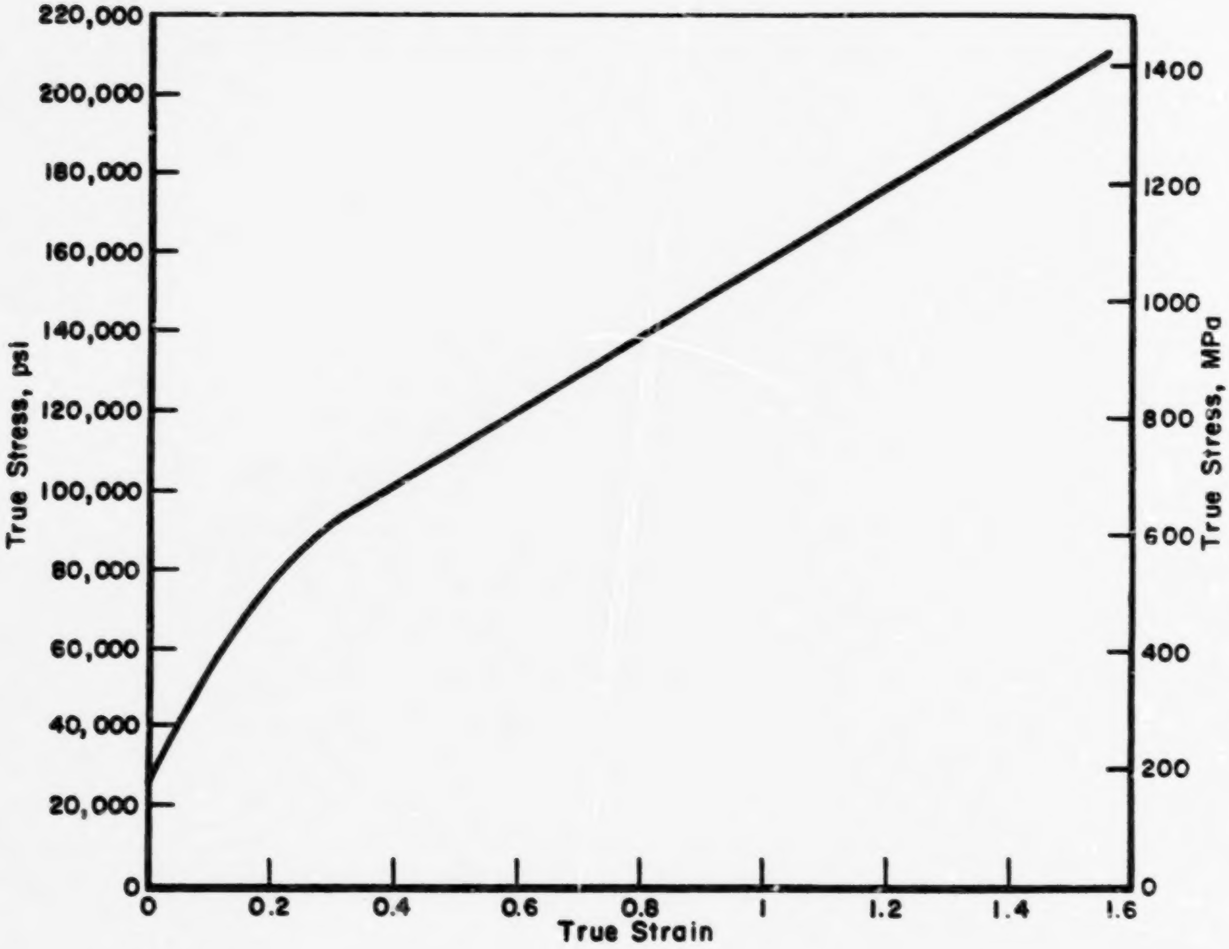

FIGURE A-2(a). UNIAXIAL TRUE STRESS VERSUS TRUE STRAIN FOR TYPE 304 STAINLESS STEEL AT 550 F (288C) USED IN 10T-C(T) SPECIMEN TEST

BEST COPY AVAILABLE

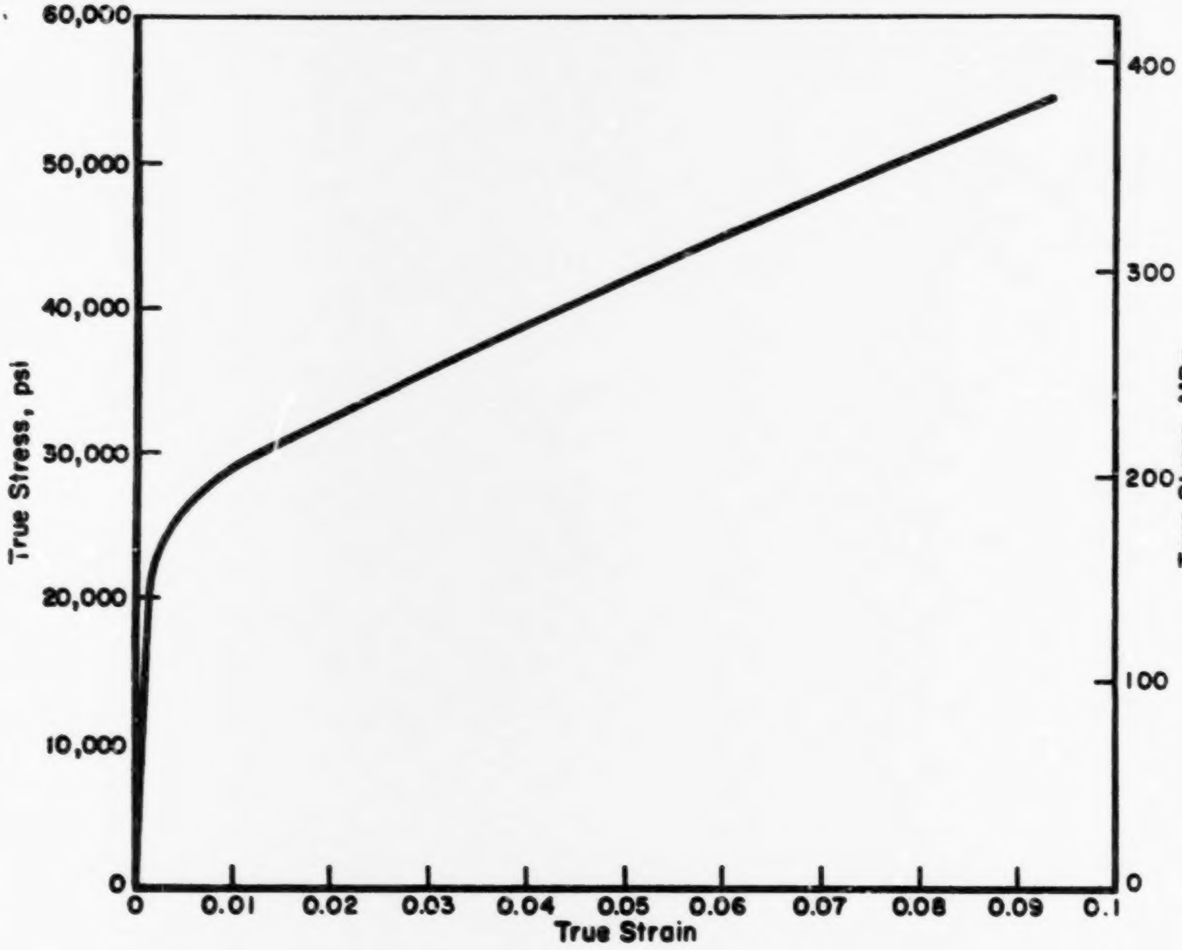

FIGURE A-2(b). UNIAXIAL TRUE STRESS VERSUS TRUE STRAIN FOR TYPE 304 STAINLESS STEEL AT 550 F (288 C) USED IN 10T-C(T) SPECIMEN TEST

157

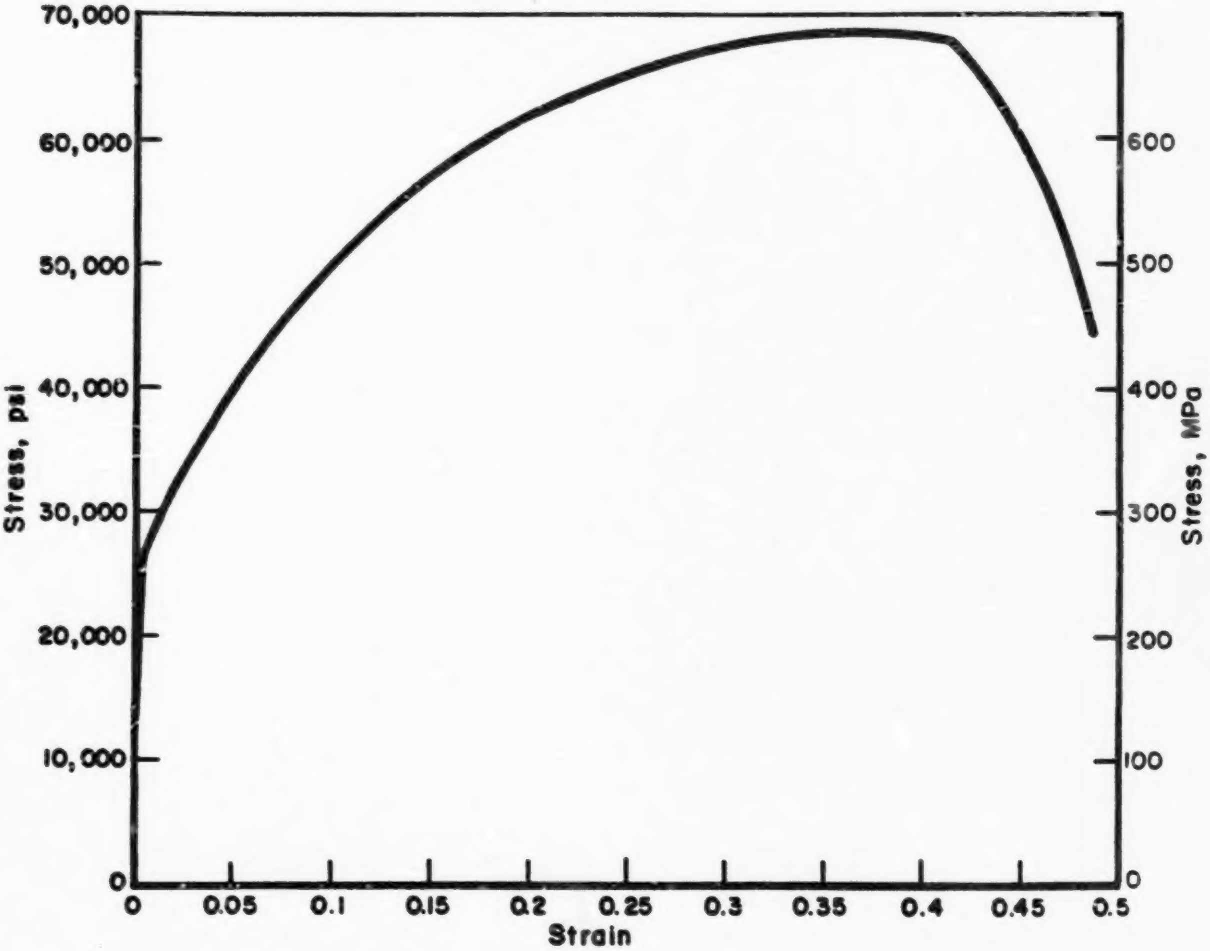

FIGURE A-2(c). ENGINEERING STRESS VERSUS STRAIN FOR TYPE 304 STAINLESS STEEL AT 550 F (288 C) USED IN 10T C(T) SPECIMEN TEST

158

BEST COPY AVAILABLE

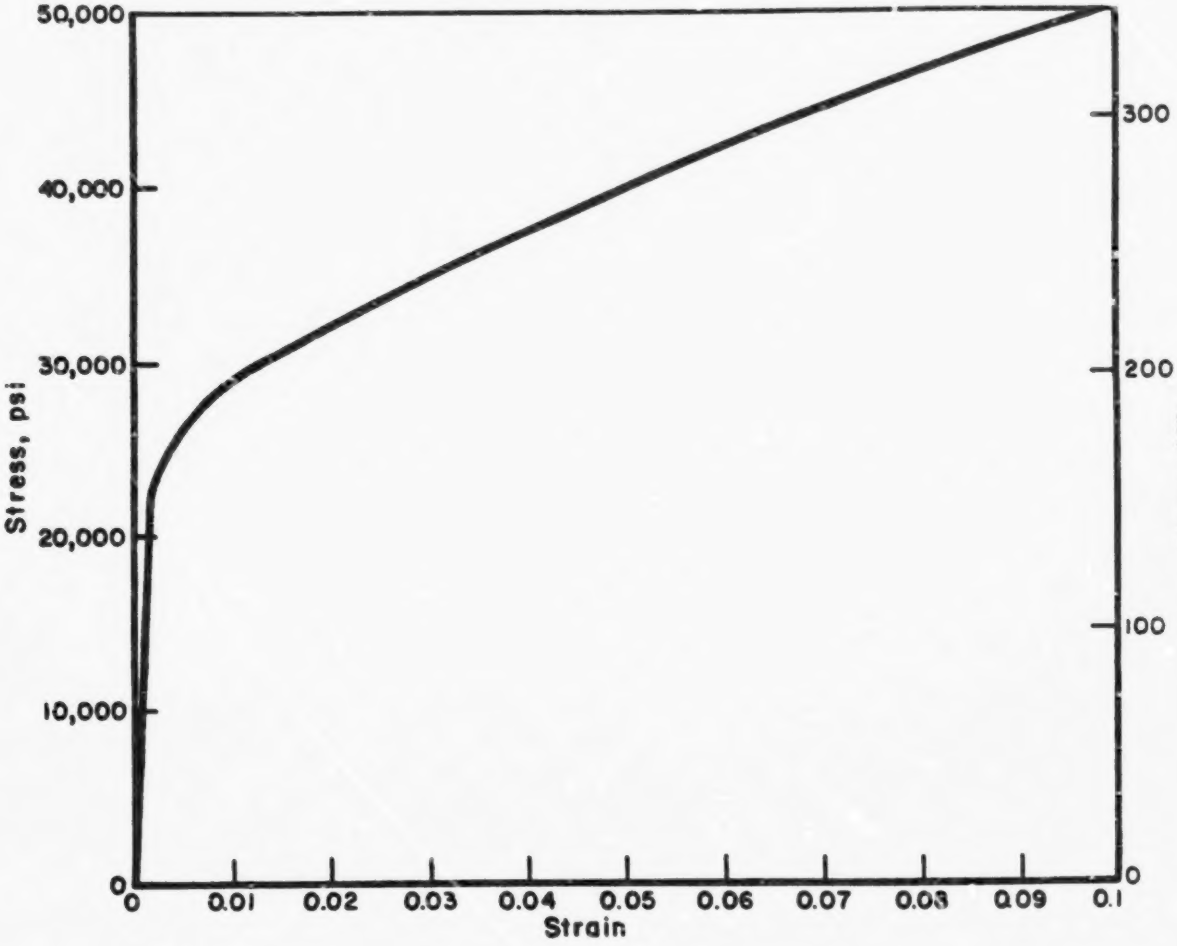

FIGURE A-2(d). ENGINEERING STRESS VERSUS STRAIN FOR TYPE 304 STAINLESS STEEL AT 550 F (288 C) USED IN 10T C(T) SPECIMEN TEST

159

BEST COPY AVAILABLE

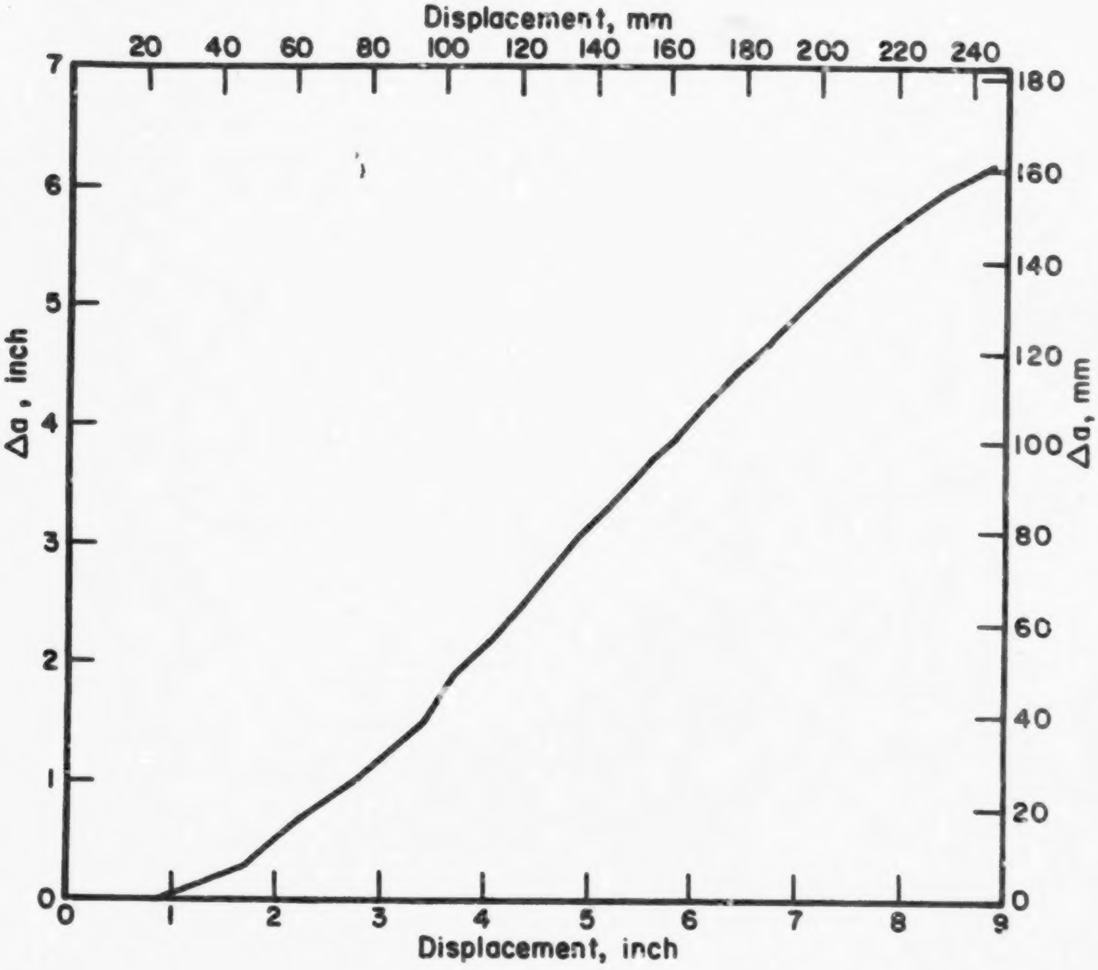

FIGURE A-3. CRACK EXTENSION VERSUS APPLIED DISPLACEMENT FOR THE 10T-C(T) TYPE 304 STAINLESS STEEL 1-INCH (25.4 MM) THICK SPECIMEN

160

BEST COPY AVAILABLE

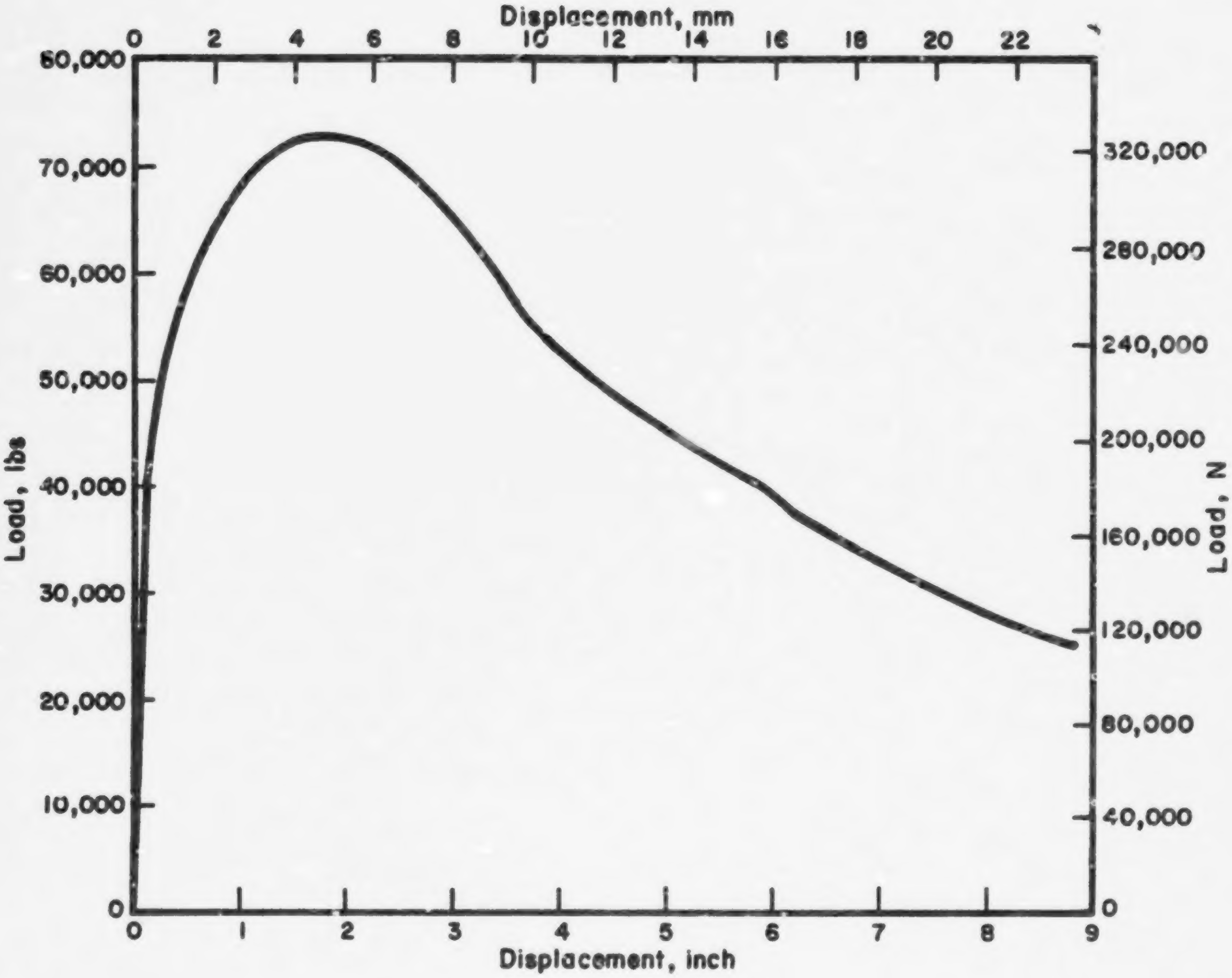

FIGURE A-4. EXPERIMENTAL LOAD VERSUS LOAD-POINT DISPLACEMENT FOR THE 10TC(T) TYPE 304 STAINLESS STEEL SPECIMEN AT 550 F (288 C)

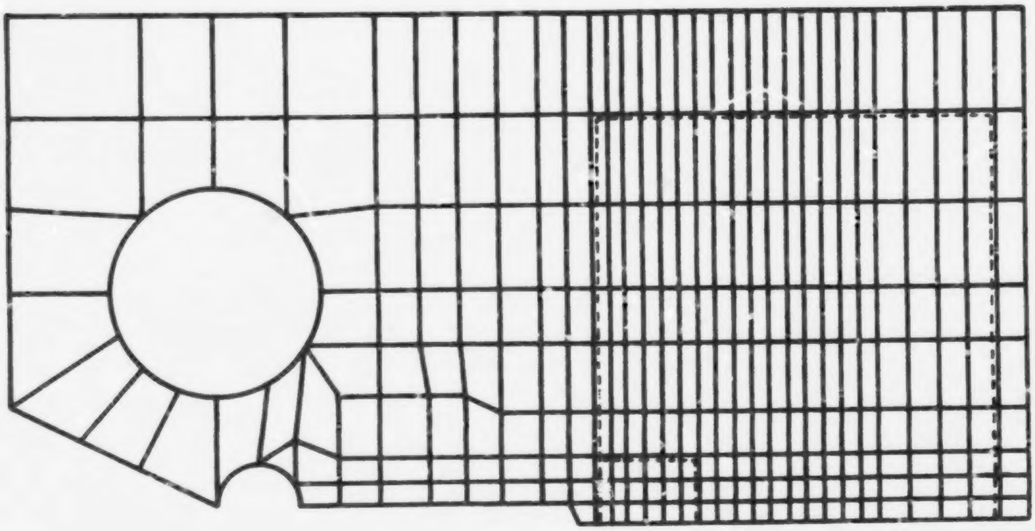

FIGURE A-5. FINITE ELEMENT MESH AND J-CONTOURS (DASHED LINES) USED BY BATTELLE FOR THE 10T COMPACT TENSION SPECIMEN ANALYSIS

162

BEST COPY AVAILABLE

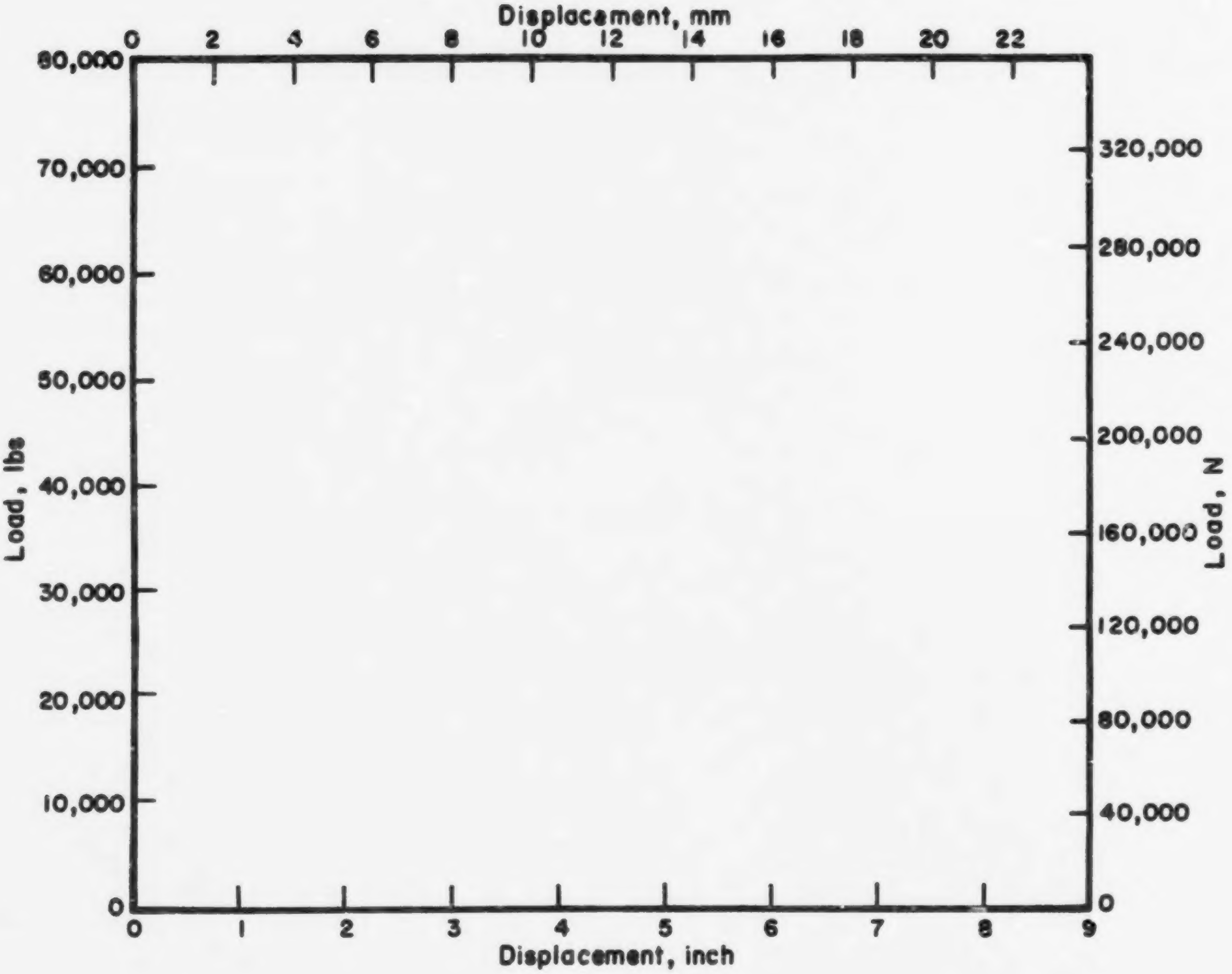

FIGURE RA-1. CALCULATED LOAD VERSUS DISPLACEMENT

BEST COPY AVAILABLE

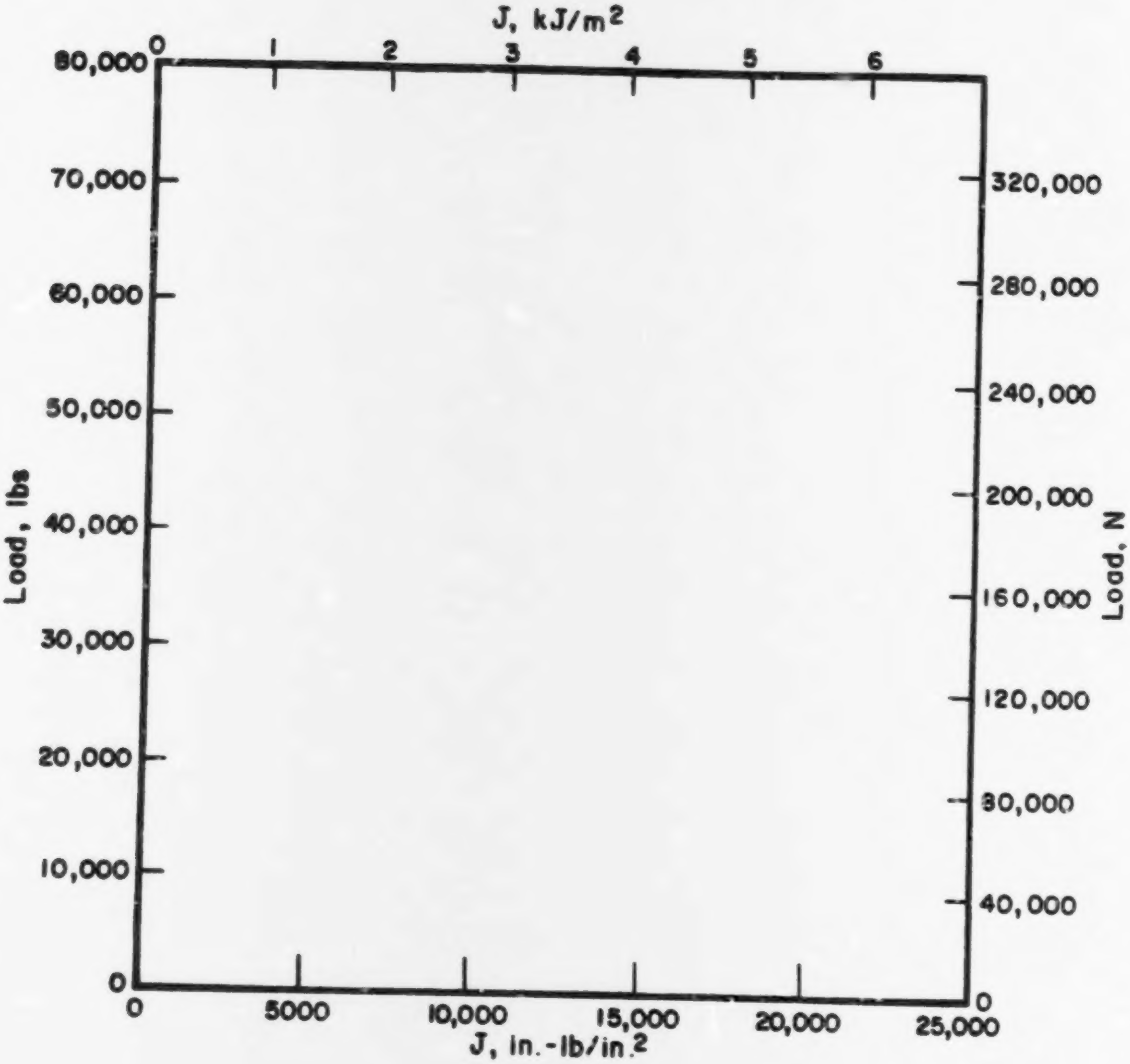

FIGURE RA-2. CALCULATED LOAD VERSUS J UP TO CRACK INITIATION

164

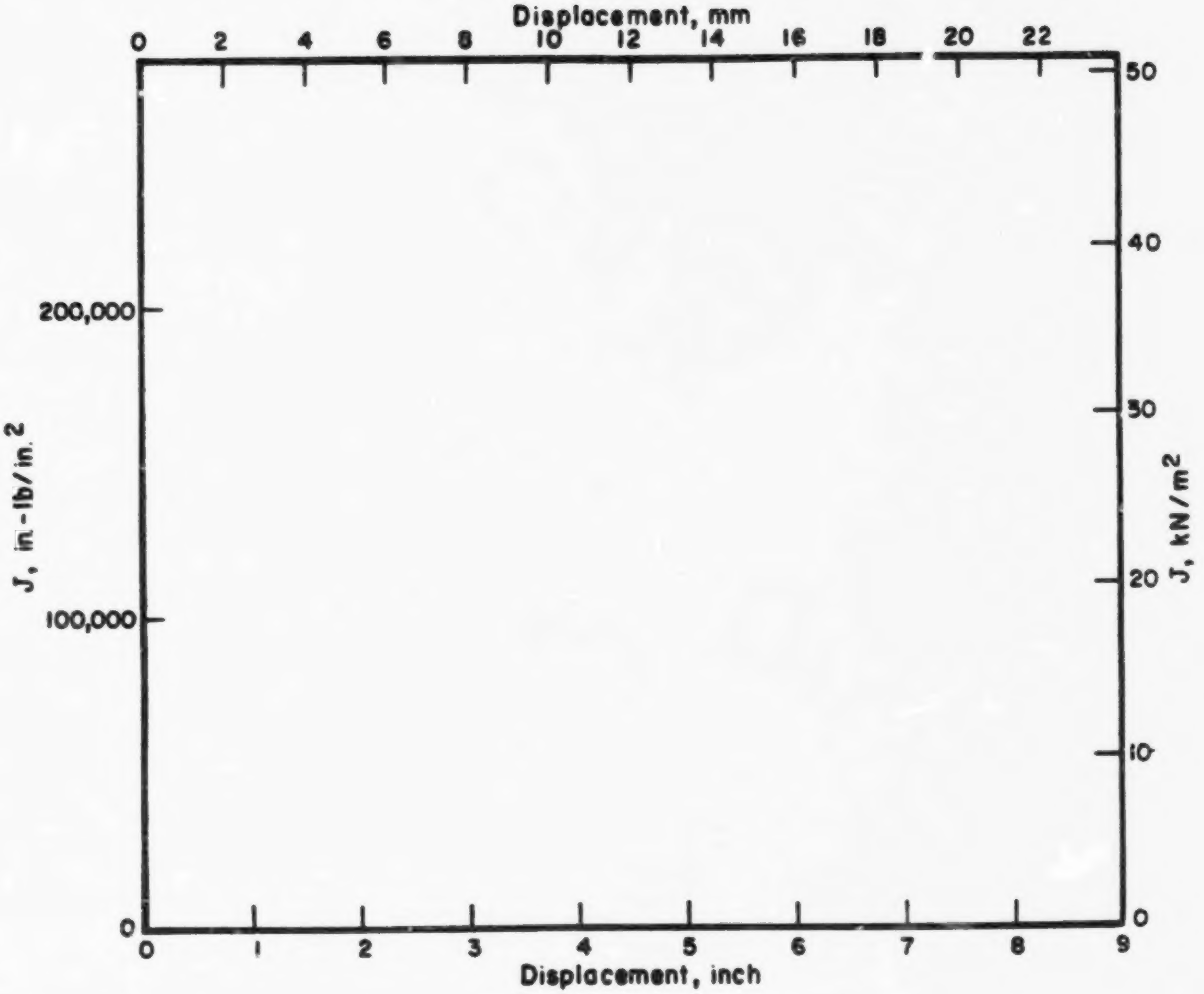

FIGURE RA-3. CALCULATED J VERSUS DISPLACEMENT

165

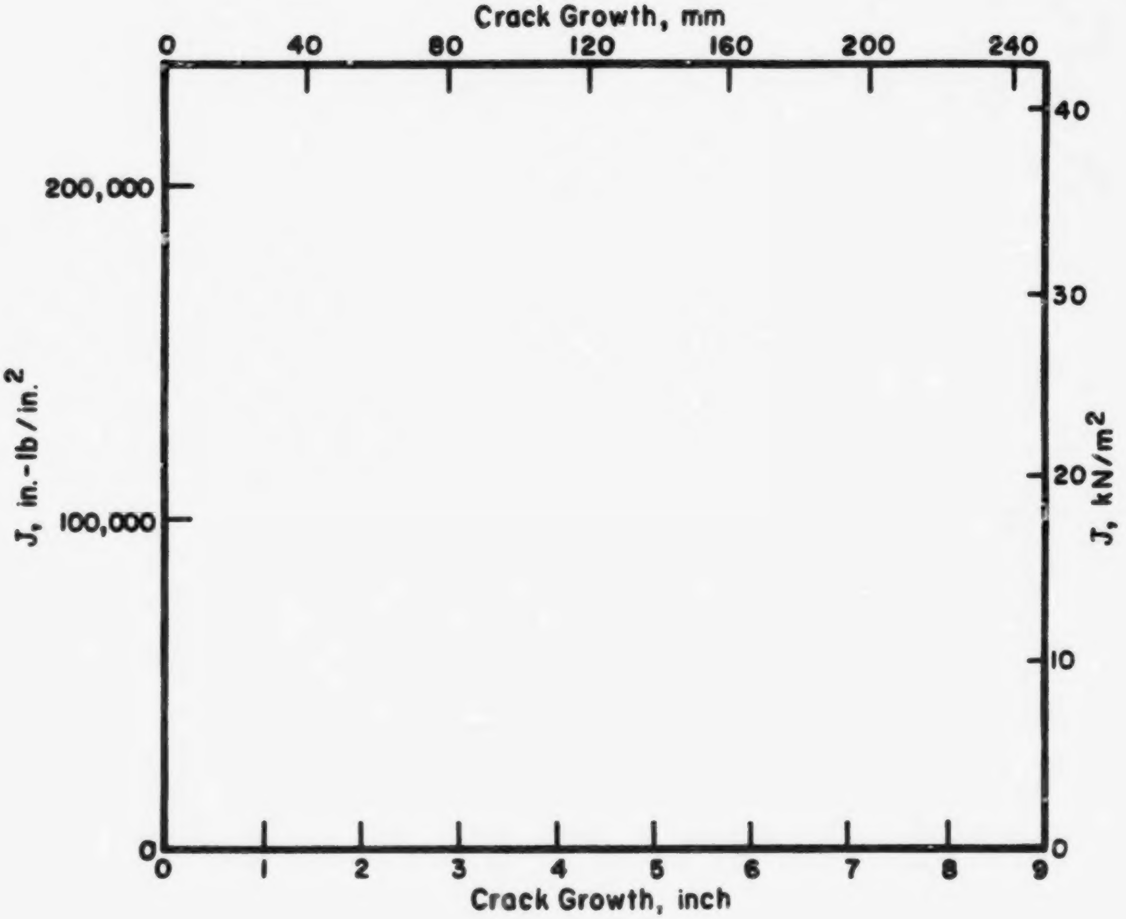

FIGURE RA-4. CALCULATED J-R CURVE

166

PROBLEM B

PIPE WITH CIRCUMFERENTIAL THROUGH-WALL CRACK

B-1: Geometry

The geometry and dimensions of the cracked pipe to be analyzed are shown in Figure B-1. Where "a" is measured at the mid thickness of the pipe.

B-2: Material Properties

The material of the pipe is Type 304 Stainless Steel. The uniaxial true stress versus true strain and engineering stress versus strain, curves to be used are shown in Figures B-2 (a and b) and B-2 (c and d), respectively. These values are also given in Tables B-1 and B-2.

Other material properties to be used are:
Young's Modulus = 26,800 ksi (185 MPa)
Poisson's Ratio = 0.3

B-3: Crack Extension versus Load Point Displacement

The experimental crack extension (Δa) versus load point displacement and load records are given in Table B-3. The displacement is to be applied at point "O" in Figure B-1.

B-4: Load Versus Load Point Displacement

The experimental load (P) versus load point displacement (δ) record is shown in Figure B-3. This curve is to be used for comparison with the computed P versus δ curve. Note that this is the total load (i.e., twice the load at each of the load points "O" in Figure B-1. These data are also given in Table B-2.

B-5: Example of Finite-Element Mesh

An example of a finite-element mesh for a circumferentially cracked pipe is shown in Figure B-4. The mesh contains twenty noded isoparametric brick elements of the serendipity kind.

Note that the mesh and element type are provided only as an example. Participants may select different models. However, the entire pipe length shown in Figure B-4 must be analyzed.

B-6: Boundary Conditions

The constraining condition must be a simple support at the ends of the pipe. The loading on the pipe can be either concentrated, distributed of $\cos\theta$ type, or other. In the experiment the pipe was supported by a rigid saddle for one third of the circumference and for one pipe diameter in axial length to prevent buckling. Appropriate boundary conditions may be assigned to account for the geometry, material, and boundary condition symmetry.

167

B-7: Presentation of Results

The results should be presented in both English and SI systems of units. The conversion factors needed to convert from English to SI system are provided in Table A-3.

Presentation of results will be in the form as shown in Figures RB-1 to RB-4, and completed Questionnaire B. The supplied sheet of graph paper should be used for completing Figures RB-1 to RB-4. In addition, the computed results must be summarized in Table B-4. This will facilitate direct comparison of results from different participants.

QUESTIONNAIRE B

1. Finite-Element Model (supply mesh picture with J-contours indicated, if contours were used).

    a. Number of elements:
    b. Number of nodes:
    c. Type(s) of elements:
    d. Type and order of integration used for stiffness matrix generation:
    e. Crack extension procedure:
    f. Equilibrium compensation procedure:

2. Plasticity model

    a. Definition of initial yield surface:
    b. Hardening model:
    c. Stress vs. strain curve used: FIGURE A-2(a) FIGURE A-2(b) (Circle one)

3. Formulation

    a. Finite deformation analysis: YES NO (Circle one)
    b. Finite strain analysis: YES NO (Circle one)
    c. Constitutive model:

4. J-computation method:

    a. Contour Integral VCE OTHER (Circle one)
    If other, specify
    b. Define the formula used.

Table B-1. True stress-strain data for Type 304 stainless steel pipe material at room temperature.

True Stress PSI	True Stress MPa	True Strain	True Stress PSI	True Stress MPa	True Strain
1950.	13.44	0.0000	101291.	698.37	0.2257
8667.	59.76	0.0001	103592.	714.24	0.2353
17664.	121.78	0.0005	105867.	729.92	0.2448
26958.	185.86	0.0011	108088.	745.25	0.2542
35145.	242.31	0.0019	110217.	759.91	0.2624
39821.	274.55	0.0035	112205.	773.62	0.2698
42051.	289.93	0.0056	114405.	788.79	0.2791
43525.	300.09	0.0079	116572.	803.73	0.2883
37685.	259.82	0.0090	118706.	818.44	0.2973
40511.	279.31	0.0092	120814.	832.98	0.3062
45099.	310.94	0.0111	122881.	847.23	0.3147
46054.	317.53	0.0134	124657.	859.47	0.3212
46908.	323.41	0.0158	126713.	873.65	0.3299
47721.	329.02	0.0180	128732.	887.57	0.3386
48480.	334.25	0.0203	130736.	901.39	0.3472
49197.	339.20	0.0225	132739.	915.20	0.3558
49901.	344.05	0.0248	134692.	928.66	0.3641
50585.	348.77	0.0270	136637.	942.07	0.3724
51249.	353.34	0.0292	138610.	955.68	0.3809
51864.	357.58	0.0313	140603.	969.42	0.3896
52490.	361.90	0.0334	142567.	982.96	0.3984
53102.	366.12	0.0355	144556.	996.67	0.4071
53709.	370.31	0.0377	146514.	1010.17	0.4158
54299.	374.37	0.0398	148431.	1023.39	0.4244
54873.	378.33	0.0419	150327.	1036.46	0.4328
55469.	382.44	0.0439	152216.	1049.49	0.4412
56021.	386.25	0.0459	154106.	1062.52	0.4496
56586.	390.14	0.0479	155972.	1075.38	0.4579
57132.	393.91	0.0500	157788.	1087.90	0.4661
57692.	397.77	0.0520	159614.	1100.49	0.4742
58777.	405.25	0.0559	161390.	1112.74	0.4823
60356.	416.14	0.0617	163163.	1124.96	0.4903
61887.	426.69	0.0674	164911.	1137.02	0.4983
63383.	437.01	0.0730	166626.	1148.84	0.5061
64816.	446.89	0.0785	168296.	1160.36	0.5140
66232.	456.65	0.0840	169922.	1171.57	0.5217
67636.	466.33	0.0894	171522.	1182.60	0.5294
69035.	475.97	0.0948	173013.	1192.88	0.5370
70368.	485.17	0.1001	174376.	1202.28	0.5446
71684.	494.24	0.1054	175363.	1209.08	0.5521
72967.	503.08	0.1106	258507.	1782.34	1.0485

170

BEST COPY AVAILABLE

Table B-1. (continued)

True PSI	Stress MPa	True Strain	True PSI	Stress MPa	True Strain
74249.	511.92	0.1157	336392.	2319.34	1.5271
75512.	520.63	0.1208			
76732.	529.04	0.1258			
77987.	537.70	0.1309			
79215.	546.16	0.1358			
80420.	554.47	0.1408			
81606.	562.65	0.1457			
82798.	570.87	0.1505			
84436.	582.16	0.1563			
87082.	600.40	0.1664			
89536.	617.32	0.1767			
91947.	633.95	0.1868			
94307.	650.22	0.1966			
96630.	666.24	0.2064			
98972.	682.38	0.2160			

Table B.2. Engineering stress-strain data for Type 304 stainless steel pipe material at room temperature.

Stress, psi	Stress, MPa	Strain	Stress, psi	Stress, MPa	Strain
1950.	13.44	0.0000	76281.	525.94	0.2054
8666.	59.75	0.0001	77471.	534.14	0.2173
17654.	121.72	0.0005	78611.	542.00	0.2292
26928.	185.66	0.0011	79742.	549.80	0.2411
35077.	241.85	0.0019	80825.	557.27	0.2532
39681.	273.59	0.0035	81871.	564.48	0.2653
41815.	288.30	0.0056	82879.	571.43	0.2773
43183.	297.73	0.0079	83828.	577.97	0.2894
37345.	257.48	0.0091	84778.	584.52	0.3001
40138.	276.74	0.0093	85673.	590.69	0.3097
44599.	307.50	0.0112	86544.	596.70	0.3219
45439.	313.29	0.0135	87377.	602.44	0.3341
46175.	318.36	0.0159	88177.	607.95	0.3462
46868.	323.14	0.0182	88946.	613.26	0.3583
47507.	327.54	0.0205	89699.	618.45	0.3699
48100.	331.64	0.0228	90406.	623.33	0.3788
48680.	335.64	0.0251	91108.	628.17	0.3908
49238.	339.48	0.0273	91753.	632.61	0.4030
49776.	343.19	0.0296	92387.	636.98	0.4151
50265.	346.57	0.0318	92994.	641.17	0.4274
50766.	350.02	0.0340	93586.	645.25	0.4392
51248.	353.34	0.0362	94156.	649.18	0.4512
51723.	356.62	0.0384	94700.	652.93	0.4637
52182.	359.78	0.0428	95716.	659.59	0.4764
52623.	362.82	0.0428	95716.	659.94	0.4895
53086.	366.02	0.0449	96207.	663.33	0.5025
53506.	368.91	0.0470	96673.	666.53	0.5156
53937.	371.88	0.0491	97102.	669.49	0.5286
54347.	374.71	0.0513	97512.	672.32	0.5416
54771.	377.63	0.0533	97910.	675.06	0.5546
55580.	383.21	0.0575	98301.	677.76	0.5677
56745.	391.24	0.0636	98669.	680.30	0.5808
57852.	398.87	0.0697	99003.	682.60	0.5938
58920.	406.24	0.0757	99337.	684.90	0.6068
59920.	413.14	0.0817	99633.	686.94	0.6198
60895.	419.86	0.0876	99926.	688.96	0.6328
61848.	426.43	0.0936	100195.	690.82	0.6459
62790.	432.92	0.0994	100444.	692.53	0.6589
63664.	438.95	0.1053	100660.	694.03	0.6719
64515.	444.82	0.1111	100847.	695.31	0.6849
65328.	450.42	0.1169	101015.	696.47	0.6980

172

Table B.2 (continued)

Stress, psi	Stress, MPa	Strain	Stress, psi	Stress, MPa	Strain
66135.	455.99	0.1227	101128.	697.25	0.7108
66919.	461.39	0.1284	101128.	697.41	0.7239
67658.	466.48	0.1341	100962.	696.11	0.7369
68420.	471.73	0.1398	100342.	691.83	0.7499
69153.	476.79	0.1455	98710.	680.58	0.7629
69860.	481.66	0.1512			
70544.	486.38	0.1568			
71226.	491.08	0.1624			
72219.	497.93	0.1691			
73732.	508.36	0.1810			
75032.	517.32	0.1933			

Table B.3. Experimental load-displacement records for crack length for pipe experiment at room temperature.

Load Point Displacement		Total Load(a)		Half Crack Length	
in	mm	lb	kN	in	mm
3.2456	82.43	18023.	80.17	9.2362	234.59
4.1866	106.33	23073.	102.63	9.2362	234.59
5.094	129.38	27549.	122.54	9.2362	234.59
6.328	160.73	33967.	151.09	9.2362	234.59
7.811	198.41	40892.	181.89	9.2362	234.59
9.808	249.14	47543.	211.48	9.2362	234.59
11.431	290.34	50540.	224.81	9.2362	234.59
12.948	328.87	52703.	234.43	9.2362	234.59
13.769	349.73	53852.	239.54	9.2362	234.59
14.518	368.75	55796.	248.19	9.2362	234.59
14.907	378.63	56220.	250.07	9.2362	234.59
15.282	388.16	56220.	250.07	9.2854	235.84
15.978	405.84	57082.	253.91	9.3347	237.10
16.842	427.78	57411.	255.37	9.4370	239.69
17.428	442.67	57561.	256.04	9.6358	244.74
17.922	455.21	57561.	256.04	9.7362	247.29
18.686	474.62	57561.	256.04	9.8366	249.84
19.440	493.77	57561.	256.04	9.9862	253.64
19.968	507.18	57944.	257.74	10.1350	257.42
21.811	553.99	58314.	259.39	10.2360	259.99
24.078	611.58	56726.	252.32	10.7360	272.69
25.878	657.30	55522.	246.97	11.2360	285.39
28.298	718.76	54304.	241.55	11.7360	298.09
29.196	741.57	53852.	239.54	12.2360	310.79
30.386	771.80	53428.	237.65	12.4600	316.48
32.749	831.82	51457.	228.89	12.7360	323.49
34.136	867.05	50103.	222.86	13.2360	336.19
36.436	925.47	49665.	220.92	13.6100	345.69
				13.9600	354.58

(a) This is the total load as in Figure B-3. The load of one of the inner load points is half of these values.

Table B.4. Summary of computed pipe results

Crack Length		Load Point Displacement		Computed Results			
				Load		J	
in	mm	in	mm	klb	kN	klb/in	kN/m

175

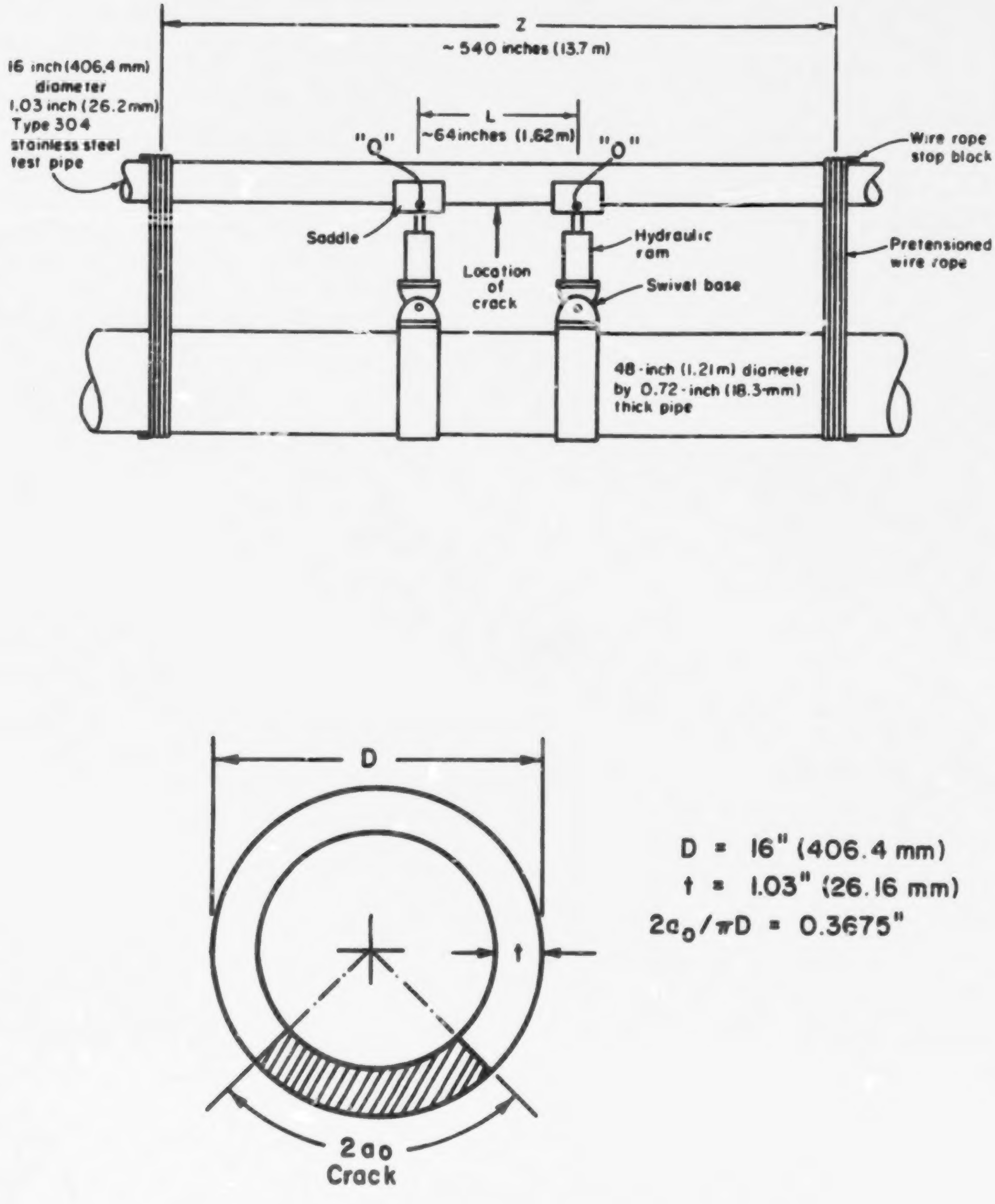
Z
~ 540 inches (13.7 m)
16 inch (406.4 mm) diameter 1.03 inch (26.2 mm) Type 304 stainless steel test pipe
L
~64 inches (1.62 m)
"O"
"O"
Wire rope stop block
Saddle
Hydraulic ram
Pretensioned wire rope
Location of crack
Swivel base
48-inch (1.21 m) diameter by 0.72-inch (18.3-mm) thick pipe
D
t
2ao
Crack
D = 16" (406.4 mm)
t = 1.03" (26.16 mm)
2a₀/πD = 0.3675"

FIGURE B-1. THE APPARATUS AND CRACKED PIPE GEOMETRY FOR 16-INCH (406.4 MM) OUTSIDE DIAMETER PIPE BENDING EXPERIMENT

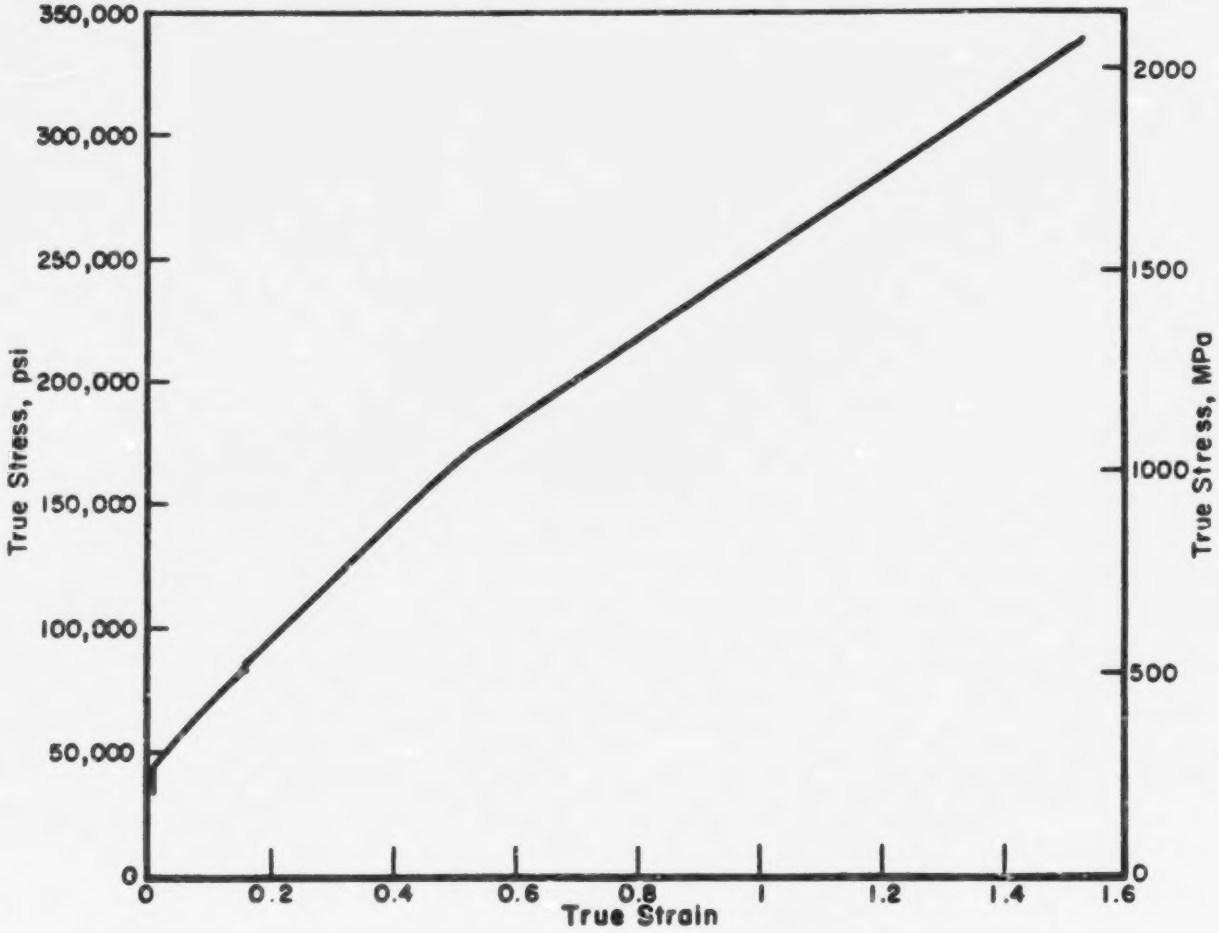

FIGURE B-2(a). UNIAXIAL TRUE STRESS-TRUE STRAIN CURVE FOR 16-INCH-DIAMETER (406.4 MM) TYPE 304 STAINLESS STEEL PIPE MATERIAL AT ROOM TEMPERATURE (LARGE STRAINS)

177

BEST COPY AVAILABLE

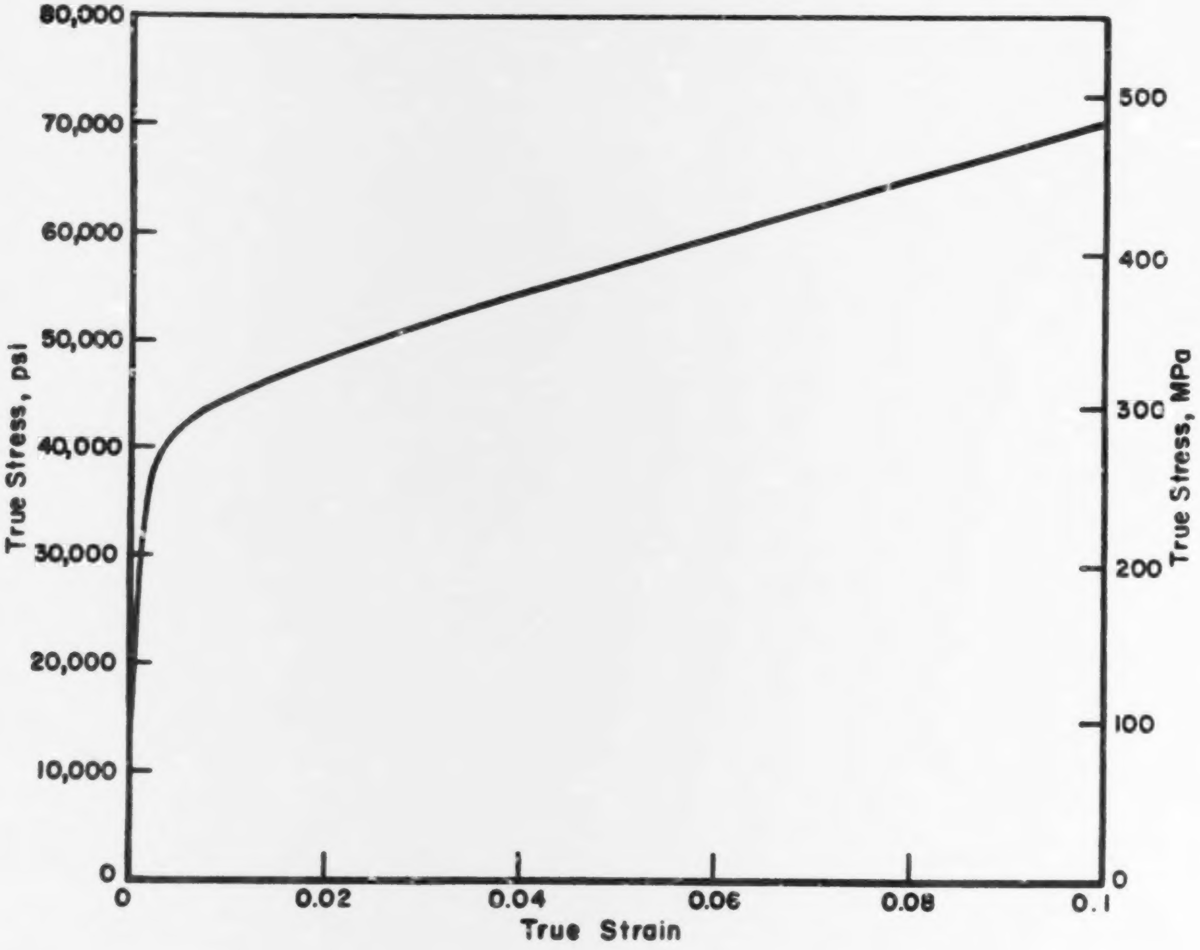

FIGURE B-2(b). UNIAXIAL TRUE STRESS-TRUE STRAIN CURVES FOR 16-INCH-DIAMETER (406-MM) TYPE 304 STAINLESS STEEL PIPE MATERIAL AT ROOM TEMPERATURE (SMALL STRAIN DATA)

178

BEST COPY AVAILABLE

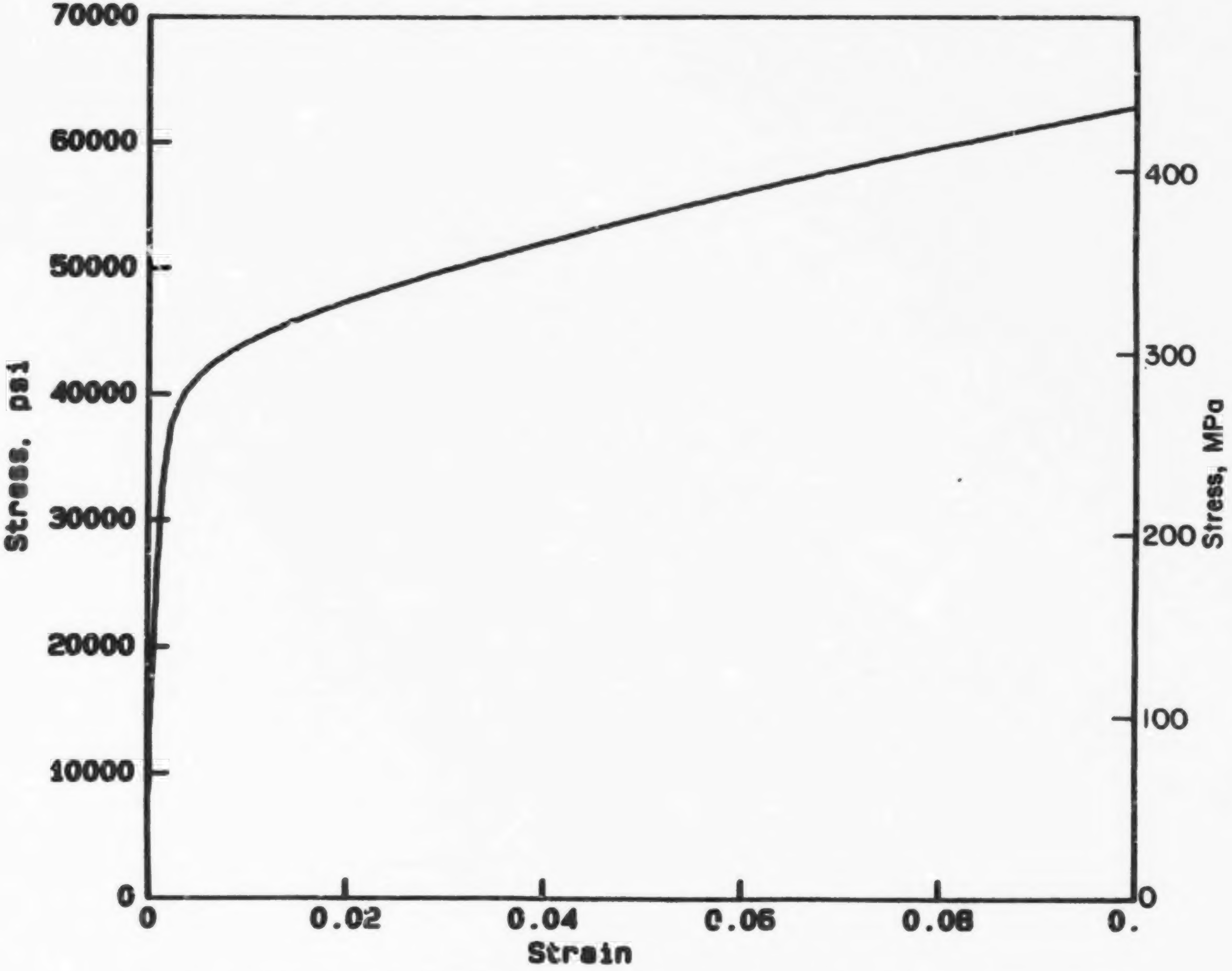

FIGURE B-2(c). ENGINEERING STRESS VERSUS STRAIN CURVE FOR 16-INCH-DIAMETER (406.4 MM) TYPE 304 STAINLESS STEEL PIPE MATERIAL AT ROOM TEMPERATURE

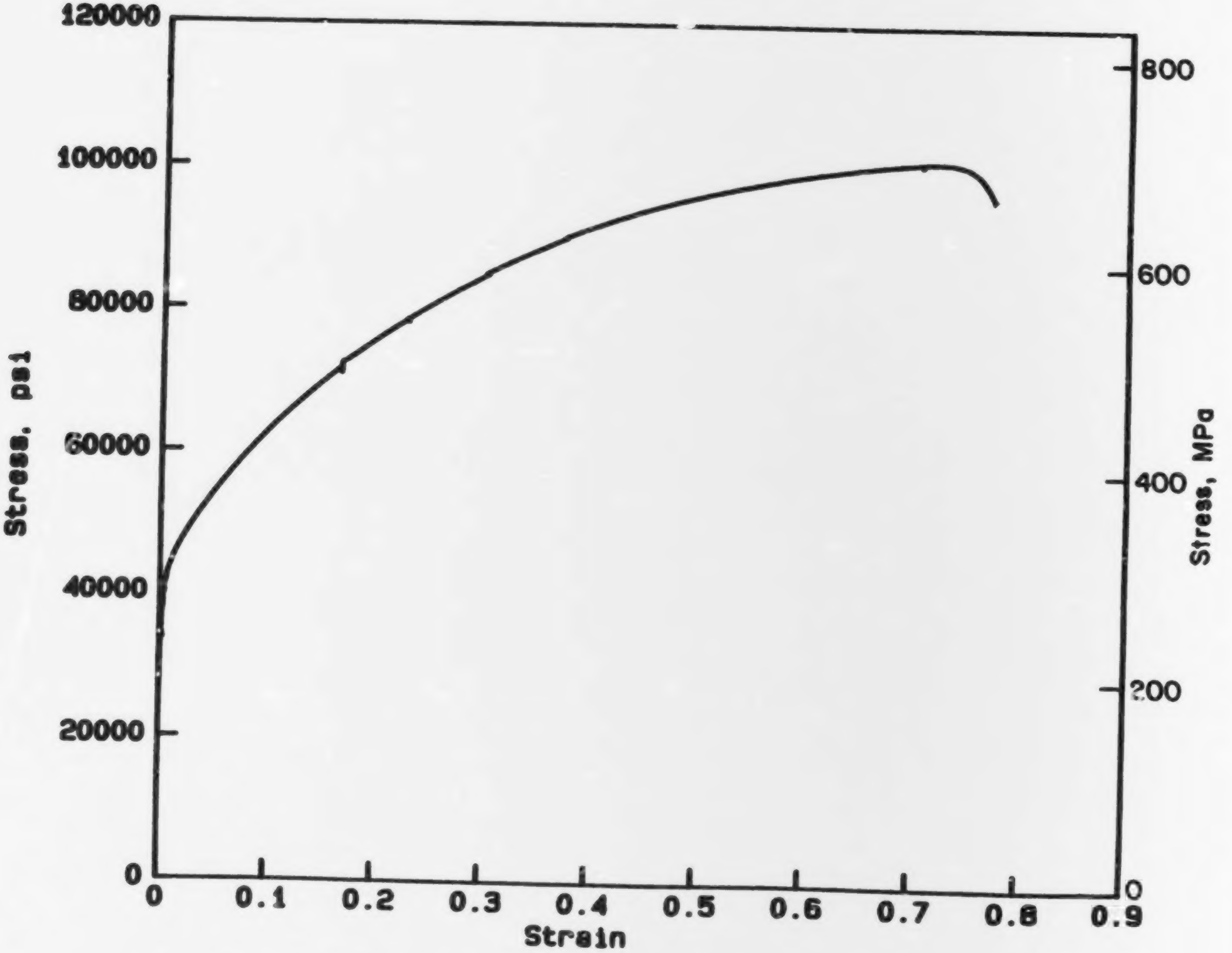

FIGURE B-2(d). ENGINEERING STRESS VERSUS STRAIN CURVE FOR 16-INCH-DIAMETER (406.4 MM) TYPE 304 STAINLESS STEEL PIPE MATERIAL AT ROOM TEMPERATURE

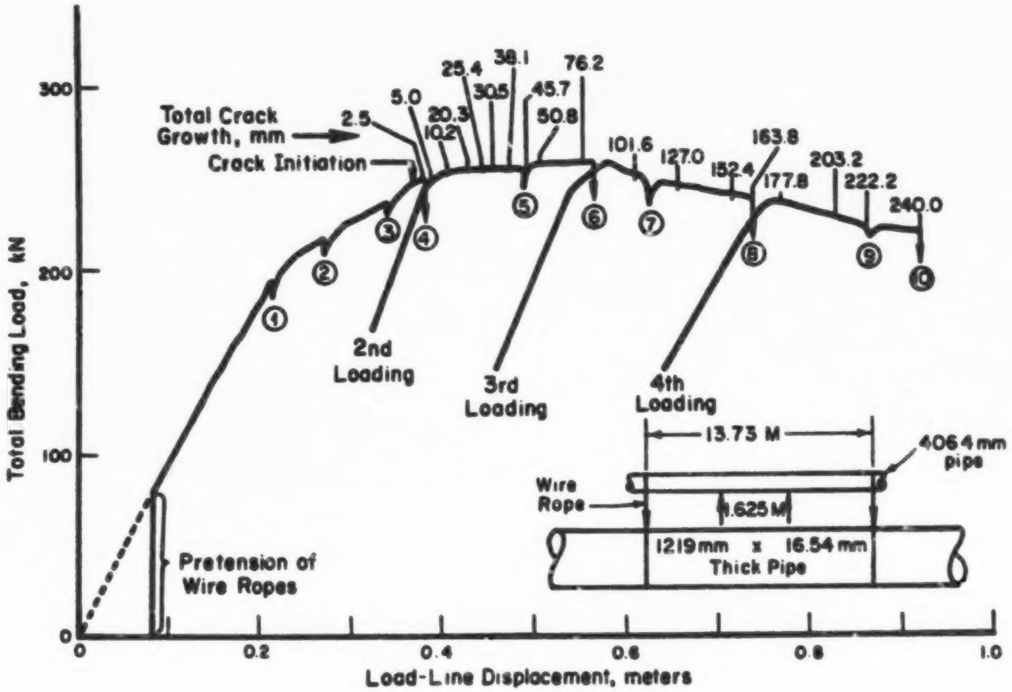

FIGURE B-3. BENDING LOAD VERSUS LOAD-LINE DISPLACEMENT DURING EXPERIMENT (406.4-MM O.D. BY 26.16-MM THICK STAINLESS STEEL PIPE. INITIAL CRACK LENGTH = 484 MM)

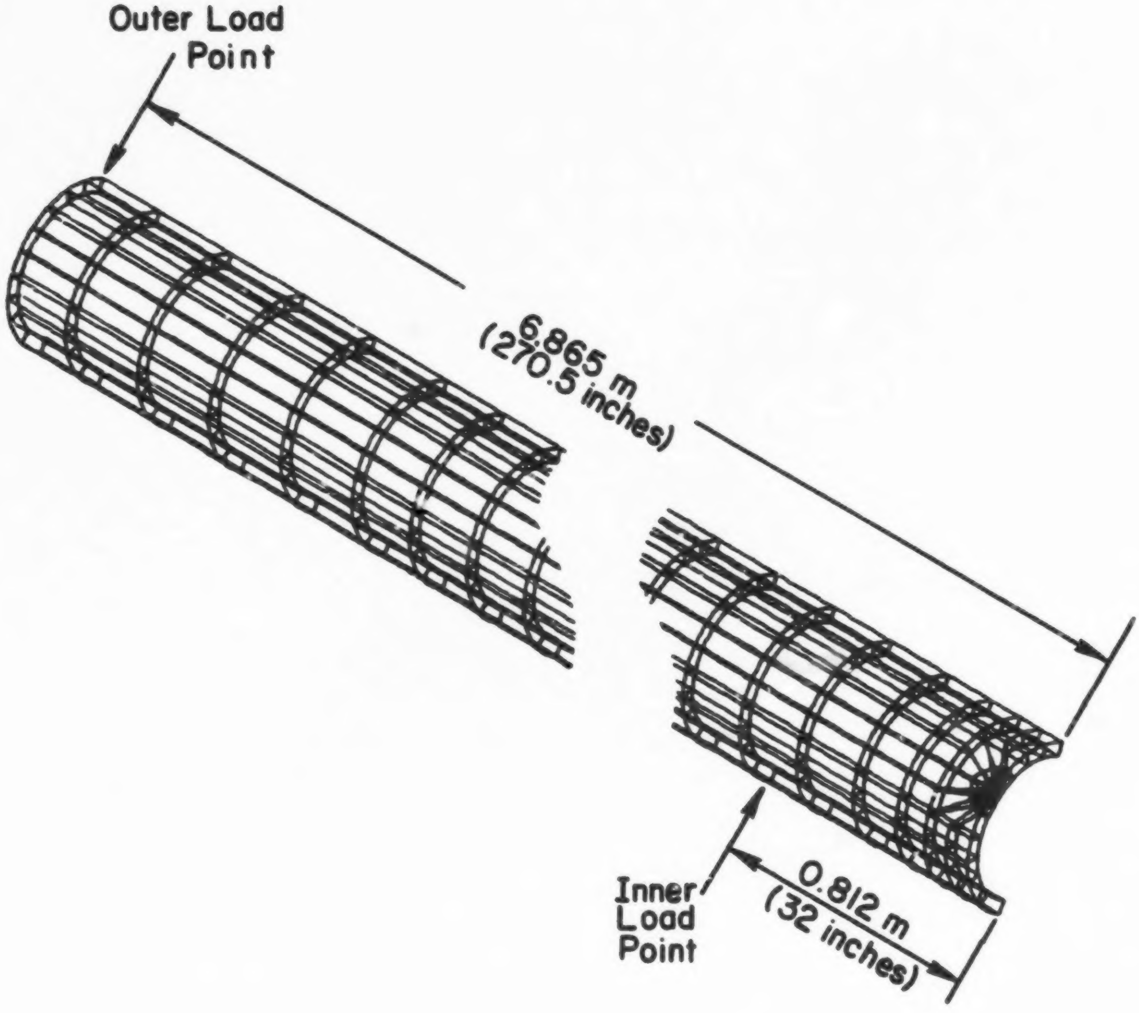

Outer Load Point
6.865 m (270.5 inches)
Inner Load Point
0.812 m (32 inches)

FIGURE B-4. AN EXAMPLE OF A 3D FINITE ELEMENT GRID USING CURVED BRICK ELEMENTS FOR MODELING A CIRCUMFERENTIALLY THROUGH-WALL CRACKED PIPE

182

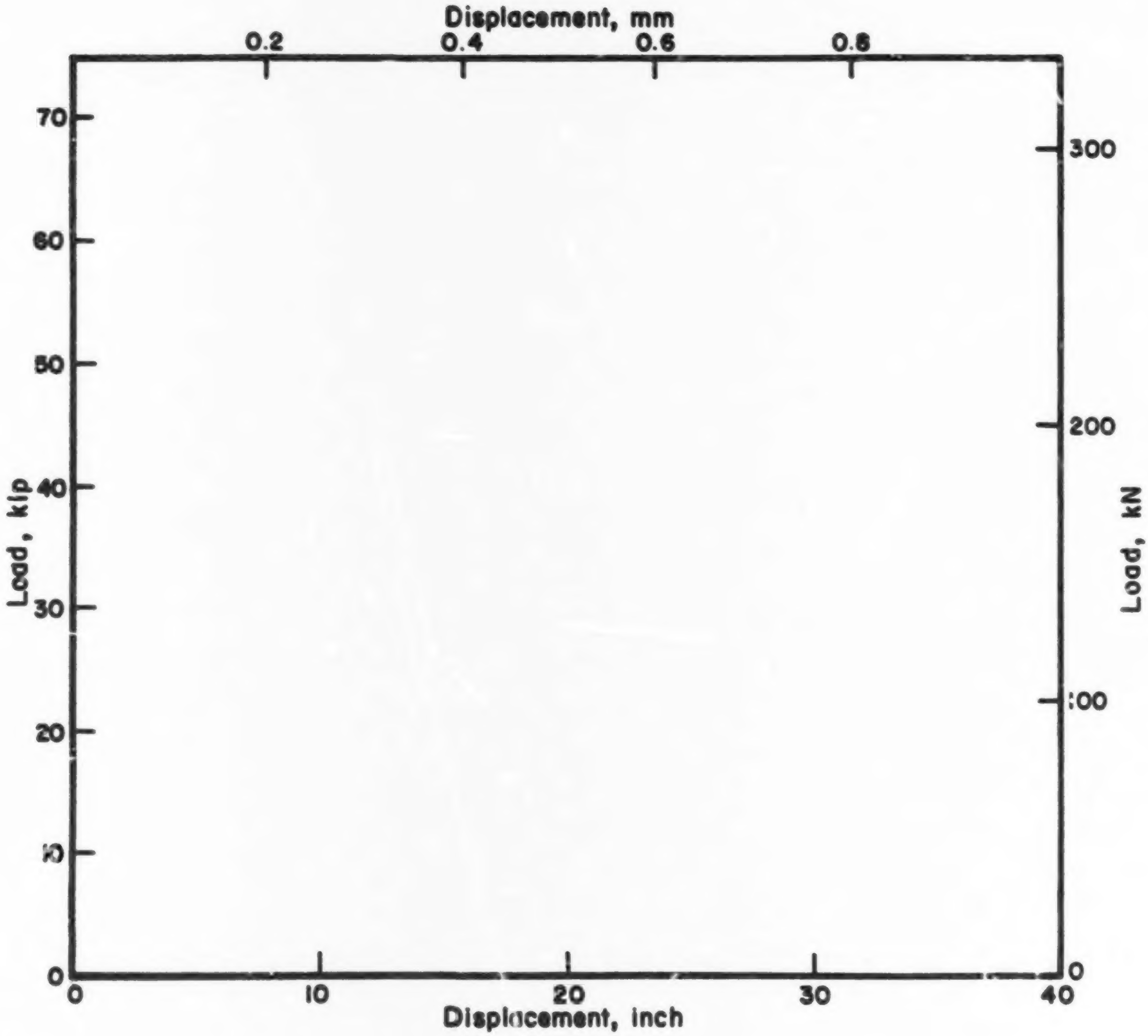

FIGURE RB-1. GRAPH OF CALCULATED LOAD-DISPLACEMENT CURVE FROM PIPE PROBLEM

183

BEST COPY AVAILABLE

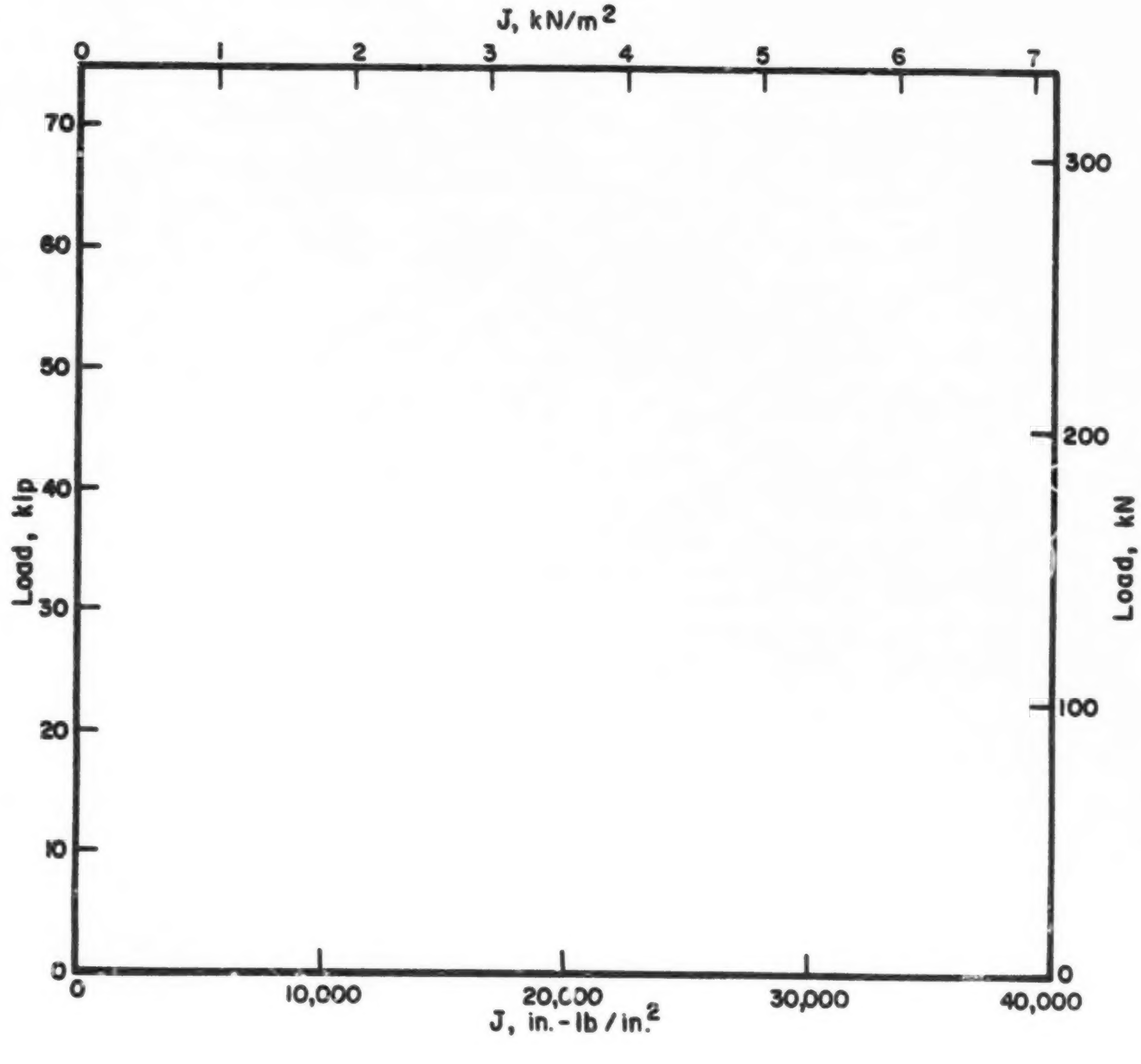

FIGURE RB-2. GRAPH OF CALCULATED J VERSUS LOAD CURVE (UP TO CRACK INITIATION)

184

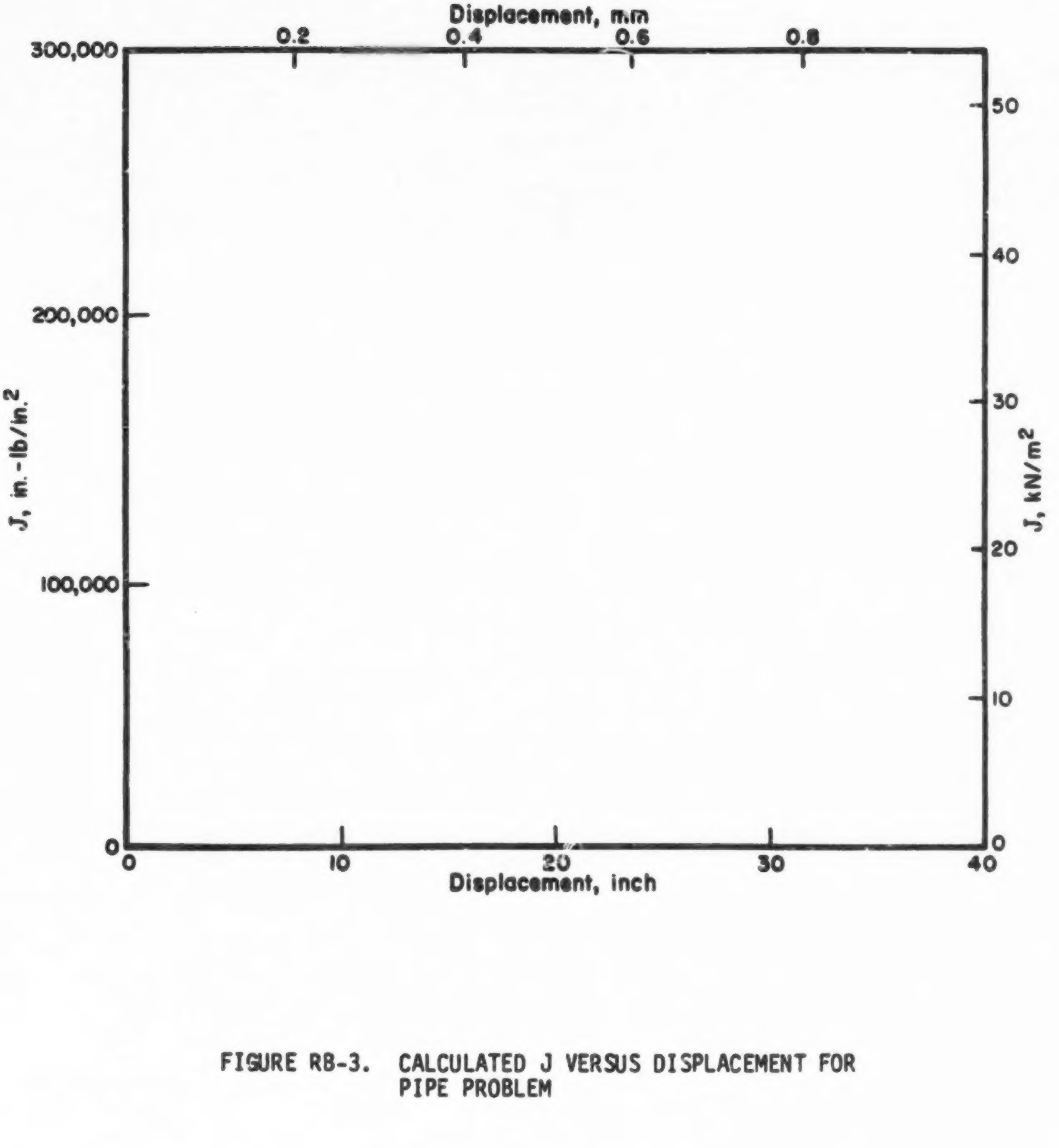

FIGURE RB-3. CALCULATED J VERSUS DISPLACEMENT FOR PIPE PROBLEM

185

BEST COPY AVAILABLE

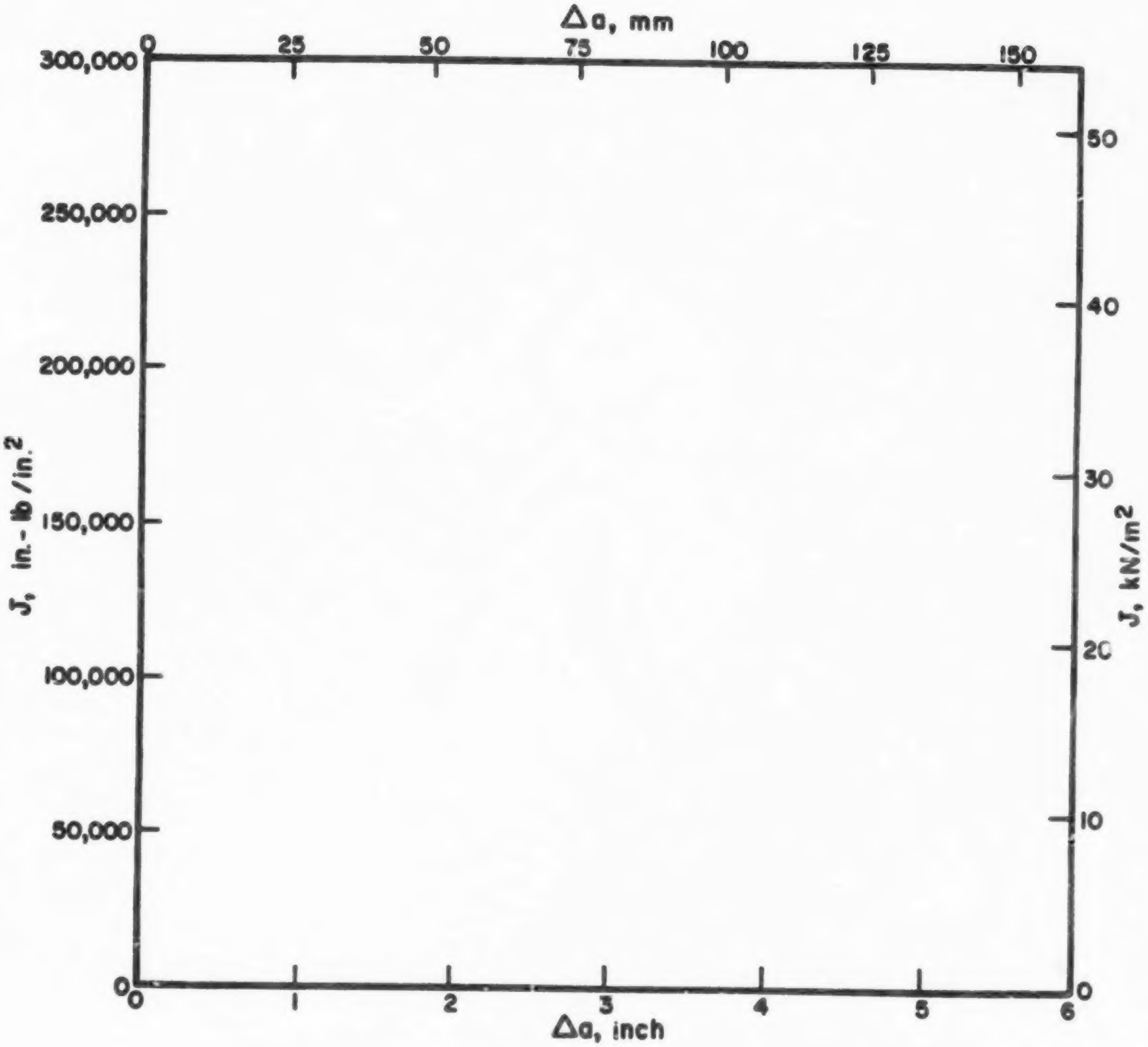

FIGURE RB-4. CALCULATED J-R CURVE

186

NRC FORM 335
(2-84)
NRCM 1102,
3201, 3202

U.S. NUCLEAR REGULATORY COMMISSION

BIBLIOGRAPHIC DATA SHEET

SEE INSTRUCTIONS ON THE REVERSE

1 REPORT NUMBER (Assigned by TIDC, add Vol. No., if any)
NUREG/CR-4573
BMI-2135

2 TITLE AND SUBTITLE
Elastic-Plastic Finite Element Analysis of Crack Growth in Large Compact Tension and Circumferentially Through-Wall-Cracked Pipe Specimen: Results of the First Battelle/NRC Analysis Round Robin

3 LEAVE BLANK

4 DATE REPORT COMPLETED

MONTH	YEAR
September	1986

5 AUTHOR(S)
J. Ahmad, M. Nakagaki, V. Papaspyropoulos, and G. Wilkowski

6 DATE REPORT ISSUED

MONTH	YEAR
October	1986

7 PERFORMING ORGANIZATION NAME AND MAILING ADDRESS (Include Zip Code)
Battelle's Columbus Division
505 King Avenue
Columbus, Ohio 43201

8 PROJECT/TASK/WORK UNIT NUMBER

9 FIN OR GRANT NUMBER
B8134

10 SPONSORING ORGANIZATION NAME AND MAILING ADDRESS (Include Zip Code)
Division of Engineering Safety
Office of Nuclear Regulatory Research
U.S. Nuclear Regulatory Commission
Washington, D.C. 20555

11a TYPE OF REPORT
Technical

b PERIOD COVERED (Inclusive dates)
3/85 through 4/86

12 SUPPLEMENTARY NOTES

13 ABSTRACT (200 words or less)

This report contains the results of a round-robin organized by Battelle as part of the Degraded Piping Program-Phase II. The round-robin involved elastic-plastic finite element analyses by the participants of two problems requiring crack growth modeling, and the computation of the J-integral as a function of crack extension. A large planform compact tension specimen, and a circumferentially through-wall-cracked pipe geometry were analyzed. The experimental data needed for the analyses were supplied by Battelle. For each problem, finite element analyses were performed by Battelle and four other organizations.

14 DOCUMENT ANALYSIS - a. KEYWORDS/DESCRIPTORS
Finite element analysis, J-integral, crack-growth, compact tension specimen, circumferential through-wall crack.

b IDENTIFIERS/OPEN ENDED TERMS

15 AVAILABILITY STATEMENT
Unlimited

16 SECURITY CLASSIFICATION
(This page)
Unclassified
(This report)
Unclassified

17 NUMBER OF PAGES

18 PRICE

187

BEST COPY AVAILABLE